



University
of Glasgow

Li, Guangrui (2019) *Multilayer waveguide modes based analysis of 2-D photonic crystals-pertinent to modelling PCSELS*. PhD thesis.

<https://theses.gla.ac.uk/73021/>

Copyright and moral rights for this work are retained by the author

A copy can be downloaded for personal non-commercial research or study, without prior permission or charge

This work cannot be reproduced or quoted extensively from without first obtaining permission in writing from the author

The content must not be changed in any way or sold commercially in any format or medium without the formal permission of the author

When referring to this work, full bibliographic details including the author, title, awarding institution and date of the thesis must be given

Enlighten: Theses

<https://theses.gla.ac.uk/>
research-enlighten@glasgow.ac.uk

**Multilayer Waveguide Modes based Analysis
of 2-D Photonic Crystals-pertinent to
Modelling PCSELS**



Guangrui Li

*Submitted in Fulfilment of the Requirements for the Degree of Doctor of
Philosophy*

School of Engineering

College of Science and Engineering

University of Glasgow

October 2018

Abstract

Semiconductor lasers with the combination of characteristics such as large output power, single mode operation and good beam quality are very often desired. The photonic crystal surface emitting laser (PCSEL) has shown significant promise and has received much attention with the purpose of achieving devices with the desired characteristics. The evaluation of the resonant modes of the structure is a primary requirement in modelling PCSELs. However, conventional techniques such as PWE, CMT and FDTD are either computationally very time consuming or mathematically rather intensive.

The aim of this thesis is to develop a new model for evaluating resonance of 2-D photonic crystal, pertinent to the lasing mode of PCSEL. Such aim is achieved by first studying wave characteristics of 1-D periodic structure and understanding the eigenmode and eigenfunction of both infinite and finite periodic structure. It is shown that the eigenmode of the infinite periodic structure is the Bloch mode while the eigenmode of the finite periodic structure is represented by optical tunnelling type of solution. The solutions correspond to the characteristic impedance of the periodic structure.

The concept of eigenmode of finite periodic structure is then used to establish the 2-D model of photonic crystal. The essential underlying concept of the analysis procedure presented in this work is based on viewing the 2-D photonic crystal as a laterally periodic multilayer waveguide which is longitudinally segmented. Such model matches with conventional model favourably and proved to be versatile, efficient, fast (for 500×500 periods takes ~ 7 min using laptop: 2 core at 1.70 GHz, negligible memory usage. (Compare to FDTD for 20×20 periods takes 5h using supercomputer system: 12 core, 24GB RAM). Thus, the model has the potential of generating more comprehensive models of photonic crystal based devices.

Experimental work including fabrication, characterisation further proved the validity of the model. PCSEL with external reflection is experimental studied. It is shown that the lasing characteristics can be modified through introduced external reflection.

Table of Content

Abstract	I
Table of Content.....	II
List of Figures	V
List of Publications	XII
Acknowledgement.....	XV
Author's Declaration.....	XVI
Definitions and Abbreviations	XVII
Chapter 1 Introduction	1
1.1 What is Laser?	2
1.2 Why Electromagnetic (EM) Theory Matters?.....	3
1.3 Photonic crystal surface emitting laser.....	6
1.4 Thesis Outline.....	9
1.5 References	12
Chapter 2 Optics of Homogeneous Isotropic Media.....	14
2.1 Maxwell's Equations	15
2.2 Waves Equations in Homogeneous Media.....	16
2.3 Plane Wave (PW) Propagation	17
2.4 Matrix Formulation for PW propagation in Layered Media	19
2.5 Transfer Matrix Method for Laser Modelling	21
2.6 Concept of Wave Impedance.....	27
2.7 Conclusions	29
2.8 Reference	30
Chapter 3 Optical Waves in Periodic Structure	32
3.1 Hill's Equation and Floquet-Bloch Method	34

3.2	Coupled Mode Theory.....	39
3.3	Transfer Matrix Method for Periodic Media.....	43
3.4	Eigenvalues in Periodic Structure	49
3.4.1	General Concept of Waveguide	51
3.4.2	Waveguide Coupling and Periodic Waveguide	53
3.4.3	Bragg Reflection Waveguide	57
3.4.4	Surface State.....	60
3.5	Conclusion.....	62
3.6	Reference.....	64
Chapter 4 Evaluating Resonances in PCSEL Structures based on Modal Indices		68
4.1	Description of model: y-direction.....	69
4.2	Description of model: x-z plane	71
4.3	Results and discussions	77
4.4	Perturbation theory representation of MIA	83
4.5	Near field to far field transformation: diffraction.....	85
4.6	Further modification and self-consistency of model.....	87
4.7	Conclusions	94
4.8	References	95
Chapter 5 Fabrication and Characterization of PCSEL		98
5.1	Semiconductor growth and photonic crystal pattern.....	98
5.2	PCSEL fabrication as mesa diode	102
5.3	Lasing characteristic of PCSEL	106
5.4	Investigation of PCSEL with external reflection	108
5.5	PCSEL area scaling and in-plane feedback.....	115
5.6	Conclusion.....	119
5.7	Reference.....	120
Chapter 6 Conclusions and Future works		121

6.1	Conclusion.....	121
6.2	Future work	123
	Appendix A Vector Operators and Maxwell's Equation	126
	Appendix B EM Waves in Layered Media: A Transfer Matrix Representation.....	131
	Appendix C The solution to the Mathieu's Equation	134
	Appendix D Coupled Mode Theory in Sinusoidally Stratified media.....	136
	Appendix E Chebyshev Identity and Power N of Unimodular Matrix	139
	Appendix F Poynting Vector Within the Stopband of the Periodic Structure	141
	Appendix G Dielectric Slab Waveguide	146
	Appendix H Waveguide Coupling: A Coupled Mode Approach	149
	Appendix I MATLAB Code for 1-D Periodic Structure	152
	Appendix J MATLAB Code Example for 2-D PC	154

List of Figures

Fig.1.1 Schematics of spontaneous emission, absorption and stimulated emission.	2
Fig.1.2 Schematic of typical laser structure.	3
Fig.1.3 Schematic of ridge waveguide FP laser.	4
Fig.1.4 Schematics of a) DBR laser and b) DFB laser.	5
Fig.1.5 Schematic of VCSEL.	6
Fig.1.6 Schematic of cross-grating DFB.	7
Fig.2.3.1 Plan wave propagating in homogeneous media.	18
Fig.2.3.2 Schematic representation of optical gain.	19
Fig.2.4.1 Plane wave propagation and reflection.	20
Fig.2.5.1 Schematic of typical semiconductor F-P laser.	22
Fig.2.5.2 F-P laser cavity.	23
Fig.2.5.3 The relationship between real and imaginary part of matrix element at lasing threshold of F-P laser.	23
Fig.2.5.4 Resonance spectrum of F-P cavity.	24
Fig.2.5.5 Schematic of typical semiconductor DFB laser.	25
Fig.2.5.6 Simplified DFB structure as 1-D grating with complex index profiles.	25

Fig. 2.5.7 The relationship between real and imaginary part of matrix element at lasing threshold of DFB laser.	26
Fig. 2.5.8 Power transmission spectrum of structure shown in Fig. 2.5.6 with varying gain.	27
Fig. 2.6.1 Impedance concept of electromagnetic wave.	28
Fig. 3.1.1 Structure with one dimensional periodicity: Λ is the period of the function $\varepsilon(x)$.	34
Fig. 3.1.2 Stability diagram of Mathieu's equation. Shaded region is the unstable region corresponds to the unbound solution while white region corresponds to the bound solution.	37
Fig. 3.2.1 Periodically stratified media with index distribution of $\eta(x) = \eta_0 + \eta \cos(Kx)$ along x direction.	39
Fig. 3.2.2 1-D Photonic band structure corresponds to the structure shown in Fig 3.2.1 with index profile $\eta_0 = 2.05$, $\eta = 0.6$, $\Lambda = 0.401\mu m$	41
Fig. 3.2.3 density of states calculated using CMT	42
Fig. 3.3.1 Periodic media with piece-wise constant index profile. The excitation plane wave at angle θ is such that all electric fields are in x - z plane.	43
Fig. 3.3.2 Periodic structure along x -axis excited using plane wave with different angle θ . $\eta_a = 3.13$, $\eta_b = 3.46$, $L_a = 105.5nm$, $L_b = 180.75nm$.	45
Fig. 3.3.3 Power transmission spectrum (blue lines) when varying the number of period as $N = 10$, $N = 30$ and $N = 100$.	46
Fig. 3.3.4 Power reflectance spectrum with different number of period and 1-D photonic band structure obtained using TMM	47

Fig 3.3.5 field intensity (red line) within the periodic structure when the frequency lies inside stopband	48
Fig. 3.4.1 Schematic of metal slab waveguide	51
Fig. 3.4.2 Schematic of dielectric slab waveguide	52
Fig. 3.4.3 Identically coupled waveguide: with $N = 9$ (nine identity coupled waveguides) is shown, the refractive index profiles are $\eta_a = 3.2$; $\eta_b = 3.5$ and the dimension is chosen as $L_a = 0.156\mu m$; $L_b = 0.143\mu m$.	53
Fig. 3.4.4 Bound mode profile of the coupled waveguide. (referring to Fig.3.4.4)	54
Fig. 3.4.5 Identically coupled waveguide with an extra excitation layer. $N = 9$ (nine identity coupled waveguides) is shown, the refractive index profiles are $\eta_a = 3.2$; $\eta_b = 3.5$ and the dimension is chosen as $L_a = 0.156\mu m$; $L_b = 0.143\mu m$.	55
Fig. 3.4.6. a) Power reflectance spectrum of the structure referred to Fig.3.4.5. The red triangle represents the conventional bound mode while the black circle represents the mode due to the optical tunnelling b) wave impedance representation of the optical tunnelling.	56
Fig. 3.4.7 Mode profile of BIC mode: Solution within the continuum region while energy remain bounded rather than dissipated.	57
Fig. 3.4.8 Schematic of Bragg reflection waveguide.	57
Fig. 3.4.9 Power transmission spectrum of Bragg reflection waveguide	58
Fig. 3.4.10 Impedance matching representation of photonic crystal cavity state.	59
Fig. 3.4.11 Mode profile of cavity states: 10 period of grating is used in each side.	59
Fig. 3.4.12 Schematic of structure that supporting surface state.	60

Fig. 3.4.13 Two types of surface state. The surface boundary at $x=0$	61
Fig. 4.1.1 3-D schematic of PCSEL structure.	70
Fig. 4.2.1 Schematic of PC structure. N_x and N_z are number of periods along x and z respectively.	71
Fig.4.2.2 Model description: (Refractive indices: η_a , $\eta_b = \eta_c = \eta_d$) Lateral modes propagating along the z -axis are computed for a relevant range of wavelengths.	73
Fig.4.2.3 a) Transmission spectrum of periodic structure (referring to Fig. 2a, $N = 30$, $L_b = 286.25nm$, $w_b = 116.5nm$, $\eta_a = 3.13$, $\eta_b = 3.46$.) b) Examples of eigen-mode solutions $f_m(x)$ of 1-D periodic structure (Fig.4.2.2)	75
Fig.4.2.4 Model description: The shaded area with dark blue region representing the multilayer waveguide in Fig.4.2.1 is replaced by a homogeneous medium of effective modal index $\eta_{eff, m}$, thus resulting in a 1-D periodic grating along z with an unit cell composited of $\eta_{eff, m}$ and η_b	75
Fig.4.2.5 Flowchart of the modelling process	76
Fig.4.3.1 2-D resonances of PC calculated using MIA. (Band edge resonances: Mode 1 and Mode 2)	78
Fig.4.3.2 Photonic band structure around Γ point calculated using PWE. (Band edge resonances: Mode 1 and Mode 2). Inserted figure shows the full band calculated using PWE.	79
Fig.4.3.3 band edge resonance identified using active media	79
Fig.4.3.4 Band edge resonances calculated with varying filling factor. w^2/L^2	80
Fig. 4.3.5 Band edge resonances calculated with varying η_a	81

Fig.4.3.6 Finite size effect on band edge resonance.	82
Fig.4.3.7 Plot of field distribution $ \hat{F}(x, z) $ for band-edge mode. $N_x = N_z = 250$	82
Fig.4.3.8 a) A detail of the plot of $ \hat{F}(x, z) $ at the centre of the lobe using MIA. b) A detail plot of $ \hat{F}(x, z) $ using PWE by assuming infinite number of periods ($N \rightarrow \infty$).	83
Fig.4.4.1 Schematic of waveguide discontinuity. In principle, all modes including bound mode and continuum modes exist	84
Fig.4.5.1 interface of two media in x - z plane.	85
Fig.4.5.2 Modelling result of Far-field pattern of PCSEL	87
Fig.4.6.1 Model description with consideration of in-plane diffraction	88
Fig.4.6.2 Examples of Eigen-mode profile and in-plane diffraction spectrum of transverse wavevector dependency.	89
Fig.4.6.3 2-D resonance solutions solved using MIA a) without in-plane diffraction, and b) with in-plane diffraction	91
Fig. 4.6.4 Schematic of PC structure. With rectangular atoms and rectangular lattice	92
Fig.4.6.5 2-D resonance solution for photonic crystal with rectangular geometry solved by MIA from a) x to z direction, b) z to x direction	93
Fig. 5.1.1 Schematic of VPE process	99
Fig. 5.1.2 Schematic of MBE machine	100
Fig. 5.1.3 Photonic crystal pattern, lithography and regrowth	101

Fig. 5.1.4 a) and b) are SEM image of PC pattern. Nomarski microscope image of PC area before clean c) and after clean d)	101
Fig. 5.2.1 mesa etch (shallow) etch process	103
Fig. 5.2.2 n-contact metallization and dielectric deposition.	104
Fig. 5.2.3 dielectric etching to create p-contact window	105
Fig. 5.2.4 p-contact metallization and lift-off.	105
Fig. 5.2.5 Device schematics after fabrication	106
Fig. 5.2.6 SEM image of device	106
Fig. 5.3.1 LI characteristic of PCSEL at room temperature under CW condition.	107
Fig. 5.3.2 EL spectrum of PCSEL below threshold	107
Fig. 5.3.3 EL spectrum of PCSEL above threshold	108
Fig. 5.4.1 Schematic of PCSEL with a) no cleave, b) single cleave and c) double cleave	108
Fig. 5.4.2 LI characteristics of PCSEL with no cleave (black square), single cleave (red circle) and double cleave (blue triangle)	109
Fig. 5.4.3 MIA modelling result of threshold gain of PCSEL with and without single or double external reflection	110
Fig. 5.4.4 Experimental results of far-field pattern at $I=1.1I_{th}$ for a PCSEL with a) no cleave, b) one cleave, and c) two cleaves.	111
Fig. 5.4.5 Modelling results using MIA of far-field pattern for the lasing mode of PCSEL with a) no cleave, b) one cleave, and c) two cleaves.	112

Fig. 5.4.6 EL experimental results of PCSEL with varying CW injection current. **a)** no cleave, **b)** one cleave, and **c)** two cleaves.
113

Fig. 5.4.7 CW room temperature EL spectra at 150mA for PCSEL device with no cleave (black), 1 cleave (blue), and 2 cleaves (red).
114

Fig. 6.1 Lasing threshold for PCSEL with varying number of periodic and different termination (external feedback)
120

Fig. 6.2 Lasing threshold for PCSEL with varying phase of external reflection
121

Fig. 6.3 Lasing wavelength for PCSEL with varying phase of external reflection
121

Fig. 6.4 Threshold gain margin with different number of period
122

Fig. 6.5 Threshold gain of PCSEL with different number of period and different external in-plane phase reflectivity
122

Fig. 6.6 In-plane field distribution changes introduced by external reflection
123

List of Publications

Journal publications

1. **Li G**, Sarma J, Hogg R. *Evaluating resonances in PCSEL structures based on modal indices*[J]. IET Optoelectronics, Vol 13 (1), February 2019, p. 17 – 22
2. **Guangrui Li**, Jayanta Sarma, Richard Taylor, David T.D. Childs, Richard Hogg. “Modelling and Device Simulation of Photonic Crystal Surface Emitting Lasers Based on Modal Index Analysis.” IEEE Journal of Selected Topics in Quantum Electronics (**under review**)
3. Taylor R J E, **Li G**, Ivanov P, et al. *Mode Control in Photonic Crystal Surface Emitting Lasers Through External Reflection*[J]. IEEE Journal of Selected Topics in Quantum Electronics, 2017, 23(6): 1-8.
4. Taylor, R. J. E., Ivanov, P., **Li, G.**, Childs, D. T. D., & Hogg, R. A. (2017). *Optimisation of photonic crystal coupling through waveguide design*. Optical and Quantum Electronics, 49(2), 47.

Conference publications:

1. **Li G**, Sarma J, Butler I, et al. Modelling and Device Simulation of Photonic Crystal Surface Emitting Lasers Based on Modal Index Analysis[C]//2018 IEEE International Semiconductor Laser Conference (ISLC). IEEE, 2018: 1-2.
2. **Li G**, Sarma J, Hogg R A. Modal Index Analysis of Resonances of PCSEL[C]//2018 International Conference on Numerical Simulation of Optoelectronic Devices (NUSOD). IEEE, 2018: 131-132.
3. Taylor R J E, **Li G**, Ivanov P, et al. *Mode control in photonic crystal surface emitting lasers (PCSELS) through in-plane feedback (Conference Presentation)* [C]//Laser Resonators, Micro-resonators, and Beam Control XIX. International Society for Optics and Photonics, 2017, 10090: 100900L.
4. Taylor R J E, **Li G**, Ivanov P, et al. *Photonic crystal surface emitting lasers—Coherent arrays and external feedback*[C]//Laser Optics (LO), 2016 International Conference. IEEE, 2016: R3-23-R3-23.
5. Ivanov P, Taylor R J E, **Li G**, et al. *Three-dimensional finite-difference time-domain modelling of photonic crystal surface-emitting lasers*[C]//Novel In-Plane Semiconductor Lasers XV. International Society for Optics and Photonics, 2016, 9767: 976721.

Conference presentation:

1. **G. Li**, J. Sarma, P.S. Ivanov, R.J.E. Taylor, D.T.D. Childs, and R.A. Hogg. *Analysis of Photonic Crystal Surface Emitting Lasers with External In-Plane Feedback*. UK semiconductor 2017. **(Oral)**
2. **G. Li**, J. Sarma and R. A. Hogg. *Wave Impedance Analysis of Modes of Photonic Crystal Surface Emitting Lasers*. PIERS 2017. Singapore. **(Oral)**
3. **G. Li**, J. Sarma and R. A. Hogg. *Computing Resonant Modes of PCSELS using the Transfer Matrix Method*. SIOE 2017. Cardiff. **(Poster)**
4. **Li G**, Sarma J, Butler I, et al. *Modelling and Device Simulation of Photonic Crystal Surface Emitting Lasers Based on Modal Index Analysis*[C]//2018 IEEE International Semiconductor Laser Conference (ISLC). IEEE, 2018: 1-2. **(Poster)**
5. **Li G**, Sarma J, Hogg R A. *Modal Index Analysis of Resonances of PCSEL*[C]//2018 International Conference on Numerical Simulation of Optoelectronic Devices (NUSOD). IEEE, 2018: 131-132. **(Oral)**
6. **Li G**, Sarma J, Hogg R A. *Discontinuities in Multilayer Waveguides to Model 2-D Photonic Crystal Structures* [C]//2019 URSI Asia-Pacific Radio Science Conference (AP-RASC). IEEE, 2019 **(invited)**

Preface

Acknowledgement

This thesis is a documentation of my four years' journey into the fascinating area of wave propagation in periodic structure. First of all, I would like to thank to my parents for their unconditional support on my pursuit of the scientific research. I cannot express how lucky I am to have them by my side during the ups and downs of this PhD work.

I began this PhD study at University of Sheffield following my MSc studies at the same university. I then moved, with my research supervisor, Professor Richard Hogg to continue my PhD research at the University of Glasgow. I am most indebted to my research supervisor, for not only enabling me to work on this research topic of Photonic Crystal Surface Emitting Lasers (PCSELs) but also for his encouragement and instructive supportive and help in all aspects of the research throughout.

I cannot express how grateful I am to our research visitor Dr. Jayanta Sarma for his continuous, dedicated scientific support and discussions on almost all aspect of my PhD work, from theory to practice. Prof. Hogg introduced Dr. Sarma to me in 2015 and since then we began on the developing of the new model presented in this thesis. His cyclopaedic knowledge, attitude towards science, patience and importantly, wines, Bacardi, whisky encourages me throughout this PhD work.

I thank Dr. David Childs for taking the time to often help with ideas and suggestions particularly on experimental matters. I express my appreciation to Ken, Pavlo and Nasser for their help on the fabrication and experimental setup.

I have to thank to my colleagues, Danqi, Razvan, Graham, Soroush, etc. for the smiles and cheerful time they offered to me.

I acknowledge University of Sheffield for semiconductor regrowth and James Watt nano-fabrication centre of University of Glasgow for the electron beam lithography.

There are many people I would like to acknowledge for helping me in various ways in this work, but just as *Bilbo Baggins* said in the book *Lord of Rings: I don't know half of you half as well as I should like; and I like less than half of you half as well as you deserve.*

Author's Declaration

I declare that, except where explicit reference is made to the contribution of others, that this dissertation is the result of my own work and has not been submitted for any other degree at the University of Glasgow or any other institution

Printed Name: GUANGRUI LI

Signature: _____

Definitions and Abbreviations

$c = 299792458 \text{ m/s}$	Speed of light in free space
$e = 1.6022 \times 10^{-19} \text{ C}$	Electronic charge
$h = 6.626 \times 10^{-34} \text{ J} \cdot \text{s}$	Planck's constant
$\epsilon_0 = 8.854 \times 10^{-12} \text{ F/m}$	Electric permittivity of free space
$\mu_0 = 4\pi \times 10^{-7} \text{ H/m}$	Magnetic permeability of free space
Al	Aluminium
AlGaAs	Aluminium Gallium Arsenide
As	Arsenic
Au	Gold
CMT	Coupled mode theory
DBR	Distributed Bragg reflector
DFB	Distributed feedback
EM	Electromagnetic
FDTD	Finite Difference Time Domain
FP	Fabry Perot
FWHM	Full width half maximum
GaAs	Gallium Arsenide
Ge	Germanium
He	Helium
IPA	Isopropyl alcohol
IR	Infrared
LED	Light emitting diode
MBE	Molecular beam epitaxy
MIA	Mode index analysis
MOVPE	Metal-organic vapour phase epitaxy

Ni	Nickle
PC	Photonic crystal
PCSEL	Photonic crystal surface emitting laser
Pt	Platinum
PW	Plane wave
PWE	Plane wave expansion
QD	Quantum dot
QW	Quantum well
RTA	Rapid thermal annealing
SiO ₂	Silicon dioxide
SiN	Silicon nitride
TE	Transverse electric
TEC	Thermoelectric cooler
Ti	Titanium
TIR	Total internal reflection
TM	Transverse Magnetic
UHV	Ultrahigh vacuum
UV	Ultraviolet
VCSEL	Vertical cavity surface emitting laser
VPE	Vapour phase epitaxy
Zn	Zinc

Chapter 1

Introduction

With their robust, compact, light-weight and high efficiency advantages, semiconductor lasers have been extensively applied in nearly all aspects of modern society and their potential for application can hardly be overestimated [1]. Lasers are devices that amplify or generate coherent radiations. The name laser came from the action of light amplification by stimulated emission of radiation, or laser action. Here, ‘light’ is a rather broad concept. Actually, laser action can happen in a great range: from the very long infrared region [2], millimetre [3] or microwave [4], to visible light [5], ultraviolet [6] and even X-ray [7]. Although a variety of lasers are well studied and many of those sophisticated devices were developed as the mature of technology, ‘laser’ is still the subject of intensive research efforts.

Such efforts are driven by the desire for improving almost all aspects of the characteristics of lasers including high power combined with narrow beam divergence and monochromatic (narrow linewidth) output. Various device geometries and structures have been designed and developed over the years to achieve as many of these desired characteristics. Some very fundamental theoretical research is also driven by the desire of understanding the mechanisms to seek its ultimate limit of operation. Currently, one of very advanced topics is in the control of photon and electron states and their interactions using structures such as micro- or nano cavities, photonic crystal, or quantum wires and quantum dots.

The photonic crystal surface emitting laser (PCSELs) is one such device that has been investigated over the years with the purpose of using two-dimensional periodic structure to achieve single transverse mode operation over a large area while ensuring high power output in a narrow far-field beam[8]. Apart from the flourishing of the experimental works about PCSEL, the theoretical development has always been a daunting task since the existing modelling techniques, although producing very satisfactory results, have entailed very intensive and complicated theory and/or time-consuming computation. Hence, the motivation for the present effort has been to judiciously combine the physical features and concepts essential to the device with pertinent wave propagation properties

to develop a quasi-analytic model that yields acceptably satisfactory results with modest computational effort.

1.1 What is Laser?

So, what is a laser? As it is known that physical phenomenon at the quantum level are governed by the quantum laws which are described by Schrödinger and Hamiltonian formulations. It was Max Planck who first showed formally that a quantum description is the correct way to explain the anomalies arising in the classical description of heat radiation from ‘black-body’. A very direct and explicit application of the quantum phenomenon is the explanation by Einstein of the ‘photoelectric effect’.

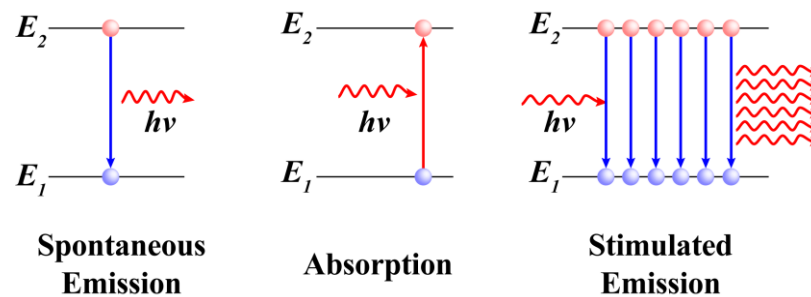


Fig.1.1 Schematics of spontaneous emission, absorption and stimulated emission

At quantum level, particles increase or decrease in energy by discrete amounts, with refer to Fig. 1.1. The electron can move from energy E_1 to E_2 if it receives energy $\Delta E = E_2 - E_1$ from some external source (e.g. a photon of energy $h\nu = E_2 - E_1$). Such effect is known as photon absorption. The opposite phenomenon can also occur such that an electron sitting at higher energy level E_2 can by itself fall down to lower energy level E_1 and emit a photon with energy $h\nu = E_2 - E_1$. Such effect is known as spontaneous emission.

However, most interestingly, Einstein showed that there is another kind of emission: stimulated emission. In this scenario, electrons from higher energy level E_2 fall down to lower energy level E_1 and emit a photon at frequency $\nu = (E_2 - E_1)/h$, but very importantly, the difference between stimulated emission and spontaneous emission is that stimulated emission is triggered (initiated) by an input photon. With spontaneous emission, all the transitions emit at same frequency $\nu = (E_2 - E_1)/h$, but, in general, all other features such as phase, polarizations, direction of emissions are not the same. With

stimulated emission, however, all the emitted photons have the same characteristics as the input photon.

As mentioned, lasers are devices that amplify or generate coherent radiation and the coherent radiation requires stimulated emission. However, note that all three processes: absorption, spontaneous emission and stimulated emission happen at the same time, and, absorption and spontaneous emission are by far the dominant effect under normal circumstance. The stimulated emission is only larger when electron population in the ‘upper’ energy level is larger, this is referred to as ‘inversion population’. The larger the inversion population, the stronger the stimulated emission. When net stimulated emission is larger than zero, the material will have positive (optical) gain $g > 0$. Thus, optical gain is essentially a macroscopic representation of stimulated emission.

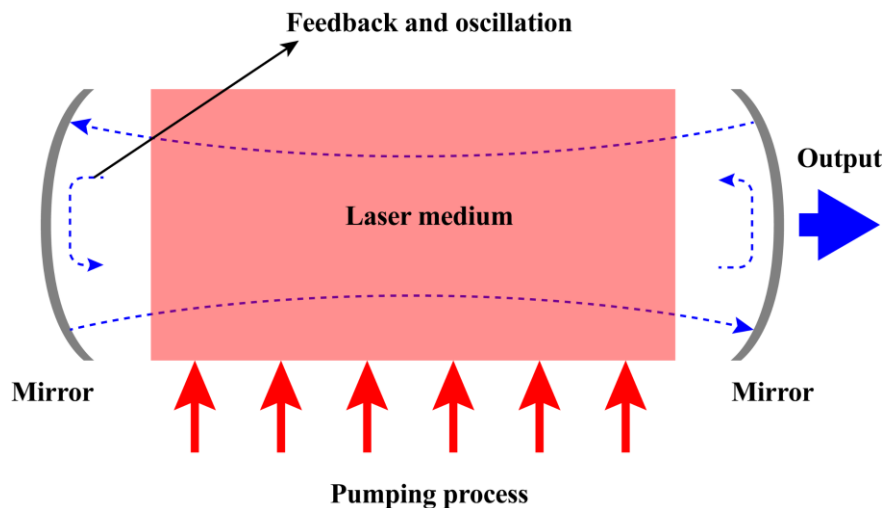


Fig.1.2 Schematic of typical laser structure

Thus, as illustrated in Fig.1.2 the three essential elements of laser device are: (i) a gain medium which can be gas (He, Ne, etc.) [9], solid state [10], or semiconductor [11]; (ii) a ‘pumping’ process to achieve inversion population (this can be done optically or electrically); (iii) importantly, to obtain sufficient amount of stimulated emission, the feedback element is required to allow radiation pass through gain medium more than once.

1.2 Why Electromagnetic (EM) Theory Matters?

Quite often, laser actions are described as Fig.1.1 in which billiard-ball-like photons travel through gain media. However, certain questions arise such as “where is the wave nature of light fit-in to the picture” and “where the coherency comes from”. The answer to the question requires an alternative representation of laser action. Actually, when light

(electromagnetic wave) travel through such media, the group of atoms interact with the light in a way that the electric charges begin to oscillate in a coherent relationship as the driving electromagnetic field. Then each atom starts to re-radiate like an elemental dipole antenna. In stimulated emission, field emitted by such ‘antenna’ combines coherently and provide amplification[12].

Einstein points out that stimulated emission rate is proportional to the photon density and also the number of atoms in the ‘excited’ state. The later requirement is met via inversion population. However, to achieve higher photon density, the light is ideally to be ‘confined’ in a small volume. Although by the good fortune of nature that typical optical gain materials of semiconductor have higher refractive indices in which the electromagnetic field tends to be localized (i.e. lateral confinement), simple layered planar structure is not a desirable design. Since not only the driving current tends to be large and results in an impractically high temperature generated by non-radiative transitions and free carrier (Ohmic) losses, large lateral dimension also leads to multi-mode operation characteristics of laser which results in a highly non-uniform intensity distribution across the output beam and a very low coupling efficiency into fibre [13].

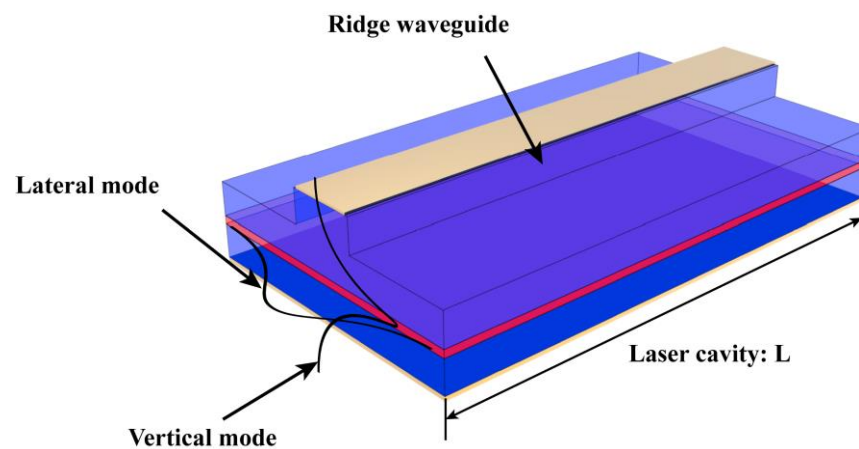


Fig.1.3 Schematic of ridge waveguide FP laser.

Such problem is solved by introducing lateral confinement (ridge waveguide laser, buried heterostructure laser, etc; a schematic of ridge waveguide Fabry-Perot (FP) laser is shown in Fig.1.3) In this configuration, the waveguide optics in EM theory which is governed by the Maxwell’s equations and the laser theory start to merge and for typical device characteristics, quasi-classical EM wave analysis is valid with the quantum mechanics features of the optically active medium represented as macroscopic material parameters.

Perhaps, the simplest type of laser is a gain media located between two parallel mirror facets. Such a laser is known as Fabry-Perot (FP) laser and in semiconductors the mirror facets are introduced by cleaving along the semiconductor crystalline structure. However, since the length of a typical FP laser device is large (usually hundreds of microns), the separation between FP resonance frequencies between two adjacent mode can be very small which leads to a narrow mode spacing and eventually undesirable multi-mode (multi-wavelength) operation. However, as is known in waveguide theory that mode with different frequency propagates at different phase velocity. Such effect is known as dispersion and will severely affects the optical signal in communication. Hence, considering about monochromacy requirement, the basic FP laser is not ideal for optical fibre communication. Moreover, the weaker transverse optical confinement than lateral dimension generates widely asymmetric diverging beams which requires complicated external optics for fibre coupling.

One possible solution to overcome the multi-moding issue is to replace two mirror facets by two Bragg mirrors. A Bragg mirror is a periodic multilayer structure which is highly frequency (wavelength) selective. Such laser structure is call distributed Bragg reflector (DBR) laser, referring to Fig1.4a. The periodic corrugation can be also included in the gain region which is known as distributed feedback (DFB) laser, referring to Fig.1.4b. DFB laser gives even better single mode (wavelength) output property[14].

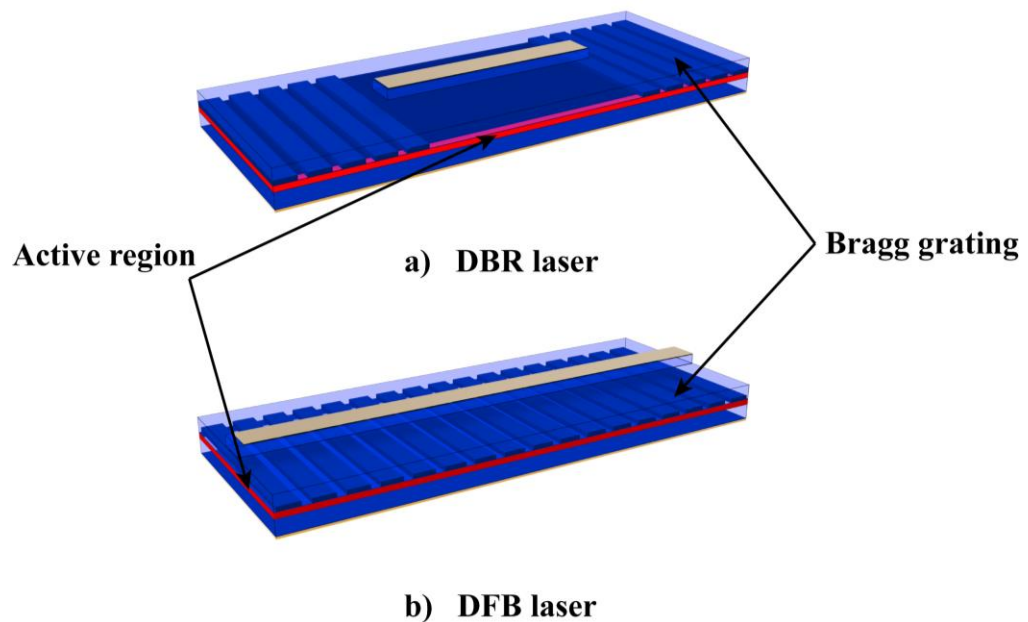


Fig.1.4 Schematics of **a)** DBR laser and **b)** DFB laser

Another approach for single mode emission is known as vertical cavity surface emitting laser (VCSEL) [15]. As illustrated in Fig.1.5, a typical VCSEL structure is a gain region sandwiched by two DBR mirror. Since the longitudinal dimension (vertical direction) of gain region is usually very small (in the range of nanometre), large mode spacing can be achieved, hence single longitudinal mode emission. The top and bottom DBR structure in VCSEL is not for mode selection, it is to provide high reflectivity for lasing condition. The transverse mode is controlled by the small lateral dimension. To maintain single transverse mode property, the transverse dimension of VCSEL is limited around $5\mu\text{m}$ diameter. Although VCSEL have advantages such as better beam shape, 2-D integration, the output power of VCSELs is limited to several milli-Watt due to small transverse dimension.

Apart from above-mentioned laser structures, various other device geometries and structures have also been designed and developed over the years such as coupled parallel stripe contact, adiabatically tapered stripe contact, etc. to achieve as many of the desired laser characteristics. One promising solution is to use 2-D periodic structures.

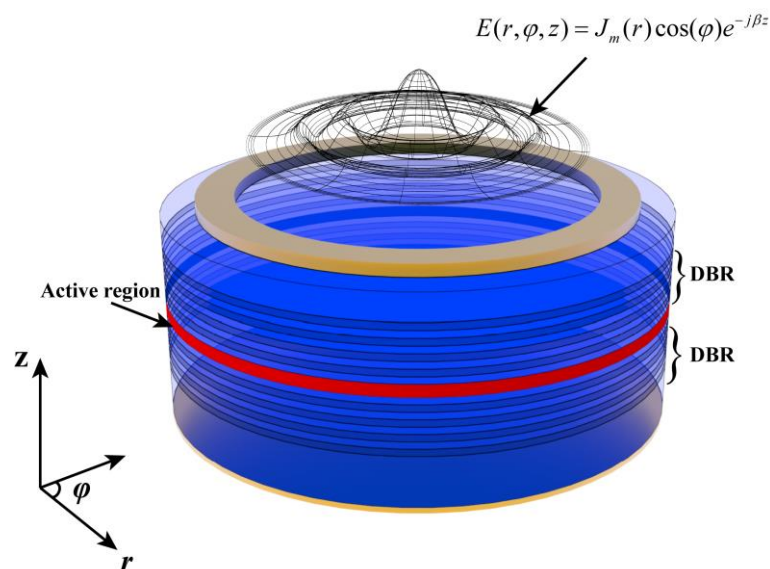


Fig.1.5 Schematic of VCSEL

1.3 Photonic crystal surface emitting laser

The fascinating features of wave propagation in periodic structures (media) have been investigated by Léon Brillouin, Felix Bloch, William Bragg, etc.; the theories have been applied to study sound, water, electromagnetic waves and, most famously, used to

develop and describe the properties of crystalline solids. In optics, the use of Bragg-gratings in passive devices have been prevalent for nearly a century and in active devices, such as edge-emitting distributed Bragg mirror (DBR) and distributed feedback (DFB) lasers which have become ubiquitous since the 1980s. DBR and DFB lasers use the properties of periodic structures to realise, essentially, single wavelength operation. However, the edge-emitting output beams tend to be divergent.

Meanwhile, one of the devices using periodic structure that has gained particular prominence in realizing desirable lasing characteristic is the photonic crystal surface emitting lasers (PCSELS). The original idea of PCSEL is rather intuitive. The output power of conventional DFB laser can be improved by increasing transverse dimension of DFB which will, however, lead to lateral multi-moding. Thus, a periodicity is then introduced in transverse dimension as further mode selection and the result is effectively cross grating DFB [16] [17]. The vertical emitting nature is merely a result of the second order grating (referring to Fig.1.6).

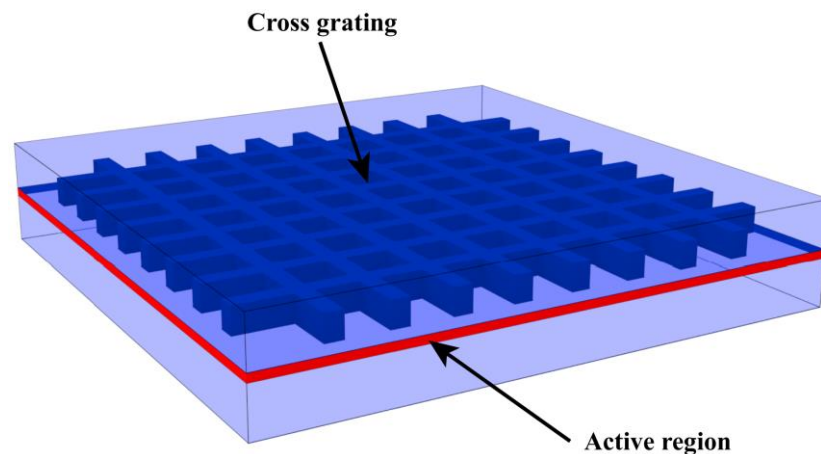


Fig.1.6 Schematic of cross-grating DFB

The name PCSEL does not come into picture until early 1990s when the concept of photonic crystal (which is actually brought up a long time ago) is utilized and opened up a completely new territory in semiconductor laser. Photonic crystal is essentially a media with periodic material distribution in one, two or even three dimensions. It is known that a crystal (e.g. semiconductor) is a periodic arrangement of atoms which presents a periodic potential for the electron waves. Such periodic potentials introduce certain energy regions within which the electron wave can/cannot propagate (i.e. passband and stopband). Similarly, in (dielectric) photonic crystal, the periodic ‘potentials’ due to the

periodic arrangement of material introduce certain wavelength region within which the light can/cannot propagate.

Although one dimensional periodic structures (or 1-D photonic crystal) have been studied as early as 1887 by Lord Rayleigh, serious consideration of 2-D or even 3-D photonic crystals did not appear until 1987 when such concept was brought up for studying inhibition of spontaneous emission [18] and photon localization [19]. Furthermore, with the introduction of the concept of photonic crystals, the theory of periodic structure has received very significant resurgence afterward and massive volumes of research have subsequently emerged in the study and application of photonic crystals in such diverse areas as photonic crystal fibres [20], photonic crystal waveguides and resonators [21] [22] and most relevant to this project: optical sources such as PCSELs.

In order to understand the optical properties of photonic crystals and design the device based on the properties of photonic crystal, many modelling techniques have been developed and play an essential role in the study of this subject. Broadly speaking, the modelling of photonic crystal involves two categories. One emphasis is to obtain the eigenmodes of photonic crystal, including the dispersion relation of the Bloch modes (photonic band structure) and the defect state of the photonic crystal cavity, surface states, etc. The other emphasis is on the reflection or transmission properties of photonic crystal, e.g. how the light behaves when travelling through a photonic crystal.

Thus, several techniques have been developed and used for analysing (especially optical) waves in periodic structure exist in the published literature, but the three, plane wave expansion (PWE), coupled mode theory (CMT), and the purely numerical finite difference time domain (FDTD), are by far the most extensively used.

Probably, FDTD is the most popular method among those techniques and widely used for studying EM wave propagating in photonic crystal since it can be applied to very complicated geometries while yielding accurate results. However, as a pure numerical method, FDTD requires considerable amount of computing time and resources which perhaps reduces its attraction. Moreover, the pure numerical process provides less physical insight which make FDTD a powerful tool for designing rather than understanding and analysing photonic crystal.

PWE, however, is based on expanding eigenmodes in photonic crystal as an orthogonal and complete set (plane waves), but the results (eigenmodes) are obtained effectively through the numerical process (solving the determinant of infinite matrix) hence also provides less physical feeling. Moreover, fundamental concept of PWE is based on Floquet theorem which can not apply to the photonic crystal with finite extent. Hence, PWE is a powerful tool in obtaining dispersion relation of eigenmodes and its frequency rather than designing particular photonic crystal related devices (especially with defect states).

There are many analytical methods and CMT is the most popular one among those techniques. Undoubtedly, CMT provides certain physical understanding of photonic crystal, however, the nature of CMT is built on expanding the fields and dielectric tensors as Fourier components and the actual boundary of photonic crystal is introduced via mode matching. The mathematics involved is very complicated and daunting for average user to approach. Moreover, such technique cannot really explain what is the eigenfunction and eigenmode of the photonic crystal with finite extent.

As one of the applications using 2-D photonic crystal, PCSEL requires the above-mentioned conventional modelling techniques which in turn limit the design and analysing process. In view of the above, it is felt that an alternative modelling approach is required for (2-D) photonic crystal especially with finite extent which can be applied to the relevant devices such as PCSELS. It is shown that such model is modest and fast while yields satisfactory results especially for analysing the 2-D resonance of PCSEL which corresponds to the laser mode.

1.4 Thesis Outline

The main emphasis and essential work of this PhD study is to build up a new model to elegantly and conveniently analyse the resonance in photonic crystals, especially in PCSEL. The study of wave propagation in periodic media is large undertaking subject. In this thesis, it is envisaged to cover as much as the aspect of this subject in a systematic way that enables a coherent understanding of the aspects pertinent and most relevant to the design of PCSEL devices.

The layout of the thesis is as follow:

- Chapter 2 reviews some basic concepts of EM theory including Maxwell's equations, plane wave propagation and reflection, Poynting vector, etc. Moreover, a transfer matrix technique is introduced as a powerful tool for modelling waves in multilayer media. Then an impedance representation of plane wave characteristics is developed based on matrix elements. Such representation provides more physical insight about the wave behaviour especially in multilayered media and will be used in the subsequent discussions.
- To develop an alternative model requires comprehensive study of certain subjects in a wide range. Such a study has been one of the major tasks of this PhD project and is presented in Chapter 3. It will be shown that the modelling of waves in periodic structure is about finding the eigenmode. As for photonic crystal with infinite extent, such eigenmode (Bloch mode) is merely a solution of Hill's equation which is effectively have been done in PWE and CMT. As for photonic crystal with finite extent, the sought about eigenmode is effectively matching the 'characteristics impedance' of such structure by using excitation techniques and thus the linkage between the excitation problem and eigenvalue problem appears. Several numerical examples are given to support such concept.
- The actual model for PCSEL is introduced in Chapter 4 with all 'building blocks' developed in chapter 2 and chapter 3. Such model is known as Modal Index Analysis (MIA) and can be applied to evaluate 2-D resonance of PCSEL in a rectangular geometry corresponding to the lasing mode. MIA method is then used to compared with other well-established modelling techniques by evaluating the resonances of PCSEL structures. It is shown that such new model is versatile, efficient and fast. Hence it is envisaged that the implementation of this method will enhance the potential to generate more comprehensive models of photonic crystal based devices, say, PCSELS, that include, for example, aspects of inversion population distribution and also time dependence while still retaining relatively modest demands on computational resources. The consistency and validity of MIA is also discussed in this chapter.
- The fabrication and experiment of PCSEL to further prove the validity of the model constructs another part of this PhD study which is then presented in Chapter 5. Basic experiments such as LIV characteristics of PCSEL and PCSEL with different termination boundary are also studied in this chapter. It is shown both experimentally and theoretically that the lasing characteristics can be modified through external reflection.

- Finally, the conclusion and future outlooks are presented in Chapter 6.

1.5 References

- [1] E. Kapon, *Semiconductor Lasers I: Fundamentals*. Elsevier Science, 1999.
- [2] A. Ashkin, J. M. Dziedzic, and T. Yamane, "Optical trapping and manipulation of single cells using infrared laser beams," *Nature*, vol. 330, no. 6150, p. 769, 1987.
- [3] D. Kim, M. Pelusi, Z. Ahmed, D. Novak, H.-F. Liu, and Y. Ogawa, "Ultrastable millimetre-wave signal generation using hybrid modelocking of a monolithic DBR laser," *Electronics Letters*, vol. 31, no. 9, pp. 733-734, 1995.
- [4] E. Widmann *et al.*, "Hyperfine structure of antiprotonic helium revealed by a laser-microwave-laser resonance method," *Physical review letters*, vol. 89, no. 24, p. 243402, 2002.
- [5] L. Johnson and H. Guggenheim, "Infrared-Pumped Visible Laser," *Applied Physics Letters*, vol. 19, no. 2, pp. 44-47, 1971.
- [6] Z. Tang *et al.*, "Room-temperature ultraviolet laser emission from self-assembled ZnO microcrystallite thin films," *Applied Physics Letters*, vol. 72, no. 25, pp. 3270-3272, 1998.
- [7] M. Rosen *et al.*, "Exploding-foil technique for achieving a soft x-ray laser," *Physical review letters*, vol. 54, no. 2, p. 106, 1985.
- [8] K. Hirose, Y. Liang, Y. Kurosaka, A. Watanabe, T. Sugiyama, and S. Noda, "Watt-class high-power, high-beam-quality photonic-crystal lasers," *Nature photonics*, vol. 8, no. 5, p. 406, 2014.
- [9] L. Hargrove, R. L. Fork, and M. Pollack, "Locking of He-Ne laser modes induced by synchronous intracavity modulation," *Applied Physics Letters*, vol. 5, no. 1, pp. 4-5, 1964.
- [10] D. Pohl, "Operation of a ruby laser in the purely transverse electric mode TE₀₁," *Applied Physics Letters*, vol. 20, no. 7, pp. 266-267, 1972.
- [11] G. H. B. Thompson, "Physics of semiconductor laser devices," *Chichester, Sussex, England and New York, Wiley-Interscience, 1980. 572 p.*, 1980.
- [12] A. E. Siegman, *Lasers*. University Science Books, 1986.

- [13] L. A. Coldren, S. W. Corzine, and M. L. Mashanovitch, *Diode Lasers and Photonic Integrated Circuits*. Wiley, 2012.
- [14] J. E. Carroll, J. Whiteaway, D. Plumb, R. G. S. Plumb, and I. o. E. Engineers, *Distributed Feedback Semiconductor Lasers*. Institution of Electrical Engineers, 1998.
- [15] K. Iga, "Surface-emitting laser-its birth and generation of new optoelectronics field," *IEEE Journal of Selected Topics in Quantum Electronics*, vol. 6, no. 6, pp. 1201-1215, 2000.
- [16] L. Luk'yanova, V. N. Luk'yanov, N. Shelkov, and S. D. Yakubovich, "Thin-film laser with a two-dimensional diffraction grating," *Soviet Journal of Quantum Electronics*, vol. 9, no. 4, p. 496, 1979.
- [17] M. Toda, "Proposed cross grating single-mode DFB laser," *IEEE journal of quantum electronics*, vol. 28, no. 7, pp. 1653-1662, 1992.
- [18] E. Yablonovitch, "Inhibited spontaneous emission in solid-state physics and electronics," *Physical review letters*, vol. 58, no. 20, p. 2059, 1987.
- [19] S. John, "Strong localization of photons in certain disordered dielectric superlattices," *Physical review letters*, vol. 58, no. 23, p. 2486, 1987.
- [20] J. C. Knight, "Photonic Band Gap Guidance in Optical Fibers," *Science*, vol. 282, no. 5393, pp. 1476-1478, 1998.
- [21] T. F. Krauss, "Slow light in photonic crystal waveguides," *Journal of Physics D: Applied Physics*, vol. 40, no. 9, p. 2666, 2007.
- [22] S. Noda, M. Fujita, and T. Asano, "Spontaneous-emission control by photonic crystals and nanocavities," (in English), *Nature Photonics*, vol. 1, no. 8, pp. 449-458, Aug 2007.

Chapter 2

Optics of Homogeneous Isotropic Media

Optics, is a well-established branch of physics and describes the phenomenon, properties and behaviours of light. Perhaps, the development of this subject runs through the history of mankind from 500 BC when ancient Greeks speculate the nature in a ‘philosophical’ way. It was not until 1864 when James Clerk Maxwell demonstrated brilliantly by his field equations that the wave nature of light is fully understood. It appears that light is the oscillation of electric and magnetic field. However, in parallel with such development, there were other worrying concerns about the wave theory of light. In 1900, Planck first treated light as discrete packets, or ‘quanta’ to describe the particle nature of light. Einstein then immediately grasped the discovery and beautifully explained the photoelectric effect. Now, the wave-particle dualities of light are recognized: it appears either as particles or as waves, its entire true nature is somewhat beyond our modes of thought.

Despite of the wave/particle duality of light, it is sufficient to consider light as an electromagnetic (EM) phenomenon from classic wave mechanics point of view throughout this thesis. Hence optics is simply a branch of electrodynamics. (For more detailed history of EM theory, refer to [1]) In fact, optics is treated as a separate subject simply because of its historical reason: optics is studied long before the establishment of EM theory which is robustly described by the most famous Maxwell’s equations.

In the present chapter, we first familiarise the reader about the basic concepts that will be used in the later chapters. Plane wave propagation in isotropic homogeneous media is introduced as a simplest case and then Fresnel equations are used as the basis of describing wave behaviour in layered structures. One of the most fundamental issues in optics is the wave reflection and transmission at the dielectric discontinuity. In this chapter, we consider plane electromagnetic waves at plane boundary between two homogeneous isotropic media. A matrix technique for analysing wave propagation in the isotropic layered structure will also be introduced and will be used in the later chapters. Wave impedance concept is also introduced in the later part of this chapter. It provides an alternative way to describe and formulate wave reflection and transmission in the

media. By evaluation of wave impedance across any section, one could design optical “source” and “load” specifically in various applications [2].

2.1 Maxwell’s Equations

As an electromagnetic phenomenon, optics can be completely described by the most fundamental equations in electrodynamics: Maxwell’s equations, which are given as follow in commonly used **MKS** units [1,2]. (A more detailed explanation of Maxwell’s equation and vector relations can be found in **Appendix A**):

$$\nabla \cdot \mathbf{D} = \rho \quad (2.1)$$

$$\nabla \cdot \mathbf{B} = 0 \quad (2.2)$$

$$\nabla \times \mathbf{E} = -\frac{\partial \mathbf{B}}{\partial t} \quad (2.3)$$

$$\nabla \times \mathbf{H} = \mathbf{J} + \frac{\partial \mathbf{D}}{\partial t} \quad (2.4)$$

In these equations, for any variable denoted by \mathbf{F} means a vector \mathbf{F} with implicit space \mathbf{r} and time t dependence “ \sim ”: $\mathbf{F} = \mathbf{F}(\mathbf{r}, t)$. Where \mathbf{E} and \mathbf{H} are electric and magnetic field, \mathbf{D} is the electric displacement field and \mathbf{B} is the magnetic flux density, \mathbf{J} is the conduction current density and ρ is the electric charge density. Equations (2.1) and (2.2) are result from electric and magnetic Gauss’s law (Gauss’s flux theorem); they give the relationship of the net flux through any hypothetically closed surface with the net charge within the surface. Equation (2.3) is the result from Faraday’s law of induction: a changing magnetic field gives rise to an electric field. Maxwell added a new idea, equation (2.4), that a changing electric field also gives rise to a magnetic field, even in vacuum, thus establishing the interdependence of the electric and magnetic field.

In addition to the Maxwell’s equation, there are certain parameters, permeability μ_c and permittivity ε_c , to describe material properties:

$$\mu_c = \mu\mu_0 \quad (2.5)$$

$$\varepsilon_c = \varepsilon\varepsilon_0 \quad (2.6)$$

Where μ is relative permeability and ε is relative permittivity; μ_0 and ε_0 are permeability and permittivity in vacuum respectively. For nonmagnetic material, $\mu = 1$ is

used throughout this thesis and the refractive index of the material is defined as

$$\eta_c = \sqrt{\mu_c \varepsilon_c} = \sqrt{\varepsilon_c} \cdot \mu_0. \text{ (refer to **Appendix A**)}$$

All electromagnetic problems require the solution of Maxwell's equation, the appropriate source functions and boundary conditions specified for the problem. In this thesis, it will be assumed that in the region of interest, charge density is identically zero $\rho \equiv 0$ (electrically neutral), and source current density is identically zero $\mathbf{J} \equiv 0$ (do not conduct any electric current).

In general, the behavior of electromagnetic wave can be expressed by the superposition of wave with different frequencies via Fourier transform. It is often sufficient to solve Maxwell's equation for harmonic time dependence. Wave with single frequency is called time-harmonic or monochromatic wave [3]. By assuming harmonic time dependence $\exp(j\omega t)$, the Maxwell's equations become:

$$\nabla \cdot \mathbf{E} = 0 \quad (2.7)$$

$$\nabla \cdot \mathbf{H} = 0 \quad (2.8)$$

$$\nabla \times \mathbf{E} = -j\omega\mu_0\mathbf{H} \quad (2.9)$$

$$\nabla \times \mathbf{H} = j\omega\varepsilon_0\varepsilon_c\mathbf{E} \quad (2.10)$$

2.2 Waves Equations in Homogeneous Media

All important features of the behaviour of light can be obtained by solving the Maxwell's equations with different boundary conditions. Maxwell's equations can be 'reduced' correspondingly to specific application. Here, we shall limit the discussion to few particular situations. For example, by rearranging equation (2.7) - (2.10), it is possible to get wave equations in Cartesian co-ordinates:

$$\nabla^2 \mathbf{E} + k_0^2 \varepsilon_c \mathbf{E} = 0 \quad (2.11)$$

$$\nabla^2 \mathbf{H} + k_0^2 \varepsilon_c \mathbf{H} = 0 \quad (2.12)$$

Where $k_0^2 = \omega^2 \varepsilon_0 \mu_0 = (2\pi/\lambda_0)^2$ and λ_0 is the wavelength in vacuum. Since for any vector in rectangular coordinate:

$$\mathbf{F} = \mathbf{u}_x F_x(x, y, z) + \mathbf{u}_y F_y(x, y, z) + \mathbf{u}_z F_z(x, y, z) \quad (2.13)$$

Where, the vector \mathbf{F} represents either \mathbf{E} or \mathbf{H} which has three components and each component can vary in three directions. Hence, vector equations (2.11) and (2.12) can

produce six scalar wave equations. Which components, if any, will be identically zero depend on the particular problem.

Another important quantity is the power flow density vector, also known as Poynting vector which is defined as $\mathbf{S} = \mathbf{E} \times \mathbf{H}$. It is interpreted as the power density (power flux per unit area) with the unit of watts/metre². In many situations, it is more convenient to use time averaged Poynting vector and its real part (denoted by $\text{Re}\{\}$) represents the physical power flow vector:

$$\mathbf{S} = \frac{1}{2} \text{Re}\{\mathbf{E} \times \mathbf{H}^*\} \quad (2.14)$$

The asterisk indicates the complex conjugation. The imaginary part of Poynting vector can be thought as reactive power. For detailed Poynting theorem and complex vector definition, refer to [4] and **Appendix A**.

2.3 Plane Wave (PW) Propagation

Due to the simplicity of plane wave solutions of Maxwell's equations, it is important to start with plane wave solution as the elementary part of the electromagnetic problem. Moreover, classical theories of radiation, propagation and diffraction of electromagnetic waves can be illustrated as the spectrum of the plane wave. Plane wave is defined such that no field variation except the direction of propagation. With reference to equations (2.11), (2.12) and (2.13), the wave equation for one of the non-zero component, e.g. F_y , is:

$$\left[\frac{\partial^2}{\partial x^2} + \frac{\partial^2}{\partial y^2} + \frac{\partial^2}{\partial z^2} + k_0^2 \varepsilon \right] F_y(x, y, z) = 0 \quad (2.15)$$

A separation of variable procedure yields a solution of the form:

$$F_y(x, y, z) = A e^{-j(\kappa x + \gamma y + \beta z)} + B e^{+j(\kappa x + \gamma y + \beta z)} \quad (2.16)$$

Such that $\kappa^2 + \gamma^2 + \beta^2 = k_0^2 \varepsilon$.

As will be evident later, for the purpose of the work presented in this thesis, it will be sufficient to consider field variation only along two axes, x and z , so that:

$$F_y(x, y, z) = F_y(x, z) = A e^{-j(\kappa x + \beta z)} + B e^{+j(\kappa x + \beta z)} \quad (2.17)$$

Considering special case that plane wave is propagating in a homogeneous media along x axis, as illustrated in Fig. 2.3.1, where $\partial^2/\partial y^2 = \partial^2/\partial z^2 = 0$ is satisfied. Thus,

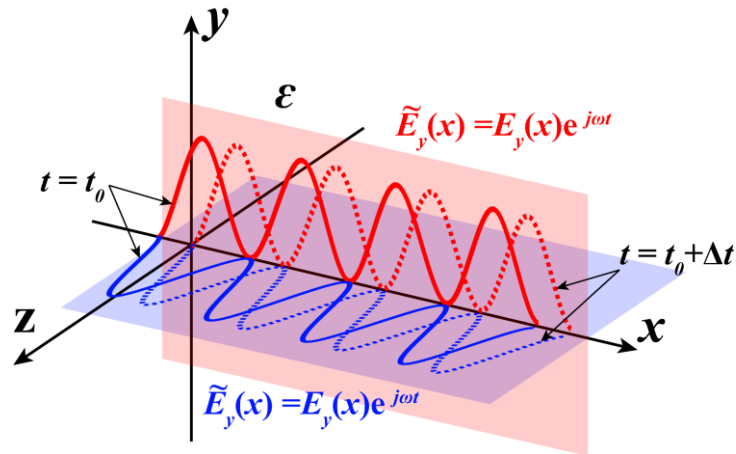


Fig. 2.3.1 Plan wave propagating in homogeneous media.

$$\frac{\partial^2}{\partial x^2} E_y(x) + \kappa^2 E_y(x) = 0 \quad (2.18)$$

$$\frac{\partial^2}{\partial x^2} H_z(x) + \kappa^2 H_z(x) = 0 \quad (2.19)$$

where $\kappa^2 = k_0^2 \epsilon$ is satisfied and ϵ is the permittivity of the media. Note that in general, ϵ could be complex. The plane wave solution of the wave equation of uniform media is the one dimensional plane wave, the following expression can be checked to satisfy the wave equations (2.18), (2.19):

$$E_y(x) = Ae^{-j\kappa x} + Be^{+j\kappa x} = E_{fy}(x) + E_{ry}(x) \quad (2.20)$$

$$H_z(x) = \sqrt{\frac{\epsilon}{\mu}} (Ae^{-j\kappa x} - Be^{+j\kappa x}) = H_{fz}(x) + H_{rz}(x) \quad (2.21)$$

In above two equations, terms with $F_f(x) = e^{-j\kappa x}$ referred as forward travelling waves and terms with $F_r(x) = e^{+j\kappa x}$ referred as reverse travelling waves. The ratio Z_0 is defined as $Z_{0x} = E_{fy}(x)/H_{fz}(x) = -E_{ry}(x)/H_{rz}(x) = \sqrt{\mu/\epsilon}$ and is known as characteristic impedance of the medium. Notice that the characteristic impedance of plane wave in vacuum (free space) is 377Ω . The reciprocal of Z_0 is often referred to as the characteristic admittance of the medium.

As stated above, in general, material permittivity ϵ and refractive index η are complex quantities. (Valid for sinusoidal time dependency). The complex representation takes account of loss or gain in the medium. In semiconductor, optical gain ‘g’, unit of m^{-1} , is a macroscopic representation of stimulated emission. The definition of ‘g’ and optical gain is given in **Appendix A**. There are three processes happen at the same time in

semiconductor as mentioned in the introduction chapter: optical absorption, spontaneous emission and stimulated emission and the amount of each of the three is in general linked to the other two. Absorption and spontaneous emission are the dominant process under normal circumstance. It is when nett stimulated emission (stimulated emission-absorption) is larger than zero, which requires the ‘inversion population’, the material will have positive gain, $g > 0$. In terms of optical power (Poynting vector), the optical gain can be understood schematically below:

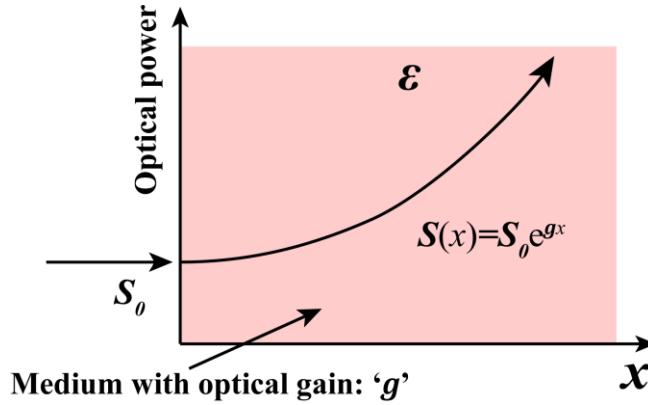


Fig. 2.3.2 Schematic representation of optical gain

As shown in Fig.2.3.2, to relate ‘ g ’ to classic EM theory, optical gain is measured as plane wave in homogeneous medium. Note that in general, dielectric permittivity ϵ_c is complex, i.e. $\epsilon_c = \epsilon_{re} - j\epsilon_{im}$ and similarly refractive index $\eta_c = \eta_{re} - j\eta_{im}$. Thus, the wave vector also become complex:

$$\kappa = \kappa_{re} - j\kappa_{im} \quad (2.22)$$

By rearranging equation (2.14), (2.20) and (2.21), the real part of Poynting vector which represent the actual energy flow is thus given by:

$$\text{Re}(S) = \frac{\kappa_{re}}{\omega\mu_0} A^2 e^{-2\kappa_{im}x} \quad (2.23)$$

which yields $g = -2\kappa_{im} = -2k_0\eta_{im}$. i.e. optical gain and loss can be represented by imaginary part of refractive index as defined above.

2.4 Matrix Formulation for PW propagation in Layered Media

Consider plane wave propagation in homogeneous isotropic media (with refractive index η_q) over a distance L from x_0 to $x_0 + L$ as shown in Fig. 2.4.1. From (2.20), it is

easily to write a field component $F(x)$ at $x = x_0$ into a matrix form. From equation (2.20) and (2.21), it follows that:

$$\begin{pmatrix} F_f(x_0) \\ F_r(x_0) \end{pmatrix} = \begin{pmatrix} Ae^{-j\kappa_q x_0} \\ Be^{j\kappa_q x_0} \end{pmatrix} \quad (2.24)$$

Similarly at $x = x_0 + L$:

$$\begin{pmatrix} F_f(x_0 + L) \\ F_r(x_0 + L) \end{pmatrix} = \begin{pmatrix} Ae^{-j\kappa_q(x_0+L)} \\ Be^{j\kappa_q(x_0+L)} \end{pmatrix} \quad (2.25)$$

From equation (2.20) it yields:

$$\begin{pmatrix} Ae^{-j\kappa_q x_0} \\ Be^{j\kappa_q x_0} \end{pmatrix} = \begin{pmatrix} e^{j\kappa_q L} & 0 \\ 0 & e^{-j\kappa_q L} \end{pmatrix} \begin{pmatrix} Ae^{-j\kappa_q(x_0+L)} \\ Be^{j\kappa_q(x_0+L)} \end{pmatrix} = \mathbf{P} \begin{pmatrix} Ae^{-j\kappa_q(x_0+L)} \\ Be^{j\kappa_q(x_0+L)} \end{pmatrix} \quad (2.26)$$

Matrix \mathbf{P} is known as propagation matrix which describes wave propagating in the homogeneous material.

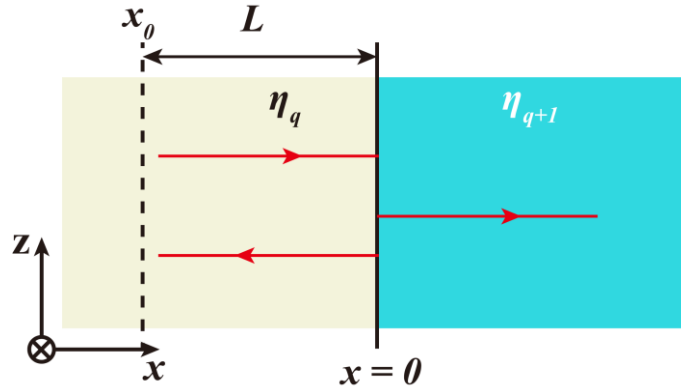


Fig. 2.4.1 Plane wave propagation and reflection

Next, we consider dielectric discontinuity at $x = x_0 + L$ from η_q to η_{q+1} (Referring to figure 2.4.1). Wavevector in two regions can be written as $\kappa_{q,q+1} = k_0 \eta_{q,q+1}$. Two independent categories of field solutions, one with polarisation, $(TM)_y \Rightarrow E_y = 0$ and the other $(TE)_y \Rightarrow H_y = 0$ can be sustained. Wave incident at discontinuity at an angle can also be written into the matrix form \mathbf{D} (see **Appendix B** for more on the derivation of transfer matrix):

$$\mathbf{D}_{(TM)_y} = \begin{pmatrix} \frac{\kappa_q + \kappa_{q+1}}{2\kappa_q} & \frac{\kappa_q - \kappa_{q+1}}{2\kappa_q} \\ \frac{\kappa_q - \kappa_{q+1}}{2\kappa_q} & \frac{\kappa_q + \kappa_{q+1}}{2\kappa_q} \end{pmatrix} \quad (2.27)$$

$$\mathbf{D}_{(TE)_y} = \begin{pmatrix} \frac{\varepsilon_{q+1}\kappa_q + \varepsilon_q\kappa_{q+1}}{2\varepsilon_{q+1}\kappa_q} & \frac{\varepsilon_{q+1}\kappa_q - \varepsilon_q\kappa_{q+1}}{2\varepsilon_{q+1}\kappa_q} \\ \frac{\varepsilon_{q+1}\kappa_q - \varepsilon_q\kappa_{q+1}}{2\varepsilon_{q+1}\kappa_q} & \frac{\varepsilon_{q+1}\kappa_q + \varepsilon_q\kappa_{q+1}}{2\varepsilon_{q+1}\kappa_q} \end{pmatrix} \quad (2.28)$$

Thus, the field reflection and transmission coefficient (Fresnel equations) can be written as:

$$t_{(TM)_y} = \frac{2\kappa_q}{\kappa_q + \kappa_{q+1}} \quad (2.29)$$

$$r_{(TM)_y} = \frac{\kappa_q - \kappa_{q+1}}{\kappa_q + \kappa_{q+1}} \quad (2.30)$$

$$t_{(TE)_y} = \frac{2\varepsilon_{q+1}\kappa_q}{\varepsilon_{q+1}\kappa_q + \varepsilon_q\kappa_{q+1}} \quad (2.31)$$

$$r_{(TE)_y} = \frac{\varepsilon_{q+1}\kappa_q - \varepsilon_q\kappa_{q+1}}{\varepsilon_{q+1}\kappa_q + \varepsilon_q\kappa_{q+1}} \quad (2.32)$$

2.5 Transfer Matrix Method for Laser Modelling

High speed optical communication requires laser with single mode operation (monochromatic), narrow linewidth and good output beam properties. Theoretical analysis of such single mode (i.e. longitudinal mode) behaviour is based on solving 1-D wave equations. In the case of Fabry-Perot (F-P) laser, the problem is straight forward. In DFB or DBR lasers, by assuming weak mode coupling (small perturbation), the problem leads to solving the coupled mode equations derived by Kogelnik and Shank in 1972 [5]. However, as the structure of laser become more complicated, especially due to the multiple reflection of the internal mirrors, analytical solutions for resonance frequency and threshold gain become almost impossible to find.

Meanwhile, it is well known that transfer matrix method has been used for network theory in microwave engineering (two-port problem). Researchers found that lasers can be described by “transfer matrix”: assuming laser has finite numbers of elementary part and each part could be described by a two by two matrix. Such elementary part is conveniently chosen as semiconductor facets.

Instead of solving the resonance frequency analytically, the matrices are evaluated numerically. The advantage of this matrix method is numerous since rather than solving the coupled mode equations which requires weakly coupling assumption, the transfer matrix method gives exact solution. Moreover, numerical procedure is dramatically reduced especially when the structures become periodic. The detailed properties of periodic structure will be given in next chapter, here, two types of widely used laser structure are analysed as an illustration of such method for laser modelling. It shall be noticed here that the analysis of laser below is restricted in ‘optics’ aspect, i.e. any ‘carrier’ effect such as diffusion, spacial/spectral hole burning are not included and the optical gain is treated as imaginary part of refractive index as discussed before.

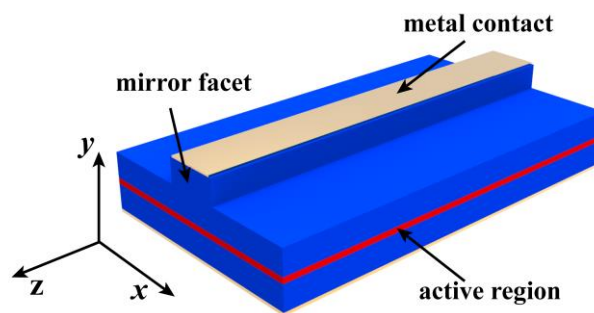


Fig. 2.5.1 Schematic of typical semiconductor F-P laser.

F-P laser is one of the simplest laser structures which consists of an optically active medium sandwiched by two reflection mirrors. Fig. 2.5.1 illustrate a schematic of typical semiconductor F-P laser structure. Optically active region with higher refractive index is sandwiched by lower index semiconductors which provides effectively optical guiding structure in ‘y’ direction. Electrical pumping is through top and bottom metal contacts. The ‘rib’ structure is etched during fabrication process for efficient current injection and transverse optical guiding. In semiconductor laser, mirror facet is produced by cleaving semiconductor and is automatically formed by its crystalline structure.

F-P laser structure can be simplified as a 3-layers media as shown in figure 2.5.2. For more realistic 3-D structure, effective index method [6] and Marcatili’s approximation [7] are usually used to convert material into effective indices and reduce the problem to 1-D case, e.g. η_a and η_b are the real part of the effective refractive index in each region. The length of laser cavity is $200 \mu m$. From the matrix elements (equation (2.26) and (2.27)) derived in section 2.4, we obtain the total transfer matrix \mathbf{M} from region I to III (Fig. 2.5.2):

$$\mathbf{M} = \mathbf{D}_{I \rightarrow II} \mathbf{P}_{II} \mathbf{D}_{II \rightarrow III} \quad (2.33)$$

The field reflectance of such structure can be written as $r = \mathbf{M}_{21}/\mathbf{M}_{11}$ where \mathbf{M}_{11} and \mathbf{M}_{21} are two matrix elements. At lasing condition, the field reflection or transmission tends to infinite (oscillation condition) which gives $\mathbf{M}_{11} = 0$. Generally speaking, \mathbf{M}_{11} is a complex number. It is very convenient to plot \mathbf{M}_{11} value in a complex plane. As shown in Fig. 2.5.2. the net gain in region II is included as imaginary part of refractive index varying from 0 cm^{-1} to 33 cm^{-1} .

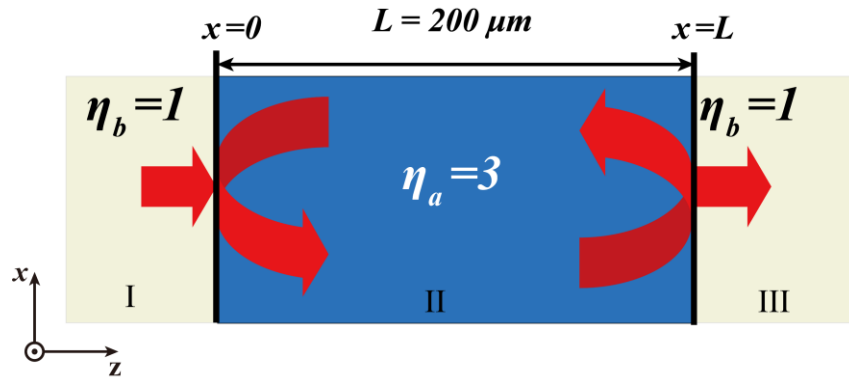


Figure 2.5.2 F-P laser cavity.

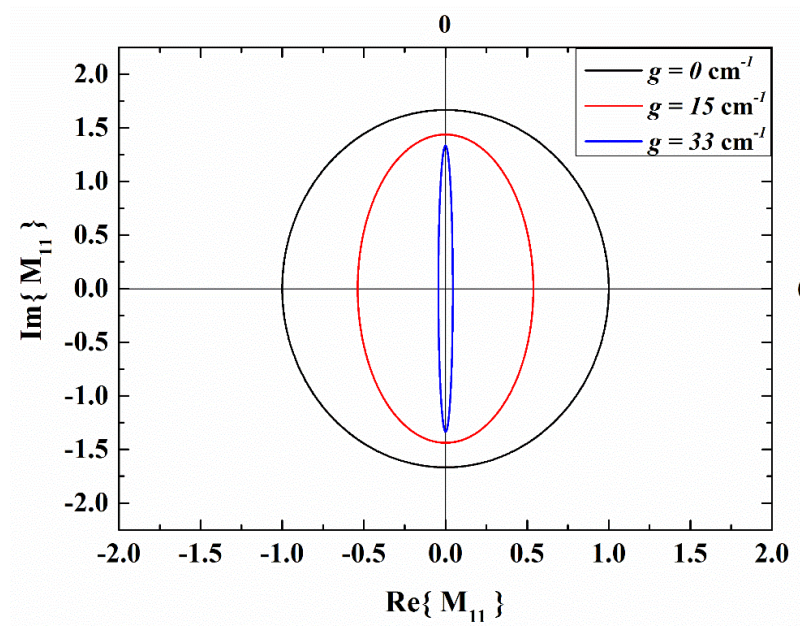


Figure 2.5.3 The relationship between real and imaginary part of matrix element at lasing threshold of F-P laser

When net gain value g is zero the locus of \mathbf{M}_{11} rotates counter-clockwise in the complex plane around coordinate origin. As we increase the net gain value, the locus become smaller. At threshold, it become a straight line lies on the imaginary axis. As illustrated

in the Fig.2.5.3, the threshold gain of such F-P laser device is about 33 cm^{-1} . Theoretically, the net threshold gain of F-P laser is

$$g_{th} = \frac{1}{2L} \ln \left(\frac{1}{r_1 r_2} \right) \quad (2.34)$$

Where r_1 and r_2 are field reflectance of cavity mirror. In this device ($200 \mu\text{m}$ and field reflectance $r_1 = r_2 = 0.55$), the net threshold gain is $g_{th} = 34.66 \text{ cm}^{-1}$. It fits the numerical result. After the threshold, the locus will orbit clockwise. It is not physical to have the gain value large than the threshold since in real device, the moment when laser reaches the threshold, lasing will clamp.

Although being one of the earliest lasers, Fabry-Perot (FP) edge-emitting laser still remains widely used in many general purposes. However, the long cavity of FP laser leads to multi-wavelength emission (multi-moding) and thus is not desirable in optical communication. It is shown in Fig.2.5.4 that the mode spacing is about 1nm for typical FP laser ($\Delta\omega \propto 1/L$, where $\Delta\omega$ is mode spacing and L is the cavity length).

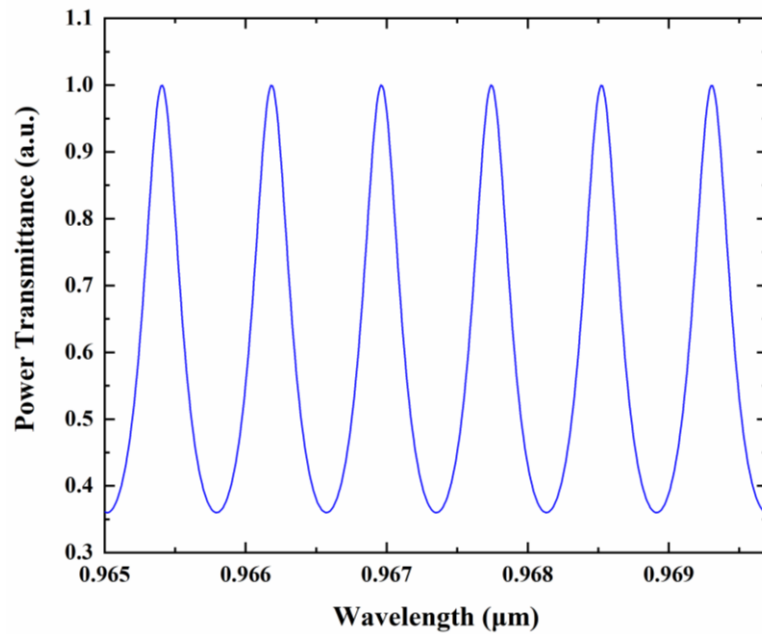


Fig. 2.5.4 resonance spectrum of F-P cavity

One possible solution to overcome this issue is to replace two mirror facets by two wavelength selection mirrors (Bragg gratings). A Bragg mirror is a periodic multilayer structure which is highly frequency (wavelength) selective. Such laser structure is known as distributed Bragg reflector (DBR) laser. The periodic corrugation can be also included

in the gain region which is known as distributed feedback (DFB) laser. DFB laser gives even better single mode output property.

Matrix method can be applied also in DFB laser modelling. Unlike F-P laser, DFB laser has active region with effectively periodic index distribution. Such structure is usually produced by semiconductor etching and regrowth. As shown in Fig. 2.5.5, Bragg grating designed above the active region leads to a periodically changing effective refractive index along z-axis.

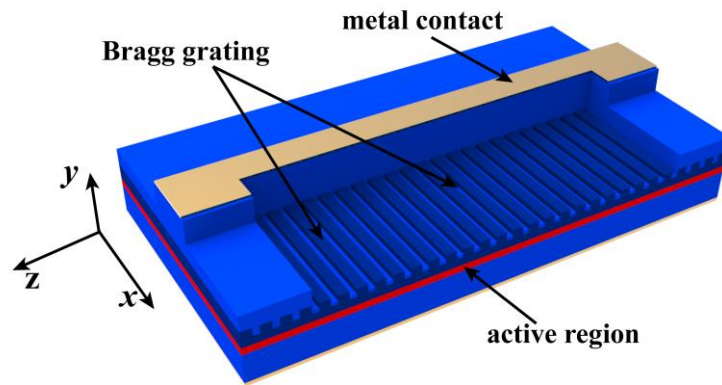


Figure 2.5.5 Schematic of typical semiconductor DFB laser.

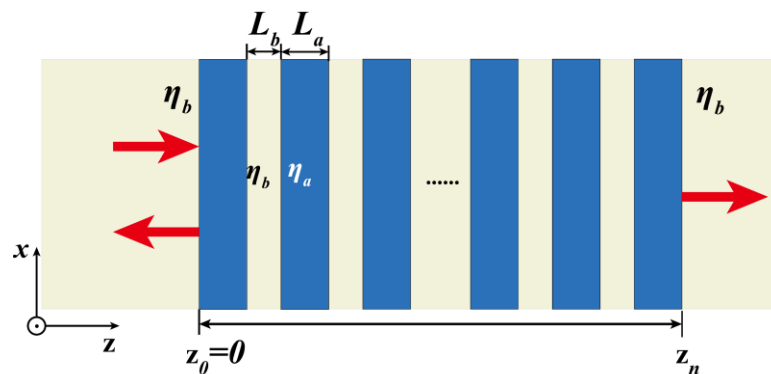


Fig. 2.5.6 Simplified DFB structure as 1-D grating with complex index profiles

Fig 2.5.6, shows a simplified DFB laser with 1-D periodic structure consists of complex index profile η_a and η_b and the dimension L_a and L_b along x direction. The periodicity is $\Lambda = L_a + L_b$. From the matrix formulation derived in section 2.4, the total transfer matrix \mathbf{m}_T for N period satisfy $\mathbf{m}_T = \mathbf{M}^N$, where \mathbf{M} is the transfer matrix for single period. Similarly, at lasing threshold, the reflection of entire periodic structure will become

infinite which means the matrix element \mathbf{M}_{11} become zero. Generally speaking, \mathbf{M}_{11} is a complex number. It is very convenient to plot \mathbf{M}_{11} value in a complex plane.

Figure 2.5.7 shows an example of the real and imaginary part of \mathbf{M}_{11} . The structure analyzed is DFB laser with symmetric terminating material/condition at lasing threshold. As it is shown, at threshold, the locus will pass through coordinate origin twice which indicating two lasing mode on each side of Bragg frequency. If we increase the gain further, we will find another root of g_{th} which satisfy $\mathbf{M}_{11} = 0$. This is unphysical since the laser medium will be clamped when achieving threshold pumping. The difference between the lowest g_{th} and next higher g_{th} indicated the gain margin, it represents how stable the laser will be under modulation.

Fig.2.5.8 shows a power transmission of such structure. As we can see, the Bragg wavelength is at $1.5 \mu\text{m}$. When increasing the gain value, the wavelength at the edge of the band gap shoot up, which also indicates the double mode behavior. Such behavior is not favorable in real application. In practice, one lasing mode is designed to be suppressed through artificially created defects in the periodic structure [8], first order radiation loss [9], or gain grating DFB laser structure [10]. A detailed study of periodic structure is shown in chapter 3.

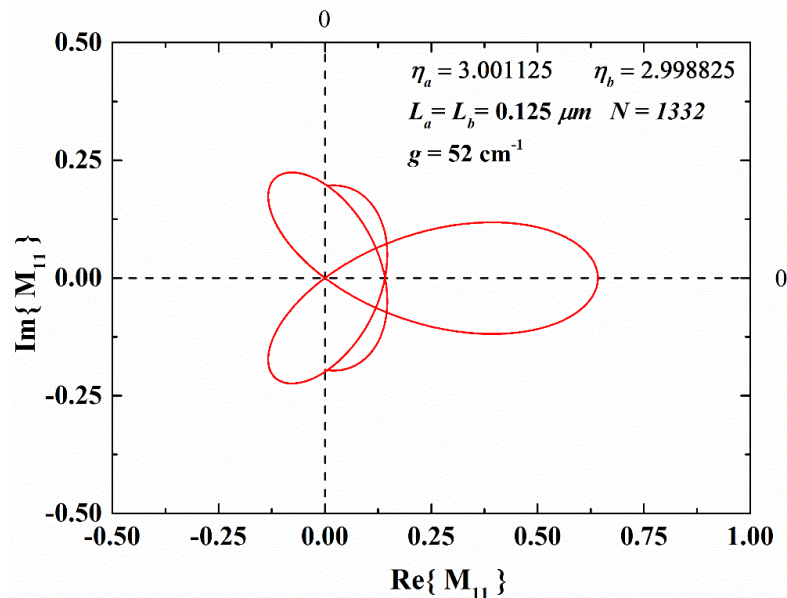


Fig. 2.5.7 The relationship between real and imaginary part of matrix element at lasing threshold of DFB laser

The limitation of transfer matrix method is obvious: the theory is linear; hence it cannot explain the saturation behavior in amplifiers or oscillators. However, numerous results can be obtained from such technique: the device with multiple reflection mirror (either periodic or non-periodic) and the structure of cleaved coupled cavities can be analyzed essentially the same method as shown above. The carrier effect can be included separately: the refractive index and the gain are depending on photon energy.

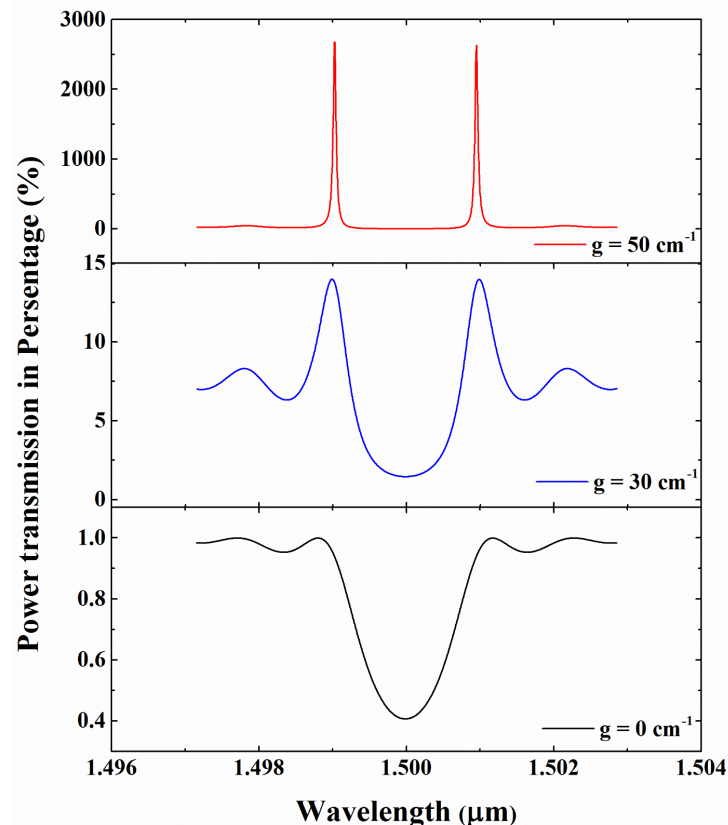


Fig. 2.5.8 Power transmission spectrum of structure shown in Fig. 2.5.6 with varying gain.

2.6 Concept of Wave Impedance

In optics, quite often, the numerical calculation is inevitable for obtaining exact solutions. However, deep physical insight into underlying process is also (if not more) important for simplified analytical treatment of different problems. Wave impedance is one of the concepts providing such physical insight. Impedance is an intrinsic property of the media and can be treated as one absolute quantity applicable to any structure or components [11]. It represents the transmission and reflection at the interface between two adjacent media.

Previously, a transfer matrix method is developed to explain and analyze electromagnetic wave properties in layered media. It is also known that the transmission line method has been used to analyze the EM wave propagating in space. The next task is to introduce the concept of wave impedance and implant the impedance concept into the matrix method. From section 2.3, for plane wave propagating in homogeneous media, the wave impedance is defined as the ratio of tangential field components, i.e. $Z_0 = E_T/H_T$ where E_T and H_T are the tangential field components of the electric and magnetic field referring to the interface.

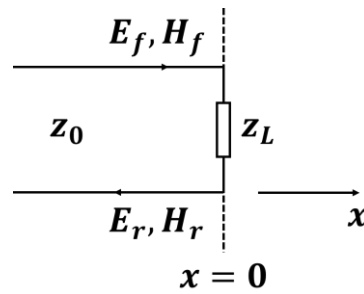


Fig. 2.6.1 Impedance concept of electromagnetic wave

Here, we extend the definition of the impedance. The characteristic impedance of $x < 0$ semi-infinite region (referring to figure 2.4.1) is defined as

$$Z_0 = \frac{E_f}{H_f} = -\frac{E_r}{H_r} \quad (2.35)$$

The load impedance at $x = 0$ is Z_L which is defined as

$$Z_L = \frac{E_f + E_r}{H_f + H_r} = \frac{E_f + E_r}{E_f - E_r} Z_0 \quad (2.36)$$

Note here, Z_L can represent not only a single interface, but also a complicated multilayer structure. Hence

$$\frac{Z_L}{Z_0} = \frac{E_f + E_r}{E_f - E_r} \quad (2.37)$$

For analyzing wave propagation in a layered media, the exact value of Z_0 and Z_L are not of particular interest. It is Z_L/Z_0 which gives us information of impedance matching and allows us to synthesize the phenomenon of EM wave in layered media.

We noticed that E_f and E_r are given from the matrix method. For wave propagating inside a multilayer structure, the input and output have a simple relationship:

$$\begin{pmatrix} E_{f,in} \\ E_{r,in} \end{pmatrix} = \begin{pmatrix} M_{11} & M_{12} \\ M_{21} & M_{21} \end{pmatrix} \begin{pmatrix} E_{f,out} \\ E_{r,out} \end{pmatrix} \quad (2.38)$$

Where $E_{r,out} = 0$ simply means there is no signal back from the far end. So

$$\frac{Z_L}{Z_0} = \frac{E_f + E_r}{E_f - E_r} = \frac{M_{11} + M_{21}}{M_{11} - M_{21}} \quad (2.39)$$

Where M_{11} and M_{21} are two matrix elements of the transfer matrix for the entire multilayer structure which can be calculated quasi-numerically. In general, Z_L/Z_0 is a complex number, we need to analyse both real and imaginary part separately. The advantage of this matrix method implantation is that it links the Fresnel equations with impedance representation through matrix elements with TE or TM polarization characteristics built in:

$$r = \frac{Z_L - Z_0}{Z_L + Z_0} \quad (2.40)$$

The advantage of applying impedance concept in optical wave characteristics of media is enormous. Since once the Fresnel reflection coefficient is obtained the effective impedance (characteristic impedance) can be determined from a simple relationship and *vice versa* if the effective impedance is known. Such technique has been adopted by many researchers in analysing metamaterial and is known as effective impedance method [12] [13].

2.7 Conclusions

This chapter has briefly reviewed the propagation and reflection of the plane wave in both passive and active homogeneous media. Some basic concept such as Poynting vector and optical gain are introduced and will be used in later part of the thesis. A transfer matrix method analysis of laser structure is also introduced. Such technique essentially treats the laser structure as different element part and can be represented as two by two matrix. Effective impedance concept is further introduced. Such concept provides a better physical insight of the wave behaviour in different media.

2.8 Reference

- [1] M. Born and E. Wolf, *Principles of optics: electromagnetic theory of propagation, interference and diffraction of light*. Elsevier, 2013.
- [2] H. A. Haus, "Waves and Fields in Optoelectronics, Prentice-Hall Series in Solid State Physical Electronics," 1984.
- [3] R. F. Harrington, *Time-Harmonic Electromagnetic Fields*. Wiley, 2001.
- [4] S. Ramo, J. R. Whinnery, and T. Van Duzer, *Fields and Waves in Communication Electronics*. Wiley, 1994.
- [5] H. Kogelnik and C. Shank, "Coupled-wave theory of distributed feedback lasers," *Journal of applied physics*, vol. 43, no. 5, pp. 2327-2335, 1972.
- [6] J. Buus, "The effective index method and its application to semiconductor lasers," *IEEE Journal of Quantum Electronics*, vol. 18, no. 7, pp. 1083-1089, 1982.
- [7] E. A. Marcatili, "Dielectric rectangular waveguide and directional coupler for integrated optics," *Bell System Technical Journal*, vol. 48, no. 7, pp. 2071-2102, 1969.
- [8] Y. Kotaki, S. Ogita, M. Matsude, Y. Kuwahara, and H. Ishikawa, "Tunable, narrow-linewidth and high-power lambda/4-shifted DFB laser," *Electronics Letters*, vol. 25, no. 15, pp. 990-992, 1989.
- [9] R. Kazarinov and C. Henry, "Second-order distributed feedback lasers with mode selection provided by first-order radiation losses," *IEEE Journal of Quantum Electronics*, vol. 21, no. 2, pp. 144-150, 1985.
- [10] K. David, G. Morthier, P. Vankwikelberge, R. G. Baets, T. Wolf, and B. Borchert, "Gain-coupled DFB lasers versus index-coupled and phase shifted DFB lasers: a comparison based on spatial hole burning corrected yield," *IEEE journal of quantum electronics*, vol. 27, no. 6, pp. 1714-1723, 1991.
- [11] R. E. Collin, *Foundations for Microwave Engineering*. McGraw-Hill, 1966.
- [12] F. J. Lawrence, L. C. Botten, K. B. Dossou, C. M. de Sterke, and R. McPhedran, "Impedance of square and triangular lattice photonic crystals," *Physical Review A*, vol. 80, no. 2, p. 023826, 2009.

- [13] K. B. Dossou, C. G. Poulton, and L. C. Botten, "Effective impedance modeling of metamaterial structures," *JOSA A*, vol. 33, no. 3, pp. 361-372, 2016.

Chapter 3

Optical Waves in Periodic Structure

The properties of wave behaviour in homogeneous medium have been generally discussed in the preceding chapter. However, the media exhibits more complicated characteristics in real-life situation such as inhomogeneity or anisotropy. Several topics based on the application of those media has been developed and hence stimulated a variety of studies along those lines. One of the subjects is about wave behaviour in periodic structures.

The propagation of wave in periodic structure has been studied intensively for more than a century since 1887, Lord Rayleigh brought up this problem for analysing waves in periodically stratified media. He recognized that the problem involves solving Mathieu and Hill's differential equations [1]. (Actually, Mathieu and Hill's equations have been studied long before Lord Rayleigh with other applications such as the vibration of string). Later in 1920s, Bloch generalized the result and obtained the solution, known as Bloch waves, formed the foundation theory of electron waves in crystalline solid [2]. For electron wave motion in periodic structure (potentials), the electron states fall into different 'bands' within which the wave can propagate 'freely' inside periodic structure. Such bands are separated by forbidden gaps which prohibits the free propagation of wave without attenuation.

At the same time, there was strong interest in wave propagation in multilayer structures. In 1950s, Abele first discovered that finite periodic structure could be solved analytically [3]. Some interesting and detailed reviews could also be found in Brillouin's book [4]. From 1950s to 1970s, the interest in periodic structure stimulated a range of detailed study, basically about slow-wave structure, especially in microwave engineering (helix [5], travelling wave antenna [6], etc.). The technology progress also flourished in active material, famously DBR and DFB laser, which laid a solid foundation for optical communications, and such structure have now been widely used in various applications.

The actual concept of photonic crystal (PC) was then introduced in late 1980s [7], ever since 2-D and even 3-D periodic structure of dielectric media has been seriously studied. Although it is plausible to superficially regard 2-D photonic crystal just as well-known

one-dimensional Bragg grating merely with extra dimension in periodic, there is still a whole range of new phenomena to be discovered. Periodic structure in optics has strong analogy to the electrons in crystal. Just like real crystal, PC exhibits ‘stop-band’ and ‘pass-band’ regions in frequency spectrum when light wave propagates in it. Such property is fascinating since by artificially arranging PC period and/or index profile, one could control the flow of light. Hence PC is also known as metamaterial. Such property also stimulated the birth of several novel concepts such as perfect lens [8], optical cloaking [9] [10], etc. As the developing of state-of-art technology, especially realizing 2-D photonic crystal nanofabrication on semiconductor, several devices such as photonic crystal waveguide [11], photonic crystal nano-cavity [12], photonic crystal laser [13], etc. has been studied enormously both experimentally and theoretically which made it one possibility of realizing photonic integrated circuits [14].

In this chapter, the objective is to provide a physical insight and a quantitative description of wave propagation in one dimensional (1-D) periodic media which will form a solid building block for 2-D PC modelling developed in next chapter. Although sufficient mathematics is essential in understanding different subjects from a fundamental basis, we focus ourselves on the physical concept appeared in the theory of periodic system.

Hence, the discussion is arranged as follow. The dispersion of this chapter can be separate into two parts: infinite periodic structure and finite periodic structure. The first half of this chapter mainly deal with eigenfunction (Bloch mode) of periodic structure with infinite extent and it begins with introducing Mathieu’s equation and its classic solving technique known as Floquet-Bloch method which is particular suitable for numerical simulation. Such method is therefore often used in obtaining specific results rather than understanding general properties of wave behaviour in periodic media. Floquet-Bloch method also give rise to the plane wave expansion method in periodic system since Bloch mode in periodic potential can be written as plane wave multiplies a periodic function. The discussion continues by considering approximate analytical theory of coupled wave developed by Kogelnik [15] [16]. Such approximate method is valid for small refractive indices modulation depths.

In the later part of this chapter, the eigenmode and eigenfunctions of the finite (locally) periodic structure is discussed. Mostly importantly, for piece-wise constant medium, the

transfer matrix method is used, which simply consists of the derivation of a characteristic matrix of one period (unit cell). Such method is astonishingly useful for solving periodic structure with finite extent since Bloch's theorem used in conventional techniques does not apply for finite periodic structure. Several applications using periodic structure are also reviewed in this chapter.

3.1 Hill's Equation and Floquet-Bloch Method

1-D periodic structure, such as the widely used Bragg gratings, has been very well studied and served for many applications in modern photonic devices, e.g. wavelength filter, laser and telecom systems. In general, 1-D periodic structure consists of medium with permittivity $\varepsilon(x) = \varepsilon(x + \Lambda)$ varies periodically (e.g. along x axis, referring to Fig. 3.1.1). The period Λ is of the order of the wavelength of light, so that when light (monochromatic) propagates in such structure, although each discontinuity in periodic structure may has negligible reflection, the forward and backward propagating wave can add up in phase to have a dramatic effect such that high reflection or transmission can be produced. If the medium has gain or loss properties, the permittivity become complex: $\varepsilon = \varepsilon_r + j\varepsilon_i$, $j = \sqrt{-1}$. As discussed in chapter 2, the imaginary part, ε_i , corresponds to the field intensity attenuation or amplification and usually, $\varepsilon_i \ll \varepsilon_r$. Hence the discussion begins by assuming $\varepsilon_i = 0$.

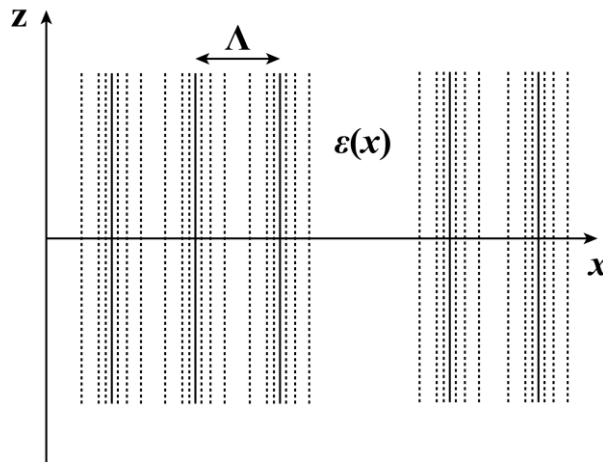


Fig. 3.1.1 Structure with one dimensional periodicity: Λ is the period of the function $\varepsilon(x)$

With mathematics laxity, considering wave propagation in such unbound (the number of period is infinite) periodic medium with the period Λ . For any arbitrary polarized field, the wave equation can be reduced form Maxwell's equation, and takes the form:

$$\frac{d^2}{dx^2} F(x) + k_0^2 \varepsilon(x) F(x) = 0 \quad (3.1)$$

Equation(3.1), which is homogeneous linear differential equation of second order with real periodic coefficient, is known as Hill's equation. Since Hill's equation is linear, the most general solution is a superposition of two linear independent special solutions.

$$F(x) = AF_1(x) + BF_2(x) \quad (3.2)$$

A and B are arbitrary constants. For a periodic medium, according to Floquet's theorem, it is possible to choose $F(x)$ in a convenient form.

In an infinite periodic structure, field at x and $x + \Lambda$ has no difference except a complex constant:

$$\frac{F(x + \Lambda)}{F(x)} = \frac{F(x + 2\Lambda)}{F(x + \Lambda)} = \frac{F(x + 3\Lambda)}{F(x + 2\Lambda)} = \dots = C \quad (3.3)$$

C is a complex number. Note here that the function $F(x)$ is not a periodic function.

From above relation we obtain:

$$F(x + m\Lambda) = C^m F(x) = e^{-jm\beta_B \Lambda} F(x) \quad (3.4)$$

β_B is a complex number. Considering a function:

$$G(x) = e^{j\beta_B x} F(x) \quad (3.5)$$

It can be proved that $G(x)$ is a periodic function with the period Λ , thus can be represented as a Fourier series:

$$G(x) = \sum_{m=-\infty}^{m=+\infty} f_m e^{-j\left(\frac{2m\pi}{\Lambda}\right)x} \quad (3.6)$$

Hence:

$$F(x) = G(x)e^{-j\beta_B x} = \sum_{m=-\infty}^{m=+\infty} f_m e^{-j\left(\beta_B + \frac{2m\pi}{\Lambda}\right)x} \quad (3.7)$$

Define $K_{B,m} = \beta_B + 2m\pi/\Lambda$ and $K = 2\pi/\Lambda$. β_B is known as Bloch wavevector, which is a function of wavelength. The different components of $F_m(x)$ is known as m th space harmonic of Bloch wave or Bloch mode. The value $K_{B,m}$ represent the propagation properties of these space harmonic. Noting that single space harmonic cannot exist independently in general, these space harmonics are portions of total solutions. Generally speaking, all space harmonics are coupled together through periodic boundary condition, and together they make up the periodic wave. Unlike conventional wave phenomenon exists in elementary physics such as traveling wave and standing wave, periodic wave

shows a different wave motion for which the wavelength fall into different allowed ‘bands’ (continuous since the number of period is infinite) and separate by forbidden ‘gaps’ [17].

Equation (3.7) indicates that the Bloch wave is the product of the plane wave $f_m \exp(-j\beta_B x)$ and a periodic function $\exp[-j(2m\pi/\Lambda)x]$ (with same period of the structure) and such idea forms the basis of plane wave expansion method. However, important to notice that β_B is not conventional propagation constant and can be complex in general. If one only concentrate on the real value of β_B and plot $\text{Re}\{\beta_B\}$ against the corresponding wave frequency ω , it results the most commonly used photonic band structure in the study of periodic system. (More detailed explanation is shown in the later part of this chapter)

Since $\varepsilon(x) = \varepsilon(x + \Lambda)$ is a periodic function, it can be written as Fourier series:

$$\varepsilon(x) = \varepsilon(x + \Lambda) = \sum_{n=0}^{n=\infty} \xi_n \exp(+jnKx) \quad (3.8)$$

where ξ_n is the Fourier coefficient of the periodic function. Introducing (3.7) and (3.8) into (3.1), it yields:

$$\sum_{m=-\infty}^{m=+\infty} \left\{ f_m [-(\beta_B + mK)^2] + \frac{1}{2} k_0 \sum_{n=-\infty}^{n=+\infty} \xi_n [\exp(-jnKx) + \exp(+jnKx)] \right\} f_m \exp[j(\beta_B + mK)x] = 0$$

Which gives

$$f_n [-(\beta_B + mK)^2] + \frac{1}{2} k_0 \sum_{n=-\infty}^{n=+\infty} \xi_n [f_{n+m} + f_{n-m}] = 0 \quad (3.9)$$

(3.9) represents an infinite set of equations.

In practice, higher order harmonics are discarded in numerical calculation so that a finite set of equations is obtained and the dispersion relation for β_m can be solved accordingly. Such classic technique is known as Floquet-Bloch method [18]. Despite of the mathematical complexity of such method, the advantage is clear: it is particularly suitable for computer evaluation since the numerical calculation comes out directly from the formulation of the problem. Hence Floquet-Bloch method is main used in specific calculation such as photonic band structure, stability diagram, rather than obtaining general physical properties of wave transformation in 1-D media.

When the periodic function $k_0^2 \varepsilon(x)$ has only sinusoidal modulation, i.e. $k_0^2 \varepsilon(x) = p - 2q \cos(\zeta x)$, where p , q and ζ are constant, the equation is known as Mathieu's Equation:

$$\frac{d^2}{dx^2} F(x) + [p - 2q \cos(\zeta x)] F(x) = 0 \quad (3.10)$$

Due to the complexity of the Mathieu's equation, they are not commonly discussed in many monographs. Although there are indeed many exceptions: [19], [20], [21], etc., the mathematical language contains in those references are somehow daunting for average users to understand.

Thus, the objective here is, without going too much into mathematic details of solving Mathieu's equation, to obtain the stability diagram using infinite matrix method, referring to **Appendix C** where the derivation of the infinite matrix is given. (another method by solving continuum fraction can be found in [21], [22] and [23]). The advantages of using matrix representation is that numerical calculation such as diagonalization, determinant calculation and matrix multiplication can be achieved using few commands in MATLAB.

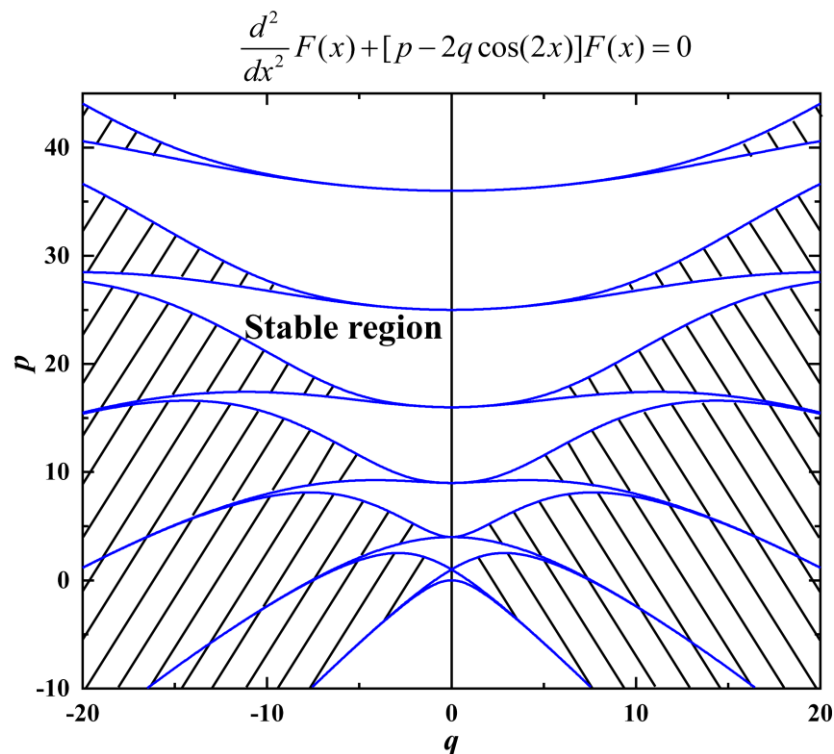


Fig. 3.1.2 Stability diagram of Mathieu's equation. Shaded region is the unstable region corresponds to the unbound solution while white region corresponds to the bound solution.

Here the value $\zeta = 2$ is used as an example. Following the Floquet-Bloch method introduced previously and expand $F(x)$ into Fourier series, the infinite matrix of the Mathieu's equation can be written as:

$$\left[\begin{array}{cccccccc} \dots & \dots \\ \vdots & (\beta_B - 4)^2 & q & 0 & 0 & 0 & \vdots & \vdots \\ \vdots & q & (\beta_B - 2)^2 & q & 0 & 0 & \vdots & \vdots \\ \vdots & 0 & q & \beta_B^2 & q & 0 & \vdots & \vdots \\ \vdots & 0 & 0 & q & (\beta_B + 2)^2 & q & \vdots & \vdots \\ \vdots & 0 & 0 & 0 & q & (\beta_B + 4)^2 & \vdots & \vdots \\ \dots & \dots \end{array} \right] - p\mathbf{I} \begin{bmatrix} \vdots \\ \zeta_{-2} \\ \zeta_{-1} \\ \zeta_0 \\ \zeta_{+1} \\ \zeta_{+2} \\ \vdots \end{bmatrix} = 0 \quad (3.11)$$

where \mathbf{I} is the identity matrix. Then the problem become $\det(\overline{\overline{\mathbf{M}}} - p\mathbf{I}) = 0$ which is effectively the eigenvalue of the matrix $\overline{\overline{\mathbf{M}}}$.

In general, eigenvalue calculation is one of the most complicated computational mathematics problems. Here, rather than obtaining the entire solution, we focus on the special case that the real part of β_B is zero, i.e. $\text{Re}\{\beta_B\} = 0$, representing the boundary between the stable and unstable solution region. The definition of stable solution become clear in the following discussion. Then the relationship between p and q can be obtained accordingly and represented as blue lines in Fig 3.1.2. Such diagram is known as stability diagram.

As shown in Fig 3.1.2, the shaded region is the unstable region where β_B is complex or real, corresponding to the 'unbound' solution that wave will attenuate inside periodic structure (stopband). The white region corresponds to the 'bound' solution where β_B is pure imaginary and wave propagates unattenuated inside periodic structure (passband). $q = 0$ axis represent continuous uniform medium with no periodic modulation.

In practice, there are two categories of (special) 1-D periodic structure that are analysed frequently: (1) a harmonically varying permittivity and (2) a piece-wise constant variation in $\varepsilon(x)$. For piece-wise constant layered periodic media, there is transfer matrix method available for the analyse and will be discussed later in this chapter. Our first task is to introduce and review the coupled mode theory applied to harmonically stratified media.

3.2 Coupled Mode Theory

Apart from classic Floquet-Bloch approach and solving the infinite matrix as shown previously, another approximate analytical method also widely used is known as coupled mode theory (CMT). CMT is based on perturbation method and is first used by Kogelnik when analysing light scattering by a thick hologram grating [15]. By assuming small refractive indices modulation amplitude and near the Bragg resonance frequency, the wave equation leads to two coupled equations. An example of sinusoidally stratified dielectric media analysed using CMT is shown below. Although sinusoidal varying media is barely used in real device application, the study of EM wave behaviour in such media is vital since the easier mathematical approach behind makes it an extremely powerful tool for understanding and synthesizing the wave mechanism in the periodic structure.

As illustrated in Fig. 3.2.1. Assuming the inhomogeneous media with sinusoidal variation of refractive index and a plane wave along x direction interacts with the media. The period of such structure is Λ . The index profile is given by a periodic function conveniently written as $\eta(x) = \eta_0 + \eta \cos(Kx)$, where $K = 2\pi/\Lambda$ and η is the amplitude of the index modulation. Although both η_0 and η are allowed to be complex as the media can be lossy/gain, we assume that there is no absorption/amplification presents so that η_0 and η are purely real. However, the solution technique is also valid for complex media.

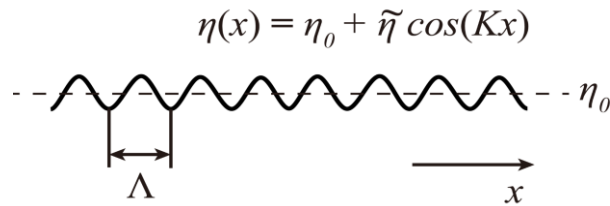


Fig. 3.2.1 Periodically stratified media with index distribution of $\eta(x) = \eta_0 + \eta \cos(Kx)$ along x direction.

Define $k_0 = \omega_0/c = 2\pi/\lambda_0$, our CMT is based on scalar wave equation:

$$\frac{d^2}{dx^2} F(x) + k_0^2 \eta^2(x) F(x) = 0 \quad (3.12)$$

Assuming a general solution of (3.12) is a perturbation of the original equation

$$\frac{d^2}{dx^2} F(x) + k_0^2 \eta_0^2 F(x) = 0 \quad (3.13)$$

with the form of $F(x) = A(x)\exp(-j\bar{\beta}x) + B(x)\exp(+j\bar{\beta}x)$ implies that the amplitudes $A(x)$ and $B(x)$ depends on x , where $\bar{\beta} = k_0\eta_0$. After some algebra (detailed derivation is shown in **Appendix D**), applying widely used slowly varying envelope approximation and assuming $2\bar{\beta} \cong K$, equation(3.12) ended up with two coupled equations:

$$\frac{d}{dx} A(x) = -j\kappa B(x)e^{+j\Delta\beta x} \quad (3.14)$$

$$\frac{d}{dx} B(x) = +j\kappa A(x)e^{-j\Delta\beta x} \quad (3.15)$$

where $\kappa = k_0^2\eta_0\eta/2\bar{\beta}$ is known as (complex) coupling coefficient of the grating and $\Delta\beta = 2\bar{\beta} - K$ is called (complex) detuning. Equations (3.14) and (3.15) are known as coupled mode equations. In this particular case, coupled mode equations represent the amplitude linkage between the forward and backward traveling waves (modes).

Although here coupled mode equations are obtained through sinusoidal index variation, the equation form can be applied to more general (but still have to be periodic) cases of $\eta(x)$ [24]. The final solution is the linear combination of the two solutions:

$$A(x) = C_1 e^{j\frac{\Delta\beta}{2}x+sx} + C_2 e^{j\frac{\Delta\beta}{2}x-sx} \quad (3.16)$$

$$B(x) = D_1 e^{-j\frac{\Delta\beta}{2}x+sx} + D_2 e^{-j\frac{\Delta\beta}{2}x-sx} \quad (3.17)$$

Where C_1, C_2 and D_1, D_2 are constants. The general solutions of (3.12) can be written as:

$$E(x) = \sum_{m=\pm 1} C_m e^{-j\left[j\sqrt{\kappa^2 - \left(\frac{\Delta\beta}{2}\right)^2} + \frac{2m\pi}{\Lambda}\right]x} + \sum_{m=\pm 1} D_m e^{+j\left[j\sqrt{\kappa^2 - \left(\frac{\Delta\beta}{2}\right)^2} + \frac{2m\pi}{\Lambda}\right]x} \quad (3.18)$$

Recall the definition of $K_{B,m}$ and Bloch wavevector β_B in section 3.1. In this particular case, $K_{B,m} = j\sqrt{\kappa^2 - (\Delta\beta/2)^2} + 2m\pi/\Lambda$ and $\beta_B = j\sqrt{\kappa^2 - (\Delta\beta/2)^2}$. In general, β_B can be either real or imaginary which corresponds to the passband and stopband respectively.

Quite often, the real and imaginary part of β_B is plotted as a function of frequency. Such dispersion relation is known as (photonic) ‘band diagram’. For convenience, the Bloch wavevector is often plotted within the reduced Brillouin zone analogue to the well-known semiconductor band structure. Here the first Brillouin zone is defined such that the value β_B satisfy $\beta_{B,i}\Lambda_i \in [0, \pi]$ where i denotes the direction in the reciprocal lattice.

e.g. $\beta_{B,x}, \beta_{B,y}, \beta_{B,z}$, etc. $\beta_{B,i}\Lambda_i = 0$ is often referred to as ‘ Γ ’ point. As shown in Fig. 3.2.2, for sinusoidal varying media, the red line and blue line represents the real and imaginary part of the Bloch wavevector respectively. When $\beta_{B,i}\Lambda_i$ become pure imaginary, such wavelength corresponds to the ‘stopband’, within which the reflected wave can add up in phase to produce strong reflection (non-propagating).

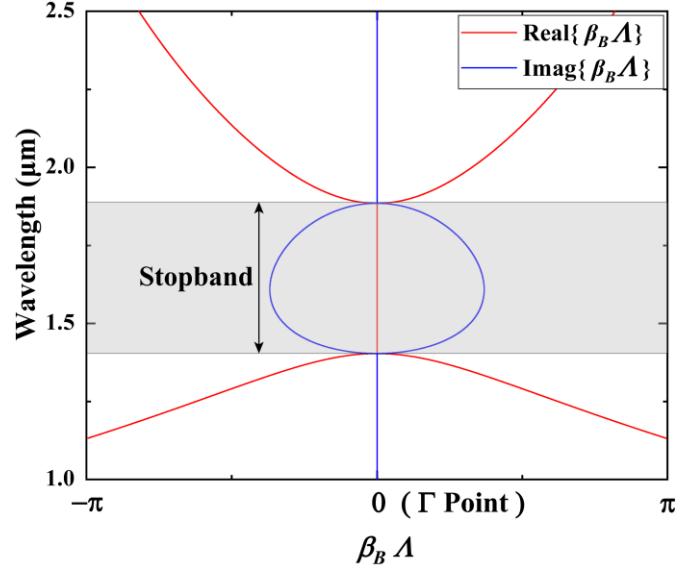


Fig. 3.2.2 1-D Photonic band structure corresponds to the structure shown in Fig 3.2.1 with index profile $\eta_0 = 2.05$, $\eta = 0.6$, $\Lambda = 0.401\mu m$

Previously, the solution of the coupled equation is found. However, we noticed that the solving of the problem does not necessarily require the implicitly assumed Floquet form. To understand the mathematics behind CMT better, we considering Mathieu equation introduced in previous section. It turns out that, when solving Mathieu equation, if only the zeroth and first order of Fourier components is considered, i.e.

$$\left\{ \begin{pmatrix} \beta_B^2 & q \\ q & (\beta_B + 2)^2 \end{pmatrix} - p\mathbf{I} \right\} \begin{bmatrix} \zeta_0 \\ \zeta_{+1} \end{bmatrix} = 0 \quad (3.19)$$

the solution of such equation results in solving the determinant of the following matrix:

$$\begin{pmatrix} \beta_B^2 & q \\ q & (\beta_B + 2)^2 \end{pmatrix} \quad (3.20)$$

which gives a quartic equation with one variable β_B . In general, quartic equation can have analytical solution but the expression can be rather complicated. Here, we took advantage of numerical software ‘Mathematica’ which yields:

$$\begin{aligned}
\beta_B^{(1)} &= -\sqrt{-\sqrt{q^2 - 4p + p + 1} - 1} \\
\beta_B^{(2)} &= \sqrt{-\sqrt{q^2 - 4p + p + 1} - 1} \\
\beta_B^{(3)} &= -\sqrt{\sqrt{q^2 - 4p + p + 1} - 1} \\
\beta_B^{(4)} &= \sqrt{\sqrt{q^2 - 4p + p + 1} - 1}
\end{aligned} \tag{3.21}$$

Such solutions corresponds to the four β_B values obtained from equation (3.14) and (3.15). At this stage, it becomes clear that mathematically speaking, CMT is effectively very approximate solution to Mathieu equation with only zeroth and first order of Fourier component.

Another interesting concept arises in periodic system is known as density of state (DOS). In photonic crystal, the calculation of DOS starts by first assuming the allowed ‘states’(wavevectors β_B) between a certain range of states ($\beta_B, \beta_B + \Delta\beta_B$) being uniform. Thus, the corresponding number of states that are contained within the frequency range ($k_0, k_0 + \Delta k_0$) is $(\Delta\beta_B / \Delta k_0) \Delta k_0$. Hence, the value $\Delta\beta_B / \Delta k_0$ is known as the density of state in frequency space (k -space).

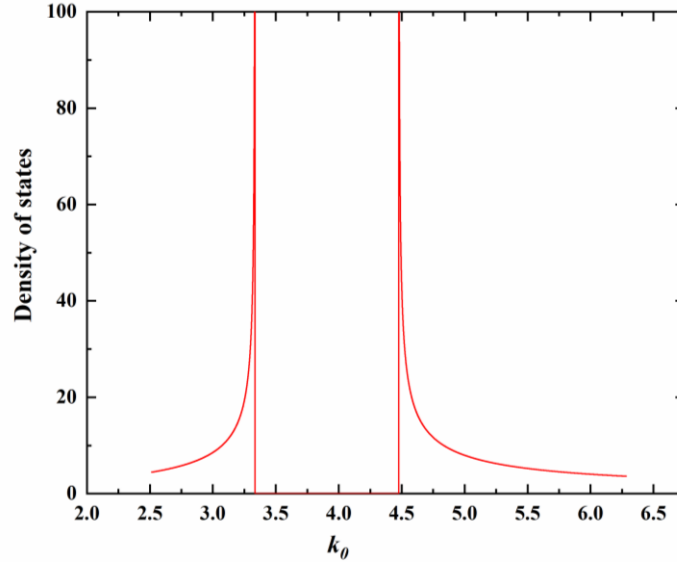


Fig. 3.2.3 density of states calculated using CMT

We then apply differentiation on the β_B value derived using CMT, which yields:

$$\frac{d\beta_B}{dk_0} = \text{Re} \left\{ \frac{|k_0(\eta - \eta_0) + K/2|}{\sqrt{(\beta - K/2)^2 - \kappa^2}} \right\} \tag{3.22}$$

The relationship between DOS and k vector is shown in Fig.3.2.3.

It is shown in the figure that the DOS is maximum in the band edge and zero within the band gap. Such effect is significant in some device application such as DFB laser. As mentioned in previous chapter, unlike FP laser that two parallel mirrors are used for the feedback, the feedback for DFB laser happens continuously at each corrugation. The numerical results shown previously suggest that the lasing happens at the edge of the pass band. Thus, although the reflection is high within the stop-band, there is no allowed optical state. In general, the lasing cannot happen within the stop band of DFB structure and that makes DFB laser a ‘band-edge’ laser [25]. There is certain technique known as ‘ $\lambda/4$ DFB laser’ which create ‘defect’ state within photonic forbidden gap. In that case, lasing will happen at the defect state rather than the band-edge.

3.3 Transfer Matrix Method for Periodic Media

Apart from periodic structure with harmonically varying index, another category of structure with piece-wise constant index profile has also been analysed intensively. When the piece-wise constant condition of the dielectric media is satisfied, there is another technique known as transfer matrix method (TMM) available for analysing such structure. It is well known that TMM has been used for network theory in microwave engineering. Meanwhile, researcher found that laser can be described by the product of different transfer matrix. The idea is to assume laser has finite numbers of elementary part. Each part could be described as a two by two matrix, the properties of the entire device is simply the multiplication of the transfer matrix.

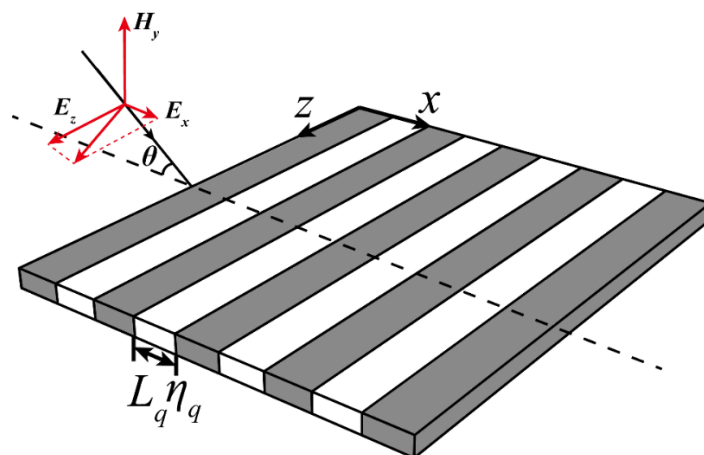


Fig. 3.3.1 Periodic media with piece-wise constant index profile. The excitation plane wave at angle θ is such that all electric fields are in x - z plane.

The advantage of such method is clear: unlike CMT, the weak coupling assumption is not necessarily required. Moreover, TMM is easy for numerical calculation. For periodic structure, the final result is effectively the N th power of the matrix of single period. Gain and loss can be included through complex refractive indices. This matrix method also works for F-P laser, DBR laser and DFB lasers as shown in previous chapter. Hence, rather than obtaining numerical results, the main objective of this section is to study the periodic structure in a certain degree of mathematical detail to further understand the behaviour of electromagnetic wave in periodic structure.

As shown in Fig. 3.3.1, refractive index pattern $\eta(x, z)$ is periodic along x direction and satisfy $\eta(x, z) = \eta(x) = \eta(x + \Lambda)$. The excitation is such that any non-zero field component satisfies $\partial/\partial y \approx 0$. Two independent categories of field solutions, one with polarisation $TE_y \Rightarrow E_y = 0$ and the other $TM_y \Rightarrow H_y = 0$ can be sustained. To be specific, $F(x, z)$ will be used to represent the non-zero y -directed field component. $F(x, z)$ satisfies wave equation:

$$\left[\frac{d^2}{dx^2} + \frac{d^2}{dz^2} + k_0^2 \eta^2(x, z) \right] F(x, z) = 0 \quad (3.23)$$

And thus, it is noticed that separation of variable $F(x, z) = f(x) \exp(-\beta z)$ is applicable. In x direction, piece-wise constant condition is satisfied $f_q(x) = f_q^+ e^{-j\kappa_q x} + f_q^- e^{+j\kappa_q x}$ where $\kappa_q = k_0 \eta_q$, f_q^+ and f_q^- are decided by the interface condition. From section 2.4, the transfer matrix for a single period can be written as:

$$\mathbf{M}_n = \begin{pmatrix} A & B \\ C & D \end{pmatrix} \quad (3.24)$$

Where

$$A = \frac{(\kappa_{q+1} + \kappa_q)^2}{4\kappa_{q+1}\kappa_q} e^{+j(\kappa_q L_q + \kappa_{q+1} L_{q+1})} - \frac{(\kappa_{q+1} - \kappa_q)^2}{4\kappa_{q+1}\kappa_q} e^{+j(\kappa_q L_q - \kappa_{q+1} L_{q+1})} \quad (3.25)$$

$$B = -\frac{\kappa_q^2 - \kappa_{q+1}^2}{4\kappa_{q+1}\kappa_q} e^{+j(\kappa_q L_q + \kappa_{q+1} L_{q+1})} - \frac{\kappa_q^2 - \kappa_{q+1}^2}{4\kappa_{q+1}\kappa_q} e^{+j(\kappa_q L_q - \kappa_{q+1} L_{q+1})} \quad (3.26)$$

$$C = -\frac{\kappa_q^2 - \kappa_{q+1}^2}{4\kappa_{q+1}\kappa_q} e^{-j(\kappa_q L_q - \kappa_{q+1} L_{q+1})} - \frac{\kappa_q^2 - \kappa_{q+1}^2}{4\kappa_{q+1}\kappa_q} e^{-j(\kappa_q L_q + \kappa_{q+1} L_{q+1})} \quad (3.27)$$

$$D = -\frac{(\kappa_{q+1} - \kappa_q)^2}{4\kappa_{q+1}\kappa_q} e^{-j(\kappa_q L_q - \kappa_{q+1} L_{q+1})} + \frac{(\kappa_{q+1} + \kappa_q)^2}{4\kappa_{q+1}\kappa_q} e^{-j(\kappa_q L_q + \kappa_{q+1} L_{q+1})} \quad (3.28)$$

After certain amount of algebra, it can be proved that for periodic structure, the determinate of the matrix \mathbf{M}_n , $\det(\mathbf{M}_n) = AD - BC = 1$. Hence matrix \mathbf{M}_n is an unimodular matrix. If the structure is periodic with the periodicity N , then the following condition:

$$\begin{pmatrix} f_1^+ \\ f_1^- \end{pmatrix} = \mathbf{M}_1 \mathbf{M}_2 \mathbf{M}_3 \cdots \mathbf{M}_n = \mathbf{M}_n^N \begin{pmatrix} f_N^+ \\ f_N^- \end{pmatrix} \quad (3.29)$$

is satisfied. Thus, input and output characteristics of the periodic structure with N periods can be expressed by N th power of unimodular matrix. There are many ways to calculate N th power of unimodular matrix existing in the literature. One widely used approach is using Chebyshev identity:

$$\mathbf{M}_n^N = \begin{pmatrix} A & B \\ C & D \end{pmatrix}^N = \begin{pmatrix} AU_{N-1} - U_{N-2} & BU_{N-1} \\ CU_{N-1} & DU_{N-1} - U_{N-2} \end{pmatrix} \quad (3.30)$$

where

$$U_N = \frac{\sin(N+1)\beta_B \Lambda}{\sin \beta_B \Lambda} \quad (3.31)$$

is known as Chebyshev polynomial of the second kind. The detailed derivation can be found in **Appendix E**.

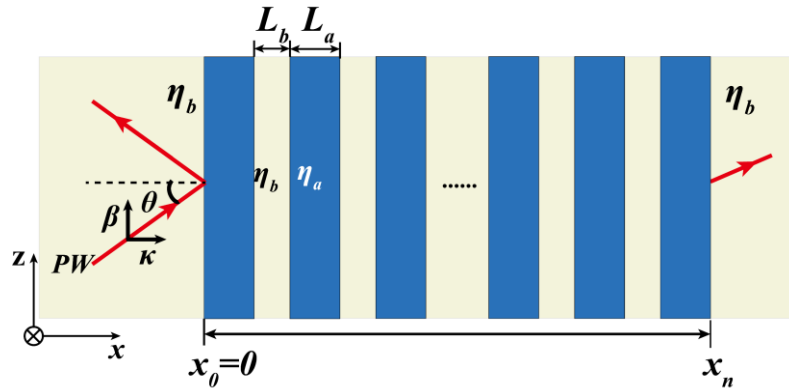


Fig. 3.3.2 Periodic structure along x -axis excited using plane wave with different angle θ . $\eta_a = 3.13$, $\eta_b = 3.46$, $L_a = 105.5nm$, $L_b = 180.75nm$.

As mentioned earlier in this chapter, in practical application, periodic structure can be used as filter, grating and high reflection mirror. All such application involves the study of the excitation in periodic structure, i.e. initial value problem. Meanwhile, TMM provides an easy approach of such problem. As derived from equation (3.29), the input and output of the periodic structure (with period N) is linked by the total transfer matrix \mathbf{M}_T , satisfying:

$$\begin{pmatrix} f_1^+ \\ f_1^- \end{pmatrix} = \mathbf{M}_T \begin{pmatrix} f_N^+ \\ f_N^- \end{pmatrix} = \mathbf{M}_n^N \begin{pmatrix} f_N^+ \\ f_N^- \end{pmatrix} = \begin{pmatrix} \mathbf{M}_{1,1} & \mathbf{M}_{1,2} \\ \mathbf{M}_{2,1} & \mathbf{M}_{2,2} \end{pmatrix} \begin{pmatrix} f_N^+ \\ f_N^- \end{pmatrix} \quad (3.32)$$

where $f_N^- = 0$ since no field coming back from the terminal layer. The total field reflection r of such structure is thus given by:

$$r = \frac{f_1^-}{f_1^+} = \frac{\mathbf{M}_{2,1}}{\mathbf{M}_{1,1}} \quad (3.33)$$

Referring to Fig. 3.3.2, $\eta_a = 3.13$, $\eta_b = 3.46$, $L_a = 105.5nm$, $L_b = 180.75nm$. The number of period is N . The structure is excited such that the incident beam has fixed wavelength at $\lambda_0 = 980nm$ while varying the incident angle which is linked to the effective indices via the following relationship: $\eta_{eff} = \eta_b \sin \theta$. Note here that varying incident angle θ and varying input wavelength λ_0 are the same since both changes the parameter known as ‘optical length’ effectively.

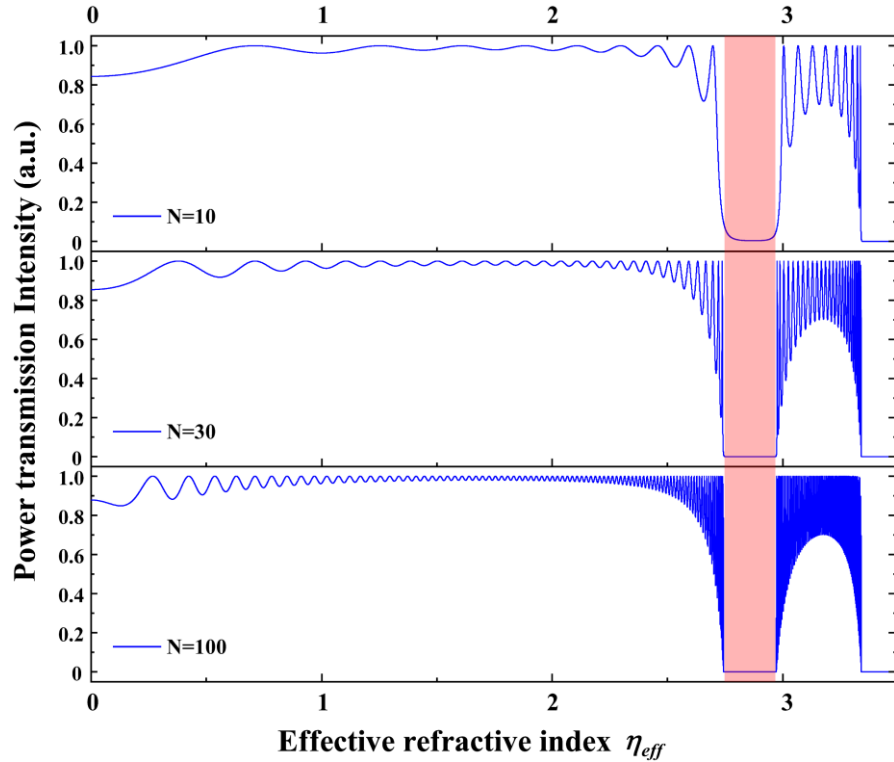


Fig. 3.3.3 Power transmission spectrum (blue lines) when varying the number of period as $N = 10$, $N = 30$ and $N = 100$. Note varying η_{eff} corresponds different excitation angle. The regions with light red colour represent the optical stop-band.

Fig. 3.3.3 illustrates the power transmission spectrum when varying the number of period as $N = 10$, $N = 30$ and $N = 100$. Other parameter of the structure refers to Fig. 3.3.2. It is shown that when increase the number of period, the resonance (transmission maximum) points become sharper and denser and then eventually forms a ‘continuum

band' if the number of period become infinite. Such continuum bands, also known as passband, are separated by the forbidden gaps where the total reflection occurs (shown as red shades region in figure). Also, it can be seen qualitatively that the resonance points (transmission maxima) become denser near the forbidden gap, such phenomenon has strong analogy to that of electrons states in 1-D crystal lattice: density of state for is higher near the band edge. The DOS is higher near the band edge is also proved previously using CMT.

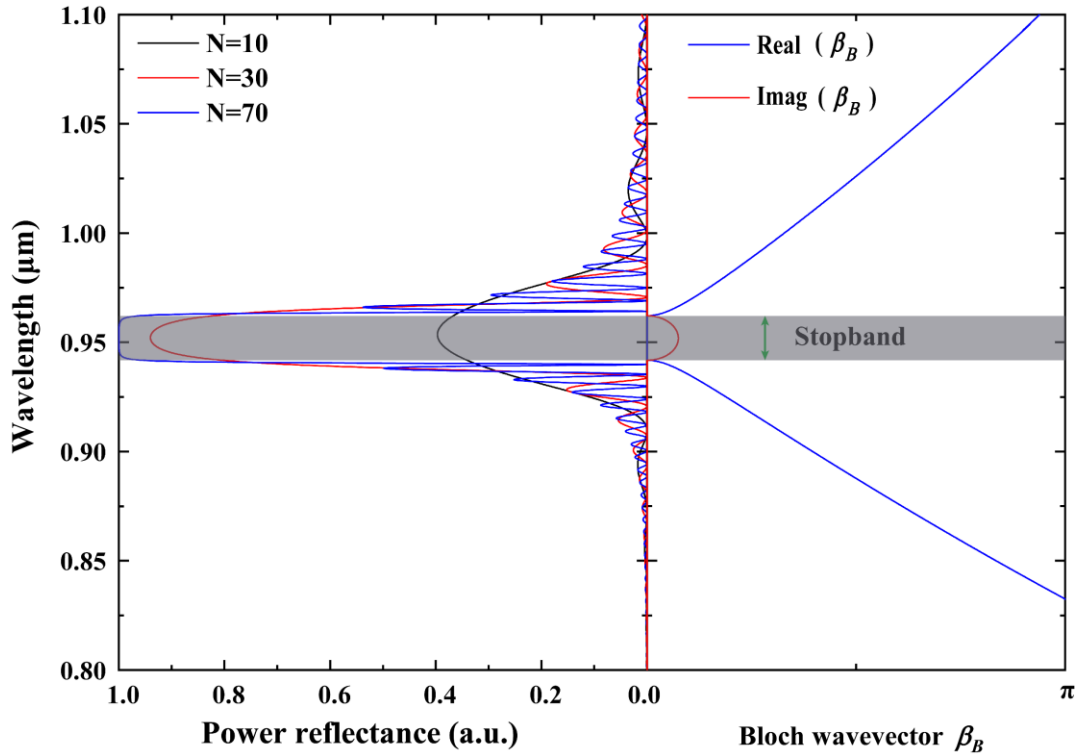


Fig. 3.3.4 power reflectance spectrum with different number of period and 1-D photonic band structure obtained using TMM. Grey shaded region represents optical stopbands within which the Bloch wavevector become pure imaginary.

According to the Floquet theorem, for periodic structure, the solution of wave equation is a periodic function multiply a general complex:

$$F(x, z) = f_B(x) e^{-j\beta z} e^{-j\beta_B x} \quad (3.34)$$

Where $f_B(x) = f_B(x + \Lambda)$ and Λ is the period. β_B is called Bloch wave vector number as designed previously. We can easily find out:

$$F(x + \Lambda, z) = f_B(x + \Lambda) e^{-j\beta z} e^{-j\beta_B(x + \Lambda)} = e^{-j\beta_B \Lambda} F(x, z) \quad (3.35)$$

Alternatively, in terms of TMM:

$$\begin{pmatrix} f_n^+ \\ f_n^- \end{pmatrix} = \mathbf{M}_n \begin{pmatrix} f_{n+1}^+ \\ f_{n+1}^- \end{pmatrix} = e^{+j\beta_B \Lambda} \begin{pmatrix} f_{n+1}^+ \\ f_{n+1}^- \end{pmatrix} \quad (3.36)$$

Thus, $\exp(+j\beta_B \Lambda)$ is the eigenvalue of the ABCD matrix and the value of β_B is given by

$$\beta_B = \frac{1}{\Lambda} \cos^{-1} \left[\frac{A+D}{2} \right] \quad (3.37)$$

In general, as discussed in section 3.1, β_B can be either real or imaginary and the quantity $K_{B,m} = \beta_B + 2m\pi/\Lambda$ represents the properties of the space harmonics. Similarly, the real and imaginary part of β_B obtained using TMM can also be plotted over an appropriate range of wavelength which gives the photonic band structure as shown above with specific parameters as given in Fig.3.3.2. Note that only perpendicular excitation of plane wave is considered in this discussion. As shown in Fig.3.3.4, the reflection maxima become ‘flat’ over a range of wavelength known as stopbands as the number of period become larger. Within such forbidden gap the Bloch wave-vector become pure imaginary $\beta_B = j|\beta_B|$ and $K_{B,m}$ become complex.

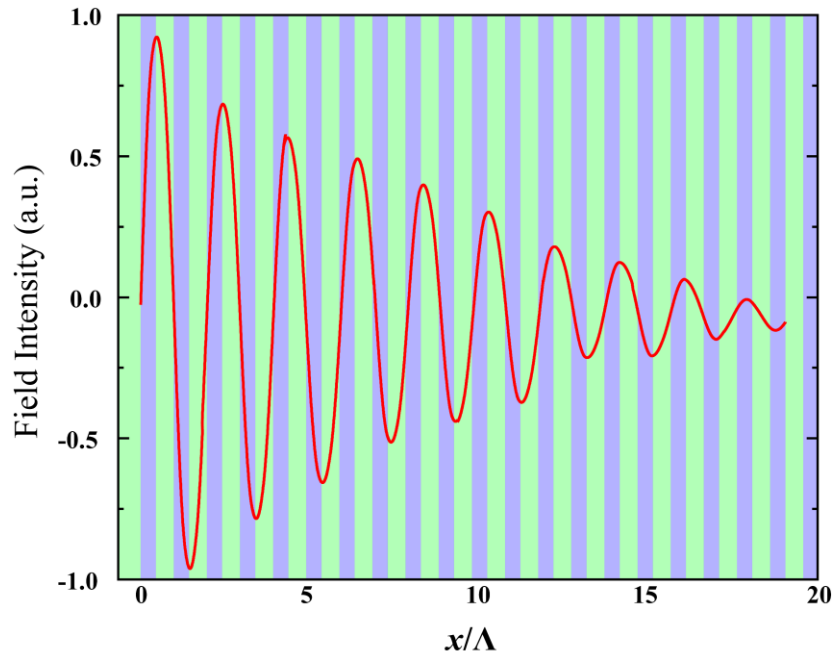


Fig 3.3.5 field intensity (red line) within the periodic structure when the frequency lies inside stopband

Note that such complex $K_{B,m}$, leads to the decaying (envelope) of electrical field distribution of a Bloch wave within the stopband. Although complex propagation constant usually leads to the dissipation of power, in this case, however, it does not

necessarily require gain or loss in the media. In other words, just like in the cladding layer of the conventional waveguide, although the field decays, the real part of Poynting vector is zero. Such issue is not trivial, a simple proof can be found in **Appendix F**. In general, the real part of Poynting vector is zero within the stopband, hence under such condition the periodic media act as an inductor/capacitor in microwave circuit, i.e. the Poynting vector is pure imaginary energy is not dissipated/lose.

Fig.3.3.5 illustrates the field intensity (red line) within the periodic structure when the frequency lies inside stopband. As it is shown, the field envelope decays as $\exp(-\beta_B x)$ where β_B is the Bloch wavevector as defined and x is the distance from the interface. Such effect is a result of the general form of Floquet-Bloch function and is explained below.

Recall derived in section 3.1 where the general expression of Floquet-Bloch function is of the form of (3.7):

$$F(x) = G(x)e^{-j\beta_B x} = \sum_{m=-\infty}^{m=+\infty} f_m e^{-j\left(\beta_B + \frac{2m\pi}{\Lambda}\right)x}$$

Where $K_{B,m} = \beta_B + 2m\pi/\Lambda$ is defined. When the frequency falls within the stop-band, the Bloch wavevector become pure imaginary $\beta_B = j|\beta_B|$ and thus, the function envelope decays as $\exp(-|\beta_B|x)$ along the periodic structure while remains varying periodically as Λ . Such effect has been used a great range of application to provide confined electromagnetic field and several examples will be given in the next section.

3.4 Eigenvalues in Periodic Structure

Perhaps, one of the most important and crucial study in physics is the calculation of the eigenvalue and eigenfunctions. Especially in quantum and electromagnetic theories, understanding physical properties by evaluation of eigenvalue has been one of the most widely used approaches in theoretical analysis. However, the eigenvalue or eigenfunctions in periodic structure is not at all obvious. In infinite periodic structure, assuming all fields have harmonic time dependency, it is found that by rearranging Maxwell's equation, for example, (2.1.9) and (2.1.10), one could get the famous ‘master equation’:

$$\nabla \times \left[\frac{1}{\varepsilon(\mathbf{r})} \nabla \times \mathbf{H}(\mathbf{r}) \right] = \left(\frac{\omega}{c} \right)^2 \mathbf{H}(\mathbf{r}) \quad (3.38)$$

define $\Phi\mathbf{H}(\mathbf{r}) = \nabla \times [1/\varepsilon(\mathbf{r}) \nabla \times \mathbf{H}(\mathbf{r})]$, hence operator $\Phi = \nabla \times [1/\varepsilon(\mathbf{r}) \nabla \times]$ is performed on an eigenvector $\mathbf{H}(\mathbf{r})$ and $(\omega/c)^2$ is a constant known as the eigenvalue of the problem, where ω is the frequency and c is the speed of light in vacuum. For a given structure, $\varepsilon(\mathbf{r})$, the objective is to find the mode solution $\mathbf{H}(\mathbf{r})$ and its corresponding frequency ω . Such technique formed a basis of one modelling technique known as plane wave expansion (PWE).

For periodic structure, the procedure is first using Bloch theorem to expand function $\mathbf{H}(\mathbf{r})$ and $\varepsilon(\mathbf{r})$ into a set of plane wave (hence the name plane wave expansion), then perform operation Φ on $\mathbf{H}(\mathbf{r})$, if $\mathbf{H}(\mathbf{r})$ is allowed mode, the result will return to a constant value multiply its original function [26]. In practice, recall Floquet-Bloch method introduced in section 3.1, this is done by using finite number of the plane wave (depends on the accuracy requirement), and the solving involves matrix-diagonalization method [18]. PWE is very important and useful for obtaining band diagram. Such study is crucial in photonic crystal since it provides the knowledge of the photonic band-gap and the interpretation of resonance modes over a range of frequency.

Despite of the success of PWE method in obtaining photonic band structure, however, it provides less physical insight and understanding of the wave propagating, coupling and scattering process inside photonic crystal. Another difficulty arises especially when the number of period become finite, since the Floquet theorem, which dramatically simplified the problem, does not apply to this situation.

In this section, an alternative but much simpler and very illustrative approach based on excitation of the periodic structure and the concept of impedance matching is used for analysing several examples. It is shown that apart from exact numerical solutions, clear physical insight can be obtained and concepts such as cavity (defect) states in PC nano-cavity laser, photonic crystal fibre and Tamm surface states in plasmonic based devices come out naturally.

3.4.1 General Concept of Waveguide

Perhaps one of the most important study of eigenvalue problem in E-M theory is about guided waves in different media. As is known, a large variety of physical environments exhibit wave phenomenon and often conditions exist naturally or can be engineered whereby these waves are preferentially directed (guided). These wave propagation forms are known as guided modes and the structure of those media that can support the modes are called waveguides. Although there are many forms of wave such as mechanic waves, water wave, acoustic wave and even quantum mechanics wave, the discussion is concentrated on the EM wave in this work. It dates back to as early as the end of 19th century when Lord Rayleigh publish the analysis of EM wave in dielectric filled conducting tube [27]. Later in 1910, guided waves in cylindrical dielectric guide (now known as optical fibre) was analysed by Hondros and Debye [28]. Since then, both theoretical and experimental work have been carried out extensively in guided EM wave which laid a solid foundation especially in practical communication elements. Guided wave optical devices such as optical fibre and semiconductor lasers have also been playing an important role in modern electrical engineering for the past few decades and the study are still revolutionizing the global industry.

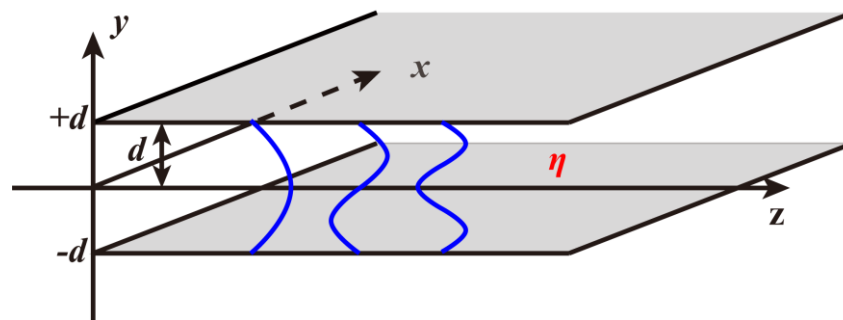


Fig. 3.4.1 Schematic of metal slab waveguide

As shown in Fig.3.4.1, the simplest waveguide consists of two metal plates. Assuming EM wave propagation is along z direction, then the TEM-type propagating waves, similar to plane waves in unbounded homogenous media, can have fields with E_y and H_x . However, unlike in unbounded homogenous media, the other combination E_x and H_y cannot be sustained. There are also other ‘modes’ composed of plane waves, at different angles to z -axis, bouncing off (reflected) from the bottom $y = -d$ and top $y = +d$ metal plates, can be considered as more complicated field distributions but propagating along the z -axis.

As illustrated in the Fig.3.4.1, generally speaking, $\sin(\kappa y)$ and $\cos(\kappa y)$ type field variations along y -axis with $\exp(-j\beta z)$ variations exist where β and κ have discrete values and relate via the dispersion characteristics of the modes. Such modes have two independent polarisations, $(TE)_z \Rightarrow E_z = 0$ and $(TM)_z \Rightarrow H_z = 0$. Each mode has a cut-off condition, i.e., each mode has a cut-off frequency below which frequency the mode will not propagate.

In practice, metal waveguides are widely used in microwave to millimetre (mm) wave application (frequency up to about 100GHz) above which the metal loss become significantly detrimental and the waveguide dimensions become impractical for mono-mode operation. At higher frequencies, from 100GHz, and beyond and way in to the optical, ultraviolet (UV) frequencies (wavelengths), dielectric materials are the most efficient for waveguiding (most commonly known such as optical fibre [29]).

The simplest geometry of the dielectric waveguide is the flat dielectric slab, similar to the two-parallel-plate metal waveguide discussed previously. As illustrated in Fig.3.4.2, the slab dielectric waveguide consists of a slab of dielectric of refractive index, η_1 , occupying the region $-d < y < +d$; the region below ($y < -d$) and above ($y > +d$) have refractive index η_2 with $\eta_1 > \eta_2$.

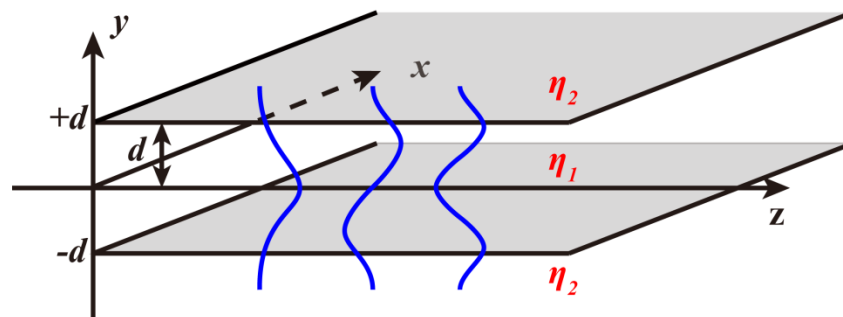


Fig. 3.4.2 Schematic of dielectric slab waveguide

With this arrangement the EM signal is bound (largely confined) to the central slab dielectric region η_1 . In this case also the ‘mode’ may be viewed as composed of plane waves at angles to the z -axis ‘bouncing-off’ the top, $y = +d$ and the bottom, $y = -d$, dielectric interfaces. In fact, this ‘bouncing-off’ from the interfaces is due to total internal reflection (TIR) as defined by Snell’s Law. Remember that TIR can occur only when the wave is incident from the high refractive index region in to the low refractive index region. Hence the dielectric waveguide has a high refractive index ‘core’ surrounded by low

refractive index regions and the signal remains ‘trapped’ in the high refractive index, core region; thus, this structure constitutes a waveguide.

The EM signal thus propagates along the z -axis while the fields are bound to the core region. But importantly, in principle, out to infinity along transverse axis finite fields exist even though energy does not flow out along the transverse axis for bound modes. Such waveguide is referred to as open waveguide. Moreover, because of being open waveguides, the rectangular slab does not admit separation of variables solution leading to considerable mathematical complexity in solving such structures. Hence, approximate analysis, such as the effective index method [30], Marcatili’s approximation [31], yield satisfactorily good results but extra care must always be taken to check validity. The simple derivation of the bound mode of dielectric waveguide and effective index method is given in many text books but briefly in **Appendix G**.

3.4.2 Waveguide Coupling and Periodic Waveguide

In general, the requirement for waveguide is to guide the EM radiation along the guiding structure. That implies that the EM signal are more appreciable in the core region. However, as mentioned previously, although energy does not flow outside the core region, the field in principle can extend to infinite. Hence, when parallel waveguides are brought together, the phenomenon known as waveguide coupling occurs.

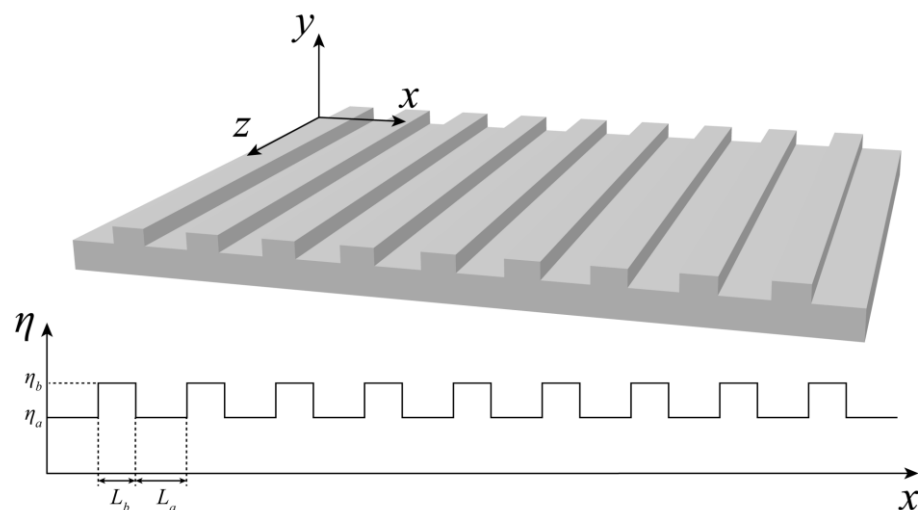


Fig. 3.4.3. Identically coupled waveguide: with $N = 9$ (nine identity coupled waveguides) is shown, the refractive index profiles are $\eta_a = 3.2$; $\eta_b = 3.5$ and the dimension is chosen as $L_a = 0.156\mu m$; $L_b = 0.143\mu m$.

The analyse of the waveguide problem often requires numerical calculation since even for dielectric slab waveguide, the solution involves solving a transcendental equation. To analyse the waveguide coupling effect, the method often used is CMT. An example showing coupling of two waveguide using CMT is given in **Appendix H**. Apart from CMT, since the coupled waveguide often satisfy piecewise constant condition, the waveguide coupling problem can also be analysed using TMM.

As illustrated in Fig.3.4.3, an example of periodic coupled waveguide with $N = 9$ (nine identity coupled waveguides) is shown, the refractive index profiles are $\eta_a = 3.2; \eta_b = 3.5$ and the dimension is chosen as $L_a = 0.156\mu m; L_b = 0.143\mu m$. The eigenvalue solution is searched such that only conventional bound modes are considered at the wavelength $\lambda = 1\mu m$, implying zero field intensity at infinite. Effectively, from equation (3.32), by setting $f_1^+ = f_N^- = 0$ (for confined mode field amplitudes must vanish at infinite) propagation constant corresponds to bound mode, in this particular case, is the solution of a transcendental equation:

$$A \frac{\sin(N\beta_B\Lambda)}{\sin(\beta_B\Lambda)} - \frac{\sin[(N-1)\beta_B\Lambda]}{\sin(\beta_B\Lambda)} = 0 \quad (3.39)$$

where A is given in equation (3.25) and $\beta_B\Lambda$ is given by equation (3.37). There are many computational techniques available for solving such equation numerically, e.g. bisection method [32], Newton's method [33] and fixed-point method [32], etc.

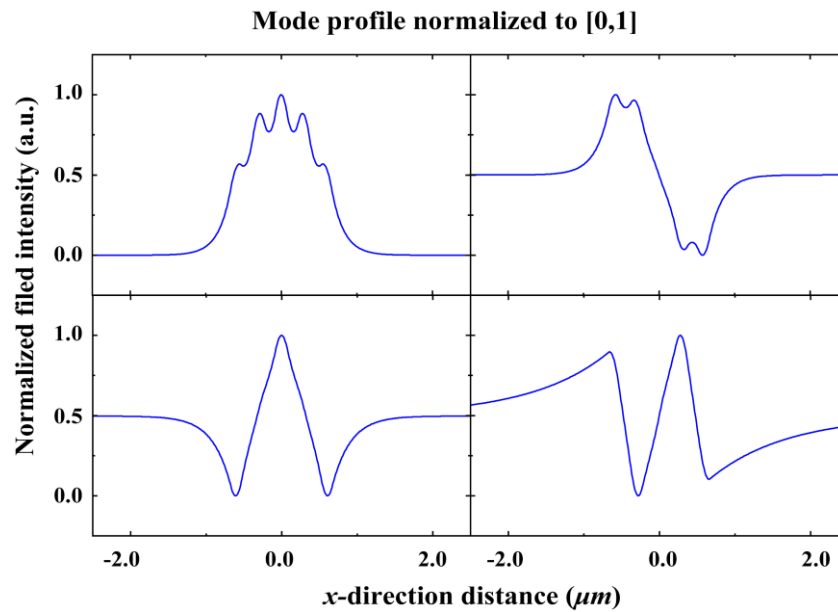


Fig.3.4.4 Bound mode profile of the coupled waveguide. (referring to Fig.3.4.4)

Fig. 3.4.4 shows several examples of the bound mode profiles of such periodic coupled waveguides. Note that importantly, only for weak waveguide coupling, N identical coupled waveguides gives exact N modes. Such effect is also seen in quantum mechanics that N states given by N coupled system are due to the splitting of the N -folded degeneracy [34]. However, in general, N identical coupled waveguides do not necessary give N bound modes depends on the strength of the coupling. (e.g. in this case only four modes). The solution shows sine/cosine type of function within the higher index region while in lower index region, the solution types are sine/cosine hyperbolic.

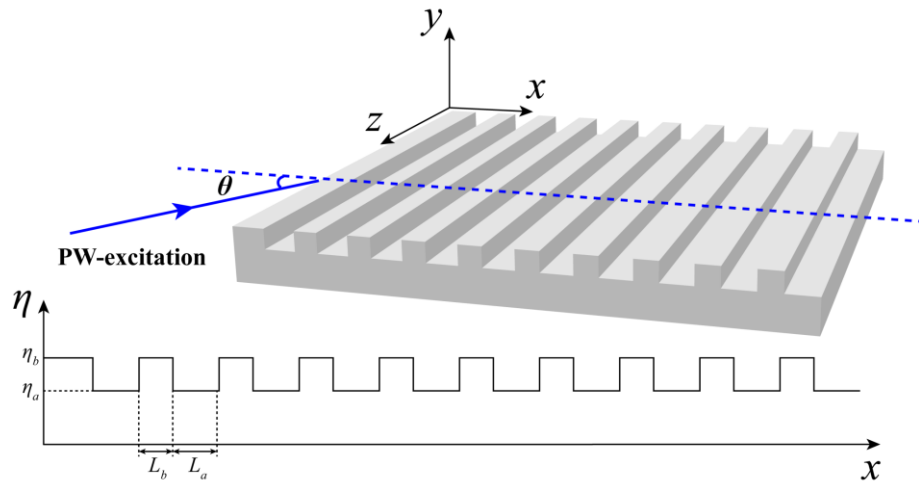


Fig. 3.4.5. Identically coupled waveguide with an extra excitation layer. $N = 9$ (nine identity coupled waveguides) is shown, the refractive index profiles are $\eta_a = 3.2$; $\eta_b = 3.5$ and the dimension is chosen as $L_a = 0.156\mu\text{m}$; $L_b = 0.143\mu\text{m}$.

Such eigenvalue problem can be also solved as initial value problem. It is known that conventional bound mode solution corresponds to the optical tunnelling solution [35]. Referring to Fig. 3.4.5, *similar structure* but with *higher index region outside* is excited at same wavelength $\lambda = 1\mu\text{m}$ at different angles. Such process effectively varying η_{eff} so that each region, $\beta = k_0\eta_{\text{eff}}$ is satisfied. Power reflectance spectrum of such structure is shown in Fig.3.4.5a. Four red triangles are the conventional mode solutions obtained previously of the structure shown in Fig.3.4.3. It is shown that conventional mode type solution corresponds to the total transmittance (optical tunnelling) type of solution. This technique of finding periodic waveguide mode is illustrative since it connects the eigenvalue problem with the excitation problem. The concept of exciting the structure to find the eigenvalue problem can also be understood using the technique of impedance matching.

Recall the wave impedance concept developed in previous chapter section 2.6, if the excitation plane wave is defined as ‘input’, the periodic structure is defined as ‘load’. Such excitation process is effectively searching for (matching) the ‘characteristic impedance’ of the ‘load’. Fig.3.4.6b shows both the real and imaginary part of the value Z_L/Z_0 . It is known from microwave engineering that the impedance matching condition occurs when real part of Z_L/Z_0 equals to one while imaginary part of Z_L/Z_0 is zero. As illustrated in the figure, all conventional mode type of solution (or optical tunnelling solution) corresponds to the impedance matching solution. In other word, the excitation process is to match (find) the characteristic impedance of the periodic structure.

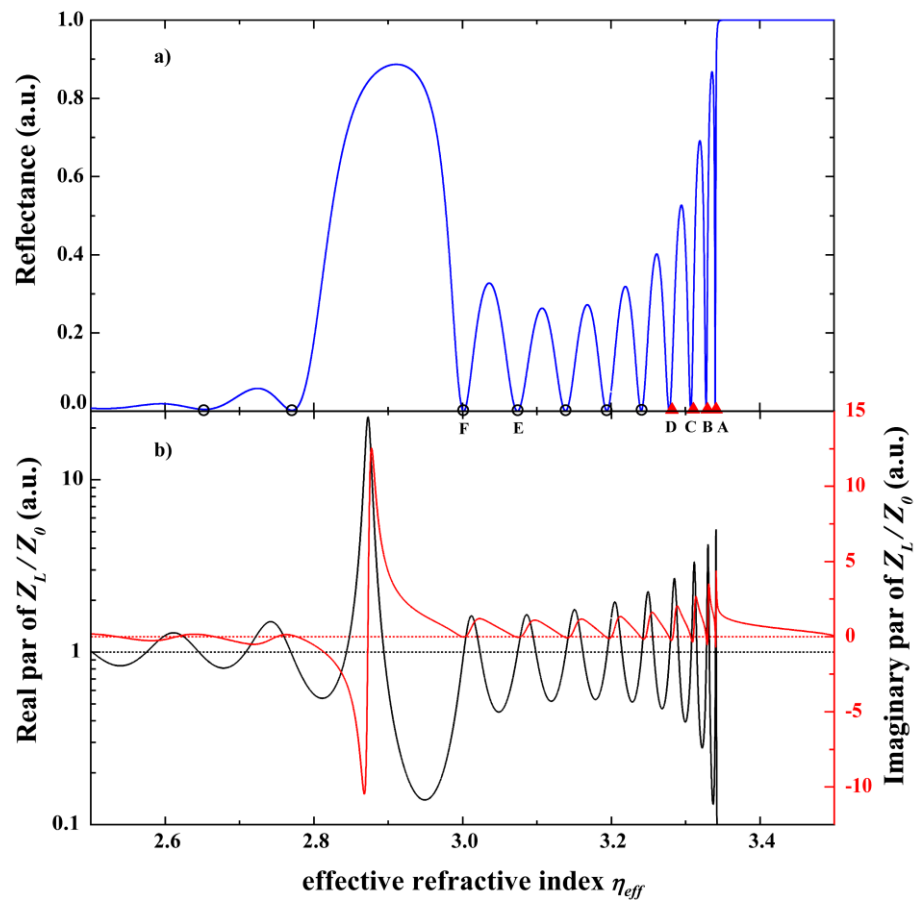


Fig. 3.4.6. a) Power reflectance spectrum of the structure referred to Fig.3.4.5. The red triangle represents the conventional bound mode while the black circle represents the mode due to the optical tunnelling b) wave impedance representation of the optical tunnelling

However, apart from the conventional bound mode solution (red triangle in Fig.3.4.6a), there are also many other solutions which corresponds to the optical tunnelling solutions and the impedances matching solutions (as shown as black circles in Fig.3.4.6a). Such solutions, although within the continuum spectrum region (the field solution is sinusoidal everywhere), the energy is still bound within the guide. As shown in Fig.3.4.7, field distribution of such solution is plotted as examples. The solutions, exhibits localized

characteristics, is observed within continuum region. If such mode is ‘excited’ in the same periodic structure without the higher index terminal region, i.e. referring to Fig.3.4.3, the energy will remain bound in the waveguide without leaking. Such mode is often referred to as bound state in continuum (BIC) mode. The concept of BIC is brought up by Von Neumann and Wigner in 1929. It is not until recently that BIC has been observed in quantum system (1-D semiconductor superlattice) [36] and more recently in optics such as 1-D Bragg grating [37].

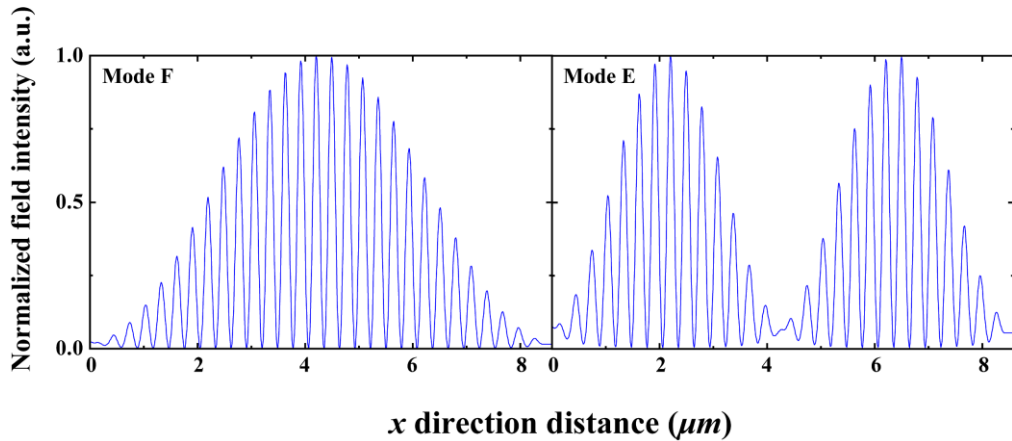


Fig. 3.4.7 Mode profile of BIC mode: Solution within the continuum region while energy remain bounded rather than dissipated.

3.4.3 Bragg Reflection Waveguide

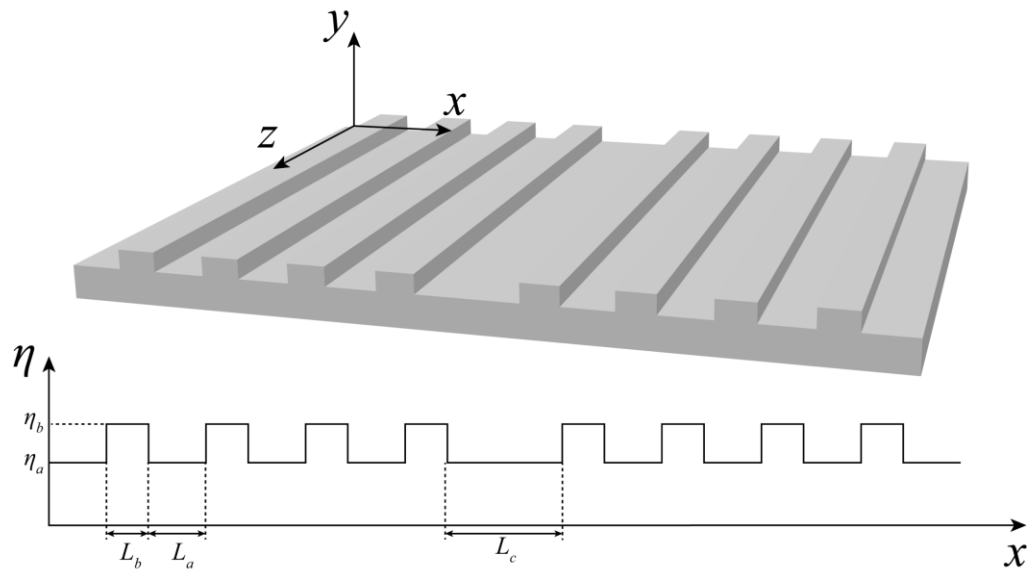


Fig. 3.4.8 Schematic of Bragg reflection waveguide.

Conventional waveguide depends essentially on total internal reflection (TIR) or Snell's law to achieve EM wave confinement, hence the core refractive index has to be larger to inhibit propagation of energy away along the transverse axis. However, as is already known, periodic structures can also inhibit propagation if appropriately designed structure dimensions and materials parameters are used at the appropriate frequencies; i.e. stop-bands and pass-bands of periodic structures have found extensive usage recently to achieve guiding characteristics that were hitherto not achievable. That is, the realm of Floquet-Bloch functions and Bragg grating phenomenon are being re-deployed to create what are now termed as photonic crystals to achieve waveguides such as photonic crystal optical fibre[38], resonators[39] etc that have hitherto been unachievable characteristics.

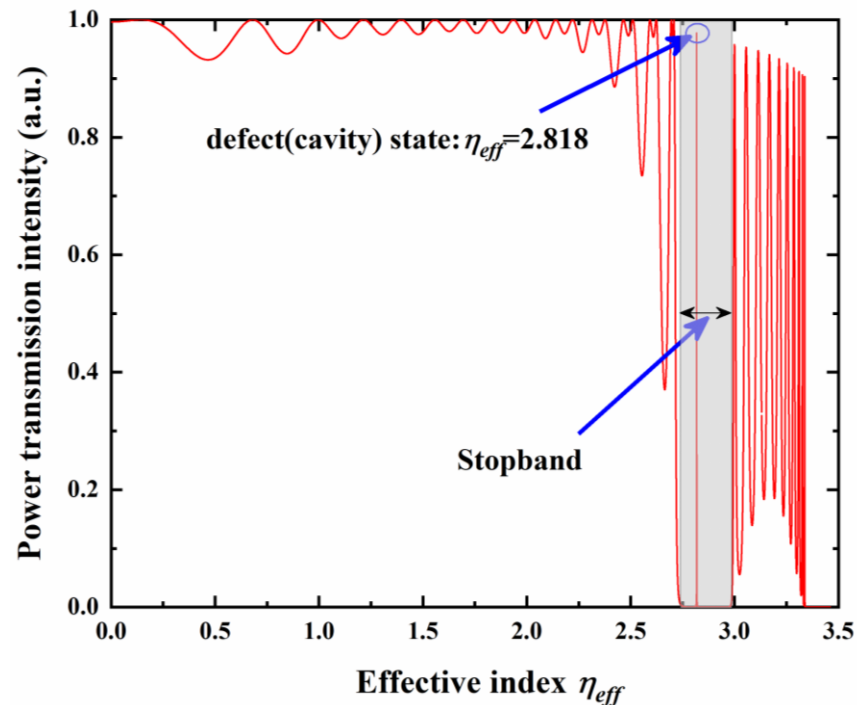


Fig. 3.4.9 Power transmission spectrum of Bragg reflection waveguide

The concept of photonic crystal waveguide is originated from the paper by Pochi Yeh where the Bragg reflection waveguide is introduced [40]. It is also suggested in their later publication that cylindrical Bragg waveguide constructed by high/low refractive indices arranged in a ring can support mode propagation in lower core region [41]. Later, a more sophisticated waveguide structure known as photonic crystal fibre is designed and fabricated by Philip Russell and University of Bath. A more comprehensive review about photonic crystal fibre can be found in [42] [43]. Basically, photonic crystal fibre supports the propagation of defect state. The detailed calculation is complicated but the idea and the concept is briefly illustrated as Bragg reflection waveguide as below.

Considering 1-D periodic structure with defect in the middle. As illustrated in Fig.3.4.8. the refractive index profiles are $\eta_a = 3.13$; $\eta_b = 3.46$ and the dimension is chosen as $L_a = 120nm$, $L_b = 170nm$ and $L_c = 290nm$. The excitation is such that the wavelength of the plane wave is chosen at $\lambda = 980nm$ with an angle of incident. Following similar technique developed previously, the transmission maximum is considered to be the eigenvalue of such problem.

Fig.3.4.9 illustrates a power transmission spectrum of such structure. However, unlike the ‘perfect’ periodic structure which has a continuous stop-band, an extra ‘state’ appears within the forbidden gap corresponds to the so-called defect sates or cavity states. Such cavity state also shows ‘impedance matching condition’, i.e. the real part of Z_L/Z_0 equals to one while imaginary part of Z_L/Z_0 is zero, which is similar to the waveguide mode, BIC mode. Such numerical evidence is given in Fig. 3.4.10.

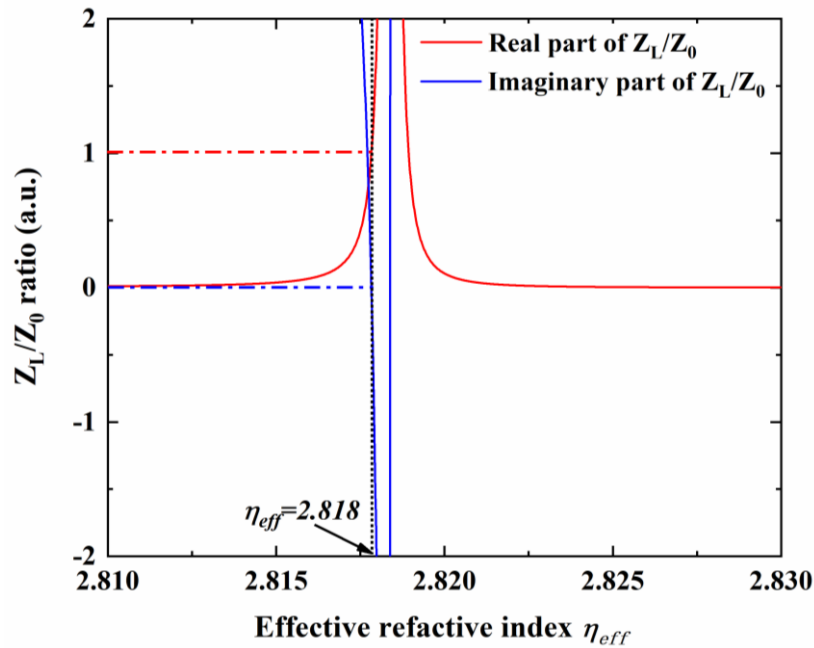


Fig. 3.4.10 Impedance matching representation of photonic crystal cavity state.

Fig. 3.4.11 illustrates a mode profile of such defect state (cavity state). It is shown that although the core region has lower refractive index, the mode is still remain ‘bound’ along its transverse direction. However, unlike conventional waveguide which relies on total internal reflection, Bragg reflection waveguide or similarly photonic crystal waveguide relies on the stop-band properties of the periodic structure. Although theoretically, ‘perfect’ bound defect mode can exist only when the periodic structure is semi-infinite,

in practice, even 10 to 20 periods give sufficient low loss and can be used in various of applications. A further notice that the defect state can be made into lasers or resonators due to the high Q-factor, famously photonic crystal nano-cavity laser [44].

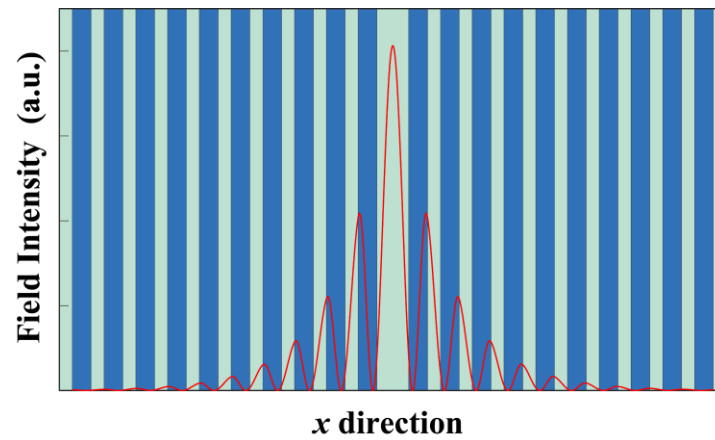


Fig. 3.4.11 Mode profile of cavity states: 10 period of grating is used in each side.

3.4.4 Surface State

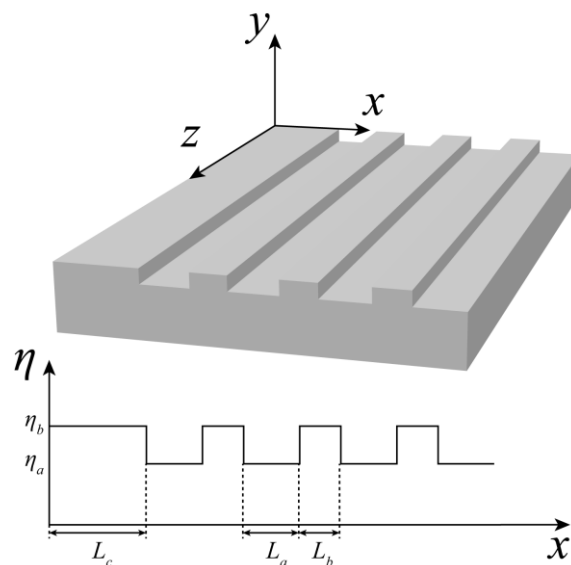


Fig. 3.4.12 Schematic of structure that supporting surface state.

Apart from guiding the electromagnetic wave as Bragg reflection waveguide as mentioned in previous section, periodic structure can provide guiding effect along its truncating surface (referring to the structure illustrate in Fig.3.4.12). Such mode, or state, is often known as Tamm state [45]. Fig.3.4.13 illustrates two types of states for truncated periodic potential: one type surface states has Floquet-Bloch type of solution (within the passband) in the periodic potential and exponentially decayed type of solution outside the

truncated structure (Fig.3.4.13b); while the other solution (Fig.3.4.13a), although the solution exponentially decayed outside the structure, the Floquet-Bloch solution within the periodic potential lies inside the ‘stopband’ which gives a decayed field envelope inside the structure. Researcher are more interested in state represented in Fig. 3.4.13a since the field is localized near the surface and thus provide a very special type of guiding structure. Such state also known as Tamm state, or optical Tamm states in optics, which is named after the Russian physicist Igor Tamm who predicted such state (electronic state) in 1933.

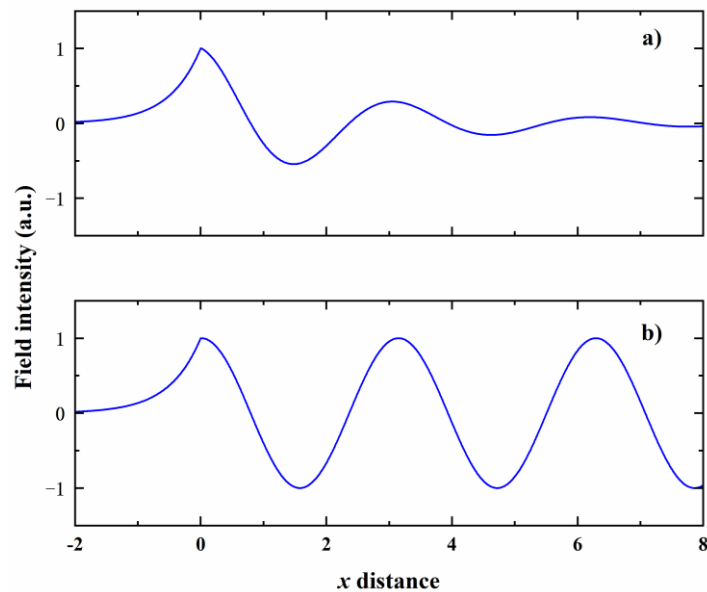


Fig. 3.4.13 Two types of surface state. The surface boundary at $x=0$

The identification of surface state can be achieved also using excitation method [46]. The technique is almost identical to the evaluation of the cavity state and hence will not be discussed again in this thesis.

Another rather interesting phenomenon when considering surface states. Apart from the guiding structure mentioned previously, electromagnetic field can also exist in the interface between two media if the dielectric constants are of the opposite sign (e.g. metal and semiconductor). Such ‘mode’ (only a single TM mode exists in such given frequency) is also known as surface plasmon because the negative dielectric constant is a result from electron plasma in metal. The limitation of this single TM mode is removed if one media exhibit periodic index profile, e.g. Bragg grating in semiconductor. Such structure supports the mode known as Tamm plasmon. The excitation of the conventional surface state usually requires a prism and the conventional plasmonic mode can be only TM mode.

Tamm plasmon, however, by combination of metal and DBR structure, can support TE and TM while easier to be excited.

3.5 Conclusion

Optical wave in periodic structure is undoubtedly a broad subject area and has been studied for over a century. However, the theory of such topic has received very significant resurgence even recently when a great range of photonic device emerges especially the application of photonic crystal. To understand the behaviour of those advanced device and design for the next level of sophistication, it is necessary or even inevitable to study the wave characteristics in periodic structure from its fundamental basis.

Such study is done as a part of this project and is reviewed in this chapter. Broadly speaking, the topic of wave mechanism in periodic structure is in general eigenvalue problems and can be grouped into two area: infinite periodicity and finite periodicity. The periodic structure with infinite extent is governed by the Hill's equation (or Mathieu equation) which effectively gives rise to the PWE method. The eigenvalue is merely the Bloch wavevector results from its numerical process. CMT used in infinite periodic structure, however, is an approximate of PWE by discarding higher order Fourier components (plane wave components).

The other group of study involves wave mechanism in finite periodic structure. Such topic is very complicated in general since the Floquet-Bloch solution, which dramatically simplified the calculation, does not apply anymore. However, when the linkage between the eigenvalue problem and the excitation problem is discovered, everything become clear:

- Conventional coupled waveguide mode corresponds to the transmission maxima when exciting the structure from one end. Such process is effectively matching the characteristic impedance of the structure.
- BIC mode can be discovered using excitation technique. Each BIC mode, although appears in the continuum spectrum region, is an eigenvalue solution and also corresponds to the characteristic impedance matching of such structure.

- The studied of cavity state and Tamm state involves investigating of the periodic structure with defect and can be also analysed using excitation and impedance matching techniques.

Such linkage investigated and summarized in this chapter forms a solid building block of the mode index analysis of 2-D photonic crystal which is developed in next chapter.

3.6 Reference

- [1] L. Rayleigh, "XVII. On the maintenance of vibrations by forces of double frequency, and on the propagation of waves through a medium endowed with a periodic structure," *The London, Edinburgh, and Dublin Philosophical Magazine and Journal of Science*, vol. 24, no. 147, pp. 145-159, 1887.
- [2] F. Bloch, "Über die quantenmechanik der elektronen in kristallgittern," *Zeitschrift für physik*, vol. 52, no. 7-8, pp. 555-600, 1929.
- [3] F. Abélès, "Recherches sur la propagation des ondes électromagnétiques sinusoïdales dans les milieux stratifiés-Application aux couches minces," in *Annales de physique*, 1950, vol. 12, no. 5, pp. 596-640: EDP Sciences.
- [4] L. Brillouin, *Wave propagation in periodic structures: electric filters and crystal lattices*. Courier Corporation, 2003.
- [5] S. Sensiper, "ELECTROMAGNETIC WAVE PROPAGATION ON HELICAL CONDUCTORS. Technical Report 194," *Research Lab. of Electronics, Mass. Inst. of Tech.* 1951.
- [6] A. Hessel, "Generalized characteristics of traveling-wave antennas," *Antenna theory*, vol. 2, 1969.
- [7] E. Yablonovitch, "Inhibited spontaneous emission in solid-state physics and electronics," *Phys Rev Lett*, vol. 58, no. 20, pp. 2059-2062, May 18 1987.
- [8] J. B. Pendry, "Negative refraction makes a perfect lens," *Physical review letters*, vol. 85, no. 18, p. 3966, 2000.
- [9] T. Ergin, N. Stenger, P. Brenner, J. B. Pendry, and M. Wegener, "Three-dimensional invisibility cloak at optical wavelengths," *Science*, p. 1186351, 2010.
- [10] M. McCall, "Transformation optics and cloaking," *Contemporary Physics*, vol. 54, no. 6, pp. 273-286, 2013.
- [11] T. F. Krauss, "Slow light in photonic crystal waveguides," *Journal of Physics D: Applied Physics*, vol. 40, no. 9, p. 2666, 2007.
- [12] Y. Akahane, T. Asano, B.-S. Song, and S. Noda, "High-Q photonic nanocavity in a two-dimensional photonic crystal," *Nature*, vol. 425, no. 6961, p. 944, 2003.

- [13] I. Vurgaftman and J. R. Meyer, "Photonic-crystal distributed-feedback lasers," *Applied Physics Letters*, vol. 78, no. 11, pp. 1475-1477, 2001.
- [14] L. Thylen, M. Qiu, and S. Anand, "Photonic crystals--a step towards integrated circuits for photonics," *Chemphyschem*, vol. 5, no. 9, pp. 1268-83, Sep 20 2004.
- [15] H. Kogelnik, "Coupled wave theory for thick hologram gratings," *Bell System Technical Journal*, vol. 48, no. 9, pp. 2909-2947, 1969.
- [16] H. Kogelnik and C. V. Shank, "Coupled - Wave Theory of Distributed Feedback Lasers," *Journal of Applied Physics*, vol. 43, no. 5, pp. 2327-2335, 1972.
- [17] D. J. Griffiths and C. A. Steinke, "Waves in locally periodic media," *American Journal of Physics*, vol. 69, no. 2, pp. 137-154, 2001.
- [18] S. Y. Karpov and S. Stolyarov, "Propagation and transformation of electromagnetic waves in one-dimensional periodic structures," *Physics-Usppekhi*, vol. 36, no. 1, pp. 1-22, 1993.
- [19] M. Abramowitz and I. A. Stegun, *Handbook of mathematical functions: with formulas, graphs, and mathematical tables*. Courier Corporation, 1965.
- [20] H. Jeffreys and B. Jeffreys, *Methods of mathematical physics*. Cambridge university press, 1999.
- [21] N. W. McLachlan, "Theory and application of Mathieu functions," 1951.
- [22] T. Tamir, H. Wang, and A. A. Oliner, "Wave propagation in sinusoidally stratified dielectric media," *IEEE Transactions on Microwave Theory and Techniques*, vol. 12, no. 3, pp. 323-335, 1964.
- [23] E. T. Whittaker and G. N. Watson, *A course of modern analysis*. Cambridge university press, 1996.
- [24] A. Yariv, "Coupled-mode theory for guided-wave optics," *IEEE Journal of Quantum Electronics*, vol. 9, no. 9, pp. 919-933, 1973.
- [25] J. P. Dowling, M. Scalora, M. J. Bloemer, and C. M. Bowden, "The photonic band edge laser: A new approach to gain enhancement," *Journal of Applied Physics*, vol. 75, no. 4, pp. 1896-1899, 1994.
- [26] J. D. Joannopoulos, S. G. Johnson, J. N. Winn, and R. D. Meade, *Photonic crystals: molding the flow of light*. Princeton university press, 2011.

- [27] L. Rayleigh, "XVIII. On the passage of electric waves through tubes, or the vibrations of dielectric cylinders," *The London, Edinburgh, and Dublin Philosophical Magazine and Journal of Science*, vol. 43, no. 261, pp. 125-132, 1897.
- [28] D. Hondros and P. Debye, "Elektromagnetische wellen an dielektrischen drahnten," *Annalen der Physik*, vol. 337, no. 8, pp. 465-476, 1910.
- [29] A. W. Snyder and J. Love, *Optical waveguide theory*. Springer Science & Business Media, 2012.
- [30] J. Buus, "The effective index method and its application to semiconductor lasers," *IEEE Journal of Quantum Electronics*, vol. 18, no. 7, pp. 1083-1089, 1982.
- [31] E. A. Marcatili, "Dielectric rectangular waveguide and directional coupler for integrated optics," *Bell System Technical Journal*, vol. 48, no. 7, pp. 2071-2102, 1969.
- [32] J. H. Mathews and K. D. Fink, *Numerical methods using MATLAB*. Pearson Prentice Hall Upper Saddle River, NJ, 2004.
- [33] F. B. Hildebrand, *Introduction to numerical analysis*. Courier Corporation, 1987.
- [34] A. Yariv, "Optical Electronics in Modern Communications, Oxford Series in Electrical and Computer Engineering," 1997.
- [35] P. Yeh, "Resonant tunneling of electromagnetic radiation in superlattice structures," *JOSA A*, vol. 2, no. 4, pp. 568-571, 1985.
- [36] F. Capasso, C. Sirtori, J. Faist, D. L. Sivco, S.-N. G. Chu, and A. Y. Cho, "Observation of an electronic bound state above a potential well," *Nature*, vol. 358, no. 6387, p. 565, 1992.
- [37] Y. Plotnik et al., "Experimental observation of optical bound states in the continuum," *Physical review letters*, vol. 107, no. 18, p. 183901, 2011.
- [38] J. C. Knight, J. Broeng, T. A. Birks, and P. S. J. Russell, "Photonic band gap guidance in optical fibers," *Science*, vol. 282, no. 5393, pp. 1476-1478, 1998.
- [39] A. Yariv, Y. Xu, R. K. Lee, and A. Scherer, "Coupled-resonator optical waveguide: a proposal and analysis," *Optics letters*, vol. 24, no. 11, pp. 711-713, 1999.

- [40] P. Yeh and A. Yariv, "Bragg reflection waveguides," *Optics Communications*, vol. 19, no. 3, pp. 427-430, 1976.
- [41] M. Toda, "Single-mode behavior of a circular grating for potential disk-shaped DFB lasers," *IEEE journal of quantum electronics*, vol. 26, no. 3, pp. 473-481, 1990.
- [42] P. Russell, "Photonic crystal fibers," *science*, vol. 299, no. 5605, pp. 358-362, 2003.
- [43] P. S. J. Russell, "Photonic-crystal fibers," *Journal of lightwave technology*, vol. 24, no. 12, pp. 4729-4749, 2006.
- [44] H. Altug, D. Englund, and J. Vučković, "Ultrafast photonic crystal nanocavity laser," *Nature physics*, vol. 2, no. 7, p. 484, 2006.
- [45] S. Kawata, "Near-field microscope probes utilizing surface plasmon polaritons," in *Near-Field Optics and Surface Plasmon Polaritons*: Springer, 2001, pp. 15-27.
- [46] M. Kaliteevski et al., "Tamm plasmon-polaritons: Possible electromagnetic states at the interface of a metal and a dielectric Bragg mirror," *Physical Review B*, vol. 76, no. 16, p. 165415, 2007.

Chapter 4

Evaluating Resonances in PCSEL Structures based on Modal Indices

Wave propagation in periodic media has been studied for over a century [1] but the topic has received a significant resurgence in recent years with the introduction of the concept of PCs [2]. Large volumes of research publications have subsequently appeared in the study and application of PCs in such diverse areas as PC fibres [3, 4], PC planar waveguides and resonators [5, 6, 7] and optical sources such as PCSELS [8]. Thus, several techniques for analysing (specially optical) waves in periodic media exist in the published literature, but the three, plane wave expansion (PWE) [9], coupled mode theory (CMT) [10], and the purely numerical finite difference time domain (FDTD) [11], are by far the most extensively used.

As introduced in the previous chapter, the PWE method is based on representing the field in the PC by a (complete) set of plane-waves (PWs) [12], while the effect of media periodicity is enforced by a Floquet-Bloch function representation. However, note that an infinitely large medium of unvarying periodicity is implicit in this formulation (i.e., an infinite number of identical periodic layers). Consequently, with the PWE method, although very powerful in some aspect, it is not readily possible to analyse periodic media of finite extent (finite number of identical periodic layers). Such limitations are removed if the CMT is used [13], and the basic concept of CMT is explained in previous chapter. However, the mathematical complexities involved are somewhat daunting for the average user and requires very considerable effort and time to implement. Apart from analytical method, there are also pure numerical method such as FDTD which may be used to solve for fields in almost any kind of structure [14]; typically, however, considerable computer resources are needed and significantly long computation times are required [15].

In view of the above, there is a noticeable need to develop another technique to solve for fields in 2-D PCs – pertinent to PCSELS - which is relatively simple, easy to implement and requires modest resources and time while retaining a ‘physical feel’. Thus, this PhD work has been to develop a simple method to solve for resonances in 2-D

periodic structures and the emphasis is on the concepts and theory that is needed for this development. Such studies are presented in the previous chapter as the ‘building blocks’ for understanding wave propagation in periodic structure.

This chapter presents a new method, mode index analysis (MIA), for evaluating the resonances, based essentially on the ‘building blocks’ developed in previous chapter such as transfer-matrix technique and wave propagation in multilayer medium, which is relatively easy to formulate, and has quite modest demands on computing requirements. Such a technique, particularly suited to rectangular geometry structures, has been developed and is described in this chapter. It is envisaged that the implementation of this method will enhance the potential to generate more comprehensive models of photonic-crystal based devices. It is shown in the chapter that the method matches well with the existing modelling techniques. Details of modelling process, analysis of finite size PCs, with discussions on the consistency and validity of the model will also be presented in this chapter.

4.1 Description of model: y-direction

In this chapter, a rectangular co-ordinate system (x, y, z) consistent with the rectangular device geometry is used throughout. As stated above, the objective is to develop a modelling technique that is easy to implement and use but which reliably yields the essential quantitative characteristics of PC structures, particularly relevant to PCSELs. However, for a 3-D dielectric system, in principle, all six field components $E_{x,y,z}$ and $H_{x,y,z}$ exist and coupled together which is not separable. There are many approximate techniques for converting vertical dimension into an effective index distribution in x - z plane but briefly here.

Since in actual PCSEL device, the vertical structure is multilayer slab achieved using semiconductor epitaxy. Here, considering multilayer slab with thickness d_q and given refractive indices $\eta = \eta(y) = \eta_q(y)$ where q is the layer number along y axis. As shown in Fig. 4.1.1. Next assume the transverse bound modes is supported by the slab along y axis and propagates in x - z plane. (e.g., suppose the propagation is along z axis). Further assume the structure along y axis ensures single bound mode $\beta = k_0 \eta_{eff,y}$, where

β is the propagation constant and $\eta_{eff,y}$ is the effective index of the mode (details on calculating bound mode for multilayer waveguide can be found in chapter 3 and **Appendix G**). The above assumptions are valid because in most of laser structure, typically PCSEL, active region has high refractive index and support a bound mode to produce high photon density which is crucial in stimulated emission.

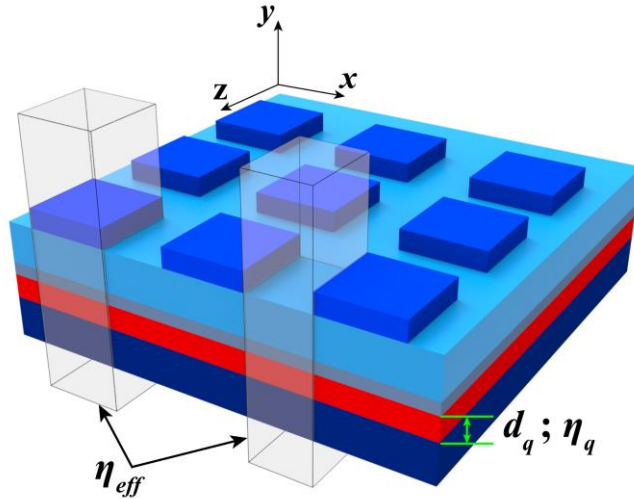


Fig. 4.1.1 3-D schematic of PC structure.

Note any structural variations along y direction (e.g. change in η_q or thickness d_q in any layer q) changes β and hence changes $\eta_{eff,y}$. In general, change in η_q or d_q will produce change in $\eta_{eff,y}$. i.e. assume that in general $\eta_{eff,y} = \eta_{eff,y}(x, z)$. Hence, by using this method, y direction structure is taken account of and replaced by equivalent structure in x - z . i.e. $\eta_{eff,y} = \eta_{eff,y}(x, z)$.

Further assumption is that mode along y axis is not significantly affected due to physical structure $\eta(y; x, z)$ and $d_q(x, z)$. The assumption is valid since in PCSEL structure, photonic crystal has small index difference and act as perturbation. Thus, the problem is reduced to 2-D x - z plane with $\eta_{eff,y} = \eta_{eff,y}(x, z)$ known and corresponding x - z plane geometrical structure given. For simplicity, we use $\eta_{eff,y}(x, z) = \eta_{eff}(x, z) = \{\eta_a, \eta_b\}$ in the following discussion.

4.2 Description of model: x - z plane

As discussed in previous session, the 3-D PCSEL structure is approximately ‘converted’ into 2-D periodic structure and the main emphasis is now in x - z plane. Referring to Fig.4.2.1 which gives a schematic representation of a planar periodic structure in the x - z plane defined by rectangular regions of widths w_a, w_b and refractive index, η_a surrounded by regions with refractive index η_b ; the periodicities of the structure are L_a, L_b . Although not essential to this method, for the purposes of this study the relative magnetic permeability $\mu=1$, is assumed throughout, as is the case for most semiconductor material for optical devices, so that the relative electrical permittivity, $\varepsilon = \eta^2$ is applicable.

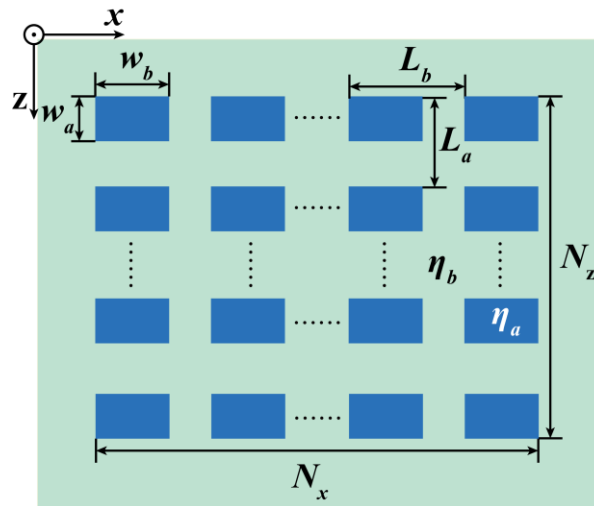


Fig. 4.2.1 Schematic of PC structure. N_x and N_z are number of periods along x and z respectively.

This refractive index pattern $\eta(x, z)$ may be produced by actual, direct material growth and/or by some post growth fabrication process. For example, appropriate variation in the material composition of the vertical layers and/or thicknesses (y axis) is often used to produce a variation in the vertical guided mode that may then be considered as creating an effective-index pattern $\eta(x, z)$ in the x - z plane [18] corresponding to that in Fig.4.2.1. (PCSEL fabrication technique will be discussed in next chapter) However, henceforth in this work, the study is restricted to a 2-D analysis (in the x - z plane); i.e., essentially $\eta(x, y, z) = \eta(x, z)$ and the excitation is such that any non-zero field component, $\hat{F}(x, y, z) = \hat{F}(x, z)$ [18], i.e., $\partial/\partial y \approx 0$ is applicable.

Then, from Maxwell's equations introduced in chapter 2, approximately, two independent categories of field solutions, one with polarisation , $TE_y \Rightarrow E_y = 0$ and the other with $TM_y \Rightarrow H_y = 0$ can be sustained [13, 16]. To be specific, $\hat{F}(x, z)$ will be used to represent the non-zero y -directed field component. For application to PCSELs the TE_y polarisation is important since the typical active-layer gain medium (quantum well or quantum dots) supports this polarisation; thus, H_y, E_x, E_z are the dominant non-zero field components in that case.

In a region with $\varepsilon(x, z) = \eta^2(x, z)$ and for harmonic time dependent $\exp(j\omega t)$ fields, the application of Maxwell's equations and following the commonly accepted assumption $\mathbf{E} \cdot \nabla \varepsilon \sim 0$ leads to the wave equation

$$\left[\frac{\partial^2}{\partial x^2} + \frac{\partial^2}{\partial z^2} + k_0^2 \eta^2(x, z) \right] \hat{F}(x, z) = 0 \quad (4.1)$$

where $k_0^2 = (2\pi/\lambda_0)^2 = \omega^2 \mu_0 \varepsilon_0$. The 2-D PC structure that is considered in this work is shown in Fig.4.2.1 where piece-wise constant, rectangular regions are assumed with abrupt transitions between regions with $\eta = \eta_a$ and $\eta = \eta_b$; this represents $\eta(x, z)$ in equation.(4.1). The field distribution $\hat{F}(x, z)$ for the resonant modes (m, n ; integers) of this PC structure are considered to be of the form

$$\hat{F}_{m,n}(x, z) = f_m(x) g_{n,m}[z; f_m(x)] \quad (4.2)$$

corresponding to the resonant wavelength $\lambda_{0,m,n}$. The notation $g_{n,m}[z; f_m(x)]$ simply emphasises the point that $\hat{F}(x, z)$ is not separable and the solution $g_{n,m}$ depends on the solution f_m , which becomes clear in the detailed discussion below. Note that $\hat{F}_{m,n}(x, z)$ is, in general, a non-separable function but in the context of present typical device parameters such as dimensions, magnitudes of refractive index discontinuities, etc., it is justifiably acceptable to assume a separated-variables form for each resonant mode of the 2D- PC.

The essential underlying concept of the analysis procedure presented here is based on viewing the 2D-PC structure of Fig.4.2.1 as a laterally (say, along x) multilayer waveguide which is longitudinally (along z) segmented. Hence the required 2D field distributions are evaluated as modes propagating in multilayer waveguides with longitudinal discontinuities.

Thus, the procedure for obtaining $\hat{F}_{m,n}(x, z)$, $\lambda_{0, m,n}$ begins by first evaluating the modes of the longitudinally uniform (i.e., *not* segmented) multilayer waveguide, structure as shown in Fig.4.2.2 with $\eta = \eta_x(x)$ corresponding to the pattern defined by Fig.4.2.1. The wave equation for the structure in Fig.4.2.2 is then

$$\left[\frac{\partial^2}{\partial x^2} + \frac{\partial^2}{\partial z^2} + k_0^2 \eta_x^2(x) \right] F(x, z) = 0 \quad (4.3)$$

Clearly, a separation of variables solution in this case is applicable with eigen-mode/eigen-value solutions (f_m, β_m) , similar to those for multilayer slab dielectric waveguides discussed in chapter 3:

$$F(x, z) = f_m(x) e^{-j\beta_m z} \quad (4.4)$$

satisfies equation (4.3). Full use is made of piecewise constant slab dielectric regions to generate a transfer matrix formulation, denoted \mathbf{M}_T , to numerically solve [17] for $f_m(x)$ and β_m . The solving technique is introduced in chapter 3.

Rather than solve for the modes in the periodic multilayer waveguide structure, Fig.4.2.2, directly as an eigenvalue problem, it is found to be more convenient and illustrative to treat it as an excitation problem. Such advantage is mentioned previously in chapter 3. It is important to recall that the eigen-mode of the finite 1-D periodic structure can be represented by the total transmittance solution of such a structure as discussed in previous chapter and also reference [18].

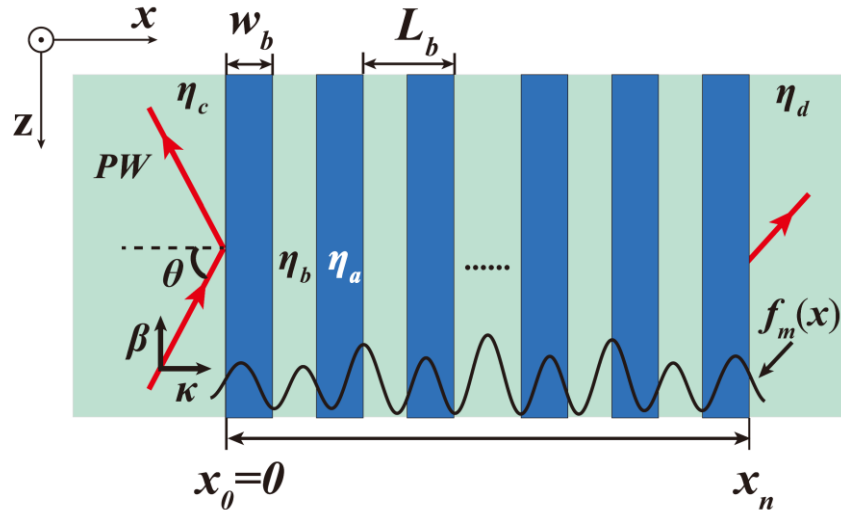


Fig.4.2.2 Model description: (Refractive indices: $\eta_a, \eta_b = \eta_c = \eta_d$) Lateral modes propagating along the z-axis are computed for a relevant range of wavelengths.

As shown in Fig.4.2.2 a plane wave (PW) incident at an angle θ excites corresponding PWs in the multilayer regions, η_a , η_b such that $\kappa_a^2 + \beta^2 = k_0^2 \eta_a^2$ and $\kappa_b^2 + \beta^2 = k_0^2 \eta_b^2$ where κ and β represent the x -directed and z -directed propagation constants in the corresponding regions. Applying the usual field matching conditions at the abrupt interfaces [19] between regions ‘a’ and ‘b’ yields the elements of the 2×2 unimodular transfer matrix, \mathbf{m} , for a typical unit cell [20].

Further, and very importantly, the periodic nature of the multilayer medium is utilised to obtain a compact and very efficient formulation for the composite transfer matrix accounting for the corresponding number, N , of periodic layers [21]. Thus, the total transfer matrix is given by $\mathbf{M}_T = \mathbf{m}^N$ where \mathbf{m} is the unimodular transfer matrix in a unit cell as already discussed in chapter 3:

$$\mathbf{M}_T = \mathbf{m}^N = \begin{pmatrix} m_{11} & m_{12} \\ m_{21} & m_{22} \end{pmatrix}^N = \begin{pmatrix} m_{11}U_{N-1} - U_{N-2} & m_{12}U_{N-1} \\ m_{21}U_{N-1} & m_{22}U_{N-1} - U_{N-2} \end{pmatrix} \quad (4.5)$$

m_{11} , m_{12} , m_{21} and m_{22} are the matrix elements, and U_N are known as Chebyshev polynomials of the second kind:

$$U_N = \frac{\sin \left[(N+1) \cos^{-1} \left(\frac{m_{11} + m_{22}}{2} \right) \right]}{\sin \left[\cos^{-1} \left(\frac{m_{11} + m_{22}}{2} \right) \right]} \quad (4.6)$$

There are many different methods to calculate power N of unimodular 2×2 matrix [51, 93] which enables analysing a truncated periodic structure since, unlike infinite periodic structures, the Bloch theorem does not strictly apply in this situation [20][23]. This procedure is also beneficial since it provides for a significantly reduced computation time. The resonant mode for the entire multilayer (periodic) structure can be calculated from the total transfer matrix, which effectively is the solution of a transcendental equation: $|m_{11}U_{N-1} - U_{N-2}| = 1$ [25].

For a relevant range of wavelengths, transmission resonances for plane waves incident on the multilayer input at $x=0$, at incident angles, $0 < \theta < \pi/2$, are used to identify the eigen-mode solutions [24]; the incident angles corresponding to transmission resonances provide the β_m and corresponding $f_m(x)$. An example of power transmittance through the 1-D periodic structure, Fig.4.2.1, with $N_x = N = 30$ is shown in Fig.4.2.3a; points a, b and c are given as examples of eigen mode solutions which corresponds to 1-

D transmission resonances. The corresponding typical field distributions labelled as $f_m(x)$ ($m = a, b, c$) are shown in Fig.4.2.3b.

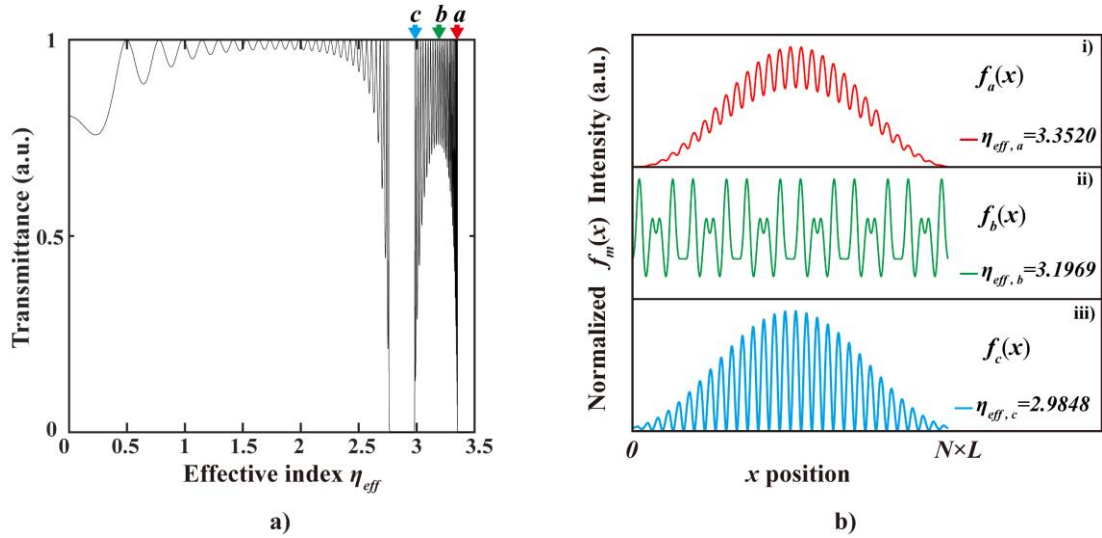


Fig.4.2.3 a) Transmission spectrum of periodic structure (referring to Fig. 2a, $N = 30$, $L_b = 286.25\text{nm}$, $w_b = 116.5\text{nm}$, $\eta_a = 3.13$, $\eta_b = 3.46$.) b) Examples of eigen-mode solutions $f_m(x)$ of 1-D periodic structure (Fig.4.2.2)

The modal propagation constant β_m is often referred to as the modal effective index $\eta_{\text{eff},m}$ and also gives the mode impedance; that is, for the next stage of the analysis, the composite multilayer structure along x -axis supporting mode $f_m(x)$ can be replaced by $\eta_{\text{eff},m}$ (or by the corresponding modal impedance).

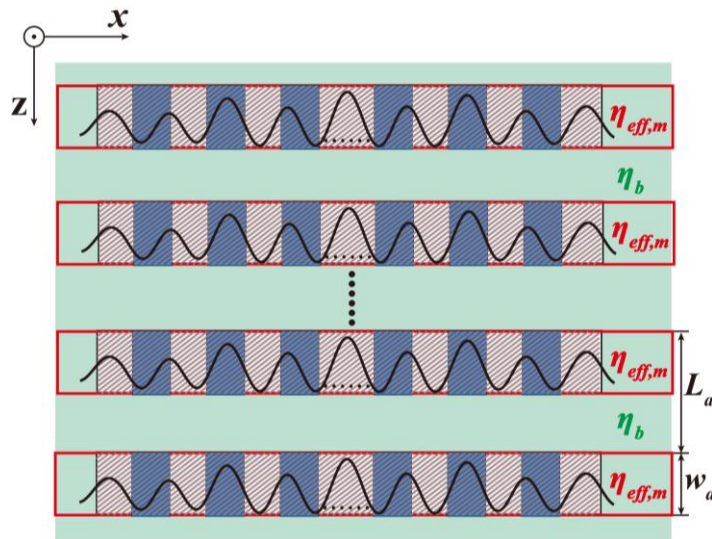


Fig.4.2.4 Model description: The shaded area with dark blue region representing the multilayer waveguide in Fig.4.2.1 is replaced by a homogeneous medium of effective modal index $\eta_{\text{eff},m}$, thus resulting in a 1-D periodic grating along z with an unit cell composed of $\eta_{\text{eff},m}$ and η_b

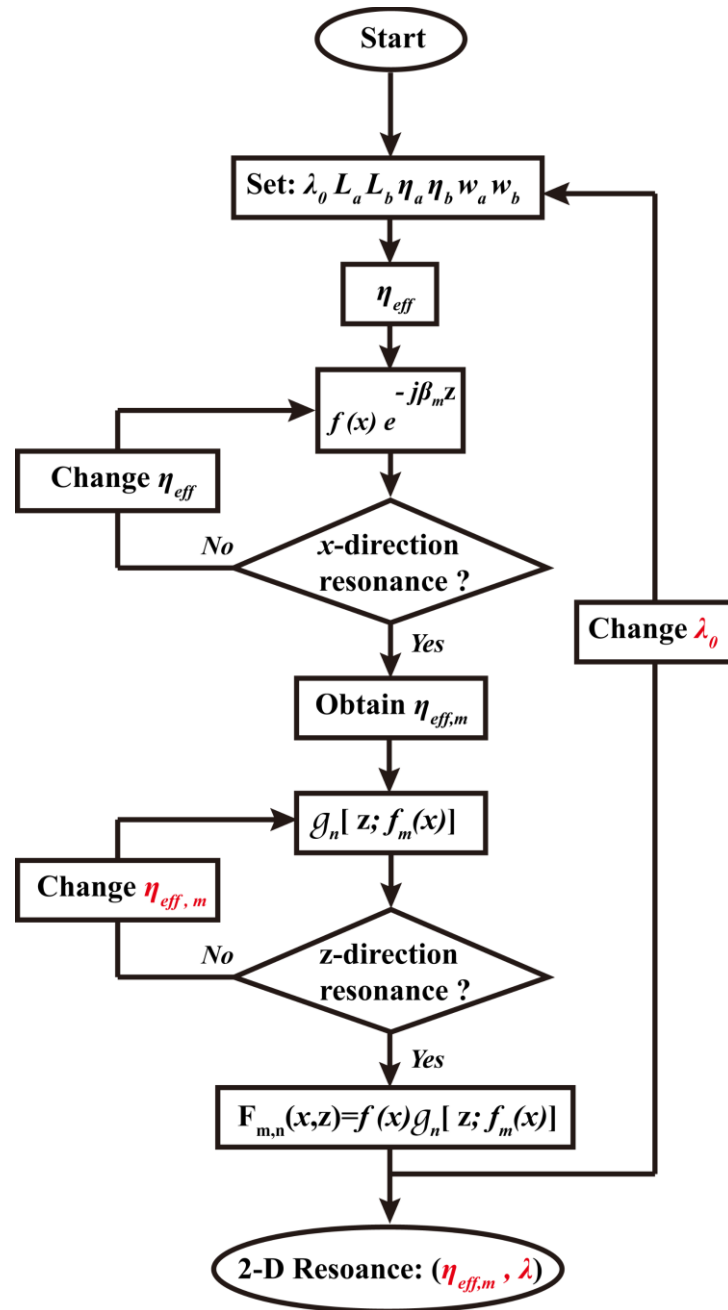


Fig.4.2.5 Flowchart of the modelling process

The second stage of the analysis proceeds by now incorporating the discontinuities along the z -axis of the multilayer waveguide. Analysing waveguide discontinuities is, in general, a rather complicated problem [25], since all the modes of the structure are excited (even with a single mode incident) – that is, a separation of variables analysis is not strictly applicable; (note that equation (4.2) suggests that the general form of the solution is NOT of the separated variables form). But in the present context of dimensions and magnitude of discontinuities it is justified to assume that only the same (single) mode as that incident exists throughout. In that sense $f_m(x)$ is the same in equation (4.2) and (4.4). This is done by representing the length along z of the multilayer waveguide region by the

corresponding mode index, $\eta_{\text{eff}, m}$, followed by the length of the discontinuity, gap region of index η_b . This results in the 1-D multilayer structure (periodic grating) as shown in Fig.4.2.4.

The resonances for this 1-D grating are now sought, over the same wavelength range as before, by considering the response to a perpendicularly incident plane wave; the transfer matrix method, as described previously with reference to Fig.4.2.2 is used also here to obtain the result. Thus, with reference to Fig.4.2.4, the field distribution along z at resonance, $g_{n,m}[z; f_m(x)]$, is obtained and the final result, in effect, includes reasonably well the characteristics of the original 2-D periodic media (Fig.4.2.1). Hence the final 2-D field distributions at resonances, $\lambda_{0 m,n}$, are $\hat{F}_{m,n}(x, z) = f_m(x)g_{n,m}[z; f_m(x)]$. The flowchart of the modelling process is shown in Fig.4.2.5. The typical running time for the program depends on the wavelength step chosen. For example, using an ordinary laptop 2 core @ 1.70 GHz with negligible memory usage, for 500×500 periods it takes 7min with wavelength step 0.2nm.

The very important point to note is that this scheme for determining 2-D PC resonances is computationally extremely fast so that results for even a very fine subdivision of wavelengths and for 2-D structures with very large N ($\sim 10^6$) can be generated in tens of minutes in a simple desktop computer. Hence a very detailed search of possible 2-D resonances becomes readily possible. Note, interestingly that there can be regions of wavelengths for which 2-D resonances do not occur even though many corresponding x -directed modes $[f_m(x), \beta_m]$ exist; this region of wavelengths correspond to stop-bands in periodic structures.

4.3 Results and discussions

The mode index analysis (MIA) modelling method described above is applied to obtain numerical results for 2-D PC structures, Fig.4.2.1, with $L_a = L_b = L$, $w_a = w_b = w$ and $N_x = N_z = N$ chosen for convenient comparison with results presented by other researchers (e.g., [26], [27]) and in the experimental work carried out in this project. In this model, as emphasised in previous section, the effect of vertical dimension is already considered and converted into 2-D effective index distribution and hence the main objective is to obtained 2-D x - z resonance.

Fig.4.3.1 shows the (final) TE_y resonances of a finite 2-D periodic structure with $N = 250$, $\eta_a = 3.13$, $\eta_b = 3.46$, $L = 286.25nm$, $w = 116.5nm$ within the wavelength range, $0.8\mu m < \lambda_0 < 1.2\mu m$; these values are chosen correspond to those used in [26] and also the fabricated devices discussed in next chapter.

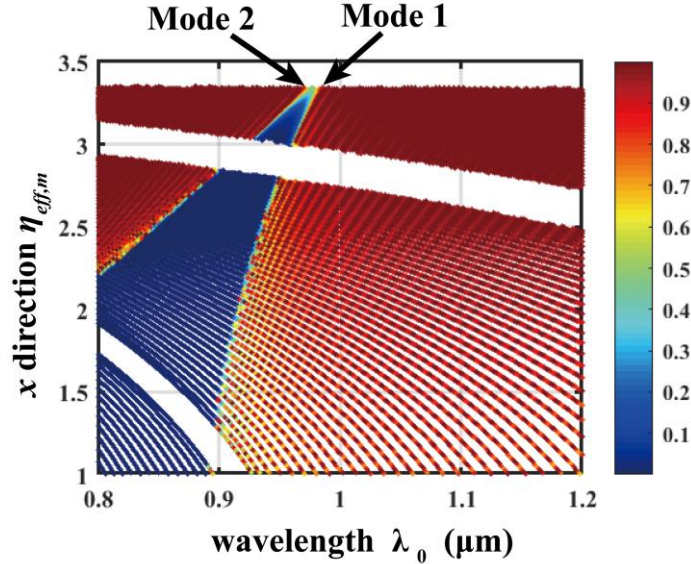


Fig.4.3.1 2-D resonances of PC calculated using MIA. (Band edge resonances: Mode 1 and Mode 2)

For each λ_0 the modes $f_m(x)$ for the periodic waveguide structure, Fig.4.2.2, are obtained and the corresponding $\eta_{eff,m}$ are represented along one axis in Fig.4.3.1. Of these, the ones that also show unity transmission along z , Fig.4.2.4, are shown as red dots in Fig.4.3.1 and correspond to the sought resonances of the 2D PC, Fig.4.2.1. Note that such results shown in Fig.4.3.1 is merely an attempt to graphically represent the numerical search for the resonances (unity transmission) along the z -axis of the multilayer structure, Fig.4.2.4; those points thus correspond to the MIA generated resonances of the 2D-PC (since the ‘ x -directed resonances’ are already ‘built-in’ by using the $\eta_{eff,m}$ corresponding to the m ’th eigen-mode). Thus, each z -direction transmission maximum point in Fig.4.3.1 corresponds to one excitation angle at which the propagation of excitation wave is allowed (allowed states).

When $N \sim 10^6$ is used, (i.e. ,representing $N \rightarrow \infty$), with the MIA method the wavelengths corresponding to the two points marked Mode 1 and Mode 2 in Fig.4.3.1 match very closely with the wavelengths corresponding to the band edge Mode 1 and Mode 2 in Fig.4.3.2 which were computed using the PWE method for a 2-D PC structure with dimensions and refractive indices identical to that used to obtain the results in

Fig.4.3.1. This demonstrates that the MIA method presented above yields reliable results. Lasing mode can be identified by introducing material gain as imaginary part of refractive index and searching for transmittance. Such technique has been discussed in chapter 2.

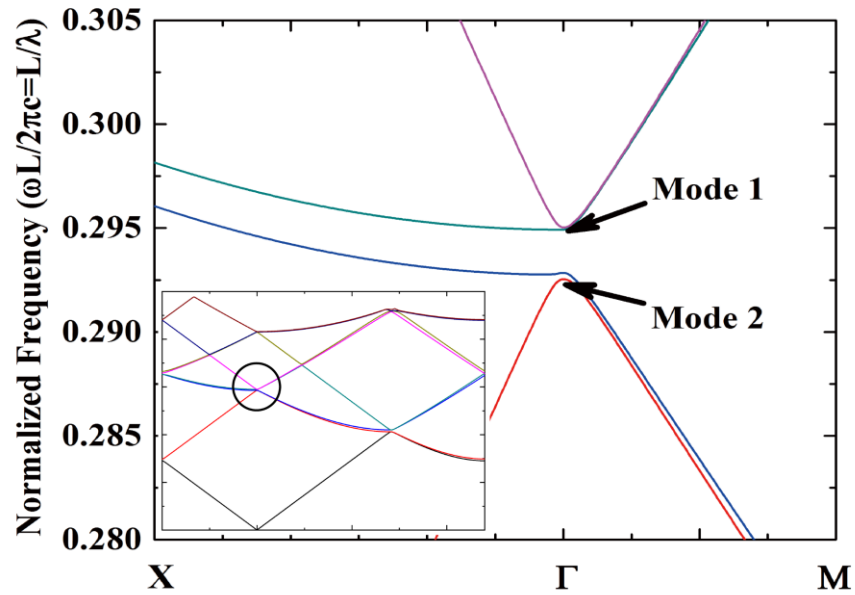


Fig.4.3.2 Photonic band structure around Γ point calculated using PWE. (Band edge resonances: Mode 1 and Mode 2). Inset figure shows the full band calculated using PWE.

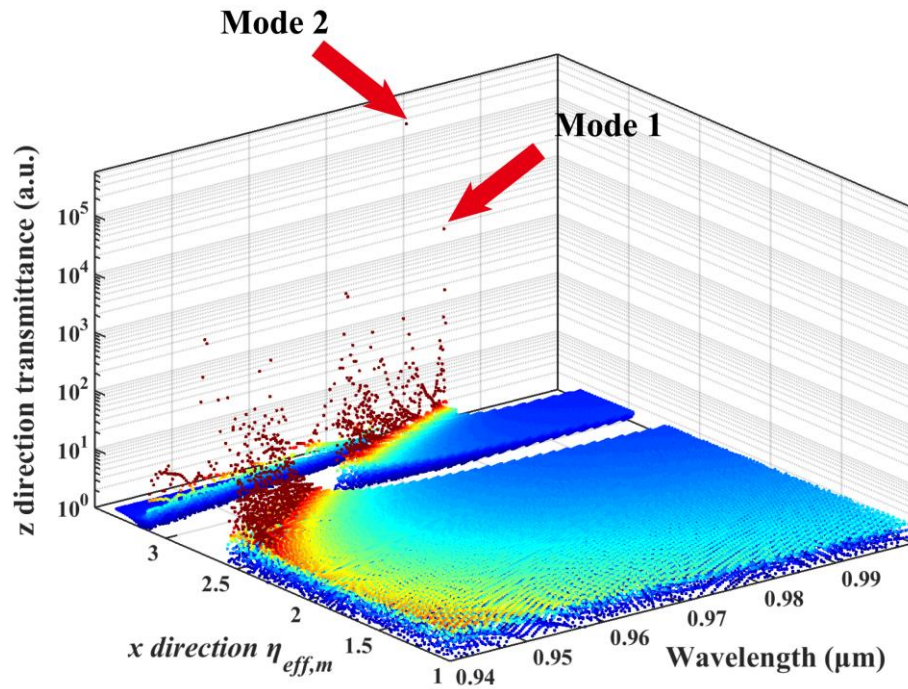


Fig.4.3.3 band edge resonance identified using active media

Further evidence of the validity of this new MIA method is seen from Fig.4.3.4 which shows the variation of the band edge resonance of TE_y polarization with the change in the filling-factor, w^2/L^2 [11]. Again, $N \sim 10^6$ has been chosen in the MIA for compatible comparisons with the PWE results. The red dots and blue triangles are two band edge modes calculated using PWE, the black circles and green triangles are the corresponding modes calculated using MIA. It can be seen that the results from the two methods match extremely well over a very large range of filling-factors. This provides further proof that the MIA method yields very reliable results. Note that the main objective here is to identify the band edge resonance rather than comparing conventional dispersion curve (band structure) with the model directly since they are two different representations. As discussed in previous chapter, 1-D dispersion curve (band structure) represents the relationship of frequency ω (wavelength) vs. Bloch wavevector β_B . In 2-D photonic crystal, the Bloch wavevector is in 2 directions, $\beta_{B,x}$ and $\beta_{B,z}$ with period L_x and L_z . Thus, Γ point is defined as $\beta_{B,x}L_x = \beta_{B,z}L_z = 0$, M point is defined as $\beta_{B,x}L_x = \beta_{B,z}L_z = \pi$, and X point means $\beta_{B,x}L_x = 0$; $\beta_{B,z}L_z = \pi$. Considering the square lattice, all other possibilities are effectively included. So Γ -X or Γ -M simply represents different $\beta_{B,x}$ and $\beta_{B,z}$ value in the band diagram obtained using PWE.

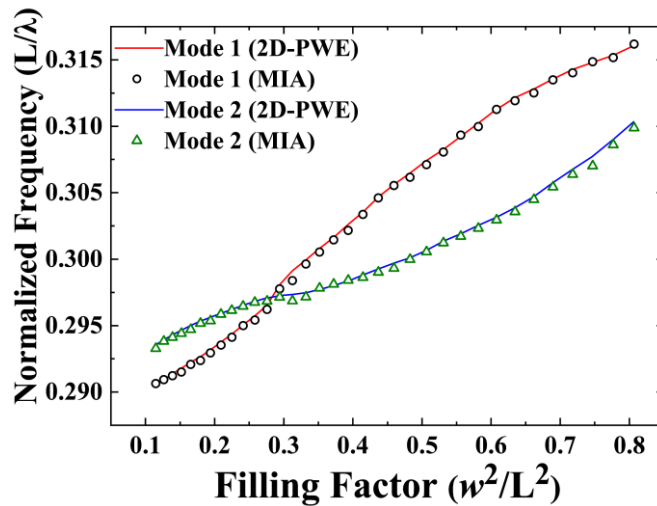


Fig.4.3.4 Band edge resonances calculated with varying filling factor. w^2/L^2

However, in MIA the 2-D resonances are represented using effective index along one direction with its relevant wavelength. In other word, conventional band structure expands the Floquet-Bloch function into PW with different angles (effectively), and

hence the Γ -X or Γ -M direction. While our model effectively expands the 2-D resonance into waveguide modes, and hence the effective indices.

Further evidence regarding the validity of MIA method is shown in Fig.4.3.5 which shows the band edge resonance variation with the change of the refractive index difference. The black and red lines are calculated using PWE method, the green and blue triangles are calculated using MIA. It is shown that the results match well over a certain range of index difference.

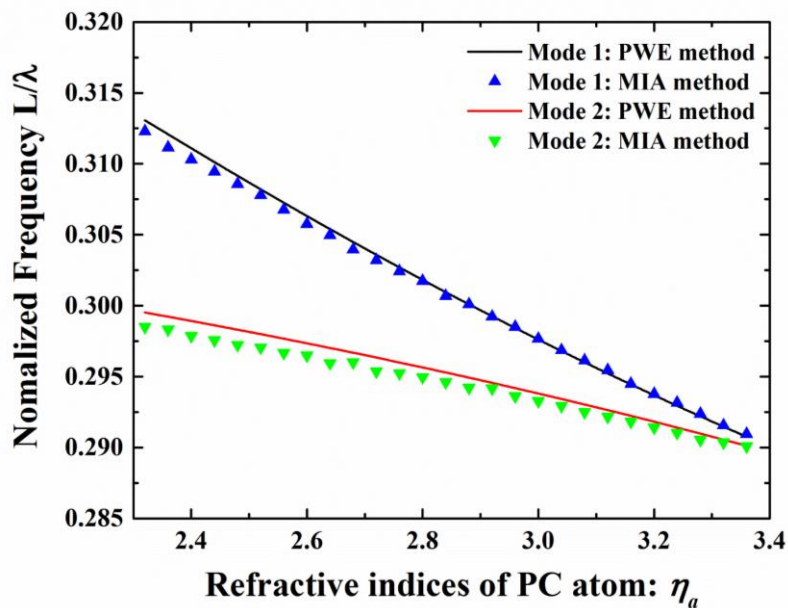


Fig. 4.3.5 Band edge resonances calculated with varying η_a

The finite size effect on the 2-D resonance of PCs has also been observed by this model. Shown in Fig.4.3.6, are the results for Mode 1 and Mode 2 (refer Fig.4.3.1 and Fig. 4.3.2) but now with a smaller N range of $20 \rightarrow 1000$. The dots and triangles are results from MIA while the dashed lines are results using the PWE method. Note that for $N < 150$ the MIA results deviate from the PWE since the latter method is valid for $N \rightarrow \infty$. This illustrates the wide range of applicability of the MIA method and so it can be used, e.g., to better identify the lasing wavelength in PCSELS when N is small.

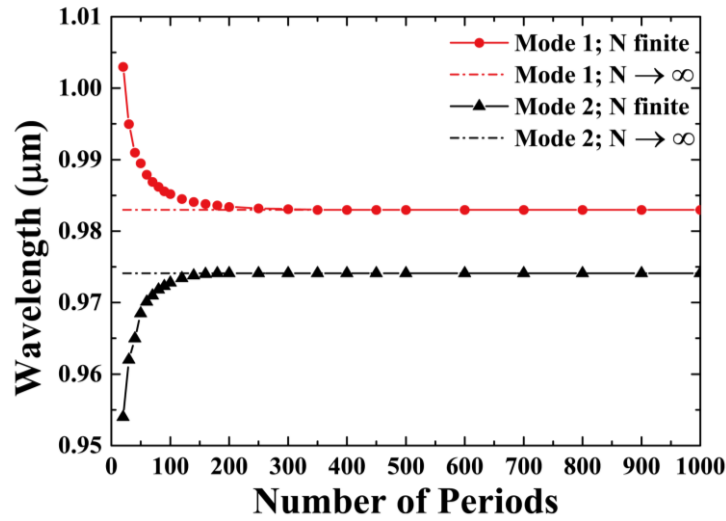


Fig.4.3.6 Finite size effect on band edge resonance.

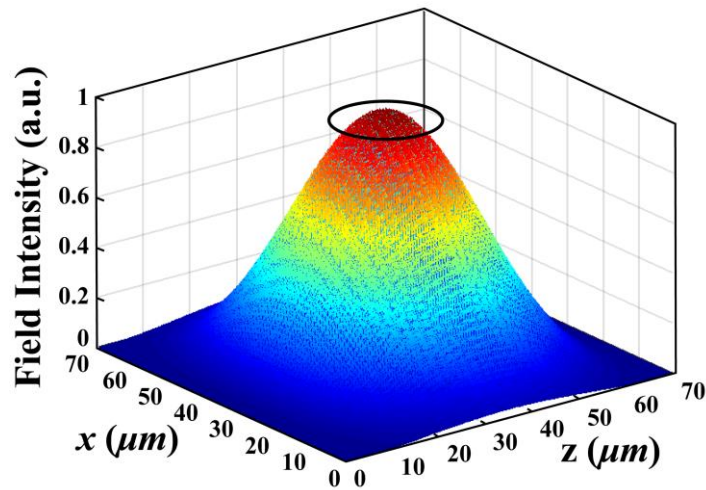


Fig.4.3.7 Plot of field distribution $|\hat{F}(x, z)|$ for band-edge mode. $N_x = N_z = 250$

Fig.4.3.7 is a MIA generated plot of $|\hat{F}(x, z)|$ for the band-edge mode of a 2-D PC structure. The size of the PC region used in modelling is $70\mu\text{m} \times 70\mu\text{m}$ with $L = 286.25\text{nm}$, $w = 116.5\text{nm}$. This single lobed field distribution corresponding to the lasing mode matches well with that obtained by CMT[27]. A detail of the plot of $|\hat{F}(x, z)|$ at the centre of the lobe (illustrated as black circle in Fig.4.3.7) using MIA is shown in Fig.4.3.8a and using PWE in Fig.4.3.8b. It is seen that the plots match very favourably.

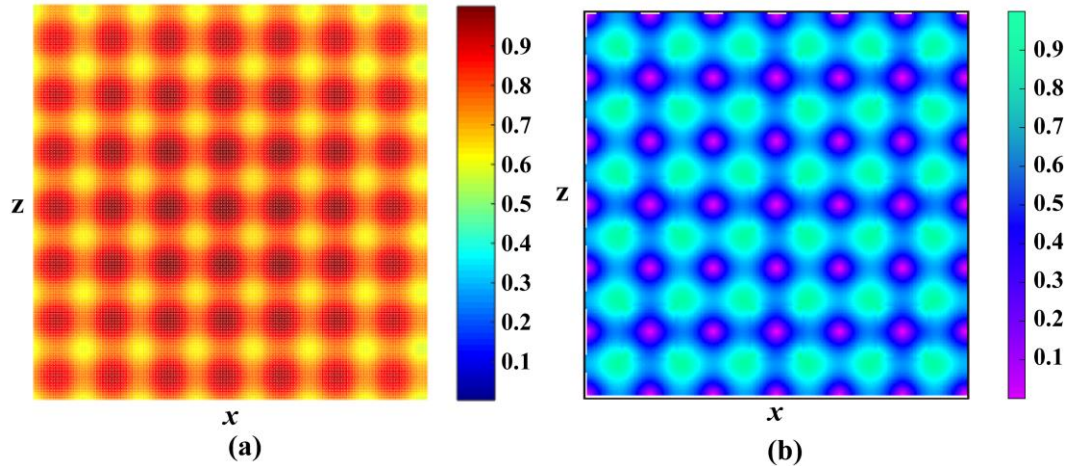


Fig.4.3.8 a) A detail of the plot of $|\hat{F}(x, z)|$ at the centre of the lobe using MIA. b) A detail plot of $|\hat{F}(x, z)|$ using PWE by assuming infinite number of periods ($N \rightarrow \infty$).

4.4 Perturbation theory representation of MIA

As mentioned previously in section 4.2 that the essential underlying concept of MIA is based on viewing the 2D-PC structure of Fig.4.2.1 as a laterally (say, along x) multilayer waveguide which is longitudinally (along z) segmented, i.e. multilayer waveguides with longitudinal discontinuities. However, in general, waveguide discontinuity problem is a rather complicated since all modes (bound modes, continuum modes) are excited even with single mode excitation. In this section, with mathematic laxity, an attempt of using another representation based on perturbation theory is presented for easier understanding the modelling process.

Suppose a 2-D dielectric permittivity variation $\varepsilon(x, z)$ can be written as the form of $\varepsilon(x, z) = \varepsilon(x) + \Delta\varepsilon(x, z)$. Note that in general, $\Delta\varepsilon(x, z)$ is not separable. First considering $\varepsilon(x)$, in this case referring to Fig.4.2.2, a multilayer periodic waveguide coupled in x direction while guide the wave along z direction. The process continuous by next considering waveguide discontinuity along z direction and given by $\Delta\varepsilon(x, z)$. The excitation is such that any non-zero field component $\hat{F}(x, z)$ satisfy $\partial/\partial y \approx 0$.

The wave equation of un-perturbed waveguide is thus given by:

$$\left[\frac{\partial^2}{\partial x^2} + \frac{\partial^2}{\partial z^2} + k_0^2 \varepsilon(x) \right] F(x, z) = 0 \quad (4.7)$$

and the eigen mode of such waveguide is:

$$F(x, z) = \sum_m f_m(x) e^{-j\beta_m z} \quad (4.8)$$

where β_m represents mode constants and can be calculated according to section 4.2. Next, for the perturbed waveguide, from the perturbation theory, the wave equation can be written as:

$$\left[\frac{\partial^2}{\partial x^2} + \frac{\partial^2}{\partial z^2} + k_0^2 \varepsilon(x, z) \right] F(x, z) = 0 \quad (4.9)$$

Suppose, $F(x, z)$ can be written into a form based on unperturbed solution $F(x, z)$, i.e.

$$F(x, z) = \sum_n A_n(z) f_n(x) e^{-j\beta_n z} \quad (4.10)$$

Here, $f_n(x)$ represents the unperturbed waveguide solution.

From the above equations and apply slow varying envelop approximation, it yields:

$$-2j \sum_n \frac{\partial}{\partial z} A_n(z) f_n(x) e^{-j\beta_n z} = -k_0^2 \sum_m \Delta \varepsilon(x, z) A_m(z) f_m(x) e^{-j\beta_m z} \quad (4.11)$$

Equation (4.11) means that in this waveguide discontinuity problem, at each corrugation, mode number n coupled into mode number m . As illustrated in Fig.4.4.1, in principle, waveguide discontinuity generates infinite number of modes (both bound mode and continuum to form a complete set). However, in MIA, such multimode generation is approximated by single (self-mode) conditions so that a simple modal index (mode impedance) analysis at discontinuities is used (as discussed in section 4.2).

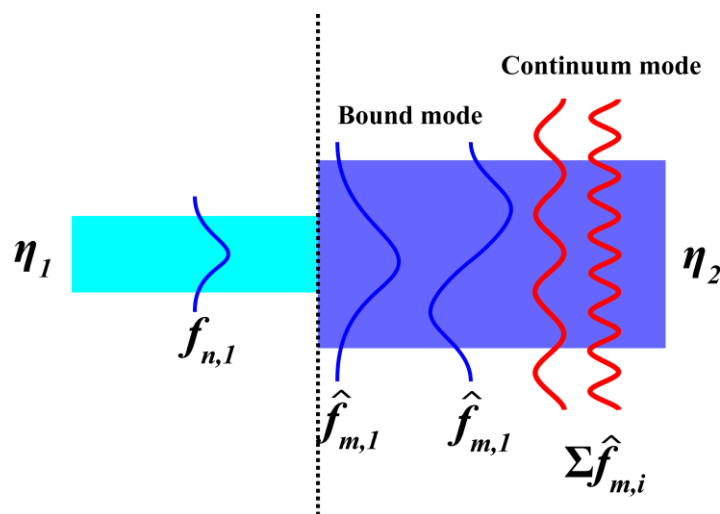


Fig.4.4.1 Schematic of waveguide discontinuity. In principle, all modes including bound mode and continuum modes exist

4.5 Near field to far field transformation: diffraction

Diffraction is a very important feature of wave propagation. The idea is that for a beam with finite transverse dimension, it can be described as a superposition of plan waves. The general diffraction analysis is one of the most complicated theory in optics. In this section, we limit ourselves to the far-field limit of Fresnel diffraction (Fraunhofer diffraction). It is then shown that the near-field to far-field transformation is merely a Fourier transform.

Considering in x - z plane, two homogeneous media with refractive indices η_a and η_b respectively and with abrupt interface at $z = 0$ (referring to Fig. 4.5.1). The excitation is such that $\partial_y \equiv 0$, i.e. uniform along y -axis. Any field components $F(x, y, z) = F(x, z)$ is satisfied giving the wave equation:

$$\left[\frac{\partial^2}{\partial x^2} + \frac{\partial^2}{\partial z^2} + k_0^2 \eta_q^2 \right] F_q(x, z) = 0 \quad (q = a, b) \quad (4.12)$$

and the solution of the equation (4.12) is of the form:

$$F_q(x, z) = A e^{-j(\kappa_q x + \beta_q z)} \quad (q = a, b) \quad (4.13)$$

where $k_0^2 \eta_q^2 = \kappa_q^2 + \beta_q^2$, i.e. $\beta_q = \beta_q(\kappa_q) = \sqrt{k_0^2 \eta_q^2 - \kappa_q^2}$.

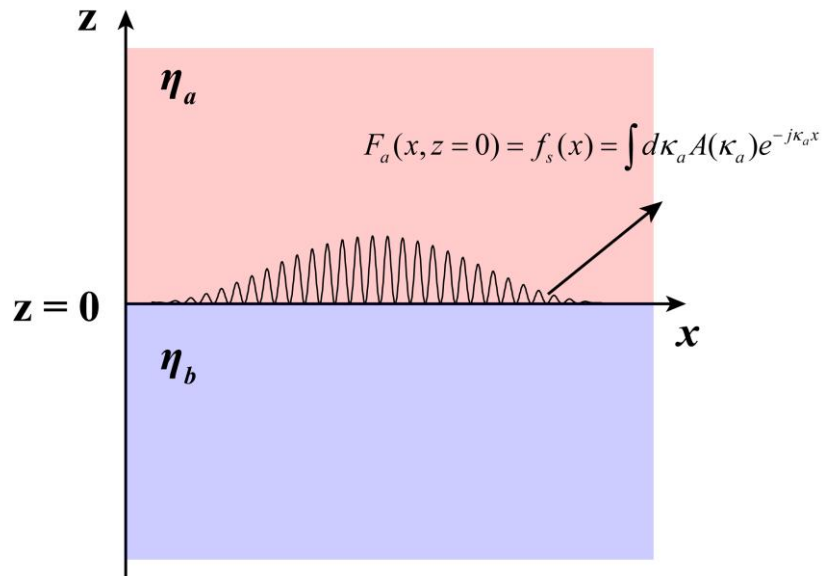


Fig.4.5.1 interface of two media in x - z plane.

The beam in region ‘a’ can be expressed as a superposition of plane wave of different amplitude (with particular transverse component κ_a). Henceforth we shall define the beam in region ‘a’ as

$$F_a(x, z) = \sum_{\kappa_a} A(\kappa_a) e^{-j(\kappa_a x + \beta_a z)} \quad (4.14)$$

or more general

$$F_a(x, z) = \int d\kappa_a A(\kappa_a) e^{-j(\kappa_a x + \beta_a z)} \quad (4.15)$$

Thus, at $z=0$, equation (4.15) reduce to

$$F_a(x, z=0) = f_s(x) = \int d\kappa_a A(\kappa_a) e^{-j\kappa_a x} \quad (4.16)$$

It is then recognized as a Fourier transform:

$$A(\kappa_a) = \frac{1}{2\pi} \int dx f(x) e^{j\kappa_a x} \quad (4.17)$$

Therefore, for a given ‘source field’ $f_s(x)$, one can obtain the amplitude distribution by Fourier transform. Such amplitude distribution, also known as angular plane wave spectrum (plane wave at different angle and different amplitude), can be used to decide the beam divergency and far-field beam pattern.

The simple diffraction analysis is then used in our model to obtain the far-field pattern and beam divergence. The source field is defined as $\hat{F}(x, z)$ which is readily obtained using MIA. Following the concept of near-field to far-field transformation mentioned previously, a 2-D Fourier transform is performed to obtain the final field distribution. Note that such analysis is very approximate since rather than a diffraction analysis, we treat the problem as an emission problem. The vertical dimension is not considered at the first stage, instead, 2-D field distribution (defined near-field) is obtained using MIA and an emission analysis is carried out to obtain far-field distribution.

As illustrated in Fig. 4.5.2, the modelling result of far-field pattern of such device is shown, such result matches favourably with the results obtained using other techniques [28]. The beam divergence is less than 1° . (Device parameters refer to section 4.3)

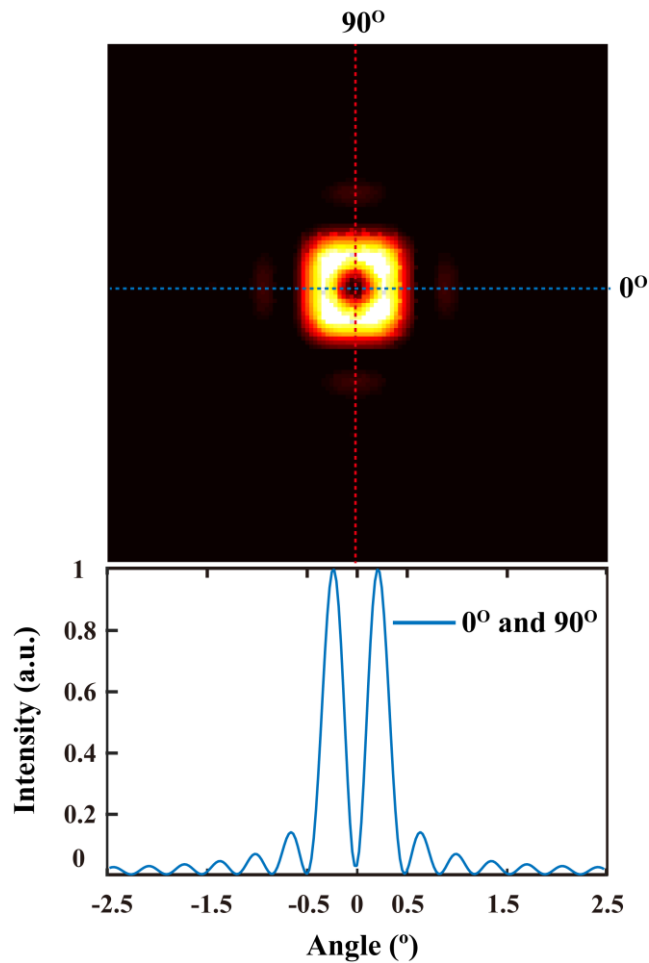


Fig.4.5.2 Modelling result of Far-field pattern of PCSEL

4.6 Further modification and self-consistency of model

As mentioned in the section 4.2, the MIA method is based on viewing the 2D-PC structure of Fig.4.2.2 as a laterally (say, along x) multilayer waveguide which is longitudinally (along z) segmented. Hence the 2D field distributions are evaluated as modes propagating in multilayer waveguides with longitudinal discontinuities. The process is first considering modes supported in the structure shown in Fig.4.2.2 propagate along the z -axis are computed by taking resonance tunnelling solution for a relevant range of wavelengths. The mode index is then used to construct finally the corresponding multilayer structure along the z -axis, Fig. 4.2.4. The second stage of the MIA method accounts for the longitudinal (multiple, periodic in this case) discontinuities in this multilayer waveguide: by considering it as a (single) mode effective-index (impedance) abruptly terminating on the homogeneous medium having refractive index n_b .

In general, as mentioned previously, waveguide discontinuities excite all the modes of the structure. But in the present context of dimensions and magnitude of discontinuities it is justified to assume that multimode generation at discontinuities [29] is approximated by single (self-mode) conditions so that a simple modal index (mode impedance) analysis at discontinuities is used.

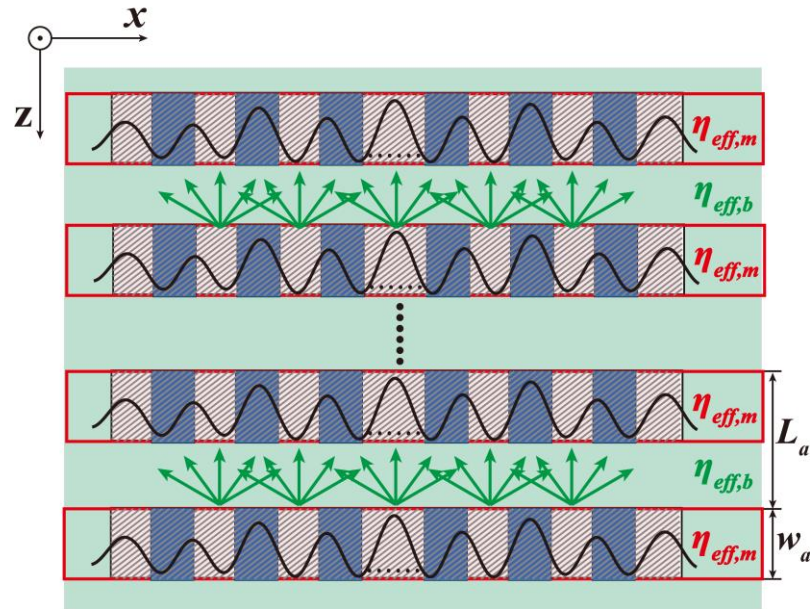


Fig.4.6.1 Model description with consideration of in-plane diffraction

However, importantly to notice that the (single) eigen-mode, $f_m(x)$, e.g. given in Fig.4.2.3b will spread in the homogeneous η_b region of the discontinuity. Hence a further modification of MIA is achieved including mode spreading. As illustrated in Fig.4.6.1, consideration of diffraction of modes in to the homogenous region η_b at the discontinuities provides a modified (effective) index for the homogenous regions. Thus, the refractive indices in segmented regions (as shown in Fig.4.6.1 with green arrows) are further modified accordingly into using in-plane diffraction.

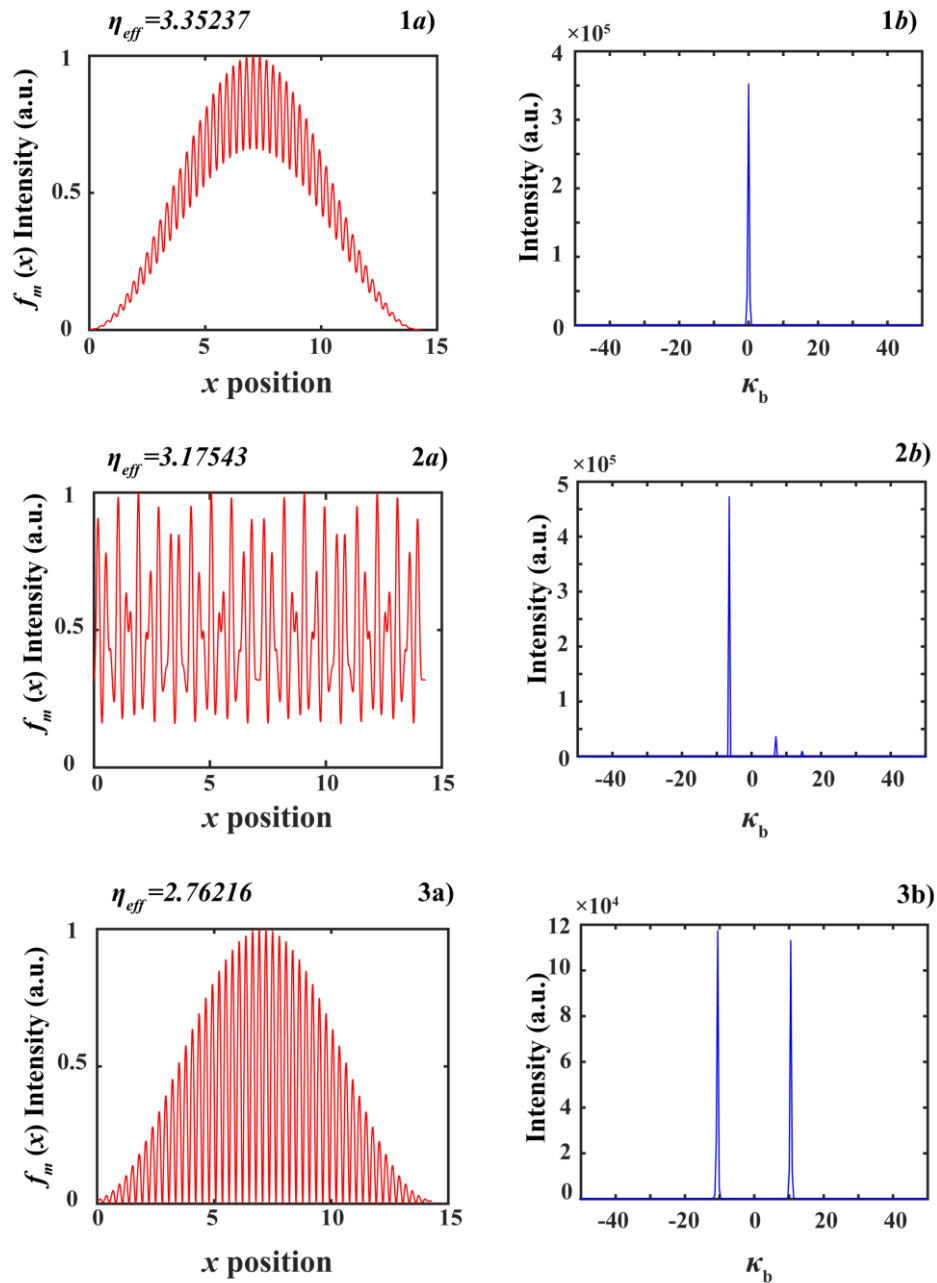


Fig.4.6.2 Examples of Eigen-mode profile and in-plane diffraction spectrum of transverse wavevector dependency.

Simple diffraction analysis is introduced in section 4.5 and same technique is used to analyse the eigen-mode solution $f_m(x)$ behaviour in the homogenous region. An example is given considering three types of modes (referring to Fig.4.2.3b) is shown in Fig. 4.6.2. As mentioned previously, the eigen-mode solution $f_m(x)$ can be described as a superposition of plane wave. Thus, in the homogeneous η_b region, $f_m(x)$ will propagate as different plane waves at different angle (or effectively, transverse wavevector κ_b). The detailed and rigorous treatment of such effective media can be complicated. Hence the

approximation is such that only the ‘dominant’ plane wave component will be considered to modified the homogeneous media further.

As illustrates in Fig.4.6.2. eigen-mode with conventional waveguide type of solution has a dominant transverse wavevector zero. i.e. such eigenmode will propagates almost perpendicularly without spreading in η_b region. Hence for such mode, the refractive index remains unchanged. That is also the reason why MIA works even at very approximate condition when analysing PCSEL, since for PCSEL, the lasing mode is given by the ‘fundamental mode’ of the coupled waveguide, i.e. type 1 $f_m(x)$ solution in Fig.4.6.2. This is also justified by the numerical results.

However, as the order of mode become higher, the spreading phenomenon become significant and the η_b region can no longer be simply treated as it was. Here, the new effective refractive index is modified into $\eta_{eff,b}$ accordingly based on the dominant plane wave component, $k_0^2 \eta_b^2 = k_0^2 \eta_{eff,b}^2 + \kappa_b^2$. The effective of such modification is not significant in PCSEL modelling as mentioned previously, however, it further proves the validity and consistency of the model as shown in the following discussion.

In principle, the solution to any physical situation does not depends on the solving technique. In other word, the result is independent of the chosen coordinate, mathematical technique used, or unit chosen, etc. as long as the physical condition is the same, it will return to the same results. In MIA, the structure in x - z plane is solved from x direction and then z -direction discontinuity. Although the square lattice is chosen in the analysis and x - z direction has identical profile, the consistency requirement of the physical condition requires the frequency of the highest order allowed mode in x -direction is the same as the lowest order allowed mode.

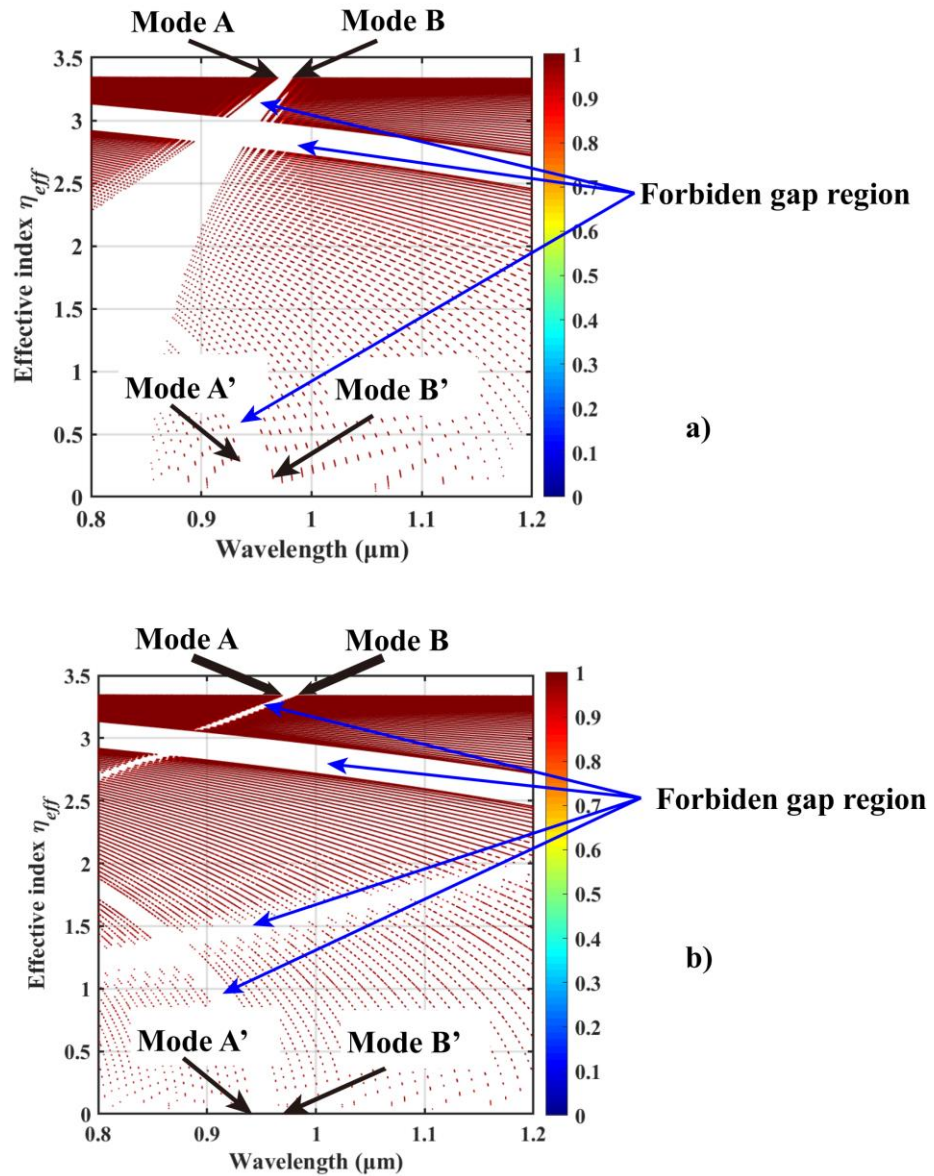


Fig.4.6.3 2-D resonance solutions solved using MIA a) without in-plane diffraction, and b) with in-plane diffraction

Fig.4.6.3 represents 2-D resonance results solved including and excluding in-plane diffraction. The structure which is still square photonic crystal with square lattice refers to as analysed in section 4.2 and section 4.3. The lowest order allowed mode at the band edge in x -direction is defined as mode A and mode B respectively and the highest order allowed mode at the band edge in x -direction is mode A' and B' (as illustrated in Fig.4.6.3). The consistency requirements suggest that if the model works perfectly, A and A' (B and B') should have same resonance wavelength.

It is shown that with the in-plane diffraction considered, such result maintains better (the resonance wavelength of mode A' and B' calculated including in-plane diffraction converges to mode A and B better than the ones excluding in-plane diffraction) compared

to the original method. Note that a difference still appears as expected due to the approximation nature of MIA.

Moreover, since the structure is symmetric and the mode index is effectively sought over an entire angle of excitation ($0^\circ \sim 90^\circ$). The results obtained should also show symmetric pattern in the ‘mode index’ (angle of excitation) domain. Although as mentioned, the detailed comparison requires rigorous calculation, such effect can still be clearly seen in Fig. 4.6.3b with four forbidden gap regions lies symmetrically corresponds to the effective index domain. By comparing with Fig.4.6.3a, it further proves that the very basic concept of MIA model is correct and some limitations can be improved using in-plane diffraction or other more rigorous techniques. However, important to notice that the inclusion of the in-plane diffraction results in an increase in the computing time.

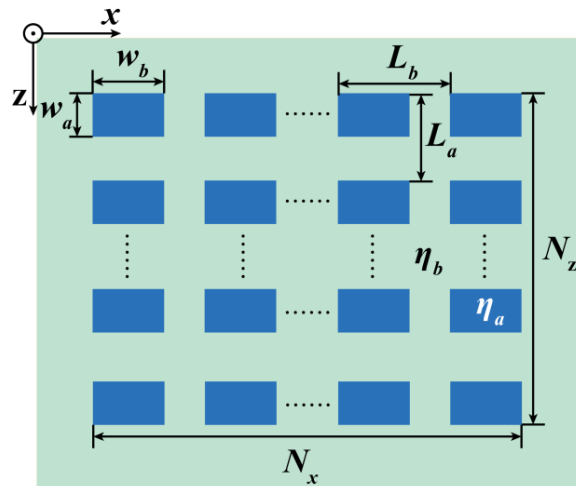


Fig. 4.6.4 Schematic of PC structure. With rectangular atoms and rectangular lattice

Another potential application of MIA is the use for analysing photonic crystal with different number of period along x and z direction and/or the asymmetric shape of photonic crystal. As shown in Fig. 4.6.4, the dimensions and index profile is given as $\eta_a = 3.13$, $\eta_b = 3.46$, $L_a = 227nm$, $L_b = 295nm$, $w_a = 170nm$, $w_b = 224nm$ within the wavelength range $0.8\mu m < \lambda_0 < 1.2\mu m$; these values are purposely chosen arbitrarily to further test the consistency of MIA (rectangular lattice and rectangular atoms). The consistency requirements suggest that for such particular structure, the final resonance should not depend on whether solving x -direction or z -direction first. It is shown that the forbidden gap when solving x -direction first (Fig.4.6.5a) is between 950nm to 980nm while when solving z -direction first the forbidden gap is between 920nm to 960nm

solving from z to x . The difference is 20nm out of 400nm scanning range. With such numerical experiment, it is justified that MIA has a potential to be applied to more complicated photonic crystal structure and still provides satisfactory results.

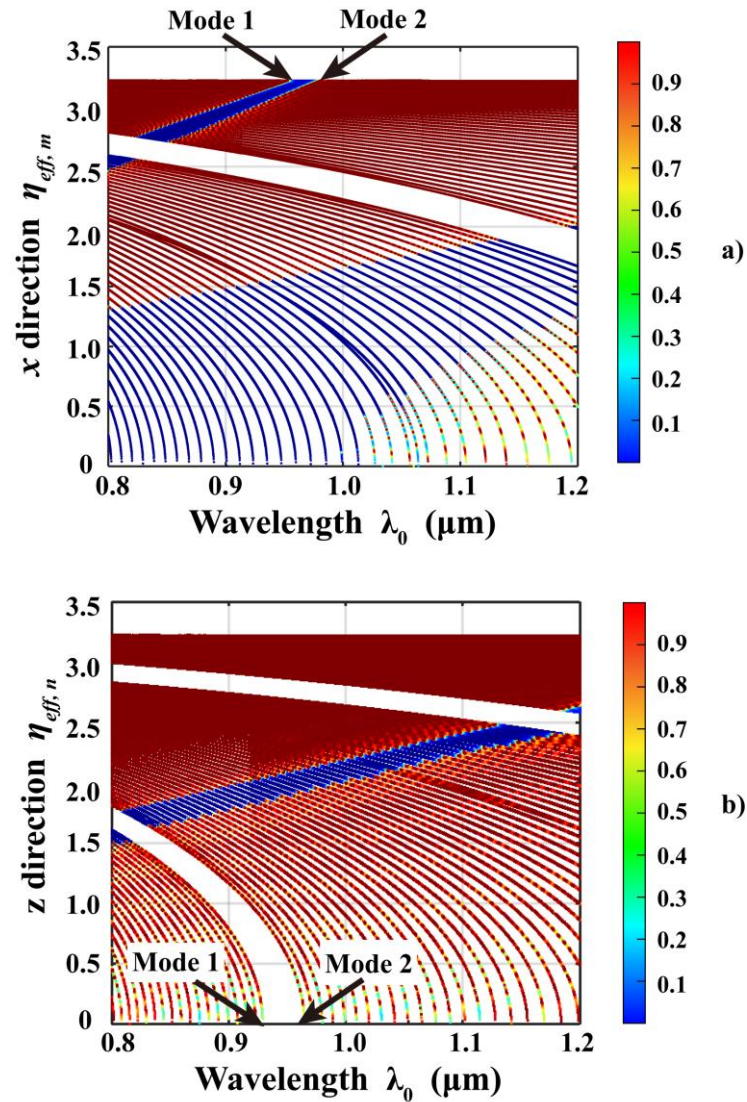


Fig.4.6.5 2-D resonance solution for photonic crystal with rectangular geometry solved by MIA from a) x to z direction, b) z to x direction

4.7 Conclusions

This chapter presents a novel, mode index analysis (MIA) method for solving the modes and resonances of 2-D PCs. The properties of wave propagation in multilayer periodic medium and transverse resonance concepts are utilised to generate a computational process that is quasi-analytic and hence considerably fast. The MIA is easy to implement and is shown here by comparisons with results from other well-established methods to yield very acceptable results for rectangular geometry structures. Several numerical experiments have been carried out to demonstrate the validity of the MIA model. In view of its convenience and speed of operation the MIA method is being developed further to enable more comprehensive modelling of active devices such as PCSEs to include, for example, spatial and temporal variation in optical gain and other PC configurations. The study of including in-plane diffraction further confirm the validity of MIA and the consistency of MIA is proved through several numerical experiments. It is shown in the next chapter that MIA also matches well with the experimental results and provides theoretical explanation and prediction.

4.8 References

- [1] L. Brillouin, *Wave propagation in periodic structures: electric filters and crystal lattices*. Courier Corporation, 2003.
- [2] E. Yablonovitch, "Inhibited spontaneous emission in solid-state physics and electronics," *Physical review letters*, vol. 58, no. 20, p. 2059, 1987.
- [3] P. Russell, "Photonic crystal fibers," *science*, vol. 299, no. 5605, pp. 358-362, 2003.
- [4] T. A. Birks, J. C. Knight, and P. S. J. Russell, "Endlessly single-mode photonic crystal fiber," *Optics letters*, vol. 22, no. 13, pp. 961-963, 1997.
- [5] D. Usanov and A. Skripal, "Photonic Crystal Waveguides," in *Emerging Waveguide Technology*: IntechOpen, 2018.
- [6] A. Mekis, J. Chen, I. Kurland, S. Fan, P. R. Villeneuve, and J. Joannopoulos, "High transmission through sharp bends in photonic crystal waveguides," *Physical Review Letters*, vol. 77, no. 18, p. 3787, 1996.
- [7] T. F. Krauss, "Slow light in photonic crystal waveguides," *Journal of Physics D: Applied Physics*, vol. 40, no. 9, p. 2666, 2007.
- [8] M. Meier et al., "Laser action from two-dimensional distributed feedback in photonic crystals," *Applied Physics Letters*, vol. 74, no. 1, pp. 7-9, 1999.
- [9] M. Plihal and A. Maradudin, "Photonic band structure of two-dimensional systems: The triangular lattice," *Physical Review B*, vol. 44, no. 16, p. 8565, 1991.
- [10] I. Vurgaftman and J. R. Meyer, "Design optimization for high-brightness surface-emitting photonic-crystal distributed-feedback lasers," *IEEE Journal of Quantum electronics*, vol. 39, no. 6, pp. 689-700, 2003.
- [11] S. Fan and J. Joannopoulos, "Analysis of guided resonances in photonic crystal slabs," *Physical Review B*, vol. 65, no. 23, p. 235112, 2002.
- [12] K. Leung and Y. Liu, "Photon band structures: The plane-wave method," *Physical Review B*, vol. 41, no. 14, p. 10188, 1990.
- [13] M. Toda, "Proposed cross grating single-mode DFB laser," *IEEE journal of quantum electronics*, vol. 28, no. 7, pp. 1653-1662, 1992.

- [14] K. B. Dossou, L. C. Botten, and C. G. Poulton, "Semi-analytic impedance modeling of three-dimensional photonic and metamaterial structures," *JOSA A*, vol. 30, no. 10, pp. 2034-2047, 2013.
- [15] K. B. Dossou, C. G. Poulton, and L. C. Botten, "Effective impedance modeling of metamaterial structures," *JOSA A*, vol. 33, no. 3, pp. 361-372, 2016.
- [16] H. Han and J. Coleman, "Two-dimensional rectangular lattice distributed feedback lasers: A coupled-mode analysis of TE guided modes," *IEEE journal of quantum electronics*, vol. 31, no. 11, pp. 1947-1954, 1995.
- [17] P. Yeh, A. Yariv, and C.-S. Hong, "Electromagnetic propagation in periodic stratified media. I. General theory," *JOSA*, vol. 67, no. 4, pp. 423-438, 1977.
- [18] D. J. Griffiths and C. A. Steinke, "Waves in locally periodic media," *American Journal of Physics*, vol. 69, no. 2, pp. 137-154, 2001.
- [19] R. E. Collin, "Field theory of guided waves," 1960.
- [20] A. Ghatak, K. Thyagarajan, and M. Shenoy, "Numerical analysis of planar optical waveguides using matrix approach," *Journal of lightwave technology*, vol. 5, no. 5, pp. 660-667, 1987.
- [21] P. Yeh, *Optical waves in layered media*. Wiley-Interscience, 2005.
- [22] C. Elachi, "Waves in active and passive periodic structures: A review," *Proceedings of the IEEE*, vol. 64, no. 12, pp. 1666-1698, 1976.
- [23] P. Pereyra, "Theory of finite periodic systems: the eigenfunctions symmetries," *Annals of Physics*, vol. 378, pp. 264-279, 2017.
- [24] P. Yeh, "Resonant tunneling of electromagnetic radiation in superlattice structures," *JOSA A*, vol. 2, no. 4, pp. 568-571, 1985.
- [25] T. Rozzi, "Rigorous analysis of the step discontinuity in a planar dielectric waveguide," *IEEE Transactions on Microwave Theory and Techniques*, vol. 26, no. 10, pp. 738-746, 1978.
- [26] K. Sakai, E. Miyai, T. Sakaguchi, D. Ohnishi, T. Okano, and S. Noda, "Lasing band-edge identification for a surface-emitting photonic crystal laser," *IEEE Journal on Selected Areas in Communications*, vol. 23, no. 7, pp. 1335-1340, 2005.
- [27] M. Koba and P. Szczepanski, "Coupled mode theory of photonic crystal lasers,"

in Photonic Crystals-Introduction, Applications and Theory: InTech, 2012.

- [28] S. Noda, K. Kitamura, T. Okino, D. Yasuda, and Y. Tanaka, "Photonic-crystal surface-emitting lasers: Review and introduction of modulated-photonic crystals," *IEEE Journal of Selected Topics in Quantum Electronics*, vol. 23, no. 6, pp. 1-7, 2017.
- [29] D. Marcuse, *Light transmission optics*. Van Nostrand Reinhold, 1972.

Chapter 5

Fabrication and Characterization of PCSEL

Semiconductor fabrication is the process that transfer the design layout into device. The process involves multi-steps of photolithography and chemical processing of the semiconductor wafer (substrate). The steps, also known as planar processing, are aimed at fabricating LED, semiconductor laser, detectors on a single substrate and then subsequently separated into individual elements by cleaving. The key point of planar processing is viewing devices as 2-D projection which allows the transfer of the mask layout using series of lithography (to create pattern), oxidation (to create insulator) and metallization (to create conductor). Such processing strategy is also commonly used in industrial mass production.

To achieve the desirable operation characteristics, it is important to optimize the device design as well as the fabrication steps. However, because the range of semiconductor device is so large, it is difficult to introduce all different techniques that are needed. Hence, in this chapter, the main objective is to focus on one particular design (mesa) of all-semiconductor PCSEL device and its fabrication process. Several standard characterisation techniques will also be introduced along with the experimental results. In the later part of the chapter, the effect of PCSEL with external reflector is experimentally studied and modelled using MIA method.

5.1 Semiconductor growth and photonic crystal pattern

Although not part of this PhD project, it is important to know the growth of semiconductor material and the patterning technique of photonic crystal in order to have a completely understanding of semiconductor fabrication technique. In this project, the semiconductor is grown in University of Sheffield and photonic crystal s pattern in University of Glasgow. In this section, two different growth techniques, molecular beam epitaxy (MBE) and metal-organic vapour phase epitaxy (MOVPE), are very briefly introduced. The photonic crystal is patterned using electron beam lithography and regrowth technique.

Broadly speaking, epitaxy refers to the method by which the crystal is grown layer by layer in special order. During the process, substrate wafer acts as “seed crystal” to establish a specific (crystal) growing orientation. The techniques such as MBE and MOVPE are most commonly used in single crystal layers growth.

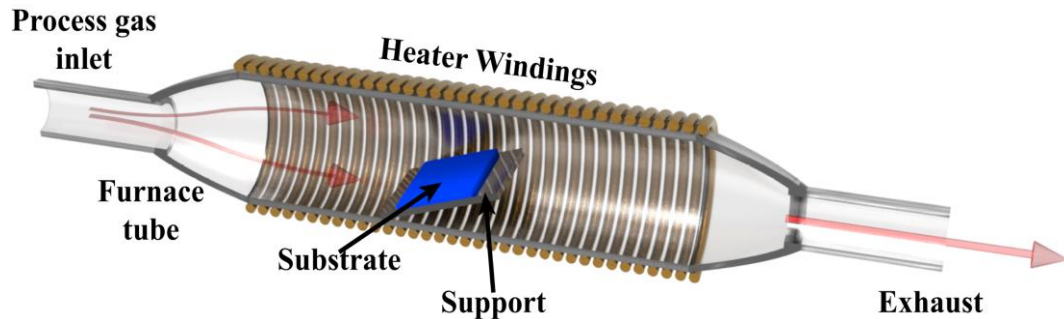


Fig. 5.1.1 Schematic of VPE process

VPE technique has been discovered for more than a century and it has become an accepted production technique for novel electronic or photonic devices [1, 2]. VPE technique uses hot gas mixture precursors (often at atmosphere pressure) to transport molecules to the substrate surface. The precursors (hydrides or chlorides for delivering group V elements and metal alkyls for delivering group III elements) deliver reactants to the growing surface region which is heated in the furnace. The actual layout of the equipment can have different forms but the concept is schematically shown in Fig. 5.1.1. hot gas precursors (metal-organic vapour) are mixed and pass through furnace. Films of composition are gradually formed on the heated substrate surface. The modern MOVPE can achieve very accurate thickness and the epitaxy process can be extremely fast.

Unlike VPE, MBE is another epitaxy process which involves beams of atoms or molecules absorbed by crystal surface under ultrahigh vacuum [3]. Fig. 5.1.2 shows a schematic of the MBE machine. Basically, the process of MBE involves two steps. In the first step, molecules such as atomic Ga and As₂ or As₄ are evaporated or sublimated from solid materials. The solid materials are contained in the heated cell which is known as “Knudsen Cell”. “Knudsen Cell” is a crucible contains solid reactants and its operation is controlled by mechanical shutter whose reaction time is less than 0.3s (less than the time to grow one monolayer). After the sublimation, the molecules are collimated into beams and go directly to the substrate. The reaction chamber is connected to ion pump, closed cycle helium pump and titanium sublimation pump and the reaction takes place in ultrahigh vacuum (usually can be lower than 10⁻⁹ Pa).

The comparison of the advantages of both techniques is difficult, for each has its strengths and weaknesses. MBE, as it is operated under ultrahigh vacuum, is carried out at a very slow growth rate. However, the controllable ultra-high vacuum (UHV) environment enables MBE a special *in-situ* diagnostic technique known as reflection high energy electron diffraction (RHEED) system (as shown in Fig. 5.1.2). On the other hand, (MO) VPE uses gaseous compound to deliver material to the substrate hence a higher growth rate but only optical techniques can be used in diagnose during growth. In this project, the sample is prepared using MOVPE and the photonic crystal is patterned using e-beam lithography and semiconductor regrowth technique.

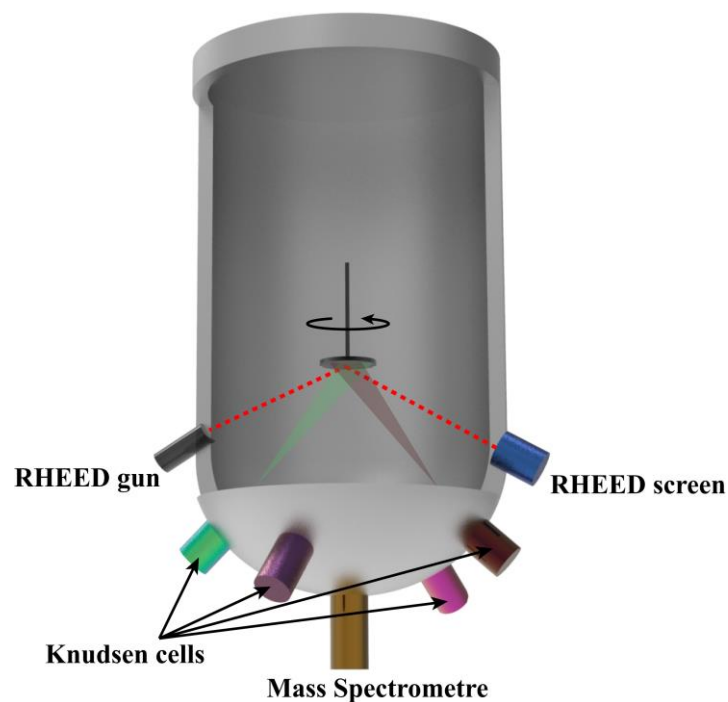


Fig. 5.1.2 Schematic of MBE machine

Devices were grown by MOVPE on GaAs substrates. As shown in Fig.5.1.3, initial growth consists of 1.5 μm n-type $\text{Al}_{0.4}\text{Ga}_{0.6}\text{As}$ lower cladding layer, 3 quantum well active region (8nm $\text{In}_{0.2}\text{Ga}_{0.8}\text{As}$ QWs' separated by 20nm GaAs layers), a 40nm p-type $\text{In}_{0.48}\text{Ga}_{0.52}$ etch stop layer, and a 150 $\text{In}_{0.48}\text{Ga}_{0.52}\text{P}$ layer. (layer forms the PC region in the following steps). Such structure is shown in Fig. 5.1.3 a).

The InGaP layer is patterned using electron beam lithography, where by circular holes are patterned into a SiO_2 hard mask. The pattern is transferred into the InGaP with a $\text{CH}_4/\text{H}_2/\text{O}_2$ reactive ion etch (referring to Fig. 5.1.2 b). The complete PC area consists of

$150\mu\text{m} \times 150\mu\text{m}$ square area where the PC consists of circles with a PC lattice constant of the 295 ± 1.1 nm and the ratio between the diameter of the air holes and the lattice constant is chosen such that a 0.5 filling factor is achieved. The SEM image of the patterned photonic crystal array is shown in Fig. 5.1.4a and Fig. 5.1.4b)

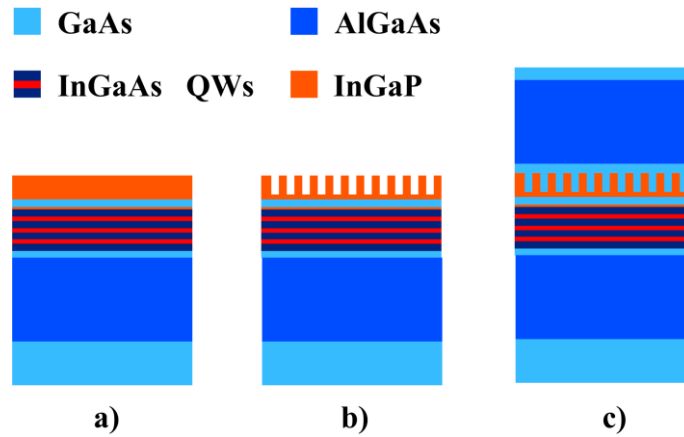


Fig. 5.1.3 Photonic crystal pattern, lithography and regrowth

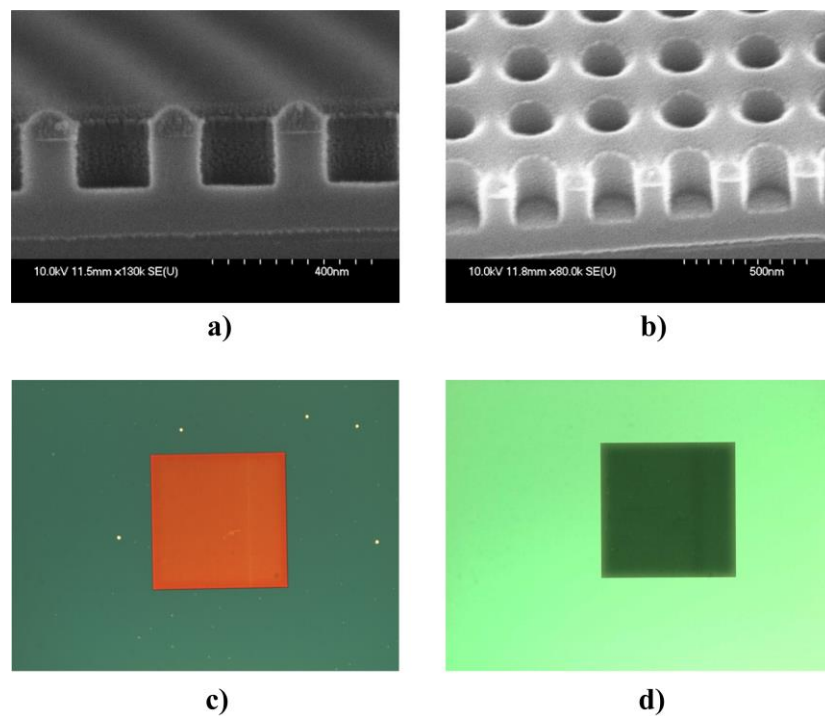


Fig. 5.1.4 a) and b) are SEM image of PC pattern. Nomarski microscope image of PC area before clean c) and after clean d)

After etching, the wafer is cleaned before regrowth. The process of this stage is first cleaning the sample using Soxhlet extractor with acetone for 2 hours before oxidation. Ozone is then used for 10 mins to form an oxidation layer contains contaminations and such layer will finally be removed completely by 1% HF acid strip for 40s. Nomarski

microscopy shows same photonic crystal pattern area before and after cleaning in Fig. 5.1.4c and Fig. 5.1.4d respectively. It is shown in the figure that such clean can effectively remove most of the contaminations and improve the surface morphology.

After the cleaning, the wafer is placed back to the MOVPE reactor chamber. An overgrowth consisting of GaAs (to infill the holes and form the PC), a 1.5 μm p-type $\text{Al}_{0.4}\text{Ga}_{0.6}\text{As}$ upper cladding layer, and finally a 400 nm p+ GaAs capping layer (referring to Fig. 5.1.3c). The growth parameters for this structure have been optimized and published elsewhere [4].

5.2 PCSEL fabrication as mesa diode

PCSEL fabrication is merely a mesa diode which is a very basic semiconductor device structure. The fabrication process begins by first cleaving a quarter out of the original full wafer using a diamond tipped hand-scribe tool. Then, the inspection of the sample under the optical microscope is necessary for checking the visible growth defect and the dirt area. The cleaning process starts by first putting the sample in n-butyl acetate then ultrasonic bath clean for 5 mins. Cotton bud can be used in this step to remove any visible particles on the sample. Then the sample is rinsed in acetone with 5 mins ultrasonic cleaning in acetone bath. The final stage is to rinse the sample with isopropyl alcohol (IPA) and then 5 mins ultrasonic clean in IPA bath. The sample is rinsed with reverse osmosis (R.O.) water before blown dry with a nitrogen gun. The last two steps can be repeated until all visible dirt is removed (checking under microscope).

Once the surface is cleaned, the next step of the fabrication is to create the mesa structure (the process referring to Fig. 5.2.1). Cleaned sample is then placed in 180°C chamber for prebaking. Such step, also known as dehydration baking, is to remove any of the cleaning solvents left on the sample. On top of the sample, a photoresist named S1818 is deposited and spun at 4000 rpm for 30 seconds on the spinner (referring to Fig. 5.2.1a). Such process forms a thin layer of photoresist whose thickness is dependent on the recipe and spinning time, in this case, the thickness is 1.8 μm . It is then followed by using cotton bud dipped with acetone to clean the backside of the sample. Such step is necessary since the backside of the sample is usually contaminated with photoresist and it makes the sample slightly tilted during the photolithography process. After the cleaning, a 120s hotplate baking at 115 °C is performed to stiffen the photoresist on the surface.

During the spinning process, quite often, the photoresist tends to be thicker at the edge of the sample. Hence, a thickness non-uniformity, known as edge bead, will be created across the sample. Such area has to be removed before the UV exposure in the photolithography process. After remove the edge bead, the sample is then placed under the mask aligner for the photolithography process.

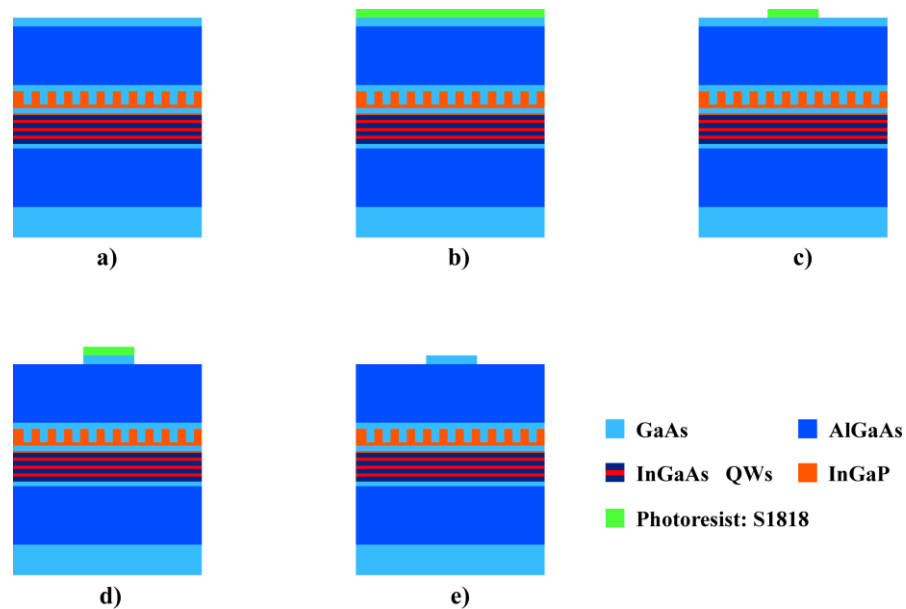


Fig. 5.2.1 mesa etch (shallow) etch process

It is important to note that the sample should be brought as close to the mask as possible ('hard contact on') since when UV light pass through different media (mask and air), the refraction will affect the final pattern. The UV exposure time is set to be 14s in this experiment and the sample is then developed using MIF319 for 80s. The photoresist exposed to UV light will be dissolved in the MIF319 in this process and a microscope check is necessary before mesa etch to ensure the remaining photoresist pattern is sharp and clear (referring to Fig.5.2.1c). It shall be noticed that the exposure time and developing time should be chosen carefully since any undeveloped or overdeveloped sample will have distorted pattern profile.

There are two ways, dry etching or wet etching, to create mesa structure. Method chosen depends on the specific process: dry etching is uniform and can be controlled precisely, while wet etching is relatively fast. In the experiment, the mesa structure is created using Inductively Coupled Plasma dry etching and the etch depth is 400nm to remove heavily doped p-region (p+ region) for better current injection (referring to Fig.5.2.1d). Thickness can be check during process or using surface profilometer

afterwards. After etched into desirable depth, the remaining photoresist is cleaned using acetone ultrasonic bath and IPA. Then, the sample is given a 1 min oxygen plasma ash to remove all remaining photoresist (referring to Fig.5.2.1e).

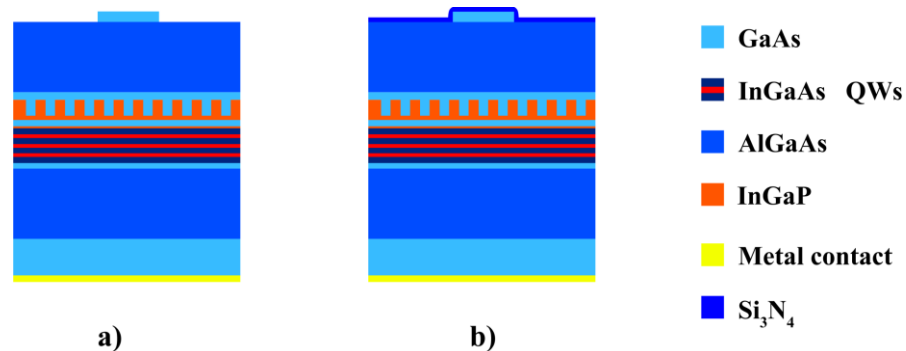


Fig. 5.2.2 n-contact metallization and dielectric deposition.

After the mesa structure, the next stage of fabrication is to deposit the n-contact (back contact). Hence, the back side rather than the top side need to be cleaned very carefully following the cleaning steps mentioned before. There are many recipes for different contact, in this experiment, we use Ni (5nm), Au (90nm), Ge (10nm), Ni (35nm), Au (200nm) for n-contact. Thickness can be controlled precisely using modern metallization machines. The reason for n-contact metallization before other steps is because such step needs annealing and the structure such as dielectric is sensitive to rapid temperature change. The rapid thermal annealing (RTA) at 400°C for 30s is performed after metallization. Such process makes the deposited metal diffuse and forms better Ohmic contact. The device after n-contact metallization is shown in Fig. 5.2.2a).

Next step of fabrication is to deposit dielectric as insulator (referring to Fig. 5.2.2 b). The recipe is chosen such that a 350nm Si_3N_4 is deposited. Note that to ensure better insulation, a minimum thickness of 80nm dielectric should be satisfied. Then same photolithography process is carried out to pattern the etching window for top contact (referring to Fig. 5.2.3a). The sample with developed photoresist is then place in the dry etching chamber. $\text{CHF}_3:\text{O}_2=50\text{sccm} : 5\text{sccm}$ is used to etch the Si_3N_4 for 4'30". Note that in this step, the dielectric must be etched completely. Any remaining dielectric will result in open circuit after the p-contact metallization. After the etching, the remaining photoresist is cleaned using acetone ultrasonic bath and IPA. Then, the sample is given a 1 min oxygen plasma ash to remove all remaining photoresist. (referring to Fig.5.2.3e)

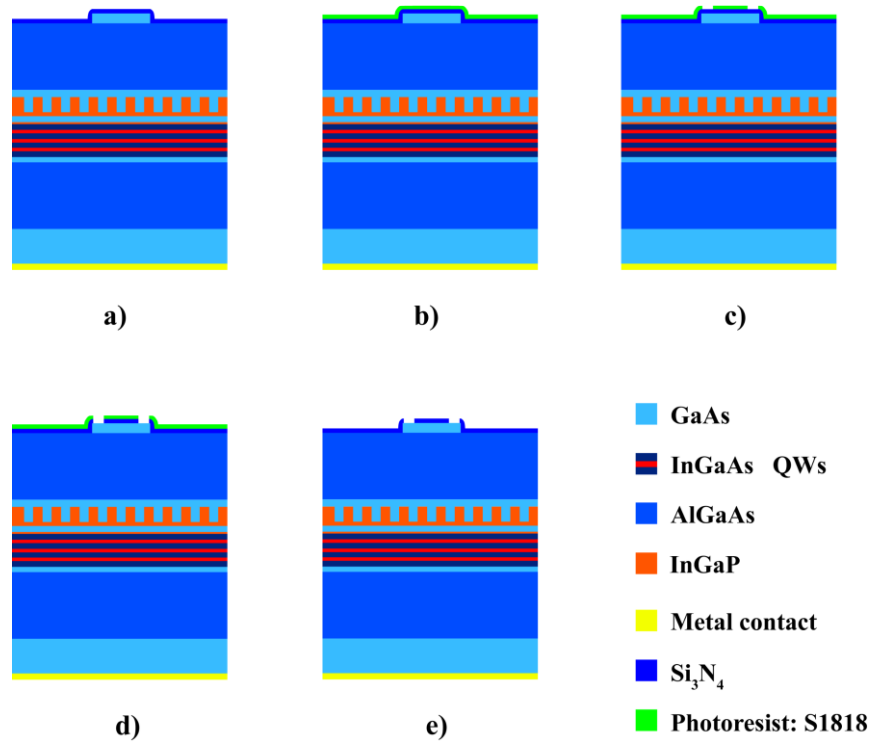


Fig. 5.2.3 dielectric etching to create p-contact window

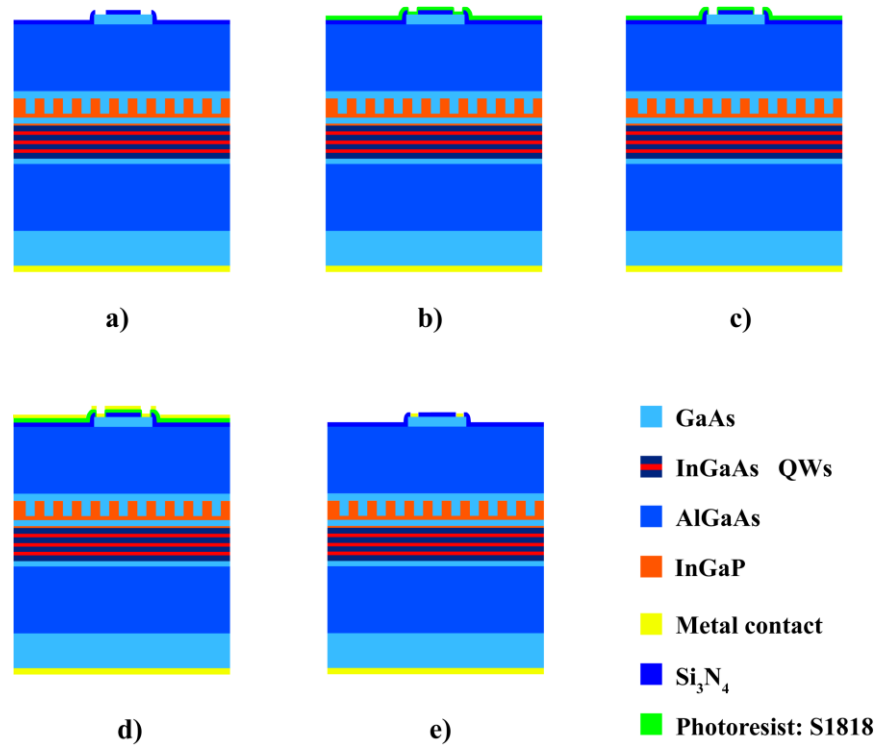


Fig. 5.2.4 p-contact metallization and lift-off.

Top contact, or p-contact is chosen to be Ti (20nm), Pt (10nm) and Au (200nm). In this process, the metal lift-off should be done in 50°C acetone for 5mins and then IPA clean. Note that for this recipe, the RTA is not required. In general, the recipe contains Ti do not require RTA since the annealing process will degrade the performance of the

Ti contained contact according to the previous experience. Finally, a bond-pad using Ti (20nm) and Au (200nm) is deposited for easier probe and bonding. The device sketch with bond pad is shown in Fig 5.2.5. Now the device fabrication is done and ready for characterisation.

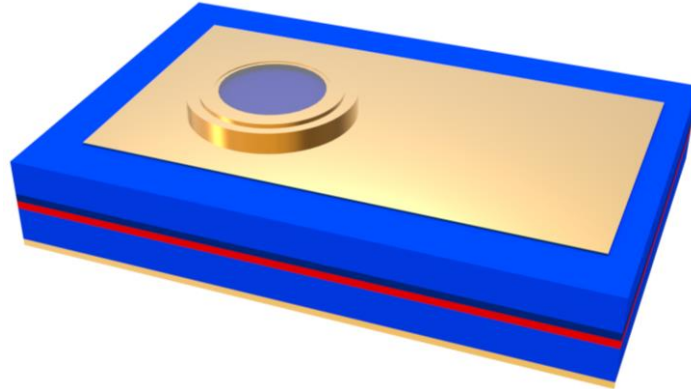


Fig. 5.2.5 Device schematics after fabrication

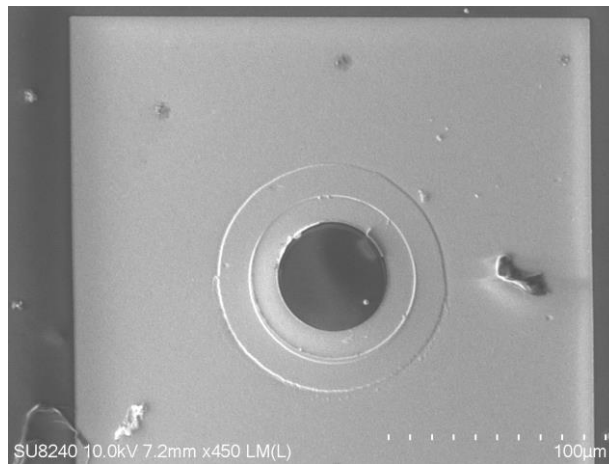


Fig. 5.2.6 SEM image of device

5.3 Lasing characteristic of PCSEL

After the fabrication and thinning, the PCSEL sample is cleaved out of the wafer and bond on a ceramic tail for further characterization. Note that in some other temperature sensitive device application, the wafer should be thinned (usually less than 100µm). However, in this project, the measurement is carried out in room temperature with active cooling system, thermoelectric cooler (TEC), at 25°C. The temperature dependency of the lasing characteristic is not the main objective of this project and has been investigated by previous researchers. The laser is operated under continuum wave (CW) room temperature (referring to Fig. 5.3.1), the device threshold is 112 mA ($J = 1.43 \text{ kA} \cdot \text{cm}^{-2}$).

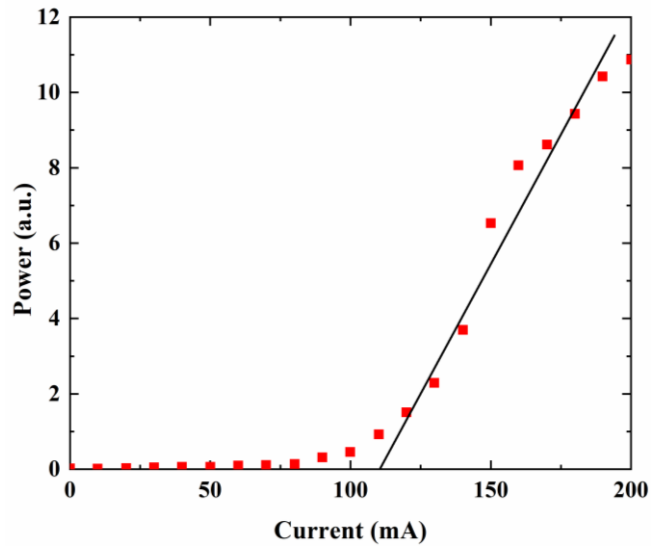
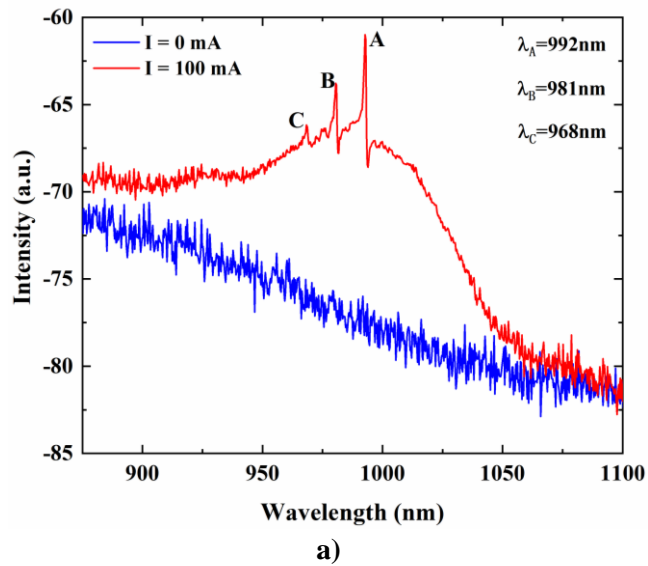
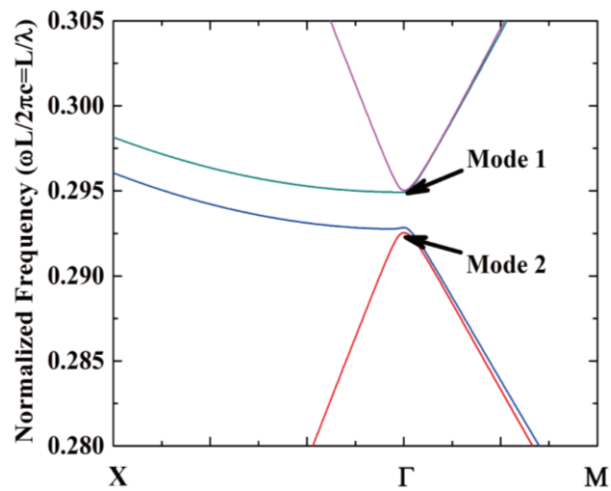


Fig. 5.3.1 LI characteristic of PCSEL at room temperature under CW condition.



a)



b)

Fig. 5.3.2 a) EL spectrum of PCSEL below threshold b) Photonic band structure

At room temperature CW condition, the spectrum first is taken below threshold. It is shown in Fig.5.3.2 that the three peaks (A, B and C) below threshold, corresponds to the three points at Gamma point in photonic band structure shown below as suggested by other study [5]. Such experimental result matches with modelling prediction that just like DFB laser, PCSEL is band edge laser. Fig.5.3.3 illustrates the spectrum of such device above threshold. It is shown that above threshold, one of the three peaks (can depends on the shape of PC, and gain spectrum, in this case is mode C) will finally lase.

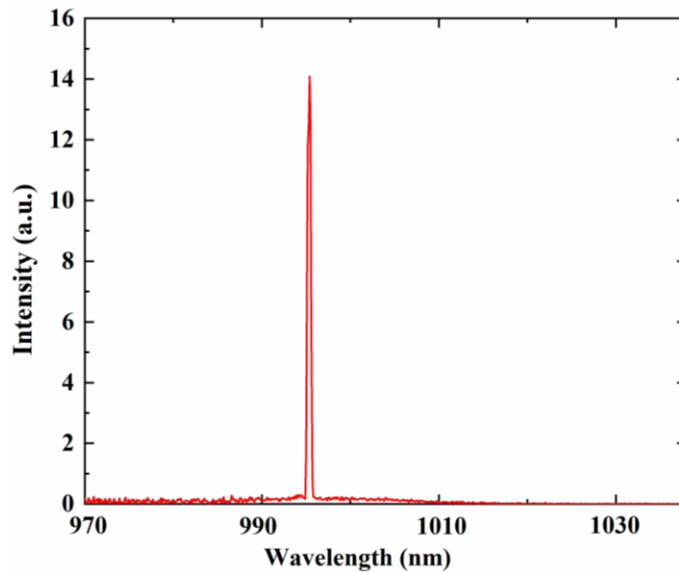


Fig. 5.3.3 EL spectrum of PCSEL above threshold

5.4 Investigation of PCSEL with external reflection

In this section, the PCSEL with external reflection introduced by cleaving along the edge of photonic crystal region has been investigated. Similar fabrication process as mentioned before is done during this experiment. The 3-D schematic of experimental process is illustrated in Fig. 5.4.1. Three categories of experimental were carried out for PCSEL with no external reflection (Fig.5.4.1a), and with single cleave at one edge (Fig.5.4.1b), and with double cleave perpendicularly at the edge (Fig.5.4.1b). The cleaving is done under microscope to ensure the number of periods is not affected during the process.

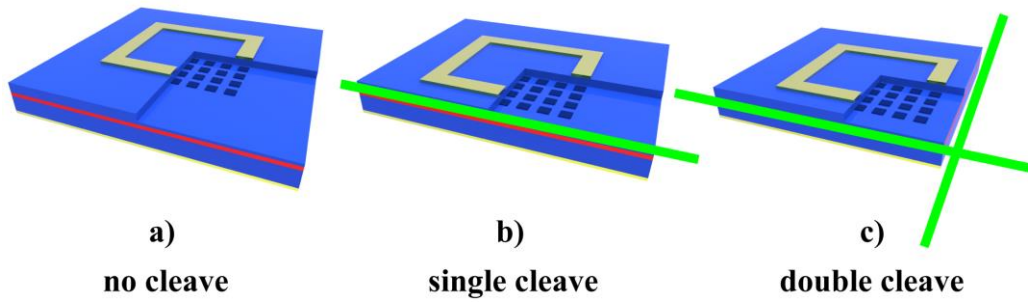


Fig. 5.4.1 Schematic of PCSEL with a) no cleave, b) single cleave and c) double cleave

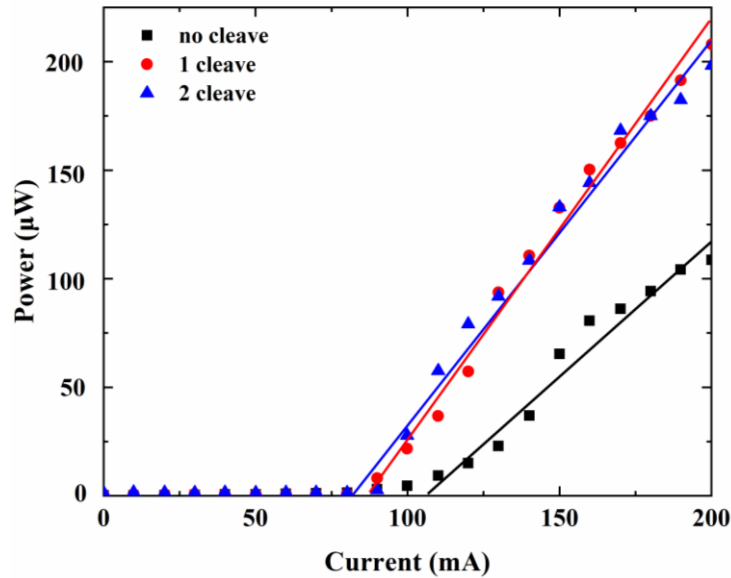
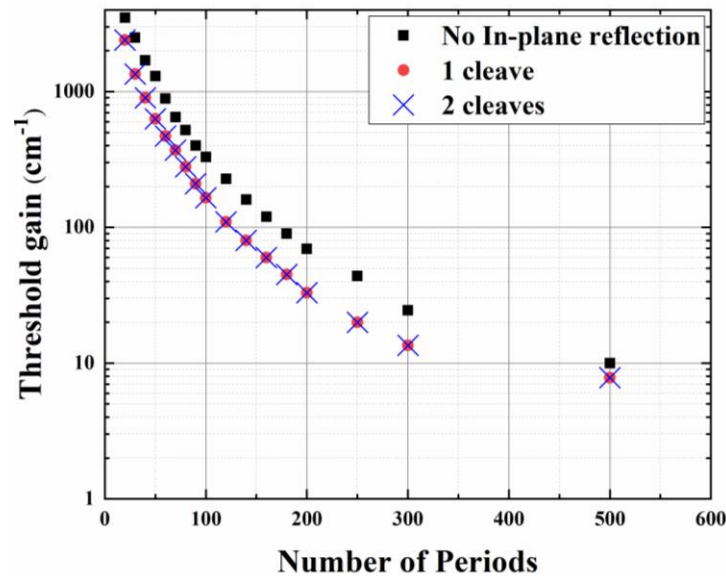


Fig. 5.4.2 LI characteristics of PCSEL with no cleave (black square), single cleave (red circle) and double cleave (blue triangle)

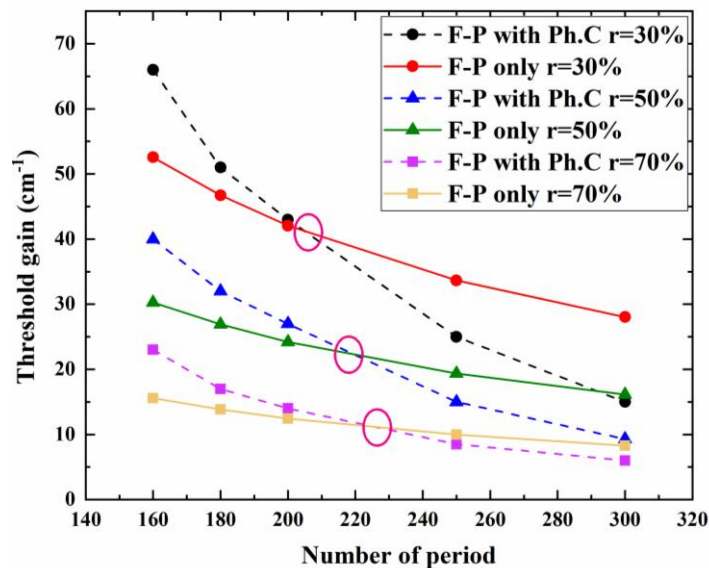
Fig.5.4.2 shows the CW room-temperature LI of the virgin (black square) PCSEL device, with 1 (red circle), and 2 (blue triangle) cleaves. The device with no cleave has a threshold current of 112mA ($J = 1.43 \text{ kA} \cdot \text{cm}^{-2}$). A reduction of lasing threshold from the original 112mA to 88 mA ($J = 1.12 \text{ kA} \cdot \text{cm}^{-2}$) can be observed when a single cleave is introduced to the PCSEL. Such effect is effectively due to the increasing of the optical pass length, since when introducing cleaving to the edge, the ending (truncating) material changes from passive (lossy) to air which gives approximately 32% power reflection. The effect also indicates that at this particular number of period ($N=500$), there is still a certain amount of light leaks outside of the photonic crystal area.

Such effect is also investigated theoretically. Important to notice that although the PC shape used in theoretical analysis is square, it can still represent the nature of PCSEL with circular ‘atom’ since the lasing characteristic of PCSEL is largely depends on the periodicity while the ‘local’ geometry will mainly have an effect on the local field

distribution which affects vertical emission power. As shown in Fig.5.4.3, MIA model developed in previous chapter is used for analysing PCSEL with external reflection. At the particular number of period used in the experiment, the external reflection introduced results in a reduction of lasing threshold. However, as the number of period increases, such effect become less strong (the threshold difference is smaller) since the most of the field is confined inside the photonic crystal region, i.e. the periodic structure has a dominant effect while the truncating structure act merely as a perturbation.



a)



b)

Fig. 5.4.3 a) MIA modelling result of threshold gain of PCSEL with and without single or double external reflection **b)** the effect of FP cavity and the effect of photonic crystal

The introduction of a second cleave (referring to Fig.5.4.1) does not reduce the threshold further (referring to the experimental result in Fig.5.4.2 and modelling results

in Fig. 5.4.3a). Indicating that the lasing mode selection is done by introducing external feedback to one side of the device. Such effect, also indicating that PCSEL operates as two orthogonal placed DFB lasers as predicted very early by other researchers [6]. In other word, the lasing effect is dominated by the direct coupling of the forward and backward traveling wave (referring to mode ‘a’ in chapter 4, Fig.4.2.3b). Higher order terms will affect the behaviour but the effect is not dominant. Such experiment, in return, proves the validity of the approximate method MIA we developed. With additional feedback (one and 2 cleaves) an increased slope efficiency is also observed. Fig.5.4.3 shows the effect of FP cavity compared to the photonic crystal. It is shown that when the periodic is small, the photonic crystal act as perturbation and the resonances are depend on the cleaved facets.

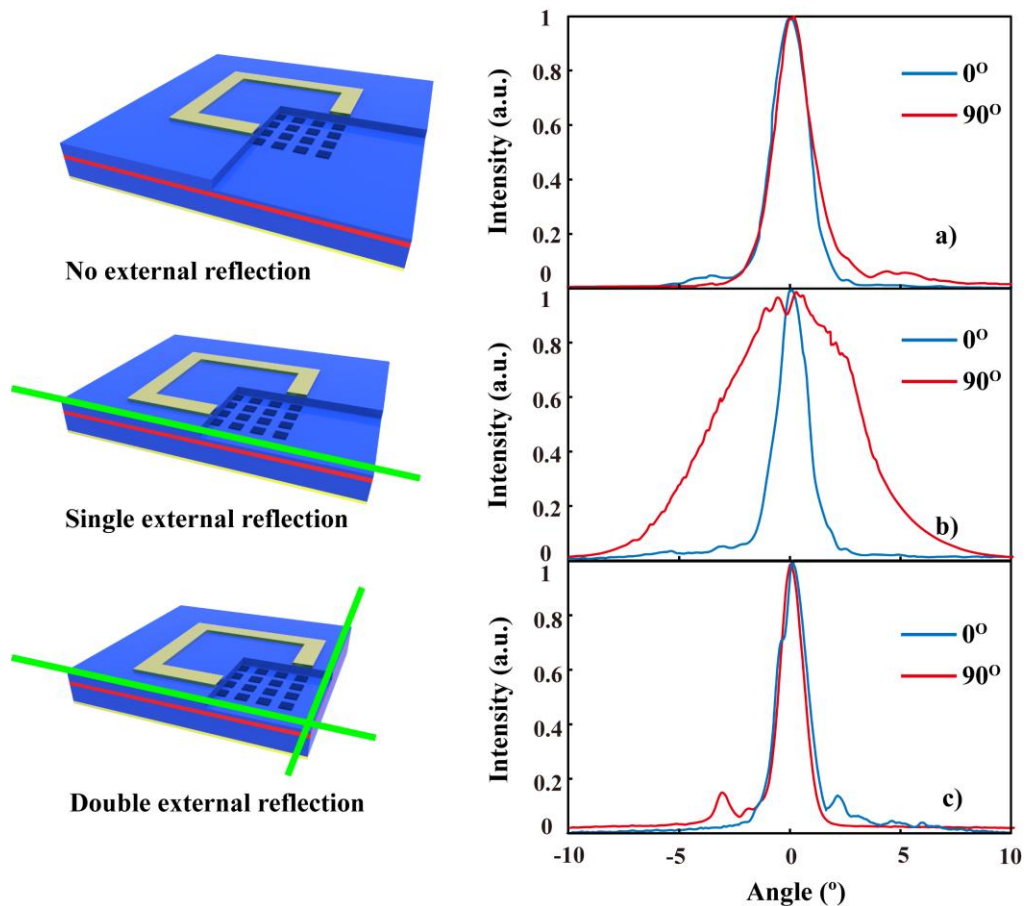


Fig. 5.4.4 Experimental results of far-field pattern at $I=1.1I_{th}$ for a PCSEL with a) no cleave, b) one cleave, and c) two cleaves.

Fig.5.4.4 shows the experimental results of far-field pattern at $I=1.1I_{th}$ for a PCSEL with no cleave (a), one cleave (b), and two cleaves (c). As shown in the figure, for the virgin device, the far field pattern is shown to be symmetric with a divergence of $\sim 1.2^\circ$. In general, typical edge emitting laser has an elliptical far field beam pattern with 40° in

vertical direction while 20° at horizontal direction. VCSEL however, usually has a far field beam divergence around 10° . PCSEL, with large in-plane area, has a very narrow beam divergence of 1° which makes it one very promising laser device.

With the addition of a single cleaved facet along the edge of the photonic crystal area, as shown in the figure, the far field pattern of the device becomes asymmetric with divergence $\sim 4^\circ$ for the 90° (perpendicular to cleave) direction and $\sim 1^\circ$ for the 0° (parallel to cleave) direction. The addition of feedback clearly modifies the field distribution (near field) within the device and eventually affects the far-field pattern. The addition of a second cleave results in a divergence of $0.8\text{-}1^\circ$ indicating lasing is now taking place over a larger area of the PCSEL as compared to the virgin device.

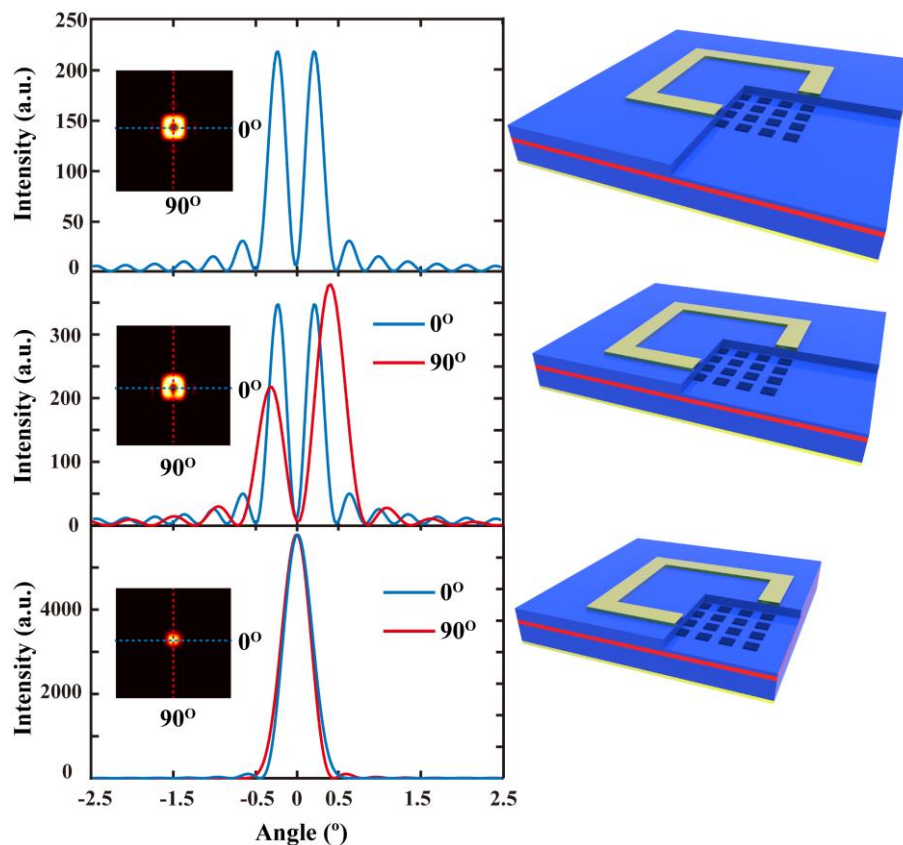


Fig. 5.4.5 Modelling results using MIA of far-field pattern for the lasing mode of PCSEL with **a)** no cleave, **b)** one cleave, and **c)** two cleaves.

To understand the experimental results obtained previously, MIA method is again used to investigate the effect of external reflection on the field distribution of PCSEL. Note that because of the MIA developed is an approximate modelling technique and also in practice laser characteristics are dynamic effect and exhibits rather complicated features such as carrier diffusion and spectral and spatial hole burning. Hence the mode cannot explain all detailed feature of PCSEL.

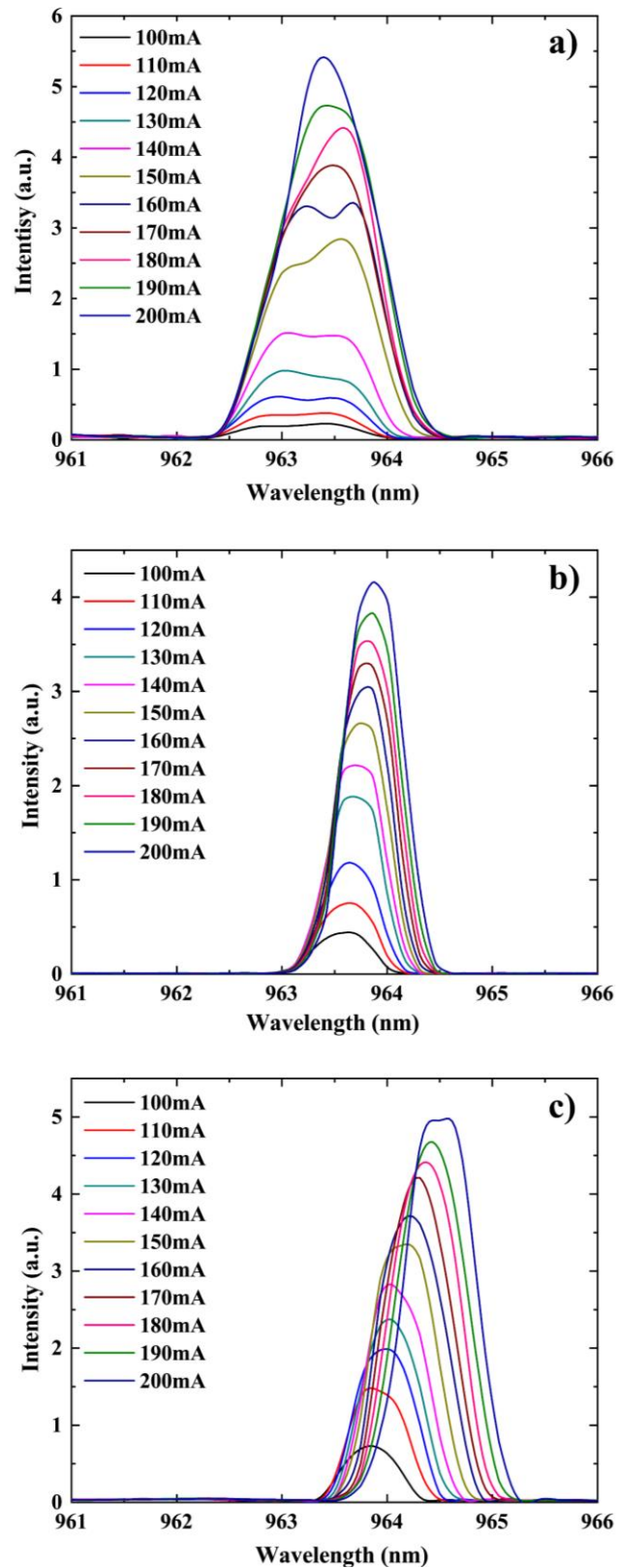


Fig. 5.4.6 EL experimental results of PCSEL with varying CW injection current. **a)** no cleave, **b)** one cleave, and **c)** two cleaves.

However, the modelling results suggests some interesting phenomenon. The modelling results of far-field distribution is shown in Fig.5.4.5. The double-lobe pattern differs from experimental results is merely due to the instrumental limit. It is shown in the figure that

the cleave introduced along the edge can lead to an increasing of beam divergence along one direction. When the second cleave is introduced, the lasing mode (frequency) also changes, which eventually leads to a reduction of far field divergence. The wavelength change is difficult to observe during experimental test since the photonic band gap for all-semiconductor PCSEL is rather small due to the small index difference. Further experiment shows the CW room temperature EL spectra of the PCSEL device with no cleave (blue), 1 cleave (red), and 2 cleaves (black) as illustrated in Fig.5.4.6. The spectrum is plotted as varying injection current from 100mA to 200mA and the red-shift of wavelength is due to the heating. The original device exhibits dual-mode lasing characteristics and such effect can be eliminated through external feedback as justified in Fig.5.4.6 that single mode lasing is maintained over all measured injection current up to 200 mA ($2.55 \text{ kA} \cdot \text{cm}^{-2}$). At 150mA injection current, the spectrum is investigated further.

As shown in Fig.5.4.7, the original device shows dual-peak nature with peaks at 963 and 963.5 nm; the introduced one cleave reduce the spectra to a single lasing peak at 963.75 nm and when a second cleave is introduced the peak wavelength increases to 964.2nm. Although the second shift might due to the heat, such effect is noticed from the study of DFB laser that a shift in wavelength is an expected effect of lateral feedback [7].

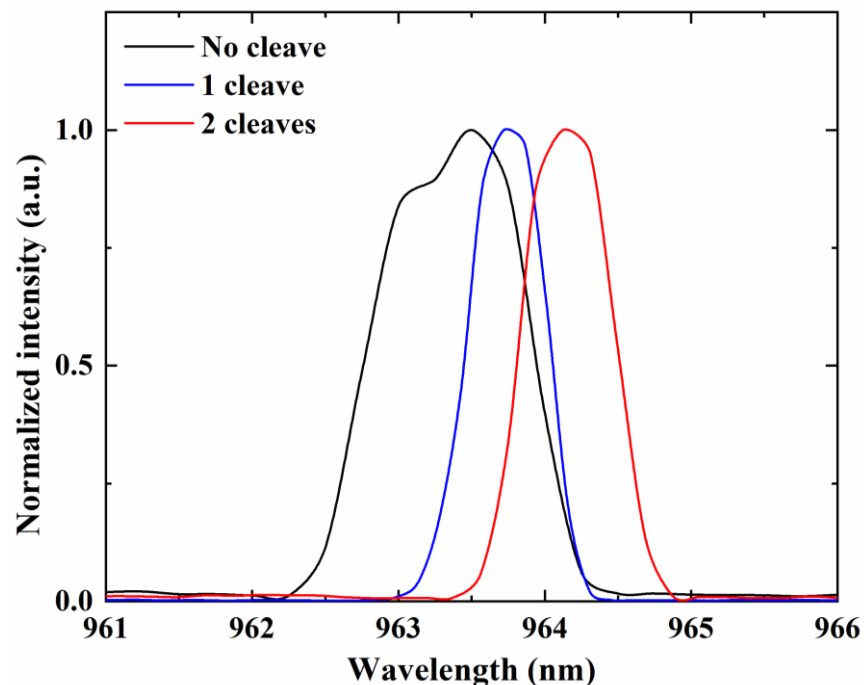


Fig. 5.4.7 CW room temperature EL spectra at 150mA for PCSEL device with no cleave (black), 1 cleave (blue), and 2 cleaves (red).

5.5 PCSEL area scaling and in-plane feedback

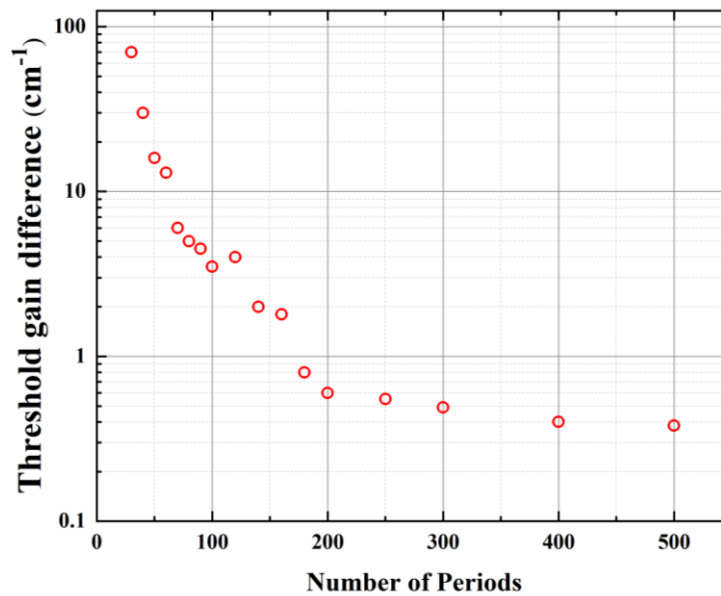


Fig. 5.5.1 Threshold gain margin with different number of period

The design of a semiconductor laser depends on its specific application. Broadly speaking, high power, narrow beam and monochromatic light are three highly desirable characteristics of semiconductor laser. It is known that large active area VCSEL devices lead to multi-transverse mode emission. Due to the 2-D feedback in transverse directions, PCSELS can support large-scale single-mode emission.

However, the transverse dimension needs to be large enough to provide sufficient feedback for a reasonable threshold (300-500 periods in a typical PCSEL device). The large lateral dimension of the PCSEL enables power scaling, and diffraction limited divergence, but limits use in applications that require high speed modulation due to the high mode volume and parasitic capacitance of the junction. Thus, a simulation-based study to explore the opportunities to reduce the scale of the PCSEL, incorporating different boundary conditions is timely. It has been discussed in the previous section that compared with conventional technique such as PWE, finite size effects can be readily obtained from the MIA method.

The threshold margin is defined as the difference in gain between the resonance mode with lowest threshold gain and the mode with next lowest threshold gain. The gain margin is important because it represents how stable the lasing will be under high speed modulation. Fig. 10 plots the gain margin as a function of PC period for $R=70\%$ with

phase $=7\pi/8$. This preliminary modelling result shows that the threshold gain margin can be increased through the reduction of the photonic crystal area, whilst incorporating in-plane external feedback with this reflectivity and phase. For device operation, it is ideal to have large threshold margin for stable lasing operation, especially under high speed modulation. We note that the reduction of PCSEL area results in an increase of the gain margin.

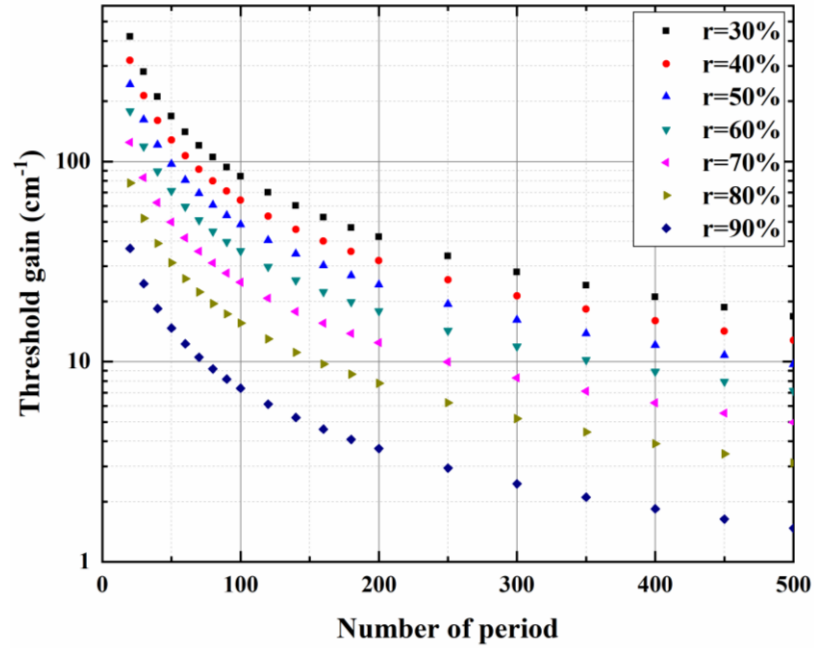


Fig. 5.5.2 Threshold gain margin with different number of period and different external reflectance strength. The reflectance value represents field reflection and the feedback is at four sides of PC region.

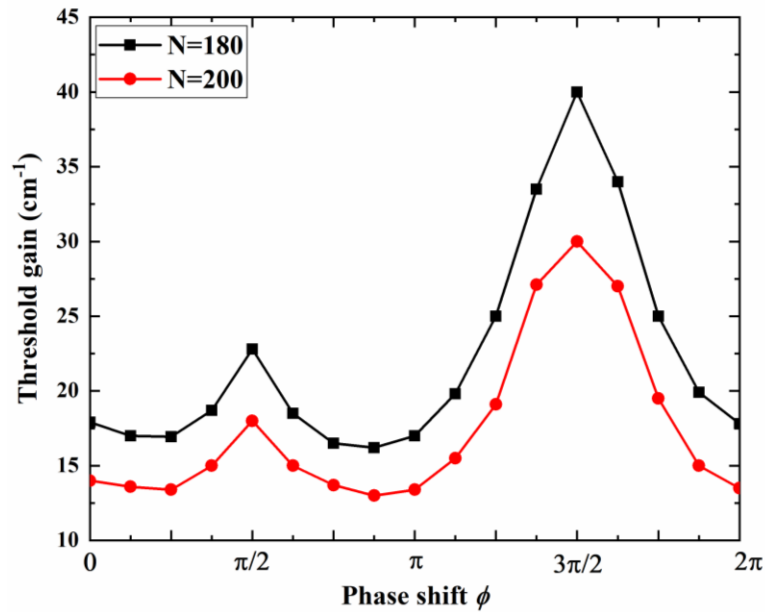


Fig. 5.5.3 Band edge resonances calculated with varying filling factor. Band edge resonances calculated with varying η_a .

Fig. 5.5.2 shows the lasing threshold of the modelled PCSEL as a function of number of photonic crystal period. The external reflection is placed along four edges of the PC region with the field reflectance varying from 30% to 90%. It is noticed that a reduction of PC period results in an increasing of the lasing threshold due to the smaller in-plane feedback and the leakage of power to the unpumped non-PC regions. It is also noticed that such a drawback can be removed through adding external in-plane feedback to increase the Q factor. In practice, the external feedback can be added through specifically designed high reflectors such as a Bragg grating, or first order PCs.

Fig.5.5.3 shows the phase effect of the external reflection at 70% of field reflectivity, the threshold gain of PCSEL is plotted as a function of reflection phase variation with different period (red circle, $N=200$, black square, $N=180$). For the band edge resonance (lasing mode), the threshold gain varies as the phase shift is varied from 0 to 2π , the threshold gain reaches a minimum at $7\pi/8$ and a maximum at $3\pi/2$. As may be expected, reflection phase of in-plane feedback plays an important role in determining the increasing or decreasing of lasing threshold. It also suggests that threshold gain can be optimized with suitable facet phase reflectivity.

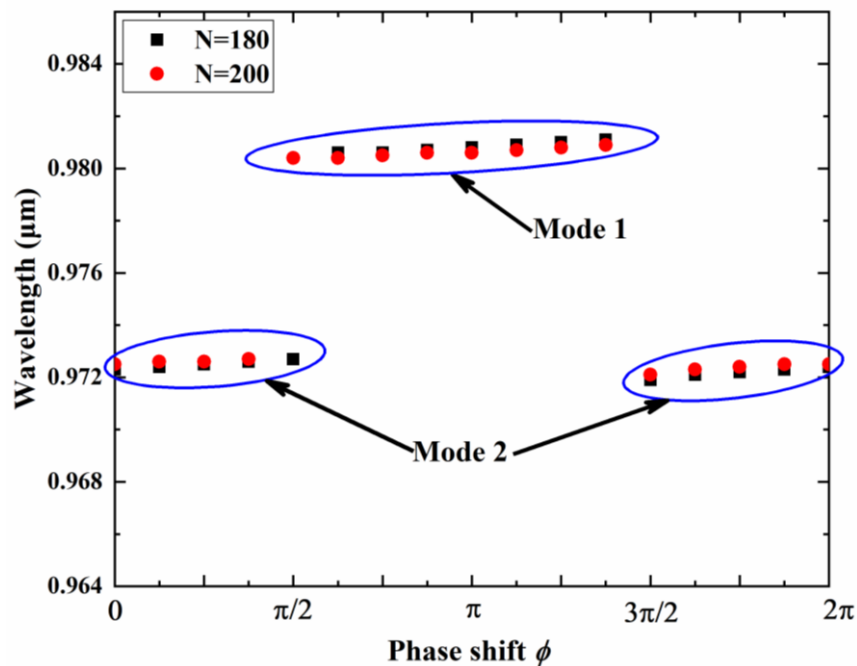


Fig. 5.5.4 Lasing wavelength for PCSEL with varying phase of external reflection

Fig. 5.5.4 illustrates for 70% of reflectivity, the band edge resonance modes of PCSEL, plotted as a function of reflection phase. It is shown from the model that although lasing still occurs at two band-edge, the lasing mode change while varying the reflection phase.

This effect can be further investigated to control the lasing mode of a PCSEL through external in-plane feedback.

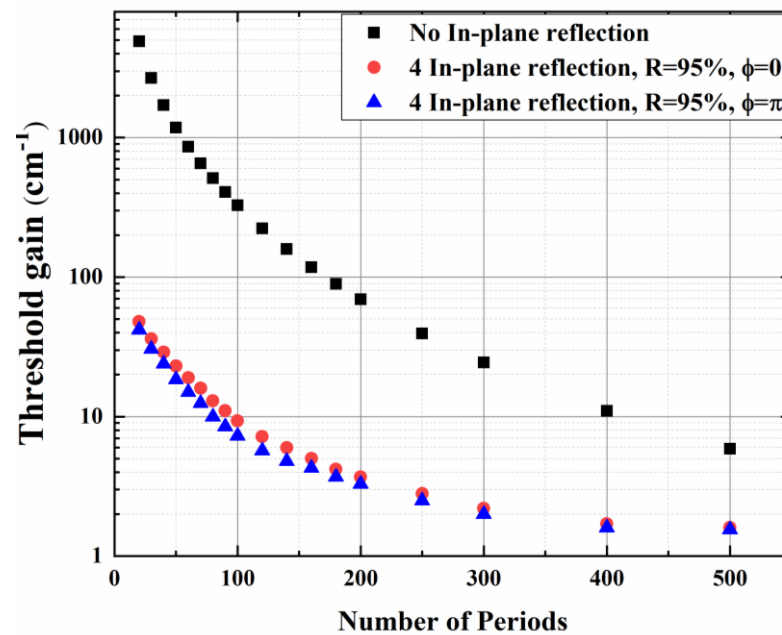


Fig. 5.5.5 Threshold gain of PCSEL with different number of period and different external in-plane phase reflectivity

The study of PCSEL threshold gain with external feedback indicates the possibility of device geometry with small PC active region. As shown in Fig. 5.5.5, an example of the threshold gain of a PCSEL is plotted as a function of number of period at 0 (black square) and 90% reflection with reflection phase at 0 (red circle) and π (blue triangle). It is shown that with appropriate reflection strength and phase, the PCSEL may be shrank down to 20×20 period with a reasonable threshold gain of 50 cm^{-1} .

5.6 Conclusion

In this chapter, the patterning and regrowth technique of PC is reviewed. The PC is patterned using e-beam lithography and the regrowth is done through MOVPE. After PC patterning, the wafer is fabricated into lasing with mesa structure. A detailed explanation of fabrication process and its effect is given in the chapter. Thickness of the dielectrics and depth of p+ etching need to be carefully designed to achieve optimized lasing characteristics.

The sample is characterized after fabrication. It is shown that the PCSEL is a band-edge laser as predicted by the model. The LIV results show that the PCSEL can achieve single mode operation and the far-field pattern of PCSEL shows that the beam divergence of PCSEL is about 1° .

PCSEL with external reflection is also studied both experimentally and theoretically in this chapter. Experimental results show that lasing threshold, lasing mode and far-field beam divergence can be controlled through external reflection. Theoretical modelling also suggests the different reflectivity as well as phase effect on the lasing mode and threshold. It is envisaged that such method could be used in the future in achieving lasing mode control of PCSEL. It is shown that by carefully designing external reflector, the dimension of the PCSEL can be shrink down and the lasing characteristic such as threshold, frequency and mode shape can be controlled accordingly.

5.7 Reference

- [1] H. M. Manasevit, "Single - crystal gallium arsenide on insulating substrates," *Applied Physics Letters*, vol. 12, no. 4, pp. 156-159, 1968.
- [2] M. Razeghi, *The MOCVD Challenge: A survey of GaInAsP-InP and GaInAsP-GaAs for photonic and electronic device applications*. CRC Press, 2010.
- [3] A. Y. Cho and J. Arthur, "Molecular beam epitaxy," *Progress in solid state chemistry*, vol. 10, pp. 157-191, 1975.
- [4] D. M. Williams et al., "Optimisation of coupling between photonic crystal and active elements in an epitaxially regrown GaAs based photonic crystal surface emitting laser," *Japanese Journal of Applied Physics*, vol. 51, no. 2S, p. 02BG05, 2012.
- [5] Sakai K, Miyai E, Sakaguchi T, et al. Lasing band-edge identification for a surface-emitting photonic crystal laser[J]. *IEEE Journal on Selected Areas in Communications*, 2005, 23(7): 1335-1340.
- [6] Meier M, Mekis A, Dodabalapur A, et al. Laser action from two-dimensional distributed feedback in photonic crystals[J]. *Applied Physics Letters*, 1999, 74(1): 7-9.
- [7] Gelleta J, Liang Y, Kitagawa H, et al. Influence of external reflection on the TE mode of photonic crystal surface-emitting lasers[J]. *JOSA B*, 2015, 32(7): 1435-1441.

Chapter 6

Conclusions and Future works

6.1 Conclusion

Wave propagation in periodic media have been investigated by researchers for over a century. In optics the use of (periodic) Bragg-gratings have been prevalent in both passive and active devices such as DBR and DFB lasers. Recently in photonics, two and three dimensional (2-D, 3-D) periodic structures, referred to as photonic crystals, have been studied intensively resulting in the realisation of devices with remarkable characteristics. The photonic-crystal-surface-emitting-laser (PCSEL) is one such device with very desirable output characteristics. It utilises large optically active, 2-D periodically ‘sculpted’ surface, to achieve single wavelength operation combined with high power output in a uniformly narrow far-field beam.

To model PCSEL, a fundamental requirement is to evaluate the optical field resonances in the structure that identify the ‘lasing mode’. Several modelling techniques widely used are plane wave expansion (PWE), coupled mode theory (CMT) and finite difference time domain technique. However, the first two require very considerable mathematical effort and the third is computationally extensive and time consuming.

In this work, an essentially analytical model for evaluating 2-D resonance of photonic crystal pertinent to PCSEL is presented. A systematic study begins by first considering eigenmode and eigenfunctions of 1-D periodic structure. Broadly speaking, the study of wave behaviour within periodic structure can be divided into two categories: infinite periodic structure and finite periodic structure. The eigenvalue of the infinite periodic structure is defined by the famous Mathieu and Hill’s equation and the result is known as Bloch wavevector. PWE is most widely used in calculating the dispersion relation of Bloch wavevector and frequency. It gives the photonic band structure which is essential in photonic crystal design and understanding.

Despite of the success in PWE, the limitation is clear: the theory is based on Floquet-Bloch method and cannot be applied to finite periodic structure. It is then found that the eigenvalue of the periodic structure with finite extent corresponds to the transmission

maxima of such structure when the structure is excited externally. The process is effectively finding the characteristic impedance of the periodic structure. Several examples are given such as modes in periodic waveguide, BIC mode, Bragg reflection waveguide and Tamm state to further illustrate and validate such concept and the solving technique is used as building block to further develop the 2-D model.

The MIA model begins by first considering a rectangular co-ordinate system (x, y, z) consistent with the rectangular device geometry. The pertinent planar periodic structure is in the x - z plane and the y dimension is multilayer structure. The main objective of this work is to consider 2-D resonance and thus the y direction effect is built in through effective index distribution in the x - z plane $\eta(x, z)$. The analysis essentially treats 2-D index distribution as coupled waveguide in x direction with z -dimension corrugation. It proceeds by first assuming uniformity along z -axis, results in a modified periodic multilayer structure $\eta(x)$. Modes propagating along the z -axis in this structure are computed by taking resonance tunnelling solution for a relevant range of wavelengths based on the discussion previously. Such modes correspond to the 1-D resonance solution and is then used to construct the corresponding effective multilayer periodic structure along the z -axis.

Several numerical comparisons are carried out between conventional modelling techniques and MIA. It is shown that the MIA matches favourably with both numerical results obtained using conventional methods and experimental results. Moreover, the effect of finite size can be obtained through MIA. Further investigation involves including in-plane diffraction to modified the effective structure obtained previously. It is shown that the consistency can be better preserved when the in-plane diffraction is included.

Experimental work is also presented in the thesis to further proof the validity of the model. The all-semiconductor PCSEL device is fabricated during the project with the measurement of the LIV characteristics. PCSEL with external reflector is also experimentally studied. It is shown that the artificially induced external reflector could leads to a reduction of the threshold. In plane field distribution and the far-field pattern can be changed through such external reflection.

6.2 Future work

The theoretical work carried out so far has demonstrated a significant potential of MIA method. During the study, several topics could be investigated further and even become individual projects.

In chapter 3, it is shown that the eigenvalue of infinite periodic structure can be expressed as superposition of Bloch modes. It is proved by other researcher that the Bloch mode are complete. However, such issue is not trivial at all since the solution involves non-Hermitian problem. The study of completeness and orthogonality of Bloch mode is certainly one of the most important aspect of future study. Moreover, even the completeness of the Bloch mode has been demonstrated by other researchers, the eigenmode of the finite periodic structure is barely considered. The eigenmodes we obtained here corresponds to the optical tunnelling or impedance matching conditions. However, are those ‘modes’ complete and orthogonal are still not clear even in the exist published literature. But such study is essential in understanding wave behaviour in periodic structure as well as the design of more advanced modelling techniques.

In chapter 3 there is also one peculiar type of mode exist in periodic structure, BIC mode. Such mode exists in the continuum spectrum region but the energy is well confined in the waveguide. To the best of our knowledge, such mode is only been experimental observed very recently but no design has been done explicitly on the relevant device based on BIC. The modelling technique shown are rather mathematically complicated. However, this work provides an alternative representation and has the potential to understand such effect better for designing more optical devices based on BIC.

Undoubtedly, devices based on Tamm state or Tamm plasmon become one of the most widely studied area recently because it opens up the possibility of enhancing or directing the emission. The concepts developed in chapter 3 can be applied in analysing such subject, e.g. do all Bragg structures support surface mode states? are Bragg modes and surface-state modes Orthogonal? etc. All such study could be done through a deeper understanding of wave behaviours in finite periodic structure.

Chapter 4 presents a new model, MIA, for analysing 2-D resonance of photonic crystal corresponds to the lasing modes of PCSEL. However, the model does not include carrier

aspects. However, such effect could be included through the spatial and temporal variation in optical gain. Other PC configurations such as asymmetries could be included in MIA.

The external reflection also leads to a change of the in-plane field distribution of lasing mode. As shown in Fig.6.6, the preliminary modelling results shows that when an external reflection is introduced (shown as red line) along one side of PCSEL, the in-plane field will move accordingly. It is believed that through dynamically changing external reflector, the lasing mode as well as the beam shape can be modified and tailored accordingly.

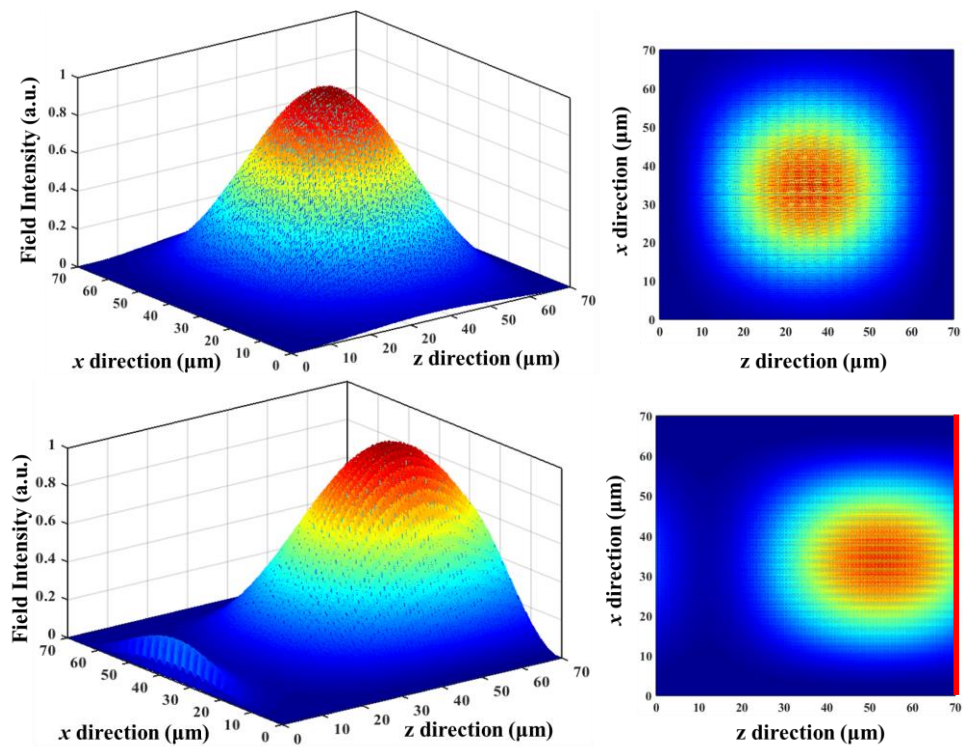


Fig. 6.6 In-plane field distribution changes introduced by external reflection

Enough of Science. Up! up! my Friend, and quit your books:

*And medicine, law, business, engineering,
these are noble pursuits and necessary to sustain life.*

*But poetry, beauty, romance, love,
these are what we stay alive for.*

----- Dead Poets Society

Appendix A

Vector Operators and Maxwell's Equation

Electric field: \mathbf{E} Volts/m

Magnetic field: \mathbf{H} Amperes/m

Electric permittivity of vacuum $\epsilon_0 = 8.854 \times 10^{-12}$ Farads/m.

ϵ_r relative electrical permittivity of medium.

Magnetic permeability of vacuum. $\mu_0 = 4\pi \times 10^{-7}$ Henry/m.

μ_r relative magnetic permeability of medium.

Electric displacement: $\mathbf{D} = \epsilon_0 \epsilon_r \mathbf{E} = \epsilon_c \mathbf{E}$

Magnetic flux (Density): $\mathbf{B} = \mu_0 \mu_r \mathbf{H} = \mu_c \mathbf{H}$

Ampère's Law: relates total electric current to magnetic field.

Faraday's Law: relates time change of magnetic flux to electric field.

In general, electric and magnetic fields are vectors (direction components). As for any vector, we have:

$$\mathbf{F} = \mathbf{u}_x F_x(x, y, z, t) + \mathbf{u}_y F_y(x, y, z, t) + \mathbf{u}_z F_z(x, y, z, t) \quad (\text{A.1})$$

This condition is in Cartesian coordinates (Other coordinates: Cylindrical, spherical, etc. may also be used). In equation (A.1), F_x , F_y and F_z are magnitude of the vector in x , y , z direction respectively and \mathbf{u}_x , \mathbf{u}_y , \mathbf{u}_z are the unit vector along each axis. Note that importantly, in equation (A.1), that \mathbf{F} is a vector but the components F_x , F_y and F_z are scalar.

Further, in general, each of these components can be a function of space and time. The squiggle “~” denotes implicit time dependence. And in that case, the compact notation for the vector field is given in equation (A.1). Most frequently, the time dependence can be given as a separated variable and can be written in vector form as:

$$\mathbf{F} = \mathbf{F}(x, y, z)h(t) \quad (\text{A.2})$$

In almost all situation, a harmonic time dependence is used, that is $h(t) = \exp(j\omega t)$ and hence:

$$\mathbf{F} = \mathbf{F}(x, y, z)h(t) = \mathbf{F}(x, y, z)e^{j\omega t} \quad (\text{A.3})$$

is used throughout. vector differential operators are defined before further derivation.

Gradient, ∇ , operates only on scalar functions. Suppose a scalar function $\psi = \psi(x, y, z, t)$. The gradient of such function is defined as:

$$\nabla\psi = \left[\mathbf{u}_x \frac{\partial}{\partial x} + \mathbf{u}_y \frac{\partial}{\partial y} + \mathbf{u}_z \frac{\partial}{\partial z} \right] \psi \quad (\text{A.4})$$

Hence the gradient operator results in a vector.

Divergence, $\nabla \cdot$, operates on a vector function $\mathbf{F} = \mathbf{F}(x, y, z, t)$ and is defined as:

$$\nabla \cdot \mathbf{F} = \frac{\partial}{\partial x} F_x + \frac{\partial}{\partial y} F_y + \frac{\partial}{\partial z} F_z \quad (\text{A.5})$$

and hence the divergence operator results in a scalar.

Curl, $\nabla \times$, operates on a vector function $\mathbf{F} = \mathbf{F}(x, y, z, t)$ and is defined as:

$$\begin{aligned} \nabla \times \mathbf{F} &= \begin{vmatrix} \mathbf{u}_x & \mathbf{u}_y & \mathbf{u}_z \\ \frac{\partial}{\partial x} & \frac{\partial}{\partial y} & \frac{\partial}{\partial z} \\ F_x & F_y & F_z \end{vmatrix} \\ &= \mathbf{u}_x \left(\frac{\partial}{\partial y} F_z - \frac{\partial}{\partial z} F_y \right) - \mathbf{u}_y \left(\frac{\partial}{\partial x} F_z - \frac{\partial}{\partial z} F_x \right) + \mathbf{u}_z \left(\frac{\partial}{\partial x} F_y - \frac{\partial}{\partial y} F_x \right) \end{aligned} \quad (\text{A.6})$$

and hence the curl operator results in a vector.

Some higher order vector differential operators is also required in EM theory. From equation (A.4), (A.5) and (A.6), it can be proved that:

$$\nabla \cdot (\nabla \psi) = \left[\frac{\partial^2}{\partial x^2} + \frac{\partial^2}{\partial y^2} + \frac{\partial^2}{\partial z^2} \right] \psi \quad (\text{A.7})$$

is a scalar and:

$$\nabla \times (\nabla \psi) \equiv 0 \quad (\text{A.8})$$

is valid for all ψ . We further define $\nabla \times (\nabla \times \mathbf{F}) \equiv \nabla(\nabla \cdot \mathbf{F}) - \nabla^2 \mathbf{F}$. And hence:

$$-\nabla^2 \mathbf{F} \equiv \nabla \times (\nabla \times \mathbf{F}) - \nabla(\nabla \cdot \mathbf{F}) \quad (\text{A.9})$$

the operator ∇^2 is called Laplace operator or Laplacian. In rectangular coordinate, the Laplacian is defined as:

$$\nabla^2 \mathbf{F} = \left[\frac{\partial^2}{\partial x^2} + \frac{\partial^2}{\partial y^2} + \frac{\partial^2}{\partial z^2} \right] \mathbf{F} \quad (\text{A.10})$$

Next, we return to the set of Maxwell's equation introduced in chapter 2:

$$\nabla \cdot \mathbf{D} = \rho \quad (\text{Gauss/Coulomb}) \quad (\text{A.11})$$

$$\nabla \cdot \mathbf{B} = 0 \quad (\text{Gauss}) \quad (\text{A.12})$$

$$\nabla \times \mathbf{E} = -\frac{\partial \mathbf{B}}{\partial t} \quad (\text{Faraday}) \quad (\text{A.13})$$

$$\nabla \times \mathbf{H} = \mathbf{J} + \frac{\partial \mathbf{D}}{\partial t} \quad (\text{Ampere}) \quad (\text{A.14})$$

Now consider harmonic time dependence so that all fields take on the form of (A.2) and (A.3). Then, noting that all the vector differential operator are partial derivatives only in space variables (x, y, z) . Thus, all of Maxwell's equations become:

$$\nabla \cdot \mathbf{E}(x, y, z) = \frac{\rho(x, y, z)}{\epsilon_0 \epsilon_r} \quad (\text{A.15})$$

$$\nabla \cdot \mathbf{H}(x, y, z) = 0 \quad (\text{A.16})$$

$$\nabla \times \mathbf{E}(x, y, z) = -j\omega\mu_0\mu_r\mathbf{H}(x, y, z) \quad (\text{A.17})$$

$$\nabla \times \mathbf{H}(x, y, z) = \mathbf{J}_s(x, y, z) + \sigma\mathbf{E}(x, y, z) + j\omega\epsilon_0\epsilon_r \mathbf{E}(x, y, z) \quad (\text{A.18})$$

The above equations are known as Maxwell's equations for harmonic time dependence.

Now, take the equation (A.18):

$$\begin{aligned} \nabla \times \mathbf{H}(x, y, z) &= \mathbf{J}_s(x, y, z) + \sigma\mathbf{E}(x, y, z) + j\omega\epsilon_0\epsilon_r \mathbf{E}(x, y, z) \\ &= \mathbf{J}_s(x, y, z) + j\omega\epsilon_0 \left[\epsilon_r + \frac{\sigma}{j\omega\epsilon_0} \right] \mathbf{E}(x, y, z) \\ &= \mathbf{J}_s(x, y, z) + j\omega\epsilon_0\epsilon_c \mathbf{E}(x, y, z) \end{aligned} \quad (\text{A.19})$$

Where the complex number $\epsilon_c = \epsilon_r + \sigma/j\omega\epsilon_0 = \epsilon_r - j\sigma/\omega\epsilon_0 = \epsilon_r - j\epsilon_i$

In general, $\epsilon_c = \epsilon_r - j\epsilon_i$ for the media is explicitly specified. This can be obtained from experiments or from fundamental solid-state (semiconductor) theory. Therefore, henceforth the Maxwell's equation will be written as:

$$\nabla \cdot \mathbf{E}(x, y, z) = \frac{\rho(x, y, z)}{\epsilon_0\epsilon_r} \quad (\text{A.20})$$

$$\nabla \cdot \mathbf{H}(x, y, z) = 0 \quad (\text{A.21})$$

$$\nabla \times \mathbf{E}(x, y, z) = -j\omega\mu_0\mu_r\mathbf{H}(x, y, z) \quad (\text{A.22})$$

$$\nabla \times \mathbf{H}(x, y, z) = \mathbf{J}_s(x, y, z) + j\omega\varepsilon_0\varepsilon_c\mathbf{E}(x, y, z) \quad (\text{A.23})$$

All electromagnetic problems require the solution of Maxwell's equation, the appropriate source functions and boundary conditions specified for the problem. In most situations in this thesis, it will be assumed that in the region of interest, charge density is identically zero, $\rho(x, y, z) \equiv 0$. And source current density is identically zero, $\mathbf{J}_s(x, y, z) \equiv 0$. Since for any vector function $\nabla \cdot (\nabla \times \mathbf{F}) \equiv 0$, if $\mathbf{J}_s(x, y, z) \equiv 0$, it gives:

$$\nabla \cdot [\nabla \times \mathbf{H}(x, y, z)] = j\omega\varepsilon_0\varepsilon_c \nabla \cdot \mathbf{E}(x, y, z) = 0 \quad (\text{A.24})$$

This is consistent with the equation $\nabla \cdot \mathbf{E}(x, y, z) = 0$ if $\rho(x, y, z) \equiv 0$.

Similarly, from $\nabla \cdot [\nabla \times \mathbf{E}(x, y, z)] = 0 \Rightarrow -j\omega\mu_0\mu_r \nabla \cdot \mathbf{H}(x, y, z) = 0$ which is consistent with (A.21). Note that Maxwell's equations in form of equation (A.20) to (A.23) must be put as differential equation of a single dependent function, \mathbf{E} or \mathbf{H} before it can be solved as follow.

From equation (A.23) with $\mathbf{J}_s(x, y, z) \equiv 0$ and from the vector differential operator relations $\nabla \times (\nabla \times \mathbf{F}) \equiv \nabla(\nabla \cdot \mathbf{F}) - \nabla^2 \mathbf{F}$, we could obtain:

$$\nabla^2 \mathbf{H} + k_0^2 \varepsilon \mathbf{H} = 0 \quad (\text{A.25})$$

where $k_0^2 = \omega^2 \varepsilon_0 \mu_0 = (2\pi/\lambda_0)$. Similar process starting with equation (A.22) yields:

$$\nabla^2 \mathbf{E} + k_0^2 \varepsilon_c \mathbf{E} = 0 \quad (\text{A.26})$$

Equation (A.25) and (A.26) are referred to as vector wave equation for harmonic time dependent electromagnetic field. In rectangular coordinates, 6 field components $E_{x,y,z}$ and $H_{x,y,z}$ can exist in general and appropriate boundary conditions may further apply for the particular problem. The velocity of light in the vacuum is defined as $c = 1/\sqrt{\mu_0\varepsilon_0}$ and velocity of light in the homogeneous media is $v = 1/\sqrt{\mu_c\varepsilon_c} = c/\eta_c$ where η_c is the refractive index of the media and for non-magnetic material $\mu = 1$ giving $\eta_c = \sqrt{\varepsilon_c}$.

As shown in Chapter 2, the Poynting vector is defined as $\mathbf{S} = \mathbf{E} \times \mathbf{H}$ and in general, $\eta_c = \sqrt{\epsilon_c}$ is a complex number $\eta_c = \eta_r + j\eta_i$. For plane wave propagates along x direction, the time averaged Poynting vector is:

$$\mathbf{S} = \frac{1}{2} \text{Re}\{\mathbf{E} \times \mathbf{H}^*\} = \text{Re}\left\{ \begin{array}{ccc} u_x & u_y & u_z \\ 0 & E_y & 0 \\ 0 & 0 & H_z^* \end{array} \right\} \quad (\text{A.27})$$

Thus, from equations (2.20) and (2.21)

$$\begin{aligned} \mathbf{S}_x &= \frac{1}{2} \text{Re}\{E_y H_z\} \\ &= \sqrt{\frac{\epsilon}{\mu}} |A|^2 e^{-jk_0(\eta_r + j\eta_i)x + jk_0(\eta_r - j\eta_i)x} \\ &= \sqrt{\frac{\epsilon}{\mu}} |A|^2 e^{2k_0\eta_i x} \end{aligned} \quad (\text{A.28})$$

The quantity $2k_0\eta_i$ is defined as optical gain $g = 2k_0\eta_i$ and thus, optical gain can be represented by the imaginary part of the refractive index.

Appendix B

EM Waves in Layered Media: A Transfer Matrix Representation

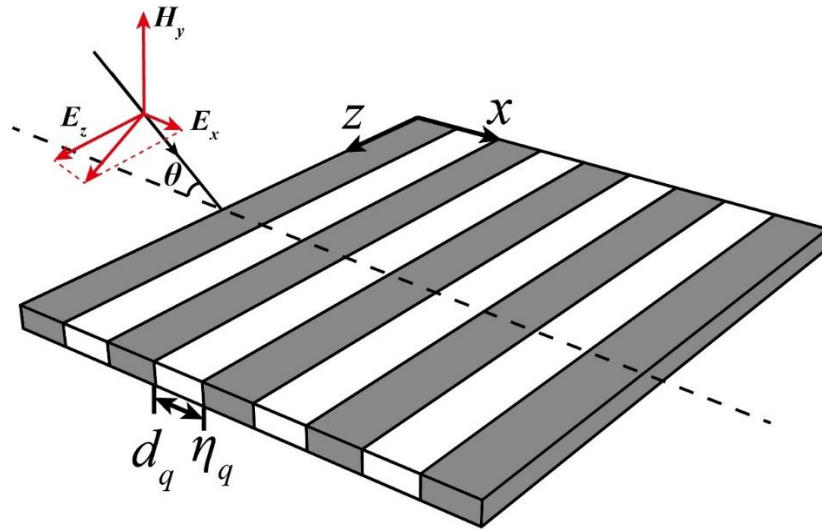


Fig. B1. Schematic of 1-D multilayer structure.

In this section, a matrix formulation waves in layered media is developed. As shown in Fig.B1. Define region q as $x_q < x < x_{q+1}$ and the incident angle is θ . The excitation is such that non-zero field components E_x , E_z and H_y exist, i.e. $(TE)_y$ polarization and $\partial_y^2 \equiv 0$. H_y component must satisfy wave equation given by:

$$\left[\frac{\partial^2}{\partial x^2} + \frac{\partial^2}{\partial z^2} + k_0^2 \eta_q^2 \right] H_y(x, z) = 0 \quad (\text{B.1})$$

A separation of variable form of solution is applicable and yields:

$$H_y(x, z) = f(x) e^{-j\beta_q z} \quad (\text{B.2})$$

The boundary condition decides that $\beta_q = \beta$ is satisfied in each layer q . Define in each region q

$$f(x) = A_q \exp(-j\kappa_q x) + B_q \exp(+j\kappa_q x) \quad (\text{B.3})$$

Thus, from equation (B.1), (B.2) and (B.3) it yields $\kappa_q^2 + \beta^2 = k_0^2 \eta_q^2$ satisfied in each homogeneous region q .

From the Maxwell's equation:

$$\nabla \times \mathbf{H} = \begin{vmatrix} \mathbf{u}_x & \mathbf{u}_y & \mathbf{u}_z \\ \frac{\partial}{\partial x} & \frac{\partial}{\partial y} & \frac{\partial}{\partial z} \\ H_x & H_y & H_z \end{vmatrix} = j\omega\varepsilon_0\varepsilon_q \mathbf{E} \quad (\text{B.4})$$

Which gives

$$H_{qy} = \left[A_q \exp(-j\kappa_q x) + B_q \exp(+j\kappa_q x) \right] e^{-j\beta z} \quad (\text{B.5})$$

$$E_{qz} = \frac{\kappa_q}{\omega\varepsilon_0\varepsilon_q} \left[-A_q \exp(-j\kappa_q x) + B_q \exp(+j\kappa_q x) \right] e^{-j\beta z} \quad (\text{B.6})$$

The local thickness is defined as $s = x - x_q$ for convenience and $0 \leq s \leq s_q$. The main objective is to consider x -direction and z -direction propagation is not of particular interest. Hence, equation (B.5) and (B.6) can be written as (in region q):

$$h_{qy} = A_q \exp(-j\kappa_q s) + B_q \exp(+j\kappa_q s) \quad (\text{B.7})$$

$$e_{qz} = \frac{\kappa_q}{\omega\varepsilon_0\varepsilon_q} \left[-A_q \exp(-j\kappa_q s) + B_q \exp(+j\kappa_q s) \right] \quad (\text{B.8})$$

and in region $q+1$

$$h_{q+1y} = A_{q+1} \exp(-j\kappa_{q+1} s) + B_{q+1} \exp(+j\kappa_{q+1} s) \quad (\text{B.9})$$

$$e_{q+1z} = \frac{\kappa_{q+1}}{\omega\varepsilon_0\varepsilon_{q+1}} \left[-A_{q+1} \exp(-j\kappa_{q+1} s) + B_{q+1} \exp(+j\kappa_{q+1} s) \right] \quad (\text{B.10})$$

Next, the interface condition is applied as $e_{q+1z}(0) = e_{qz}(s_q)$ and $h_{q+1z}(0) = h_{qz}(s_q)$ which yields:

$$A_{q+1} + B_{q+1} = A_q \exp(-j\kappa_q s_q) + B_q \exp(+j\kappa_q s_q) \quad (\text{B.11})$$

$$A_{q+1} - B_{q+1} = \frac{\kappa_{q+1}}{\omega\varepsilon_0\varepsilon_{q+1}} \left[A_q \exp(-j\kappa_q s_q) - B_q \exp(+j\kappa_q s_q) \right] \quad (\text{B.12})$$

Equation (B.11) and (B.12) are considered and gives:

$$A_q = \frac{\varepsilon_{q+1}\kappa_q + \varepsilon_q\kappa_{q+1}}{2\varepsilon_{q+1}\kappa_q} \exp(+j\kappa_q s_q) A_{q+1} + \frac{\varepsilon_{q+1}\kappa_q - \varepsilon_q\kappa_{q+1}}{2\varepsilon_{q+1}\kappa_q} \exp(+j\kappa_q s_q) B_{q+1} \quad (\text{B.13})$$

$$B_q = \frac{\varepsilon_{q+1}\kappa_q - \varepsilon_q\kappa_{q+1}}{2\varepsilon_{q+1}\kappa_q} \exp(-j\kappa_q s_q) A_{q+1} + \frac{\varepsilon_{q+1}\kappa_q + \varepsilon_q\kappa_{q+1}}{2\varepsilon_{q+1}\kappa_q} \exp(-j\kappa_q s_q) B_{q+1} \quad (\text{B.14})$$

which can be written into a matrix form:

$$\begin{bmatrix} A_q \\ B_q \end{bmatrix} = [m_q] \begin{bmatrix} A_{q+1} \\ B_{q+1} \end{bmatrix} \quad (\text{B.15})$$

where

$$m_{(1,1)} = \frac{\varepsilon_{q+1}\kappa_q + \varepsilon_q\kappa_{q+1}}{2\varepsilon_{q+1}\kappa_q} \exp(+j\kappa_q s_q) \quad (\text{B.16})$$

$$m_{(1,2)} = \frac{\varepsilon_{q+1}\kappa_q - \varepsilon_q\kappa_{q+1}}{2\varepsilon_{q+1}\kappa_q} \exp(+j\kappa_q s_q) \quad (\text{B.17})$$

$$m_{(2,1)} = \frac{\varepsilon_{q+1}\kappa_q - \varepsilon_q\kappa_{q+1}}{2\varepsilon_{q+1}\kappa_q} \exp(-j\kappa_q s_q) \quad (\text{B.18})$$

$$m_{(2,2)} = \frac{\varepsilon_{q+1}\kappa_q + \varepsilon_q\kappa_{q+1}}{2\varepsilon_{q+1}\kappa_q} \exp(-j\kappa_q s_q) \quad (\text{B.19})$$

In thesis chapter 2, a propagation matrix and a transfer matrix formulation is introduced. Here I use an alternative approach to derive it. The advantage of such derivation is that in numerical simulation, it is the thickness s rather than the actual x location is provided. The expression is found to be better for numerical approach in the study.

When the structure become periodic, the transfer matrix for a single periodic is important and is given by $[\mathbf{m}] = [m_q][m_{q+1}]$. After the considerable amount of algebra, the reader could obtain the matrix components:

$$\begin{aligned} \mathbf{m}_{(1,1)} &= \frac{(\varepsilon_{q+1}\kappa_q + \varepsilon_q\kappa_{q+1})^2}{4\varepsilon_q\varepsilon_{q+1}\kappa_q\kappa_{q+1}} e^{+j(\kappa_q s_q + \kappa_{q+1} s_{q+1})} - \frac{(\varepsilon_{q+1}\kappa_q - \varepsilon_q\kappa_{q+1})^2}{4\varepsilon_q\varepsilon_{q+1}\kappa_q\kappa_{q+1}} e^{+j(\kappa_q s_q - \kappa_{q+1} s_{q+1})} \\ \mathbf{m}_{(1,2)} &= -\frac{(\varepsilon_{q+1}\kappa_q)^2 - (\varepsilon_q\kappa_{q+1})^2}{4\varepsilon_q\varepsilon_{q+1}\kappa_q\kappa_{q+1}} e^{+j(\kappa_q s_q + \kappa_{q+1} s_{q+1})} - \frac{(\varepsilon_{q+1}\kappa_q)^2 - (\varepsilon_q\kappa_{q+1})^2}{4\varepsilon_q\varepsilon_{q+1}\kappa_q\kappa_{q+1}} e^{+j(\kappa_q s_q - \kappa_{q+1} s_{q+1})} \\ \mathbf{m}_{(2,1)} &= -\frac{(\varepsilon_{q+1}\kappa_q)^2 - (\varepsilon_q\kappa_{q+1})^2}{4\varepsilon_q\varepsilon_{q+1}\kappa_q\kappa_{q+1}} e^{-j(\kappa_q s_q - \kappa_{q+1} s_{q+1})} - \frac{(\varepsilon_{q+1}\kappa_q)^2 - (\varepsilon_q\kappa_{q+1})^2}{4\varepsilon_q\varepsilon_{q+1}\kappa_q\kappa_{q+1}} e^{-j(\kappa_q s_q + \kappa_{q+1} s_{q+1})} \\ \mathbf{m}_{(2,2)} &= -\frac{(\varepsilon_{q+1}\kappa_q - \varepsilon_q\kappa_{q+1})^2}{4\varepsilon_q\varepsilon_{q+1}\kappa_q\kappa_{q+1}} e^{-j(\kappa_q s_q - \kappa_{q+1} s_{q+1})} + \frac{(\varepsilon_{q+1}\kappa_q + \varepsilon_q\kappa_{q+1})^2}{4\varepsilon_q\varepsilon_{q+1}\kappa_q\kappa_{q+1}} e^{-j(\kappa_q s_q + \kappa_{q+1} s_{q+1})} \end{aligned}$$

Note that the above solution is obtained by considering excitation of $(TE)_y$, another polarization also exist with non-zero field components H_x , H_z and E_y , i.e. $(TM)_y$ polarization. The derivation is same as $(TE)_y$ hence only the result will be given:

$$\mathbf{m}_{(1,1)} = \frac{(\kappa_q + \kappa_{q+1})^2}{4\kappa_q\kappa_{q+1}} e^{+j(\kappa_q s_q + \kappa_{q+1} s_{q+1})} - \frac{(\kappa_q - \kappa_{q+1})^2}{4\kappa_q\kappa_{q+1}} e^{+j(\kappa_q s_q - \kappa_{q+1} s_{q+1})}$$

$$\begin{aligned}
\mathbf{m}_{(1,2)} &= -\frac{\kappa_q^2 - \kappa_{q+1}^2}{4\kappa_q \kappa_{q+1}} e^{+j(\kappa_q s_q + \kappa_{q+1} s_{q+1})} - \frac{\kappa_q^2 - \kappa_{q+1}^2}{4\kappa_q \kappa_{q+1}} e^{+j(\kappa_q s_q - \kappa_{q+1} s_{q+1})} \\
\mathbf{m}_{(2,1)} &= -\frac{\kappa_q^2 - \kappa_{q+1}^2}{4\kappa_q \kappa_{q+1}} e^{-j(\kappa_q s_q - \kappa_{q+1} s_{q+1})} - \frac{\kappa_q^2 - \kappa_{q+1}^2}{4\kappa_q \kappa_{q+1}} e^{-j(\kappa_q s_q + \kappa_{q+1} s_{q+1})} \\
\mathbf{m}_{(2,2)} &= -\frac{(\kappa_q - \kappa_{q+1})^2}{4\kappa_q \kappa_{q+1}} e^{-j(\kappa_q s_q - \kappa_{q+1} s_{q+1})} + \frac{(\kappa_q + \kappa_{q+1})^2}{4\kappa_q \kappa_{q+1}} e^{-j(\kappa_q s_q + \kappa_{q+1} s_{q+1})}
\end{aligned}$$

One very important issue comes up when doing numerical modelling. As shown previously, for the matrix element of $(TE)_y$ polarization, the dielectric constant difference will further affect the actual value of the matrix elements than $(TM)_y$. When considering actual problem, whether the terminal layer and the starter layer is the same will affect the final result and as a result, the power transmittance CAN NOT simply write into the square of the field transmittance.

Appendix C

The solution to the Mathieu's Equation

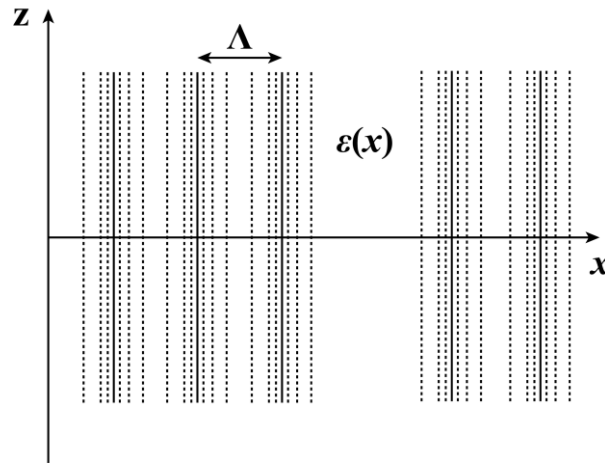


Fig. C.1 Structure with one dimensional periodicity: Λ is the period of the function $\varepsilon(x)$

Considering 1-D periodic stratified media with dielectric constant profile $\varepsilon(x)$ as shown in Fig.C.1. The medium is considered to be infinite at all direction (with 1-D in periodic). The study of wave properties within such structure were concerned with the solution to the Mathieu and Hill's equation. The general solution to the Mathieu and Hill's equation is very complicated. Here, the derivation of the infinite matrix involves solving Mathieu's equation is shown.

The Mathieu's equation is a second order homogeneous linear differential equation of the form:

$$\frac{d^2}{dx^2} F(x) + [p - 2q \cos(2x)] F(x) = 0 \quad (\text{C.1})$$

According to the Floquet theorem, there always exist one solution:

$$F(x) = e^{j\beta_B x} f(x) \quad (\text{C.2})$$

where $f(x)$ is a periodic function. Note that in general, the β_B can be both plus or minus representing waves travelling in $\pm x$ direction. However, only plus sign is necessary to be retained here in order to determine the eigen mode of the given geometry. Thus, the periodic function is expanded as Fourier series given by:

$$f(x) = \sum_{m=-\infty}^{+\infty} \zeta_m e^{j2mx} \quad (\text{C.3})$$

From equation (C.1) (C.2) and (C.3), it yields:

$$\frac{d^2}{dx^2} \sum_{m=-\infty}^{+\infty} \zeta_m e^{j(2m+\beta_B)x} + [p - 2q \cos(2x)] \sum_{m=-\infty}^{+\infty} \zeta_m e^{j(2m+\beta_B)x} = 0$$

∴

$$-(2m + \beta_B)^2 \sum_{m=-\infty}^{+\infty} \zeta_m e^{j(2m+\beta_B)x} + p \sum_{m=-\infty}^{+\infty} \zeta_m e^{j(2m+\beta_B)x} - 2q \cos(2x) \sum_{m=-\infty}^{+\infty} \zeta_m e^{j(2m+\beta_B)x} = 0$$

The term $\cos(2x)$ can be written as

$$\cos(2x) = \frac{1}{2} (e^{2jx} + e^{-2jx})$$

Thus, it yields

$$\left[p - (2m + \beta_B)^2 \right] \sum_{m=-\infty}^{+\infty} \zeta_m e^{j(2m+\beta_B)x} - q \sum_{m=-\infty}^{+\infty} \zeta_m \left\{ e^{j[2(m+1)+\beta_B]x} + e^{j[2(m-1)+\beta_B]x} \right\} = 0 \quad (\text{C.4})$$

Equation (C.4) should be satisfied for all x and thus the equation reduced to:

$$\left[(2m + \beta_B)^2 - p \right] \zeta_m + q(\zeta_{m+1} + \zeta_{m-1}) = 0 \quad (\text{C.5})$$

Equation (C.5) represents a set of equations and can be written into a matrix form:

$$\left\{ \begin{array}{ccccccc} \dots & \dots & \dots & \dots & \dots & \dots & \dots \\ \vdots & (\beta_B - 4)^2 & q & 0 & 0 & 0 & \vdots \\ \vdots & q & (\beta_B - 2)^2 & q & 0 & 0 & \vdots \\ \vdots & 0 & q & \beta_B^2 & q & 0 & \vdots \\ \vdots & 0 & 0 & q & (\beta_B + 2)^2 & q & \vdots \\ \vdots & 0 & 0 & 0 & q & (\beta_B + 4)^2 & \vdots \\ \dots & \dots & \dots & \dots & \dots & \dots & \dots \end{array} \right\} - p\mathbf{I} \left\{ \begin{array}{c} \vdots \\ \zeta_{-2} \\ \zeta_{-1} \\ \zeta_0 \\ \zeta_{+1} \\ \zeta_{+2} \\ \vdots \end{array} \right\} = 0 \quad (\text{C.6})$$

Where \mathbf{I} is the identity matrix.

Thus, the solution of the equation (C.6) can be obtained through calculating the determinate of the matrix:

$$\det(\overline{\overline{\mathbf{M}}} - p\mathbf{I}) = 0 \quad (\text{C.7})$$

Where matrix $\overline{\overline{\mathbf{M}}}$ is the tridiagonal matrix in equation(C.6)

Appendix D

Coupled Mode Theory in Sinusoidally Stratified media

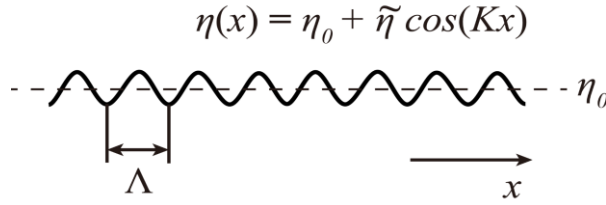


Fig. D.1 Periodically stratified media with index distribution of $\eta(x) = \eta_0 + \eta \cos(Kx)$ along x direction.

As illustrated in Fig.D.1. Assuming the inhomogeneous media with sinusoidal variation of refractive index and a plane wave along x direction interacts with the media. The period of such structure is Λ . The index profile is given by a periodic function conveniently written as $\eta(x) = \eta_0 + \tilde{\eta} \cos(Kx)$, where $K = 2\pi/\Lambda$ and $\tilde{\eta}$ is the amplitude of the index modulation $\tilde{\eta} \ll \eta_0$. Thus:

$$\eta^2(x) = \eta_0^2 + \tilde{\eta}^2 \cos^2(Kx) + 2\eta_0\tilde{\eta} \cos(Kx) \approx \eta_0^2 + 2\eta_0\tilde{\eta} \cos(Kx) \quad (\text{D.1})$$

Define $k_0 = \omega_0/c = 2\pi/\lambda_0$, our CMT is based on scalar wave equation:

$$\frac{d^2}{dx^2} F(x) + k_0^2 \eta^2(x) F(x) = 0 \quad (\text{D.2})$$

Assuming a general solution of (3.12) is a perturbation of the original equation

$$\frac{d^2}{dx^2} F(x) + k_0^2 \eta_0^2 F(x) = 0 \quad (\text{D.3})$$

with the form of:

$$F(x) = A(x) \exp(-j\bar{\beta}x) + B(x) \exp(+j\bar{\beta}x) \quad (\text{D.4})$$

implies that the amplitudes $A(x)$ and $B(x)$ depends on x , where $\bar{\beta} = k_0\eta_0$. Thus,

$$\begin{aligned} \frac{d^2}{dx^2} F(x) = & \frac{d^2}{dx^2} A(x) e^{-j\bar{\beta}x} - 2j\bar{\beta} \frac{d}{dx} A(x) e^{-j\bar{\beta}x} - \bar{\beta}^2 A(x) e^{-j\bar{\beta}x} \\ & + \frac{d^2}{dx^2} B(x) e^{+j\bar{\beta}x} + 2j\bar{\beta} \frac{d}{dx} B(x) e^{+j\bar{\beta}x} - \bar{\beta}^2 B(x) e^{-j\bar{\beta}x} \end{aligned} \quad (\text{D.5})$$

Equation (D.1) to (D.5) yields:

$$\begin{aligned}
& \frac{d^2}{dx^2} A(x)e^{-j\bar{\beta}x} - 2j\bar{\beta} \frac{d}{dx} A(x)e^{-j\bar{\beta}x} \\
& + \frac{d^2}{dx^2} B(x)e^{+j\bar{\beta}x} + 2j\bar{\beta} \frac{d}{dx} B(x)e^{+j\bar{\beta}x} \\
& + 2k_0^2 \eta_0 \tilde{\eta} \cos(Kx) [A(x)e^{-j\bar{\beta}x} + B(x)e^{+j\bar{\beta}x}] = 0
\end{aligned} \tag{D.6}$$

applying widely used slowly varying envelope approximation, i.e.:

$$\begin{aligned}
\left| \frac{d^2}{dx^2} A(x) \right| & \ll \left| \bar{\beta} \frac{d}{dx} A(x) \right| \\
\left| \frac{d^2}{dx^2} B(x) \right| & \ll \left| \bar{\beta} \frac{d}{dx} B(x) \right|
\end{aligned} \tag{D.7}$$

Equation (D.6) reduces to:

$$\begin{aligned}
& -2j\bar{\beta} \frac{d}{dx} A(x)e^{-j\bar{\beta}x} + 2j\bar{\beta} \frac{d}{dx} B(x)e^{+j\bar{\beta}x} \\
& + 2k_0^2 \eta_0 \tilde{\eta} \cos(Kx) [A(x)e^{-j\bar{\beta}x} + B(x)e^{+j\bar{\beta}x}] = 0
\end{aligned} \tag{D.8}$$

Multiply $\exp(-j\bar{\beta}x)$ on both side of (D.8) and since $\cos(Kx) = (e^{-jKx} + e^{+jKx})/2$, it yields:

$$\begin{aligned}
& -2j\bar{\beta} \frac{d}{dx} A(x)e^{-j\bar{\beta}x} + 2j\bar{\beta} \frac{d}{dx} B(x)e^{+j\bar{\beta}x} \\
& + k_0^2 \eta_0 \tilde{\eta} (e^{-jKx} + e^{+jKx}) [A(x)e^{-j\bar{\beta}x} + B(x)e^{+j\bar{\beta}x}] = 0
\end{aligned} \tag{D.9}$$

Further approximation assuming $2\bar{\beta} \cong K$, which implies that the wavelength is near the Bragg resonance. Thus, equation (D.9) ended up with equation:

$$2j\bar{\beta} \frac{d}{dx} B(x) = k_0 \eta_0 \tilde{\eta} A(x) e^{-j(2\bar{\beta}-K)x} \tag{D.10}$$

If we multiply $\exp(+j\bar{\beta}x)$ on both side of (D.8) and follow the same process, the equation ended up with:

$$2j\bar{\beta} \frac{d}{dx} A(x) = k_0 \eta_0 \tilde{\eta} B(x) e^{+j(2\bar{\beta}-K)x} \tag{D.11}$$

Equation (D.10) and (D.11) are two coupled equations and can be write into a more compact form:

$$\frac{d}{dx} A(x) = -j\kappa B(x) e^{+j\Delta\beta x} \tag{D.12}$$

$$\frac{d}{dx} B(x) = j\kappa A(x) e^{-j\Delta\beta x} \tag{D.13}$$

where $\kappa = k_0^2 \eta_0 \tilde{\eta} / 2\bar{\beta}$ is known as (complex) coupling coefficient of the grating and $\Delta\beta = 2\bar{\beta} - K$ is called complex detuning.

From the two coupled equations, it can be obtained:

$$A(x) = C_1 e^{j\frac{\Delta\beta}{2}x+sx} + C_2 e^{j\frac{\Delta\beta}{2}x-sx} \quad (\text{D.14})$$

$$B(x) = D_1 e^{-j\frac{\Delta\beta}{2}x+sx} + D_2 e^{-j\frac{\Delta\beta}{2}x-sx} \quad (\text{D.15})$$

where $s = \sqrt{-\Delta\beta^2 + 4\kappa^2}/2$. Thus, the general solution is: The general solutions can be written as:

$$E(x) = \sum_{m=\pm 1} C_m e^{-j\left[j\sqrt{\kappa^2 - \left(\frac{\Delta\beta}{2}\right)^2} + \frac{2m\pi}{\Lambda}\right]x} + \sum_{m=\pm 1} D_m e^{+j\left[j\sqrt{\kappa^2 - \left(\frac{\Delta\beta}{2}\right)^2} + \frac{2m\pi}{\Lambda}\right]x}$$

Appendix E

Chebyshev Identity and Power N of

Unimodular Matrix

According to the Floquet theorem, in an infinite periodic structure with period L , field at x and $x+L$ has no difference except a complex constant. Hence the Bloch wave satisfies the following eigenvalue problem:

$$\mathbf{m}\Psi = e^{-jKL}\Psi \quad (\text{E.1})$$

where Ψ is the eigen-vector (normalized) of the matrix \mathbf{m} whose eigenvalue is $\exp(-jKL)$. \mathbf{m} is the unit-cell translation matrix $(m_{11}, m_{12}, m_{21}, m_{22})$ and the power N of such translation matrix is given by equation:

$$\mathbf{M}_T = \mathbf{m}^N = \begin{pmatrix} m_{11} & m_{12} \\ m_{21} & m_{22} \end{pmatrix}^N = \begin{pmatrix} m_{11}U_{N-1} - U_{N-2} & m_{12}U_{N-1} \\ m_{21}U_{N-1} & m_{22}U_{N-1} - U_{N-2} \end{pmatrix} \quad (\text{E.2})$$

where U_N is known as Chebyshev polynomials of the second kind. In this section, a simple proof is given as follow.

Equation (E.1) gives:

$$\det(\mathbf{m} - e^{-jKL}\mathbf{I}) = 0 \quad (\text{E.3})$$

or equivalently:

$$e^{\pm jKL} = \frac{1}{2}(m_{11} + m_{22}) \pm \sqrt{\frac{1}{4}(m_{11} + m_{22})^2 - 1} \quad (\text{E.4})$$

Without loss of generality, the eigen-vector Ψ is often normalized to unit length and gives:

$$\Psi = \begin{pmatrix} \psi_{\pm}^+ \\ \psi_{\pm}^- \end{pmatrix} = \begin{pmatrix} \frac{m_{12}}{\sqrt{m_{12}^2 + (e^{\pm jKL} - m_{11})^2}} \\ \frac{e^{-jKL} - m_{11}}{\sqrt{m_{12}^2 + (e^{\pm jKL} - m_{11})^2}} \end{pmatrix} \quad (\text{E.5})$$

Suppose \mathbf{m} is diagonalizable, chosen \mathbf{P} such that

$$\mathbf{P}^{-1}\mathbf{m}\mathbf{P} = \begin{pmatrix} e^{+jKL} & 0 \\ 0 & e^{-jKL} \end{pmatrix} \quad (\text{E.6})$$

Then

$$(\mathbf{P}^{-1}\mathbf{m}\mathbf{P})^N = \begin{pmatrix} e^{+jNKL} & 0 \\ 0 & e^{-jNKL} \end{pmatrix} = \mathbf{P}^{-1}\mathbf{m}^N\mathbf{P} \quad (\text{E.7})$$

Hence

$$\mathbf{m}^N = \begin{pmatrix} e^{+jNKL} & 0 \\ 0 & e^{-jNKL} \end{pmatrix} = \mathbf{P} \begin{pmatrix} e^{+jNKL} & 0 \\ 0 & e^{-jNKL} \end{pmatrix} \mathbf{P}^{-1} \quad (\text{E.8})$$

i.e. the N th power of the transformed matrix is equal to the transform of the N th power of the matrix.

The matrix \mathbf{P} that can transform \mathbf{m} into a diagonal matrix can be constructed by the eigenvectors of \mathbf{m} , given by:

$$\mathbf{P}^{-1} = \frac{1}{\sqrt{(\psi_+^+ \psi_-^- - \psi_-^+ \psi_+^-)}} \begin{pmatrix} \psi_+^+ & \psi_-^+ \\ \psi_+^- & \psi_-^- \end{pmatrix} \quad (\text{E.9})$$

$$\mathbf{P} = \frac{1}{\sqrt{(\psi_+^+ \psi_-^- - \psi_-^+ \psi_+^-)}} \begin{pmatrix} \psi_-^- & -\psi_-^+ \\ -\psi_+^- & \psi_+^+ \end{pmatrix} \quad (\text{E.10})$$

From (E.5), (E.8), (E.9), (E.10) and carrying out matrix multiplication:

$$\mathbf{m}^N = \begin{pmatrix} \frac{m_{11} \sin NKL - \sin(N-1)KL}{\sin KL} & \frac{m_{12} \sin NKL}{\sin KL} \\ \frac{m_{21} \sin NKL}{\sin KL} & \frac{m_{22} \sin NKL - \sin(N-1)KL}{\sin KL} \end{pmatrix} \quad (\text{E.11})$$

And from (E.4):

$$\cos KL = \frac{1}{2}(m_{11} + m_{22}) \quad (\text{E.12})$$

Hence

$$KL = \cos^{-1} \left[\frac{1}{2}(m_{11} + m_{22}) \right] \quad (\text{E.13})$$

In mathematics, polynomial with the form of

$$U_N = \frac{\sin(N+1)\theta}{\sin\theta}$$

is known as Chebyshev polynomials of the second kind. Hence the N th power of the unimodular matrix is given by:

$$\mathbf{m}^N = \begin{pmatrix} m_{11}U_{N-1} - U_{N-2} & m_{12}U_{N-1} \\ m_{21}U_{N-1} & m_{22}U_{N-1} - U_{N-2} \end{pmatrix}$$

Appendix F

Poynting Vector Within the Stopband of the Periodic Structure

The objective of this section is to investigate the Poynting vector within periodic structure. Considering 1-D periodic structure along z direction as shown below in Fig. F.1:

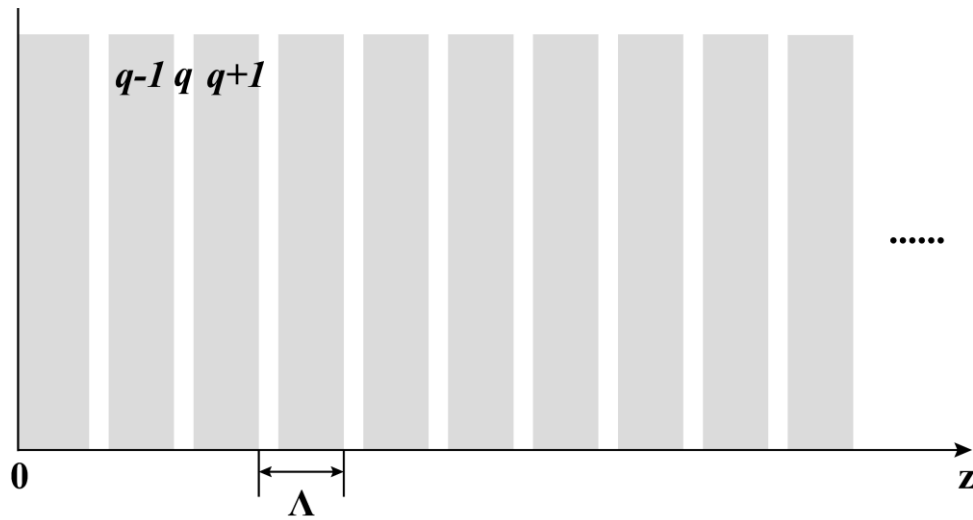


Fig F.1 Schematic of semi-infinite periodic structure

For the sake of argument, the structure is semi-infinite.

As it is already obtained from the numerical calculation (referring to Fig. 3.3.5 in chapter 3), the field distribution $E_y(z)$ of a Bloch wave is evanescent within the ‘stopband’ region of this periodic media. However, this evanescent ‘Bloch wave’ doesn’t require lossy media. The proof and analytical explanation is given as follow.

In a lossless periodic media, considering field component $E_y(z)$ and $H_x(z)$. The relationship is given by Maxwell’s equations:

$$\nabla \times \mathbf{E} = -j\omega\mu_0\mathbf{H} \quad (\text{F.1})$$

It is already known that in each region q , $q = 1, 2, 3, \dots$

$$E_y(z) = E_f e^{-j\beta_q z} + E_r e^{+j\beta_q z} \quad (\text{F.2})$$

where E_f and E_r are given by the matrix relationship and satisfied the interface condition.

The magnetic field satisfy:

$$H_x(z) = \frac{\beta_q}{\omega\mu} [E_f e^{-j\beta_q z} + E_r e^{+j\beta_q z}] \quad (\text{F.3})$$

From (F.2) and (F.3), the z component of Poynting vector is given by

$$S_z = \frac{1}{2} \text{Re} \{ E_y H_z^* \} = \frac{\beta_q}{2\omega\mu} [|E_f|^2 - |E_r|^2] \quad (\text{F.4})$$

where ‘*’ denoted complex conjugate.

Next, before further derivation, some properties of the transfer matrix have to be used. As shown in Chapter 3, the transfer matrix relationship is given by:

$$\begin{bmatrix} A & B \\ C & D \end{bmatrix} \begin{bmatrix} E_f \\ E_r \end{bmatrix} = e^{jK\Lambda} \begin{bmatrix} E_f \\ E_r \end{bmatrix} \quad (\text{F.5})$$

where A , B , C and D are matrix elements, $\exp(jK\Lambda)$ is the eigenvalue of such transfer matrix where Λ is the single period dimension. K represents the Bloch wavevector and in general can be complex (stop-band) or pure real (pass-band).

Another property of the transfer matrix is that, $C = B^*$ and $D = A^*$. It is proved that the matrix is an unimodular matrix:

$$\det \begin{bmatrix} A & B \\ C & D \end{bmatrix} = 1 \quad (\text{F.6})$$

Thus:

$$AD - BC = AA^* - BB^* = 1 \quad (\text{F.7})$$

From equation (F.5) and (F.7), it yields:

$$\begin{bmatrix} A - e^{jK\Lambda} & B \\ B^* & A^* - e^{jK\Lambda} \end{bmatrix} \begin{bmatrix} E_f \\ E_r \end{bmatrix} = 0 \quad (\text{F.8})$$

Thus:

$$\det \begin{bmatrix} A - e^{jK\Lambda} & B \\ B^* & A^* - e^{jK\Lambda} \end{bmatrix} = 0 \quad (\text{F.9})$$

Which yields:

$$(A - e^{jK\Lambda})E_f + BE_r = 0 \quad (\text{F.10})$$

Thus:

$$E_r = \frac{(e^{jK\Lambda} - A)}{B} E_f \quad (\text{F.11})$$

From equation (F.4) and (F.11)

$$S_z = \frac{1}{2} \text{Re} \{ E_y H_z^* \} \propto \left[|E_f|^2 - |E_r|^2 \right] \propto \left[|B|^2 - |e^{jK\Lambda} - A|^2 \right] \quad (\text{F.12})$$

To investigate the Poynting vector within stop band, we first consider Bloch wave vector. Since K is in general a complex number within the stop-band, more importantly, K is of the form of:

$$K = \frac{m\pi}{\Lambda} + jK_i \quad (\text{F.13})$$

where $m = 1, 2, 3, \dots$ and K_i is the imaginary part of K . Such results can be obtained through CMT or matrix method and is shown in other part of this thesis.

From Chapter 3, it is obtained that

$$\cos(K\Lambda) = \frac{1}{2}(A + D) \quad (\text{F.14})$$

Thus:

$$e^{jK\Lambda} + e^{-jK\Lambda} = A + A^* \quad (\text{F.15})$$

From equation (F.13) and (F.15), it yields:

$$A + A^* = (-1)^m (e^{K_i\Lambda} + e^{-K_i\Lambda}) \quad (\text{F.16})$$

From (F.7) and (F.12), it yields:

$$S_z \propto \left[|B|^2 - |e^{jK\Lambda} - A|^2 \right] = AA^* - 1 - |e^{jK\Lambda} - A|^2 \quad (\text{F.17})$$

From (F.13) and (F.17):

$$e^{jK\Lambda} - A = e^{j\left(\frac{m\pi}{\Lambda} + jK_i\right)\Lambda} - A = (-1)^m e^{-K_i\Lambda} - A \quad (\text{F.18})$$

\therefore

$$(e^{jK\Lambda} - A)^* = (-1)^m e^{-K_i\Lambda} - A^* \quad (\text{F.19})$$

From equation (F.12), (F.18) and (F.19):

$$\begin{aligned} S_z &\propto AA^* - 1 - |e^{jK\Lambda} - A|^2 \\ &= AA^* - 1 - [(-1)^m e^{-K_i\Lambda} - A][(-1)^m e^{-K_i\Lambda} - A^*] \\ &= (-1)^m e^{-K_i\Lambda} (A + A^*) - e^{-2K_i\Lambda} - 1 \end{aligned} \quad (\text{F.20})$$

From equation (F.16) and (F.20):

$$\begin{aligned} S_z &\propto (-1)^m e^{-K_i\Lambda} (A + A^*) - e^{-2K_i\Lambda} - 1 \\ &= (-1)^{2m} e^{-K_i\Lambda} (e^{K_i\Lambda} + e^{-K_i\Lambda}) - e^{-2K_i\Lambda} - 1 \\ &= 0 \end{aligned}$$

Hence, the real part of the Poynting vector within the stop-band is zero. Although K is complex, it is NOT lossy.

Q.E.D.

Appendix G

Dielectric Slab Waveguide

The simplest geometry of the dielectric waveguide is the flat dielectric slab, similar to the two-parallel-plate metal waveguide discussed previously. As illustrated in Fig.G.1, the slab dielectric waveguide consists of a slab of dielectric of refractive index, η_1 , occupying the region $-d < y < +d$; the region below ($y < -d$) and above ($y > +d$) have refractive index η_2 with $\eta_1 > \eta_2$.

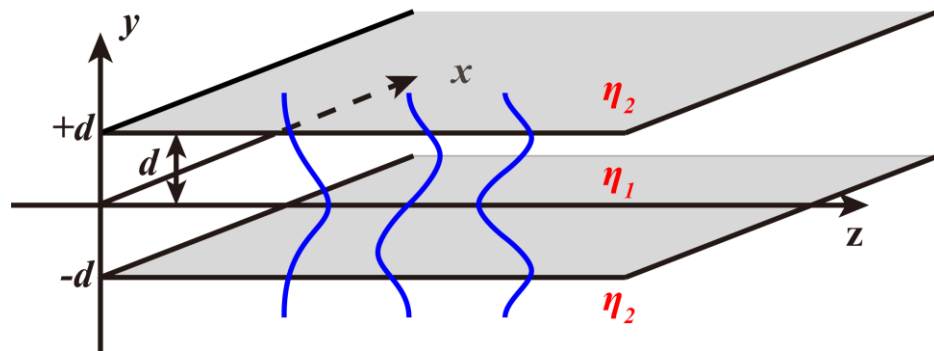


Fig G.1 Schematic of slab dielectric waveguide

For the sake of argument, assuming the waveguide is symmetric and the wave is propagating along the z direction. The relationship $\partial / \partial x \equiv 0$ is satisfied due to the geometry considered in this case. Thus, the wave equation for the tangential field is given by:

$$\left(\frac{\partial^2}{\partial y^2} + \frac{\partial^2}{\partial z^2} + k_0^2 \eta_q^2 \right) E_x(y, z) = 0 \quad (\text{G.1})$$

where $q = 1, 2$. Clearly, separation of variable is satisfied in this case:

$$E_x(y, z) = E_x(y) e^{-j\beta z} \quad (\text{G.2})$$

where β is the same in both region 1 and 2.

In region 1, define

$$k_0^2 \eta_1^2 - \beta^2 = p^2 \quad (\text{G.3})$$

In region 2, define

$$\beta^2 - k_0^2 \eta_2^2 = h^2 \quad (\text{G.4})$$

Note that there is also continuum mode exist in this situation, the discussion here focuses on the conventional bound mode, i.e. field will decay to zero at $\pm\infty$

For $y > +d$

$$E_x = A_2 e^{-hy} \quad ; \quad H_z = \frac{h}{j\omega\mu} A_2 e^{-hy} \quad (\text{G.5})$$

For $y < -d$

$$E_x = D_2 e^{hy} \quad ; \quad H_z = -\frac{h}{j\omega\mu} D_2 e^{hy} \quad (\text{G.6})$$

For $-d < y < +d$

$$E_x = B_1 \cos py + A_1 \sin py \quad ; \quad H_z = \frac{p}{j\omega\mu} (B_1 \sin py - A_1 \cos py) \quad (\text{G.7})$$

Thus, at $y = \pm d$, the tangential field must be continuous, which yields:

$$\frac{p}{h} (B_1 \sin pd - A_1 \cos pd) = B_1 \cos pd + A_1 \sin pd \quad (\text{G.8})$$

and

$$\frac{p}{h} (B_1 \sin pd + A_1 \cos pd) = B_1 \cos pd - A_1 \sin pd \quad (\text{G.9})$$

Equation (G.8) and (G.9) yields:

$$\frac{p}{h} B_1 \sin pd = B_1 \cos pd \quad (\text{G.10})$$

$$-\frac{p}{h} A_1 \cos pd = A_1 \sin pd \quad (\text{G.11})$$

Note that very importantly, B_1 and A_1 cannot be simply eliminated since the term $B_1 \sin py$ and $A_1 \cos py$ are independent which gives two independent type of solutions (conditions).

For symmetric case, i.e. considering $A_1 = 0$, from equation (G.10), it yields:

$$p \tan pd = h \quad (\text{G.12})$$

Also, it is defined that $k_0^2 \eta_1^2 - \beta^2 = p^2$ and $\beta^2 - k_0^2 \eta_2^2 = h^2$, thus:

$$k_0^2 d^2 (\eta_1^2 - \eta_2^2) = p^2 d^2 + h^2 d^2 \quad (\text{G.13})$$

From equation (G.12)

$$p^2 d^2 \tan^2 pd = d^2 h^2 \quad (\text{G.14})$$

Define two new variables: $u = hd$ and $v = pd$, thus equation (G.14) become:

$$v^2 \tan^2 v = u^2 \quad (\text{G.15})$$

where the variables $u = hd$ and $v = pd$ are linked through:

$$v^2 + u^2 = k_0^2 d^2 (\eta_1^2 - \eta_2^2) \quad (\text{G.16})$$

Now, to obtain the mode solution, equation (G.15) need to be solved numerically or graphically (no analytical solution).

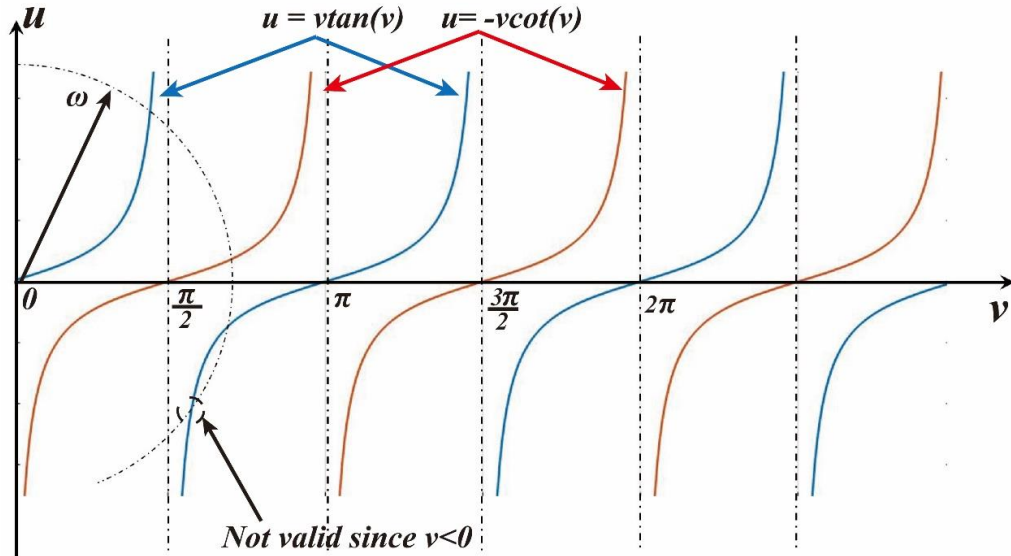


Fig G.2 Schematic of slab dielectric waveguide

As shown in Fig G.2. the plot of $\omega^2 = v^2 + u^2$ (circle with a radius of ω) and the plot of $v^2 \tan^2 v + v^2$ is plotted. The solution is the intersect points. Similarly, for anti-symmetric solution, i.e. $B_1 = 0$. Equation (G.15) become $v^2 \cot^2 v = u^2$.

Appendix H

Waveguide Coupling: A Coupled Mode Approach

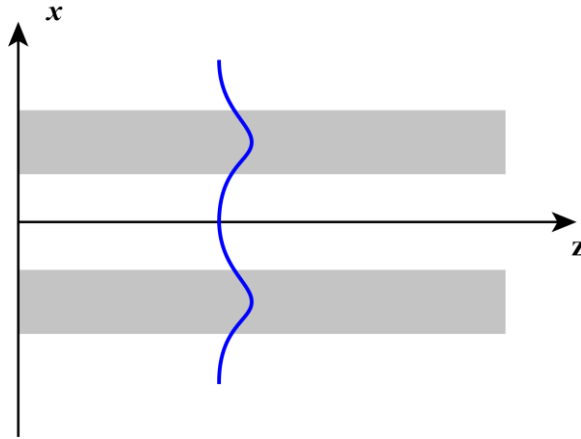


Fig H.1 Schematic of two coupled waveguides

In this section, we consider the coupling between two parallel waveguides that are separated with a finite distance. The coupling occurs when the overlap of the mode from two waveguides present. Before the derivation, let's define the permittivity distribution of the composited waveguide to be:

$$\varepsilon(x) = \begin{cases} \varepsilon_A, & \text{core A} \\ \varepsilon_B, & \text{core B} \\ \varepsilon_C, & \text{elsewhere} \end{cases} \quad (\text{H.1})$$

Further define:

$$\Delta\varepsilon_A(x) = \begin{cases} \varepsilon_A - \varepsilon_C, & \text{core A} \\ 0, & \text{elsewhere} \end{cases} \quad (\text{H.2})$$

$$\Delta\varepsilon_B(x) = \begin{cases} \varepsilon_B - \varepsilon_C, & \text{core B} \\ 0, & \text{elsewhere} \end{cases} \quad (\text{H.3})$$

$$\bar{\varepsilon}(x) = \varepsilon_C \quad (\text{H.4})$$

The permittivity profile of the composited waveguide is thus:

$$\varepsilon(x) = \bar{\varepsilon}(x) + \Delta\varepsilon_A(x) + \Delta\varepsilon_B(x) \quad (\text{H.5})$$

A schematic of simple $\varepsilon(x)$ distribution illustrated in Fig.H.1. It is assumed in this discussion that in each waveguide, only fundamental mode is supported. Thus, from waveguide A, it yields:

$$\left(\frac{\partial^2}{\partial x^2} + \frac{\partial^2}{\partial z^2} + k_0^2 [\bar{\varepsilon}(x) + \Delta\varepsilon_A(x)] \right) F_A(x, z) = 0 \quad (\text{H.6})$$

where

$$F_A(x, z) = A_0 f_A(x) e^{-j\beta_A z} \quad (\text{H.7})$$

Similarly, from waveguide B:

$$\left(\frac{\partial^2}{\partial x^2} + \frac{\partial^2}{\partial z^2} + k_0^2 [\bar{\varepsilon}(x) + \Delta\varepsilon_B(x)] \right) F_B(x, z) = 0 \quad (\text{H.8})$$

where

$$F_B(x, z) = B_0 f_B(x) e^{-j\beta_B z} \quad (\text{H.9})$$

The mode of the two coupled waveguides $F_C(x, z)$ can be written as the superposition of the two individual waveguides with some perturbation, i.e. perturbation approximation:

$$F_C(x, z) = A(z) f_A(x) e^{-j\beta_A z} + B(z) f_B(x) e^{-j\beta_B z} \quad (\text{H.10})$$

Satisfied the wave equation:

$$\left(\frac{\partial^2}{\partial x^2} + \frac{\partial^2}{\partial z^2} + k_0^2 [\bar{\varepsilon}(x) + \Delta\varepsilon_B(x) + \Delta\varepsilon_A(x)] \right) F_C(x, z) = 0 \quad (\text{H.11})$$

The next problem is to solve $A(z)$ and $B(z)$. We substitute equation (H.10) into equation (H.11), and from (H.6) to (H.9), use the assumption of slow varying envelope approximation:

$$\begin{aligned} \left| \frac{d^2}{dz^2} A(z) \right| &\ll \left| \beta_A \frac{d}{dz} A(z) \right| \\ \left| \frac{d^2}{dz^2} B(z) \right| &\ll \left| \beta_B \frac{d}{dz} B(z) \right| \end{aligned} \quad (\text{H.12})$$

It yields:

$$\begin{aligned} -2j\beta_A \frac{d}{dz} A(z) e^{-j\beta_A z} - 2j\beta_B \frac{d}{dz} B(z) e^{-j\beta_B z} \\ + k_0^2 \Delta\varepsilon_A(x) A(z) e^{-j\beta_A z} + k_0^2 \Delta\varepsilon_B(x) B(z) e^{-j\beta_B z} = 0 \end{aligned} \quad (\text{H.13})$$

To obtain $A(z)$ and $B(z)$, we multiply both side of (H.13) with $[f_A(x)]^*$ and integrated over x to get the equation only in z . Similar process is done by multiplying $[f_B(x)]^*$. After some algebra, it yields:

$$\frac{d}{dz} A(z) = -j\kappa_{AB} B(z) e^{+j(\beta_B - \beta_A)z} - j\kappa_{AA} A(z) \quad (\text{H.14})$$

$$\frac{d}{dz}B(z) = -j\kappa_{BA}A(z)e^{-j(\beta_A-\beta_B)z} - j\kappa_{BB}B(z) \quad (\text{H.15})$$

where:

$$\kappa_{AB} = C \int_{-\infty}^{+\infty} [f_A(x)]^* \Delta\varepsilon_A(x) f_B(x) dx \quad (\text{H.16})$$

$$\kappa_{BA} = C \int_{-\infty}^{+\infty} [f_B(x)]^* \Delta\varepsilon_B(x) f_A(x) dx \quad (\text{H.17})$$

$$\kappa_{AA} = C \int_{-\infty}^{+\infty} [f_A(x)]^* \Delta\varepsilon_A(x) f_A(x) dx \quad (\text{H.18})$$

$$\kappa_{BB} = C \int_{-\infty}^{+\infty} [f_B(x)]^* \Delta\varepsilon_B(x) f_B(x) dx \quad (\text{H.19})$$

κ_{AB} and κ_{BA} are the coupling coefficient between two separate waveguides. κ_{AA} and κ_{BB} represents the change in propagation of ‘self-guide’ due to the perturbation of the other guide. Note that in general, equation (H.14) and (H.15) has another term represents the overlap between two waveguide modes, however, in this discuss, the analysis is based on weak coupling, i.e.

$$\int_{-\infty}^{+\infty} [f_A(x)]^* f_B(x) dx \ll \int_{-\infty}^{+\infty} [f_A(x)]^* f_A(x) dx$$

Thus, the overlap term is neglected.

The waveguide coupling solved using coupled mode method is rather mathematically complicated. However, if the waveguides satisfy piece-wise constant condition, the solution of the coupled waveguide mode can be obtained through transfer matrix method as discussed in chapter 3.

Appendix I

MATLAB Code for 1-D Periodic Structure

```
% INITIAL VALUE PROBLEM, 1-D PERIODIC STRUCTURE, TE POLARIZATION
```

```
% INITIALIZE MATLAB
```

```
close all;
```

```
clc;
```

```
clear all;
```

```
%%%%%%%%%%%%%%%%%%%%%%%%%%%%%%%%%%%%%%%%%%%%%%%%%%%%%%%%%%%%%%%%%%%%%%%%%
```

```
%% DASHBOARD
```

```
%%%%%%%%%%%%%%%%%%%%%%%%%%%%%%%%%%%%%%%%%%%%%%%%%%%%%%%%%%%%%%%%%%%%%%%%%
```

```
n_1R=3.5;      % refractive index for region 1
```

```
n_2R=3.2;      % refractive index for region 2
```

```
n_fR=3.5;
```

```
L_1=0.1429;    % Thickness of region 1
```

```
L_2=0.1563;    % Thickness of region 2
```

```
N=100;        % Number of Period
```

```
alpha=0.00;   % Net gain
```

```
lambda=1;
```

```
n_eff=0:0.0001:3.5;
```

```
q=1;
```

```
%%%%%%%%%%%%%%%%%%%%%%%%%%%%%%%%%%%%%%%%%%%%%%%%%%%%%%%%%%%%%%%%%%%%%%%%%
```

```
%% BUILD UNIT CELL
```

```
%%%%%%%%%%%%%%%%%%%%%%%%%%%%%%%%%%%%%%%%%%%%%%%%%%%%%%%%%%%%%%%%%%%%%%%%%
```

```
for i=1:length(n_eff);
```

```
    k_0=2*pi/lambda;
```

```
    n_I=alpha*lambda/(2*pi);
```

```
    n_1=n_1R+j*n_I;
```

```
    n_2=n_2R+j*n_I;
```

```
    n_f=n_fR+j*n_I;
```

```
    epsilon_1=n_1^2;
```

```
    epsilon_2=n_2^2;
```

```
    epsilon_f=n_f^2;
```

```
    kappa_1=sqrt(k_0^2*(n_1)^2-k_0^2*(n_eff(i))^2);
```

```
    kappa_2=sqrt(k_0^2*(n_2)^2-k_0^2*(n_eff(i))^2);
```

```
    kappa_f=sqrt(k_0^2*(n_f)^2-k_0^2*(n_eff(i))^2);
```

```
%%%%%%%%%%%%%%%%%%%%%%%%%%%%%%%%%%%%%%%%%%%%%%%%%%%%%%%%%%%%%%%%%%%%%%%%%
```

```
%% BUILD MATRIX
```

```
%%%%%%%%%%%%%%%%%%%%%%%%%%%%%%%%%%%%%%%%%%%%%%%%%%%%%%%%%%%%%%%%%%%%%%%%%
```

```
D_1=[(epsilon_2*kappa_1+epsilon_1*kappa_2)/(2*epsilon_2*kappa_1),  
      (epsilon_2*kappa_1-epsilon_1*kappa_2)/(2*epsilon_2*kappa_1);...  
      (epsilon_2*kappa_1-epsilon_1*kappa_2)/(2*epsilon_2*kappa_1),  
      (epsilon_2*kappa_1+epsilon_1*kappa_2)/(2*epsilon_2*kappa_1),];
```

```
P_2=[exp(j*kappa_2*L_2),0;...  
      0,exp(-j*kappa_2*L_2)];
```

```
D_2=[(epsilon_1*kappa_2+epsilon_2*kappa_1)/(2*epsilon_1*kappa_2),  
      (epsilon_1*kappa_2-epsilon_2*kappa_1)/(2*epsilon_1*kappa_2);...  
      (epsilon_1*kappa_2-epsilon_2*kappa_1)/(2*epsilon_1*kappa_2),  
      (epsilon_1*kappa_2+epsilon_2*kappa_1)/(2*epsilon_1*kappa_2),];
```

```
P_1=[exp(j*kappa_1*L_1),0;...  
      0,exp(-j*kappa_1*L_1)];
```

```
D_f=[(epsilon_2*kappa_1+epsilon_1*kappa_f)/(2*epsilon_2*kappa_1),  
      (epsilon_2*kappa_1-epsilon_1*kappa_f)/(2*epsilon_2*kappa_1);...  
      (epsilon_2*kappa_1-epsilon_1*kappa_f)/(2*epsilon_2*kappa_1),  
      (epsilon_2*kappa_1+epsilon_1*kappa_f)/(2*epsilon_2*kappa_1),];
```

```

Y=D_1*P_2*D_2*P_1;
A=Y^N*D_f;

%%%%%%%%%%%%%%%%%%%%%%%%%%%%%%%%%%%%%%%%%%%%%%%%%%%%%%%%%%%%%%%%%%%%%%%%
%% CHEBYSHEV METHOD
%%%%%%%%%%%%%%%%%%%%%%%%%%%%%%%%%%%%%%%%%%%%%%%%%%%%%%%%%%%%%%%%%%%%%%%%

% K(q)=(1/(L_1+L_2))*acos((1/2)*(Y(1,1)+Y(2,2)));
% U_N(q)=(sin((N+1)*K(q)*(L_1+L_2)))/(sin(K(q)*(L_1+L_2)));
% U_N_1(q)=(sin(N*K(q)*(L_1+L_2)))/(sin(K(q)*(L_1+L_2)));
% U_N_2(q)=(sin((N-1)*K(q)*(L_1+L_2)))/(sin(K(q)*(L_1+L_2)));
% A_11(q)=Y(1,1)*U_N_1(q)-U_N_2(q);
% A_12(q)=Y(1,2)*U_N_1(q);
% A_21(q)=Y(2,1)*U_N_1(q);
% A_22(q)=Y(2,2)*U_N_1(q)-U_N_2(q);
B_11(q)=A(1,1);
B_12(q)=A(1,2);
B_21(q)=A(2,1);
B_22(q)=A(2,2);
Z_load_over_z0(q)=(A(1,1)+A(2,1))/(A(1,1)-A(2,1));
ref(q)=(abs(A(2,1)/A(1,1)))^2;
trans(q)=abs(1/A(1,1));
q=q+1;
end

%%%%%%%%%%%%%%%%%%%%%%%%%%%%%%%%%%%%%%%%%%%%%%%%%%%%%%%%%%%%%%%%%%%%%%%%
%% OUTOUT
%%%%%%%%%%%%%%%%%%%%%%%%%%%%%%%%%%%%%%%%%%%%%%%%%%%%%%%%%%%%%%%%%%%%%%%%

%plot(n_eff,real(Z_load_over_z0),'b');
%hold on
%plot(n_eff,imag(Z_load_over_z0),'r');
plot(n_eff,ref,'b')
%plot(n_eff,trans,'b')
%plot(real(B_11),imag(B_11),'r')
%location=find(ref<0.9);
%ref=ref(location);
%n_eff=n_eff(location);
%Location=find(diff(sign(diff(ref)))==2)+1;
%N_new=n_eff(Location);

```

Appendix J

MATLAB Code Example for 2-D PC

```

% 2-D PC, TE POLARIZATION, SQUARE CASE

% INITIALIZE MATLAB

close all;
clc;
clear all;
%%%%%%%%%%%%%%%%%%%%%%%%%%%%%%%%%%%%%%%%%%%%%%%%%%%%%%%%%%%%%%%%%%%%%%%%
%% DASHBOARD
%%%%%%%%%%%%%%%%%%%%%%%%%%%%%%%%%%%%%%%%%%%%%%%%%%%%%%%%%%%%%%%%%%%%%%%%
n_a=3.3776;          % refractive index of first
n_1=3.2953;          % refractive index for region 1
n_2=3.3776;          % refractive index for region 2
n_f=3.3776;          % refractive index for last region
L_a=2;              % Thickness of first region
L_1=0.059;          % Thickness of region 1
L_2=0.236;          % Thickness of region 2
L_f=2;              % Thickness of first region
N=5000000;          % Number of Period of Bragg region
lambda=0.8:0.0002:1.2;

%%%%%%%%%%%%%%%%%%%%%%%%%%%%%%%%%%%%%%%%%%%%%%%%%%%%%%%%%%%%%%%%%%%%%%%%
%% DESIGN ENTIRE LOOP
%%%%%%%%%%%%%%%%%%%%%%%%%%%%%%%%%%%%%%%%%%%%%%%%%%%%%%%%%%%%%%%%%%%%%%%%

for t=1:length(lambda);
    beta=2*pi*0/lambda(t):0.01:2*pi*3.3776/lambda(t);
    k_0=2*pi/lambda(t);
    alpha=0;
    N_I=alpha*lambda(t)/(2*pi);
    q=1;

%%%%%%%%%%%%%%%%%%%%%%%%%%%%%%%%%%%%%%%%%%%%%%%%%%%%%%%%%%%%%%%%%%%%%%%%
%% SOLVE X DIRECTION
%%%%%%%%%%%%%%%%%%%%%%%%%%%%%%%%%%%%%%%%%%%%%%%%%%%%%%%%%%%%%%%%%%%%%%%%

for i=1:length(beta);
    kappa_1=sqrt(k_0^2*(n_1)^2-beta(i)^2);
    kappa_2=sqrt(k_0^2*(n_2)^2-beta(i)^2);
    kappa_a=sqrt(k_0^2*(n_a)^2-beta(i)^2);
    kappa_f=sqrt(k_0^2*(n_f)^2-beta(i)^2);
%%%%%%%%%%%%%%%%%%%%%%%%%%%%%%%%%%%%%%%%%%%%%%%%%%%%%%%%%%%%%%%%%%%%%%%%
%% BUILD SINGLE CELL MATRIX
%%%%%%%%%%%%%%%%%%%%%%%%%%%%%%%%%%%%%%%%%%%%%%%%%%%%%%%%%%%%%%%%%%%%%%%%
    D_a2=[(kappa_a+kappa_2)/(2*kappa_a),(kappa_a-kappa_2)/(2*kappa_a);...
          (kappa_a-kappa_2)/(2*kappa_a),(kappa_a+kappa_2)/(2*kappa_a),];
    P_a=[exp(1j*kappa_2*L_a),0;...
          0,exp(-1j*kappa_2*L_a)];
    D_21=[(kappa_2+kappa_1)/(2*kappa_2),(kappa_2-kappa_1)/(2*kappa_2);...
          (kappa_2-kappa_1)/(2*kappa_2),(kappa_2+kappa_1)/(2*kappa_2),];
    P_1=[exp(1j*kappa_1*L_1),0;...
          0,exp(-1j*kappa_1*L_1)];
    D_12=[(kappa_1+kappa_2)/(2*kappa_1),(kappa_1-kappa_2)/(2*kappa_1);...
          (kappa_1-kappa_2)/(2*kappa_1),(kappa_1+kappa_2)/(2*kappa_1),];
    P_2=[exp(1j*kappa_2*L_2),0;...

```



```

%%%%%%%%%%%%%%%%%%%%%%%%%%%%%%%%%%%%%%%%%%%%%%%%%%%%%%%%%%%%%%%%%%%%%%%%
% K(q)=(1/(L_1+L_2))*acos((1/2)*(Y(1,1)+Y(2,2)));
% U_N(q)=(sin((N+1)*K(q)*(L_1+L_2)))/(sin(K(q)*(L_1+L_2)));
% U_N_1(q)=(sin(N*K(q)*(L_1+L_2)))/(sin(K(q)*(L_1+L_2)));
% U_N_2(q)=(sin((N-1)*K(q)*(L_1+L_2)))/(sin(K(q)*(L_1+L_2)));
% A_11(q)=Y(1,1)*U_N_1(q)-U_N_2(q);
% A_12(q)=Y(1,2)*U_N_1(q);
% A_21(q)=Y(2,1)*U_N_1(q);
% A_22(q)=Y(2,2)*U_N_1(q)-U_N_2(q);
% B_11_z(k)=A_z(1,1);
% B_12_z(k)=A_z(1,2);
% B_21_z(k)=A_z(2,1);
% B_22_z(k)=A_z(2,2);
ref(k)=(abs(A_z(2,1)/A_z(1,1)))^2;
T(k)=1-ref(k);
k=k+1;
end
Trans='T';
Neff=N_eff;
LL=lambda(t)*ones(1,length(T));
ZZ(t)={[Trans,Neff]};
%plot3(LL,Neff,abs(T),'b');
%%%%%%%%%%%%%%%%%%%%%%%%%%%%%%%%%%%%%%%%%%%%%%%%%%%%%%%%%%%%%%%%%%%%%%%%
%% ONE LOOP FINISH AND OUTPUT
%%%%%%%%%%%%%%%%%%%%%%%%%%%%%%%%%%%%%%%%%%%%%%%%%%%%%%%%%%%%%%%%%%%%%%%%
plot3(LL,Neff,T,'k','MarkerSize',0.5);

hold on

clear Trans;
clear Neff;
clear T;
clear N_eff;
clear n_eff;
clear beta;
clear Beta;
clear Location;
clear location;
clear ref;
t=t+1;
end
view(3)

```